UNIVERSIDAD
DE GRANADA

Research founded by Grant BES-2016-076749

Analytical and Numerical Solutions for Emergence of Air Cavities in Ducts and Geysering

BY:
Jorge Antonio Molina Moya

A Thesis submitted to University of Granada in partial fulfilment of the requirements for the degree of Doctor of Philosophy

Advisors:
Pablo Gregorio Ortiz Rossini
Alejandro Enrique Martínez Castro

PhD Program in Civil Engineering
Department of Structural Mechanics and Hydraulic Engineering
University of Granada
Granada (Spain)

May 2021

Editor: Universidad de Granada. Tesis Doctorales
Autor: Jorge Antonio Molina Moya
ISBN: 978-84-1306-928-9
URI: http://hdl.handle.net/10481/69641

Abstract

This Thesis presents a continuous finite element model for the computation of two-phase flows with moving interfaces. The method is based on the Non-Oscillatory Finite Element (NFEM) algorithm and integrates the sign-preserving flux correction methodology, predicting with high accuracy flow dynamics and interface motion. The procedure is composed of three main stages: transport of a bounded phase function to couple fluids motion and the contact discontinuity, reinitialisation step to recover resolution of phase field, and solution of equations of motion, where both incompressible and weakly compressible assumptions are considered. For nearly incompressible flows the continuity equation is modified to preserve mass conservation by considering the parametric definition of density. Flux correction technique takes action on the three aforementioned steps. In phase function advection, limiting process that assures positivity of solution, incorporates a straightforward refinement to remove global mass residuals present in the earliest version of algorithm. Besides, new correction does not endanger efficacy of the original. To reconstruct phase function after transport, a novel non-linear (and conservative) streamlined diffusion equation is proposed, with an anisotropic diffusivity comprising artificial compression and diffusive fluxes oriented along interface displacements direction. Iterative procedure employed to solve this equation integrates flux correction techniques to keep phase function bounds. Finally, hydrodynamics resolution incorporates an improved bound estimation that includes interface information to substantially reduce nonphysical overshoots appearing along the contact discontinuity. On the other hand, stability of artificial stratified flows has been explored in problems involving Kelvin-Helmholtz instabilities. This study indicates that, to avoid nonphysical amplification of perturbations, thickness of numerical representation of interface should be reduced to some extent. Then, strategies to decrease transition thickness between both fluids are examined, and interface refinement results the most suited. Consequently, a novel inexpensive nested-grid refinement is proposed. The algorithm is also founded in flux-correction principles, ensuring conservation and monotonicity of the variables during

dynamical adaptation. Efficacy of numerical model is assessed with stringent benchmark tests both for transport/reinitialisation and for two fluids interface propagation.

Second target of this work is to scrutinise dynamics of emergence and propagation of air cavities and resulting geysering events. Presented numerical model along with supplementary theoretical approaches have been used for this purpose. Analytical model, accomplished by a control volume analysis, is able to predict dynamics of single and consecutive elongated rising bubbles and takes into account gas expansion effects and free surface position to determine impulsion of water above the bubble. This model also reveals conditions that trigger a sudden bubble decompression, and therefore a severe geysering event. In numerical experiments, weakly compressible fluid assumption is essential for proper momentum transfer between phases in the aforementioned dynamics, particularly for bubble rising process. A first series of simulations reproduces air cavities propagating in straight and inclined ducts. Results show a good agreement with existing laboratory outputs. A second set of simulations examines flow conditions for emergence of air pockets in ducts, giving rise to simple solutions that provide the required flow rate to avoid the intrusion of air. Finally, axisymmetric and complete three dimensional versions of the numerical model are used to perform rising Taylor bubbles in vertical ducts and geysering events. These outputs complement analytical results by giving precise flow details, in particular above the ground level.

Resumen

En esta Tesis se presenta un novedoso modelo continuo de elementos finitos para el cálculo de flujos bifase con interfase móvil. Este modelo está basado en el método no oscilatorio de elementos finitos (cuyo acrónimo es NFEM), que incorpora a su vez una estrategia de corrección de flujos preservando así el signo de la solución. De esta forma, es posible predecir con precisión la dinámica de la interfase. El procedimiento completo consta de tres pasos: transporte de la función de fase, reinicialización de la función de fase para mantener la resolución de la interfase y solución de las ecuaciones del movimiento del flujo, donde se ha tenido en cuenta tantos flujos incompresibles como flujos débilmente compresibles. Para ésta segunda hipótesis, la ecuación de continuidad ha tenido que ser modificada, según la expresión paramétrica de la densidad, para mantener la propiedad de conservación de masa. Las técnicas de corrección de flujos se han implementado en los tres pasos descritos anteriormente. Para el paso de transporte, se han incorporado nuevos limitadores que eliminan errores de masa de alto orden presentes en la versión original del NFEM sin mermar la eficiencia del mismo. Por otro lado, para el paso de reinicialización se ha creado una nueva ecuación de difusión conservativa y no lineal. Dicha ecuación alberga una compresibilidad artificial y una difusión orientada en un mismo término de difusividad anisotrópica. El proceso iterativo necesario para resolver la reinicialización incorpora las técnicas de corrección de flujos para mantener los límites previamente establecidos de la función de fase. Finalmente, para la resolución de la hidrodinámica del flujo, se han incorporado, en el proceso de corrección de flujos, coeficientes de limitación mejorados que tienen en cuenta la posición de la interfase. De esta forma, se ha conseguido eliminar prácticamente por completo las transferencias espurias de cantidad de movimiento entre fases. Por otro lado, la estabilidad de flujos artificialmente estratificados ha sido estudiada en problemas que conllevan inestabilidades tipo Kelvin-Helmholtz. Se ha concluido que, para que no haya una falsa amplificación de perturbaciones, es necesario reducir el espesor de la interfase en las simulaciones numéricas. Por consiguiente, se han investigado diferentes estrategias para

conseguir esto, resultando ser el más adecuado el refinamiento de la malla en las zonas cercanas a la interfase. Así, se ha desarrollado un nuevo procedimiento de refinado/desrefinado de mallas anidadas. El nuevo algoritmo también incluye técnicas de corrección de flujos para asegurar la conservación y la monotonicidad de las variables. La eficacia de este modelo ha sido puesta a prueba mediante distintos test numéricos bastante extendidos en la literatura existente.

El segundo objetivo de esta Tesis es investigar la dinámica de las cavidades de aire que se propagan en conducciones y de los géiseres que tienen lugar a consecuencia de éstas. Para ello se ha utilizado el modelo numérico antes explicado, además de una aproximación analítica. El modelo teórico ha sido creado a partir de un análisis con volúmenes de control y es capaz de predecir la dinámica de las burbujas tipo Taylor que ascienden en tubos verticales. Además, se tiene en cuenta tanto la compresibilidad del aire dentro de la burbuja como la posición de la superficie libre dentro del tubo, permitiendo así conocer el impulso que sufre la columna de líquido situada por encima de dicha burbuja. Por otro lado, de las ecuaciones que constituyen el modelo se puede obtener una condición que al producirse genera una descompresión brusca de la burbuja y, por consiguiente, un géiser de magnitud considerable. En relación a las simulaciones numéricas, se verifica que la hipótesis de flujo débilmente compresible es crucial en los experimentos con burbujas tipo Taylor. Esta premisa es necesaria para conseguir una adecuada transferencia de cantidad de movimiento entre el gas de la burbuja y la columna de líquido. La primera tanda de experimentos numéricos trata de reproducir cavidades de aire propagándose en tubos horizontales e inclinados para comparar los resultados obtenidos con las observaciones de laboratorio (existentes en la literatura). La segunda serie está destinada a averiguar las condiciones del flujo circulante por el interior de la tubería que impediría que el aire entrase en la misma y se formase una cavidad. Gracias a los resultados obtenidos, se han podido definir expresiones semi-analíticas simples que proporcionan esta información. Finalmente se han usado dos versiones del modelo numérico (axisimétrica y tridimensional) para simular burbujas tipo Taylor y el consiguiente géiser. De esta forma, los datos obtenidos, que contienen detalles muy precisos, pueden complementar a los resultados analíticos, sobre todo por encima del nivel de calle.

Agradecimientos

Han sido varios los años de trabajo dedicados a completar mi Tesis Doctoral, y quiero aprovechar la ocasión para dar las gracias a todas las personas que me han apoyado tanto personal como profesionalmente.

En primer lugar, agradecer a mis padres y a mi hermana siempre su apoyo, que se alegren y disfruten de mis logros, y el hecho de saber que siempre estarán ahí para lo que necesite.

Igualmente comparto esta alegría con mi amor, María. Siempre es mi sustento, mi consuelo y mi alegría. Gracias por confiar en mí y compartir conmigo todo.

Por otro lado, me gustaría darle las gracias a Pablo, tutor y director de la presente tesis, por su dedicación, consejos y compromiso durante todo este tiempo. Gracias a sus conocimientos, sabiduría y la constante disponibilidad en cualquier momento que le he necesitado, ha sido posible la existencia de este documento. Así mismo, quiero agradecer a Alejandro el apoyo constante que me ha brindado desde antes incluso de ser Ingeniero.

Por supuesto, no me quiero olvidar de Juan R. Cebral, Rainald Löhner, Adesola Ademiloye y P. Nithiarasu, que me acogieron durante mis estancias en la George Mason University y en la Swansea University. Ellos me han aportado distintos enfoques del trabajo de investigación y valiosos conocimientos que me ayudaron y ayudarán en el futuro.

Por último, y no menos importante, agradezco su apoyo al resto de mi familia y amigos por los momentos de felicidad y distensión que también son siempre necesarios.

Es un orgullo para mí, presentar esta tesis y dedicársela a todas estas personas que han formado parte de ella.

Contents

List of Figures

List of Tables

Nomenclature

1. Roman letters:
    - A = Antidiffusive flux or element area
    - a = acoustic wave velocity
    - B = generic scalar field
    - $\mathbf{b}$ = control volume boundary velocity
    - C_I= parameter taking into account deviation of maximum velocity from mean velocity
    - C_d = drag coefficient
    - C_q = discharge coefficient
    - c = cavity celerity or correcting function
    - c_b = bore celerity
    - D = space dimensions
    - $\mathcal{D}$ = non-linear diffusivity coefficient
    - d = duct height or diameter
    - E = energy
    - F=$c/\sqrt{gd}$ = cavity Froude number
    - F_b=$c_b/\sqrt{gd}$ = bore Froude number
    - F_r = Froude number
    - $\mathbf{f}$ = external forces
    - f = friction factor
    - g = gravity acceleration module
    - $\mathbf{g}$ = gravity acceleration vector
    - $H(\cdot)$ = Heaviside function
    - H_2=h_2/d = downstream depth ratio

- h_2 = flow depth downstream the bore
- $i = \sqrt{-1}$
- $\mathcal{K}$ = elastic bulk modulus, artificial diffusivity tensor
- K = perturbation wave number
- K_M = added mass coefficient
- k = non-dimensional Taylor bubble velocity
- L = length
- L_I, L_ρ, L_u = parameters controlling transition thickness for interface instabilities study
- L_b = Taylor bubble length
- L_{lc} = water column length above Taylor bubble
- M = mass
- $\mathbf{M}_C$ = consistent mass matrix
- $\mathbf{M}_L$ = lumped mass matrix
- N = shape function for spatial discretisation
- $\mathbf{n}$ = interface normal
- $\mathbf{n}_b$ = boundary normal
- n_m = Manning number
- P = bubble pressure
- p = pressure
- p_0 = reference pressure
- $\mathbf{Q}$ = velocity divergence term in Navier-Stokes equation
- q = flow per unit length
- $\mathcal{R}$ = Reynolds number
- R' = source term
- $\mathbf{r}$ = radial unit vector
- r = radial coordinate
- Re = real part
- $\mathcal{S}$ = source term
- S_0 = duct slope
- s = complex grown rate

- T = final time
- $\mathbf{T}$ = surface tension term
- $\mathcal{T}$ = stress tensor
- t = time
- $\mathbf{u} = (u_1, u_2, u_3)$ = velocity vector
- U_∞ = Taylor bubble velocity in stagnant liquid
- u = velocity (scalar)
- V = volume
- $\mathbf{x} = (x_1, x_2, x_3)$ = position vector
- w = weir height
- x = horizontal coordinate (2D problems)
- y = vertical coordinate (2D problems)
- $\mathbf{z}$ = axial unit vector
- z = axial coordinate

2. Greek letters:

- Γ = boundary
- γ = gas adiabatic index
- γ^* = specific weight
- Δ = increment
- δ = average element size
- δ_d = Dirac-delta function
- δ_i = spatial increment
- δ_ν = liquid film thickness between Taylor bubble and duct wall
- ε = parameter defining interface thickness in the reinitialisation step
- ζ = small number to avoid the vanishing of denominators
- η = interface thickness
- θ = parameter for temporal discretisation
- θ_d = duct slope
- κ = interface curvature

- ϑ = parameter for density interpolation
- λ = perturbation wavelength
- μ = fluid dynamic viscosity
- ν = fluid kinematic viscosity
- ρ = fluid density
- ϱ = convergence order
- σ = surface tension coefficient
- τ = dummy time for reinitialisation algorithm
- Υ = parameter defining limits of flux correction in hydrodynamic solution
- ϕ = phase function
- Ω = domain
- ω = angular velocity

3. Superscripts:

   - $\sim$ = perturbed field or corrected values
   - $-$ = known values
   - $*$ = relative values

4. Subscripts:

   - 0 = initial values
   - 1 = properties of the lightest phase
   - 2 = properties of the heaviest phase
   - b = bubble bottom
   - fs = free surface
   - g = gas
   - l = liquid
   - o = axisymmetric term
   - r = radial component
   - z = axial component

Chapter 1

Introduction

1.1 Motivation

1.1.1 Two-Phase Flow Computation

Flows involving interaction of two or more fluids are present in a wide range of physical and engineering problems. Depending on the cohesion forces measured by the surface tension, these fluids can produce a dissolution or be immiscible. In last case, phases are delimited by a well defined contact discontinuity called interface, which normally implies steps in density and in pressure gradient. Multiple phase flows can be categorised in two groups, dispersed and segregated (or a combination of both). In first group there is a main and dominant continuous carrier phase which contains the dispersed phase. This second phase is presented in form of small droplets (see e.g. Figs. 1.1a and 1.1d) and their dynamics is mainly controlled by drag and buoyancy forces among others. Some examples of dispersed flows are the pressurised injection of fuel inside combustion engines (main phase is a gas), or that produced in boiling chambers of power plants (main phase is a liquid). Conversely, second group is characterised by having two isolated and well-defined phases (see e.g. Fig. 1.1b) where dynamics of the whole is defined by interaction forces between both fluids. Some examples are sloshing events in ship storage tanks or a dam break flow. Reader can note that same happening could be regarded as a dispersed or segregated problem depending on the scale and objective of the investigation. For example, an hydraulic jump could be a segregated flow whose phases are water and the air at atmospheric pressure situated above the free surface, or it could be regarded as a dispersed problem if the research aim is the intrusion of air inside the water.

To address the study of two-phase flows problems in any physical event, there exist three different strategies. First one is the analytical research, that aims to reproduce the reality by finding solutions to the equations governing

the problem. Main drawback of this approach is that it is often impossible to achieve these analytical responses. Second strategy is the laboratory experimentation, which consists in reproducing the problem under controlled conditions, usually varying the length scale. Third approach is the numerical experimentation, that finds approximate solutions to equations governing the problem by means of sophisticated mathematical tools. Although best results are attained by combining every kind of experimentation, there are situations where laboratory experiments are unfeasible, either due to a high economical cost, to the impossibility of achieving dynamic and kinematic scales, or to difficulties to take data without altering the physics. In these cases, numerical experimentation is the only viable alternative.

Computational fluid dynamics (CFD) has demonstrated to be a powerful and efficient tool to predict in detail flow features in problems involving one or more fluids. By means of this methodology, Navier-Stokes[1] (NS) equations are numerically solved in a computational domain that represents the discretisation of an actual region. There are two main ways to describe the motion of fluids, Eulerian and Lagrangian approaches. By one hand, Eulerian methods consider all particles constituting the fluid as a continuum and solve equations of motion on fractions of a fixed grid. In contrast, Lagrangian description captures the path of every single particle by solving the equations governing its dynamics. Hence, nodes of computational domain are moved according to the velocity field. The choose of Eulerian or Lagrangian method is highly case-dependent. For multiphase flows, both descriptions are employed. Normally, segregated flows are described with Eulerian methods because they admit large fluid deformations as computational domain is independent on motion. However, they need the implementation of the interface and ensuing additional forces and conditions. Main challenges that make the simulation of segregated flows an active field of investigation are the following:

- Higher complexity in the resolution of equations of motion due to the inclusion of space and time dependent density and viscosity functions, in addition to new interfacial forces as surface tension.

- Representation of contact discontinuities by continuous grids and models.

- The coupling of interface conditions with equations of motion.

[1]These equations describe the movement of a fluid and are derived by imposing mass and momentum (Newton's Second Law) conservation equations to an infinitesimal fluid volume.

- The capture of moving interfaces with time.
- The modelling of phases interaction without polluting flow dynamics.

On the other hand, although dispersed flows can be also reproduced with Eulerian descriptions, requirements of mesh resolution usually makes this task impossible, becoming necessary the use of Eulerian-Lagrangian models. These approaches use an Eulerian description for main phase and a Lagrangian method to simulate the dispersed phase. Thus, last phase is regarded as distributed particles, whose dynamics is simpler to calculate.

This Thesis aims to develop an efficient numerical model for the accurate simulation of segregated two-phase flows with moving interfaces, able to overcome aforementioned difficulties. This new approach will be later applied to the study of an specific phenomenon occurring in sewer system conduits.

1.1.2 Two Phase Flows in Ducts: Air Cavities

Two-phase flows inside ducts can be present in different forms. Resulting pattern depends on the ratio between gas and liquid mass fluxes, giving as a result four main different regimes for vertical conduits (see Figs. 1.1 and 1.2). Bubbly flow (Fig. 1.1a) takes place when gas forms little bubbles and its flow rate is very small compared with liquid flow rate. Conversely, for high flow rates of gas, liquid is attached to duct walls and gas occupies the centre of the pipe, giving as a result an annular pattern (Fig. 1.1c). Besides, if gas velocity increases even more, liquid detaches from walls in form of dispersed droplets or spray (Fig. 1.1d). Note that last pattern is not shown in map 1.2. Most interesting case in this work is slug flow (Fig. 1.1b), characterised by gas travelling upwards in form of elongated bubbles occupying most part of duct section, while liquid forms a thin layer attached to duct walls that flows downward. Patterns in horizontal ducts are similar to previous ones but, due to gravity effect, a new stratified flow arises. This pattern is developed for low liquid and gas flow rates and it is defined by having the fluid with higher density (normally the liquid) situated below the other one. Eventually, if gas velocity is high enough, waves can appear along the interface. Two phase flows in conduits are noticeable in several industrial processes and civil infrastructures. A current subject of research is that concerning transient air-water flows emerged in sewer systems as a consequence of severe rainfalls.

Due to the climate change, extreme weather events are increasingly common. These occurrences, along with undersized drainage infrastructures make urban floods a recurrent hazard with a very high economic and social impact on the population. Moreover, if sewer management system is combined (e.g. same network drives both low quality and surface waters),

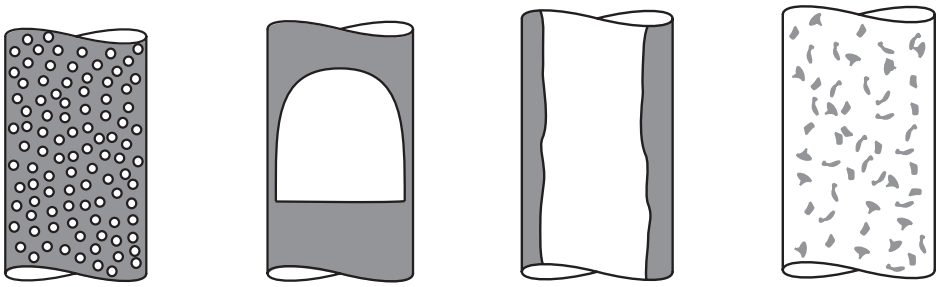

(a) Bubbly (b) Slug (c) Annular (d) Spray

Figure 1.1: Two-phase flows regimes in conduits.
Source: https://www.researchgate.net/publication/272161795

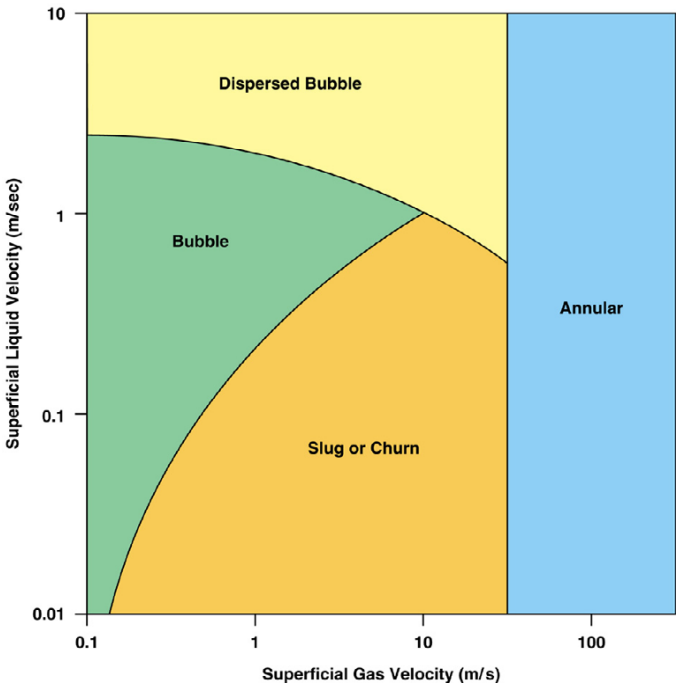

Figure 1.2: Flow patterns map for two-phase flows in vertical ducts. Source: [43]

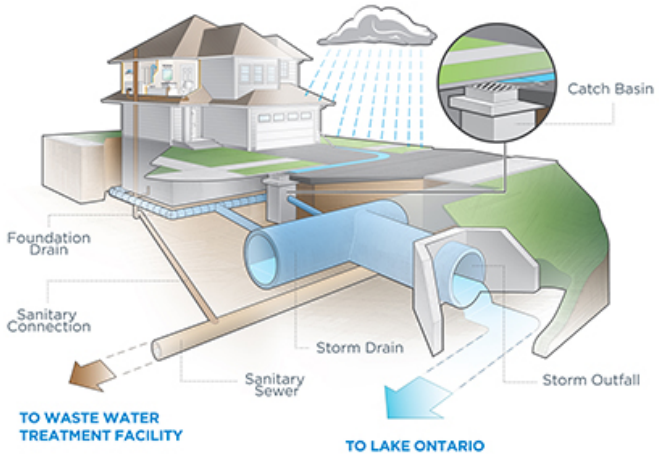

Figure 1.3: Separate stormwater management system of Mississauga. Source: https://www.mississauga.ca/

overflows can also cause public health issues. Stormwater storage tunnels avoid this problem by separating low quality water from surface water (see Fig. 1.3), or by managing flow that exceeds the normal system capacity (see Fig. 1.4a). In last case, extra runoff is driven to artificial reservoirs and is treated after the storm event. Big cities as Chicago (see Fig. 1.4b and this video[2]) have this management system due to its suitability to handle extreme rainfall events in huge urban areas.

Emergence of big air pockets in all aforementioned infrastructures is an usual phenomenon that takes place after a heavy rain episode. Some of the identified mechanisms leading to the intrusion or entrapment of air cavities are [43]: entrainment at duct inflow or outflow locations, negative pressures at the duct inlet, entrainment due to vortexes, turbulence in shafts and entrapment due to rapid filling or emptying of lines. This work focuses on air intrusion at duct outflow location. Process starts by the drainage of a saturated duct by its lower end after a heavy rain event. There, air in contact with atmosphere intrudes in form of open cavities, replacing the evacuated water (see Fig. 1.5). In some cases, due to duct inclination, partially opened gates, section changes or obstacles, cavities can be entrapped (see Fig. 1.6), and resulting air pockets travels upward because of buoyancy forces. Presence of these pressurised air bags in sewer systems and stormwater storage

[2]https://www.youtube.com/watch?v=HnOlXJxjDxk

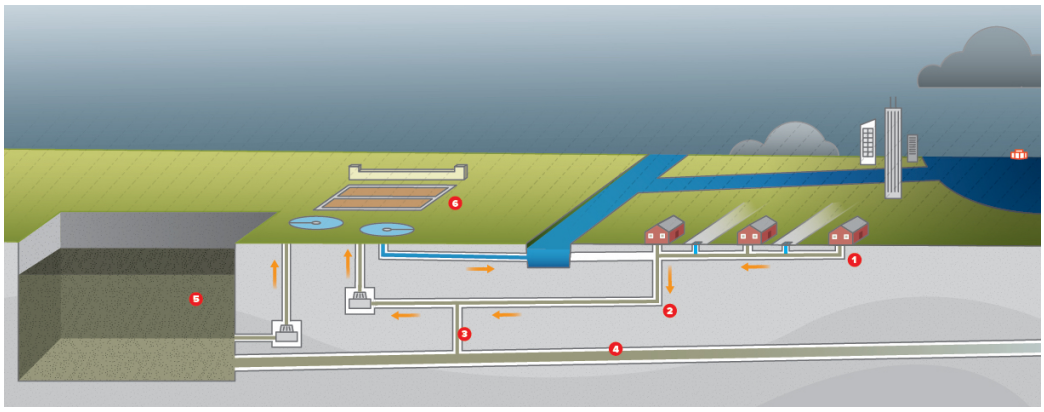

(a) Combined sewer and stormwater management systems.
Source: https://mwrd.org/understanding-your-sewer-0

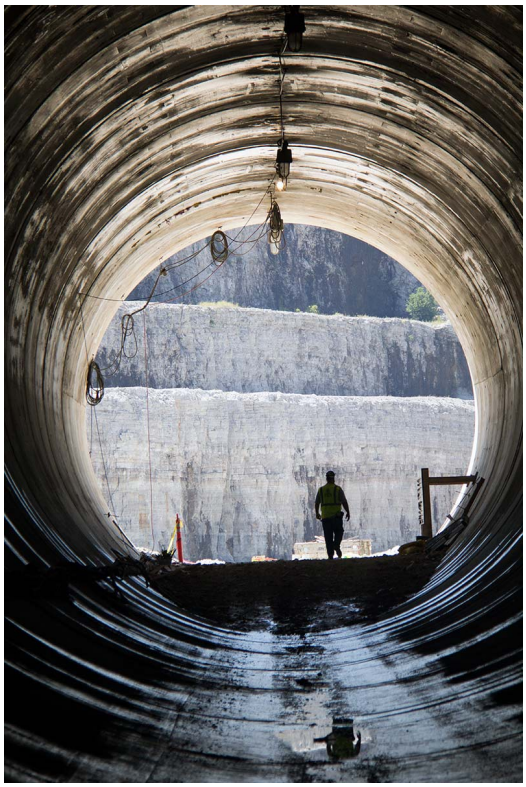

(b) Opening of Chicago stormwater tunnel at Thornton Reservoir.
Source: http://interactive.wbez.org/photos/deeptunnel/

Figure 1.4: Combined sewer system of Chicago

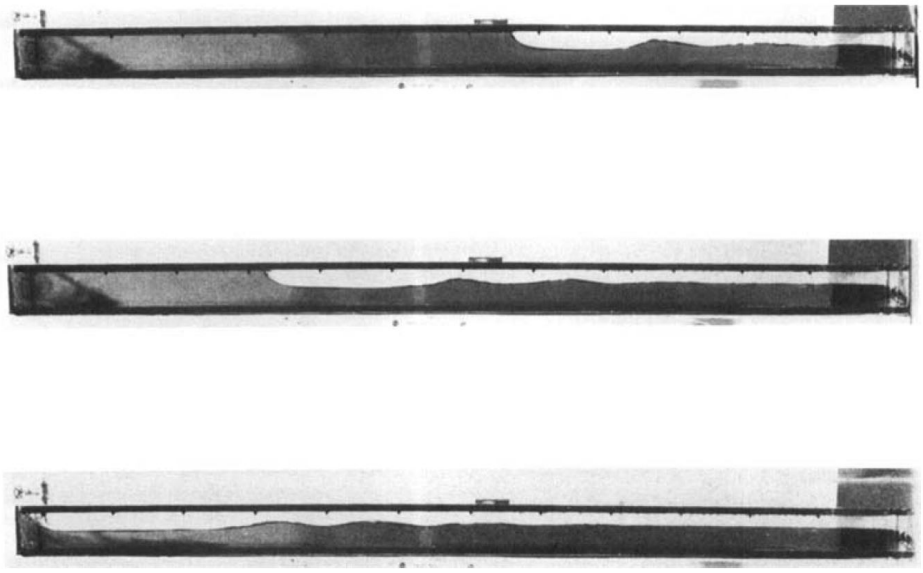

Figure 1.5: Motion of an air cavity in an horizontal duct. Source: [81].

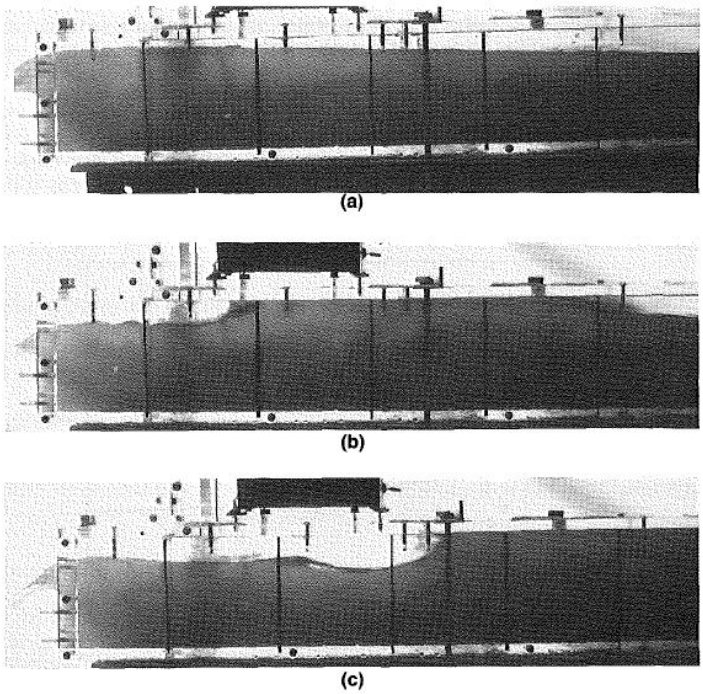

Figure 1.6: Entrapment sequence. Source: [1].

systems concern to engineers because of their harmful effects. For example, they reduce the effective pipe cross section and introduce vertical momentum into the flow due to their buoyancy. Moreover, magnitude of the induced transient pressure in the pipe may be significantly higher than if there were no air pockets [83], leading to damage in conduits. However, most dangerous consequence can appear if this pocket finds a saturated vertical shaft or pipe. In that case, part of air mass forms a rising Taylor bubble, which ascends driving the still water and violently expels a mix of water-air to the street level[3]. This event aggravate urban floodings and it is known as geysering because of its similarities with thermal geysers (see Figs. 1.7 and examples of Fig. 1.8a and 1.8b). In some cases, jet reaches tens of meters above the street level, throwing upward the manhole lid with the subsequent danger for pedestrians.

Emergence and propagation of air cavities and geysering events are constituted by almost every two-phase flow patterns presented above. By one hand, open air cavities propagating into horizontal or moderately inclined ducts resembles slug flows along with a stratified flow (see Fig. 1.1b and first plot of Fig. 1.5). Moreover, stratified pattern can be wavy as can be seen in third plot of Fig. 1.5. On the other hand, rising Taylor bubbles are mainly defined by a slug pattern; however, bubbly pattern can also be found at bubble downstream wake because small secondary bubbles are detached from the principal one. Finally, when water is spelled and it forms a geyser, part of the flow has spray pattern (see Fig. 1.8b).

Facts described above makes the complete understanding about dynamics of intrusion and entrapment of air cavities and geysering events non-trivial. In this work, the developed numerical and analytical models are employed to further investigate these phenomena and to propose some actions to ameliorate them.

1.2 State of the Art Review

1.2.1 Two-Phase Flows Computation

Computation of two-fluid flow problems involving moving interfaces has been a challenge for decades because it is necessary the representation of very sharp interfaces between both phases, and to handle large jumps in physical properties. Methods documented in the literature can be categorised into two widely recognised groups, those based on surface tracking and those based

[3]Reader can note that this phenomenon can be a consequence of almost every air intrusion mechanisms introduce above.

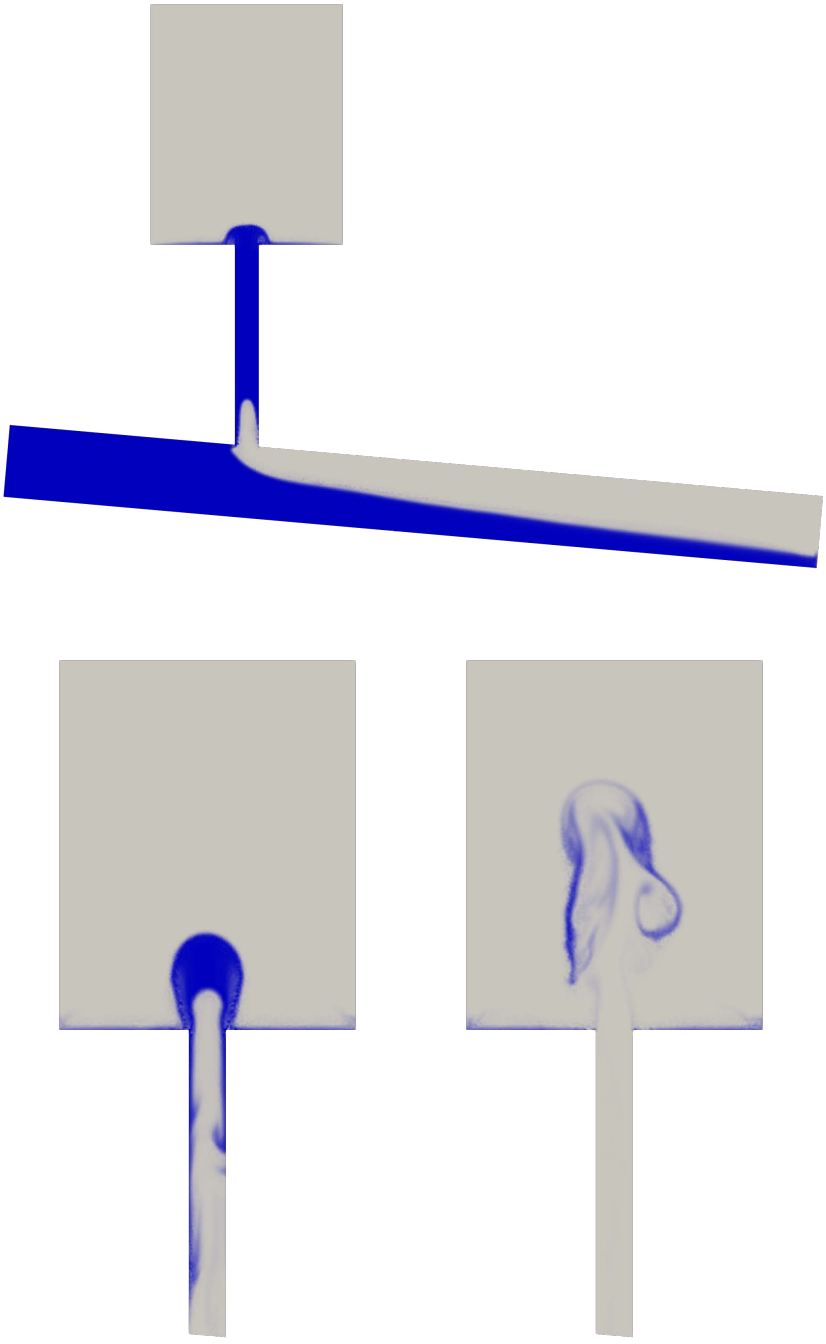

Figure 1.7: Geysering event due to an entrapped air cavity.

(a) Geysering event in St. Louis (Missouri).
Source: https://www.riverfronttimes.com/

(b) Geysering event in Montreal.
Source: https://www.huffpost.com/

Figure 1.8: Examples of geysering events.

on surface capturing. In the first methods, interface fits with a mesh boundary or is defined by faces of mesh elements. Although this kind of approaches gives better accuracy, mesh has to be updated as flow evolves, so grid adaptation or remeshing is ineludible (see e.g. Ref. [68]) with the consequential high computational cost. The second course of action establishes interface implicitly by means of a phase function that has to be advected along with the resolution of flow equations. In contrast with former case, these approximations solve dynamics of both fluids in the same fixed spatial domain, avoiding recurrent mesh adaptations and additional jump conditions at interface. Apart from these two groups, there also exist hybrid methods that use both Eulerian and Lagrangian descriptions to solve multiphase flows. As an example, model introduced in Ref. [18] works on fixed grids and employs lagrangian markers that identify interface and move according to flow velocity. Thus, each fixed mesh node has different physical properties depending on the side where it was situated with respect to the markers.

Within interface capturing models, two of the most favoured procedures in this category are the Volume Of Fluid method (VOF) [34, 77], and the Level Set method (LS) [65, 75, 27, 17]. Algorithms founded on VOF principles define a bounded phase function indicating the cell portion occupied by the heaviest fluid. This function is advected every time-step following the solution of a transport equation. Hence, VOF method preserves mass by construction but it is prone to give excessive diffusive answers. To amend this overdiffusion, some alternatives were proposed as the use of a compressive differencing scheme [77] or the introduction of an extra artificial compression term in the advection equation [71]. On the other hand, LS methods includes the advection of a signed phase function representing distance to the interface. Then, this function has negative values at phase one, positive values at second phase and zero value at interface. Once this signed distance function is advected, resolution of an extra differential equation, know as reinitialisation step, is necessary to recover the distancing property. Therefore, original level set technique gives a continuous and sharp representation of the interface, nevertheless it presents mass conservation deficiencies. To improve conservation properties, several alternative methods based on hybrid VOF/LS algorithms have been proposed (see e.g. Refs. [73, 78]). Among them, Conservative Level Set method (CLS) [59, 60] is one of the most renowned. This method enhances substantially mass conservation property by using a smeared out Heaviside function as phase indicator (resembling the intrinsic VOF idea), and also preserves a sharp interface definition by incorporating a reinitialisation step as LS procedure. In Refs. [86, 16] authors went one step further by recovering the distance level set function to compute interface normals and thus improve reinitialisation process. Although

these procedures reduce interface errors, their computational cost is higher as they involve the solution of two advection and redistancing/reinitialisation equations, or the implementation of a fast marching algorithm to reconstruct the level set field. A different strategy was presented in Refs. [29, 69], where authors proposed a way to retain reinitialisation benefits without solving additional non-linear advection-diffusion equation. There, LS was embedded into a VOF formulation in a monolithic form that includes artificial compression effect and diffusion. Nonetheless, the resulting non-linear solution requires an implicit treatment to avert spurious solutions on interface, with the subsequent higher computational effort.

As mentioned above, transport of phase function can worsen the resolution of the contact discontinuity by introducing a certain amount of diffusion to achieve the monotonicity (or at least positivity) property. This make necessary any additional action to maintain interface quality. Artificial compression [31] is used in both VOF and CLS models. The essence of the artificial compressibility method is to solve a modified equation instead of original advection equation such as analytical solution is identical in both cases, but numerical solution of modified equation has a better discontinuity resolution. In case of VOF, artificial compression is added to the advection equation to counteract diffusion induced by numerical method. On the other hand, reinitialisation of CLS consists in the iterative solution of an additional non-linear advective diffusion equation that combines artificial compression balanced with a supplementary amount of diffusion to avoid discontinuities at the interface. This continuous model has a significant attribute: both artificial compression fluxes and diffusive fluxes are oriented along interface displacement direction. For this reason, neither crosswind diffusion nor crosswind compression fluxes are allowed to grow during reinitialisation.

For the resolution of advection or reinitialisation equations in VOF and CLS approaches, it is desirable a monotonic numerical method to avoid spurious oscillations at interface neighbourhood and nonphysical phase function values (below zero and above one). However, it is well-known that a monotonic method is at most first order accurate [33]. Then, to achieve a higher order convergence, numerical model usually has to fulfil less restrictive requisites. There are several available methods that can comply this requirement. One course of action consists on adding high-order non-linear artificial viscosity terms to the numerical discretisation of the equation (see e.g. Ref. [28]). Others approaches use slope limiters to construct an hybrid solution whose accuracy is of high order far from discontinuities and of low order near discontinuities; some examples are the so-called ENO [32] and WENO [46] schemes. A different strategy is the Flux Corrected Transport Method (FCT) [10, 48, 85], which assures high order accuracy, positivity

and non-oscillatory behaviour of the final solution by correcting a low order solution with conveniently modified anti-diffusive fluxes. To this end, two solutions are needed, a high order solution and a low order solution. Depending on the selection of schemes for these answers, it can be found different versions in the literature. For example, R. Löhner [48] approach constructs the low order solution by adding a diffusion to the high order solution. This diffusion has to be tuned to assure positivity. A different course of actions was proposed by P. Ortiz [61, 62], where an independent first order upwind FEM is used to construct the low order solution following the idea of selecting a scheme with the (nearly) minimum diffusion to assure positivity.

The solution of equations of fluid motion involves the calculation of velocity and pressure fields. However, numerical computation of these equations is not trivial due to the non-linearity of convective acceleration terms or the incompressibility assumption, among other reasons. Several procedures have been developed during last decades to overcome these issues. Some examples are: the use of Taylor Galerkin method [23] for convective terms stabilisation in the field of finite element method or the employment of different interpolation functions for velocity and pressure variables to circumvent the Babuška-Brezzi stability condition (see e.g. Ref. [12]), and the employment of splitting algorithms. In this last category, one of the most famous methods is the Characteristic-Based Split (CBS) model [87, 88, 64], which is able to suppress spurious oscillations in convection-dominated flows and also fulfil stability condition with equal interpolation of variables. This method calculates solution of NS equations in three steps: first one involves the solution of an advection-diffusion equation to obtain a velocity predictor field; then, pressure field is calculated by solving a Poisson-type equation constructed from the continuity equation; finally, definitive velocity values are computed from velocity predictor and updated pressure fields. Although aforementioned algorithms give very accurate answers for single phase flows, they can present spurious momentum transfers between phases when solving multiphase flows. Several strategies have been developed to address this problem. For instance, by a special discretisation of convective terms [77], through the improvement of the pressure gradient discontinuity capturing technique [26], or by deactivating the lighter phase and extrapolating velocity and pressure fields across the interface [49].

1.2.2 Emergence of Air Cavities and Geysering

The study of air cavities in ducts is a recent field of research. Several authors have investigated lines related with intrusion, displacement and effects of air pockets. In 1968, T.B. Benjamin [8] was one of the first who studied the

problem of flow past a cavity in straight ducts. He set out the problem as an inverted gravity current, and applied mass, momentum and energy conservation equations assuming no energy loss. Considering Figure 1.9, he found that the receding stream occupies half of the duct (H_1=h_1/d=1/2) and that the non-dimensional cavity velocity was one half ($\frac{c}{\sqrt{gd}}$=$\frac{1}{2}$, where c is the cavity celerity, d is the duct height and g is the gravity acceleration). Then, he performed the same analysis considering energy loss and came to the conclusion that it was nearly impossible to produce a hydraulic jump downstream the cavity without causing an additional energy dissipation in the fluid (i.e. breaking of the free surface or generation of turbulence). Finally, he studied the energy-conserving flow in ducts of circular cross-section. Resulting non-dimensional cavity celerity was $\frac{c}{\sqrt{gd}}$=0.542, while water deep at receding stream was h_1/d=0.626; here, d is the duct diameter. These results were corroborated by laboratory experiments accomplished in Ref. [89]. Later, D.L. Wilkinson [81] extended the work of Benjamin. He studied effects on the flow due to surface tension and to a weir located across the open end of the duct. In account of the viscous and surface tension effects, author made an analysis supported by experiments and showed that cavity celerity decreases due to surface tension, then values calculated by Benjamin were overestimated as can be seen in Figure 1.10. Besides, he proved that cavity shape and stagnation point location were also affected. Conversely, with regard to the weir, he evidenced that it provokes a subcritical flow upstream the open end of the duct. As flow downstream the cavity is supercritical, a transient hydraulic jump or bore is formed, whose velocity is lower or equal to the cavity celerity. Then, resulting flow can be steady if bore and cavity have the same celerity, or unsteady if they are different. As can be noted from Figures 1.9 and 1.10, for downstream depth ratio values (H_2=h_2/d) between 0.5 and 0.78, flow is unsteady and it is defined by a front part behaving as a potential flow (see Fig. 1.11a), followed by a bore whose celerity is determined by the gate situated at conduit open end (see sketch of Fig. 1.9). This flow is associated to low weir heights. On the contrary, for H_2 values greater than 0.78, the flow is steady because bore tends to travel faster than air cavity and ends up affecting it (see Fig. 1.11b). This situation is provoked by high weir heights. W.D. Baines [1] evaluated the effect of duct slope on air cavities. His results showed that cavity celerity slightly rises as slope increases. He also studied the cavity sealing, taking place when the water surface touches the top of the duct. This event is more likely for low gate openings and steep slopes, being limit conditions those that lead to a static bore and an upstream flow having the normal depth. If bore moves toward the weir, sealing is unlikely. On the contrary, if bore moves away from the weir and

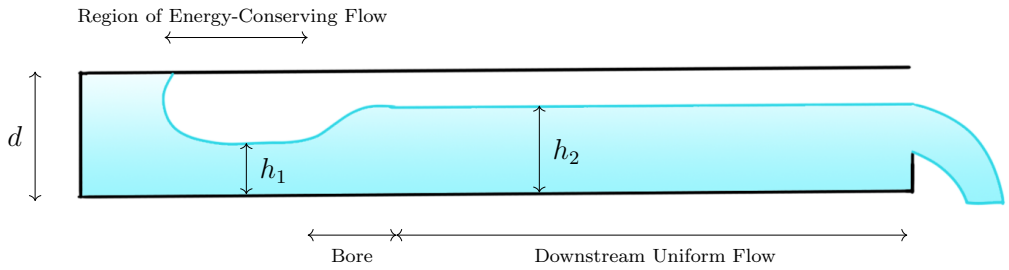

Figure 1.9: Sketch of an air cavity.

slope of downstream free surface is positive, sealing is almost assured in a long enough conduit. Air cavities have been also reproduced with simplified numerical methods. For example, authors of Refs. [4, 3] use a finite volume model including one-dimensional continuity and momentum equations and the Boussinesq approximation with the intention of reproducing the surface profile of open and closed cavities. On the other hand, dynamics of pressurised air cavities in closed ducts was investigated by several authors with the intention to define flow conditions to remove them (see e.g. Ref. [66] and references therein). Nevertheless, as far as the author knowledge, definition of similar conditions to avoid intrusion of air cavities at conduit lower end remains unexplored. In contrast, many efforts have been made to learn more about geysering events and their relation with closed air pockets. It is notable the work performed in References [79, 82, 55], where authors scrutinised geysering events with field measurements, laboratory experiments, simplified analytical approaches and open-source numerical models. They concluded that there are at least two mechanisms that explain the return of storm water to the ground level. First one is based on inertial oscillations of the water mass inside sewer systems. In this case, if hydraulic grade line is eventually situated above the street level, geysering may occur (see Ref. [30]). Second mechanism, and target of this Thesis, is that related with the release of air through vertical shafts in the form of elongated Taylor bubbles. Dynamics of this mechanism is mainly governed by three elements. First, the imbalance between rising bubble pressure and water column situated above. Second, the water film attached to duct walls which determines the flow rate passing from upstream to downstream the bubble. Third, air compression and decompression processes, governed in turn by the column water located above the bubble. Nevertheless, despite the knowledge of these three elements and the progress achieved in the study of geysering events during last years, complete comprehension of the phenomenon still remains unresolved.

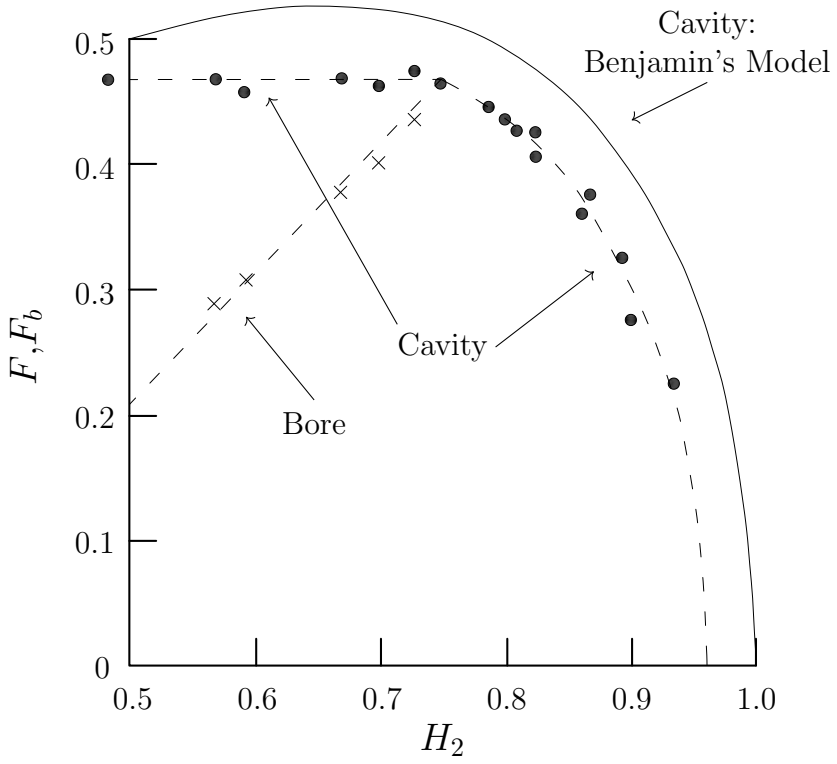

Figure 1.10: Cavity and bore Froude numbers (F=$\frac{c}{\sqrt{gd}}$, F_b=$\frac{c_b}{\sqrt{gd}}$, being c_b the bore celerity) as function of downstream depth ratio (H_2=h_2/d, being h_2 the flow depth downstream the bore). Solid line represents the cavity Froude number according to Benjamin's model and dashed line represents results obtained by Wilkinson. Circles and crosses are experimental measures of cavity and bore celerities respectively. Wilkinson's results was obtained with $\frac{4\sigma}{\rho g d^2}$=$3 \cdot 10^{-3}$ (ρ is the water density). Source [81]

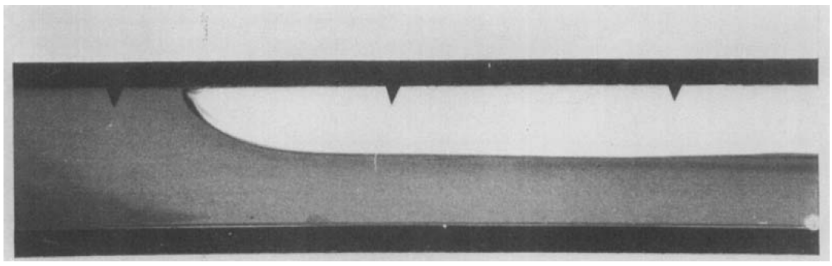

(a) Air cavity front ($H_2 < 0.78$)

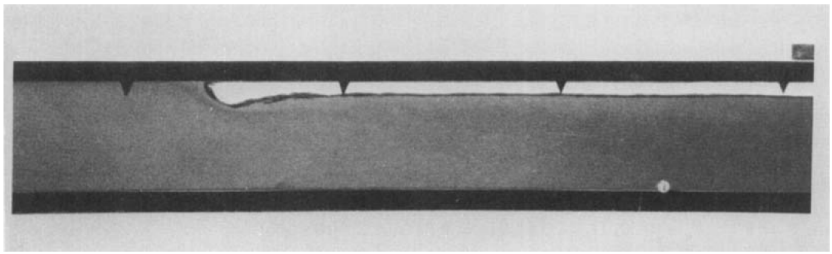

(b) Air cavity affected by the bore ($H_2 > 0.78$)

Figure 1.11: Snapshots of two air cavities. Source: [81].

1.3 Objectives

The purpose of this Thesis is to develop an efficient and accurate numerical model for the simulation of two-phase flows with moving interfaces by extending the Non-Oscillatory Finite Element Method [61, 62]. Then it will be used, along with supplementary simple analytical solutions, to broaden the knowledge about intrusion and propagation of air cavities in ducts and geysering events. Findings will be harnessed to propose preventive measures to avoid their negative effects. Hence, objectives of this work are classified in two groups: those necessary to achieve a competitive multiphase flow numerical model and those required for the comprehensive knowledge of the physical problem at hands:

1. **Development of Numerical Method**:

    - Implementation of NFEM algorithm for the advection of a phase function to get a conservative, positive definite and free of wiggles solution.
    - To develop a new reinitialisation step, compatible with flux correction techniques, to counteract diffusion introduced at advection

step and thus keeping interface definition along the complete simulation.

- Efficient improvement of interface normal calculation to avoid oscillations at phase function during reinitialisation.
- Coupling the phase function advection solution with Navier-Stokes equations for incompressible fluids. Employment of NFEM algorithm to solve the two-phase flows hydrodynamics, and to alleviate the well-known problem of spurious momentum transfers between phases.
- Extension of previous methodology to weakly compressible flows.
- To study possible negative effects of representing a physical discontinuity (interface) by means of a continuous model and to suggest actions to mitigate them.
- Evaluation of every part of the algorithm (advection, reinitialisation and hydrodynamics solution) by means of existing benchmark problems.

2. **Air Cavities and Geysering Experimentation**:

   - Development of an analytical model following studies of Refs. [8, 81, 1] to predict dynamics of air cavities advancing in inclined ducts.
   - To construct a simplified analytical model to predict rising Taylor bubbles dynamics.
   - To assess the performance of numerical method in the simulation of air cavities.
   - To explore flow conditions in ducts for air cavities intrusion and define strategies to ensure air removal.
   - Simulation of rising bubbles in saturated vertical conduits and consequent geysering events, to compare results with real cases.

1.4 Methodology

1.4.1 Two-Phase Flow Numerical Model

First task was to develop a numerical model for the solution of two-phase flows with moving interfaces. Algorithm was made according to the sequence outlined below. It has been written in C++ language and parallelized with OpenMP to speed up its performance.

Phase Function Advection

Present numerical method is a fixed mesh continuous finite element model constructed along the lines of VOF and CLS methods, implementing a bounded phase function whose value is zero at first phase, one at the other phase and one half at interface. For advection stage, standard high order algorithms as Characteristic Galerkin produce oscillations at interface neighbourhood and do not respect physical phase function bounds. Then, it has been employed the Non-Oscillatory Finite Element Method introduced by P. Ortiz, which also calculates an additional positive definite and low order solution. This second response is corrected with antidiffusive fluxes to attain a final conservative and positive definite second order solution. However, this answer gave high order mass errors, which were corrected by a straightforward mass readjustment integrated in the flux correction procedure.

Reinitialisation

Original CLS reinitialisation step involves a non-linear advection-diffusion equation that is solved by an iterative method. As first approximation, it was implemented FCT in the solution of this equation to preserve phase function bounds. However, this approach was not efficient because calculation of two solutions every iteration was computationally expensive. Second approximation consisted in computing a high order solution and then calculate the low order approach by adding an extra diffusion such that physical bounds were respected (resembling R. Löhner approach [48]). Drawbacks of this methodology are: first, iterative procedure could converge slower because of extra diffusion added later; and second, added diffusion is not oriented along the interface normal. For these reasons, second approximation was also discarded. Last and chosen approach was to couple artificial compression and oriented diffusion into a non-linear streamlined diffusive term. Although flux correction remains necessary due to the non-linearity of this term, computation of corrective fluxes is straightforward, making efficient the iterative process. Regarding others existing approaches that couple advection and reinitialisation into a non-linear monolithic equation that needs an implicit treatment (see e.g. Ref. [69]), this strategy seemed to be competitive because it involves the explicit computation of an advection equation, and the iterative solution of a straightforward diffusion equation.

On the other hand, to efficiently improve interface normals orientation without resorting to expensive procedures as fast marching methods, the following strategy was proposed: first, normal computation is limited to elements belonging to the interface neighbourhood; second, for calculation

of normals it is taken as a reference the nearest finite element where phase function has a value of one half. This is because phase function gradient is higher at this element and normal orientation is more reliable.

Hydrodynamics Solution

Firstly, density and viscosity were parametrically defined as a function of the phase field to couple it with hydrodynamics. Then, Navier-Stokes equations were solved by employing the Characteristics Based Split method. Although solutions were accurate for fluids whose density ratio was near to one, velocity overshoots appeared at interface neighbourhood when higher values of density ratio were tested, spoiling completely the results. NFEM was again implemented to amend this issue, but standard course of action implied the resolution of two Poisson equations with the subsequent extra computational cost. Hence, as source of spurious momentum transfers are the convective acceleration terms, flux correction was only applied to velocity predictor field. Experiments showed that results of both alternatives were very similar but computational cost was greatly reduced. Nevertheless, problem persisted for very high density ratios as air-water flows. An effective solution was found by defining new bounds, considering interface location, integrated in the flux correction procedure. Nearly incompressible assumption was implemented to simulate rising Taylor bubbles and geysering events. Then, to preserve mass conservation property, continuity equation was modified and density parametrical definition was adjusted by accommodating new terms that took into account small density changes due to pressure variations.

Effects of the Continuous Representation of the Interface

This study arose from a series of simulations involving air cavities where interface oscillated without any apparent physical reason. Then, due to the configuration of the problem where air advances in the opposite direction to the water, it appears that some Kelvin-Helmholtz instabilities were artificially amplified. Thus, linearised equations governing the perturbed field were solved by considering current continuous representation of the interface. Results indicated that flows with high density gradients were more unstable that non-stratified flows. Different options were considered to solve this issue. First one was to change parametrical definition of density, however this alternative was discarded because it affected to mass conservation. Second one was a local refinement to achieve an interface resolution such as perturbations were not activated. This process had to retain mass conservation property and be monotonic for new phase function, velocity and pressure fields. Hence,

a new refinement procedure for nested grids was developed, integrating flux correction principles to achieve previous aforementioned properties. Simulations did not show more nonphysical amplifications of perturbations once local refinement was activated.

1.4.2 Air Cavities and Geysering: Numerical and Analytical Experimentation

Second task involved analytical and numerical experimentation of air cavities and geysering events to achieve a deeper understanding of these phenomena. For this purpose, after constructing semi-theoretical solutions, several analytical and numerical simulations were performed.

Analytical Solutions

Control volume analysis was used to construct analytical solutions for air cavities propagation and rising Taylor bubbles. For air cavities propagation solution, additional hypothesis were necessary to make resolvable the obtained equations system since dynamics is affected by the liquid weight. In this work air cavity velocity values were assumed as known (by using experimental data of Ref. [1]) and bore topology was calculated with empirical N. Rajaratman equation for hydraulic jumps on slope [70]. On the other hand, for construction of the new theoretical model for rising Taylor bubbles, a realistic bubble shape was considered. Free surface position and gas expansion effects (by means of an adiabatic compressibility model) were also included to predict dynamics of both the bubble and liquid column situated above. Besides, equations revealed conditions for a sudden gas decompression, that provokes a huge acceleration of liquid column and a foreseeable strong geyser. Cases with multiple rising Taylor bubbles were also analysed to evaluate effects of trailing bubble on the leading one and vice versa.

Numerical Simulations

Numerical experiments can be divided in three series. First series intended to validate numerical model by reproducing laboratory experiments of D.L. Wilkinson [81] and W.D. Baines [1], involving air cavities propagation in horizontal and inclined ducts. Thus, simulations were performed by varying duct inclination and gate height, and it was noted cavity and bore celerities in addition to configurations that led to a cavity sealing. Second series aimed to scrutinise flow conditions that prevent air intrusion at conduits lower end. In this way, several simulations were accomplished with different combinations of duct inclination, gate height and inner fluid velocity. Then, it was

calculated, through interpolations, the minimum required inner fluid velocity necessary to clear air cavities for every tested combination. Last series examined rising Taylor bubbles. Assessment was carried out by reproducing laboratory experiments of Ref. [79], and then geysering events were recreated and qualitatively compared with real cases.

1.5 Thesis Structure

This Thesis is composed of five chapters that detail works published by the candidate in Refs. [52, 53, 54]. Chapter 2 describes a simplified analytical approach for air cavities propagation and a new analytical model to predict dynamics of rising Taylor bubbles. Numerical model is reported in Chapter 3, including the description of analytical equations for two-fluid flows, features about employed methods and the exploration of issues arising from representing the interface with a continuous model. Chapter 4 focusses on numerical experiments. First part covers assessment tests for advection and complete problems, while second part presents performed simulations involving air cavities, rising Taylor bubbles and geysering events. Conclusions in Chapter 5 close the Thesis.

Chapter 2

Semi-Analytical Approaches to Air Cavities and Taylor Bubbles Propagation

This chapter reports analytical models for the prediction of dynamics of air cavities and rising Taylor bubbles. In first section, the propagation of air pockets in horizontal and inclined ducts is studied with control volumes. Equations for straight conduits match with those achieved in Ref. [8]. However, when cavities propagates in inclined ducts, fluid weight must be included, making the equations system unsolvable unless additional hypothesis were applied. Hence, new assumptions are proposed to solve numerically this set of equations. In second section, a semi-analytical model examines Taylor bubbles dynamics. Unlike existing approaches that assume a potential flow around the bubble and a semi-infinite length tube (see e.g. Ref. [25, 7]), current model is based on an integral analysis and takes into account free surface position and gas expansion effects for the calculation of bubble rising velocity. Besides, solution is formulated without resorting to simplified bubble shapes (as for example Ref. [79]). Resulting approach predicts accurately the bubble rising dynamics, and permits to infer conditions for a sudden gas expansion, which produces a huge bubble acceleration and, therefore, a severe ejection of water to the street level (geyser). Model is assessed by comparing its results with existing laboratory results. Finally, formulation for multiple rising bubbles is introduced to scrutinise the impact of trailing bubbles on the leading one, and vice versa.

2.1 Air Cavities Propagation

Figure 2.1 shows an air pocket propagating inside an inclined duct. It can be identified three regions: the air cavity head where flow is almost potential, the transient hydraulic jump or bore, and the flow regime before the discharge over a weir. The formulation is made with pseudo-stationary control volumes,

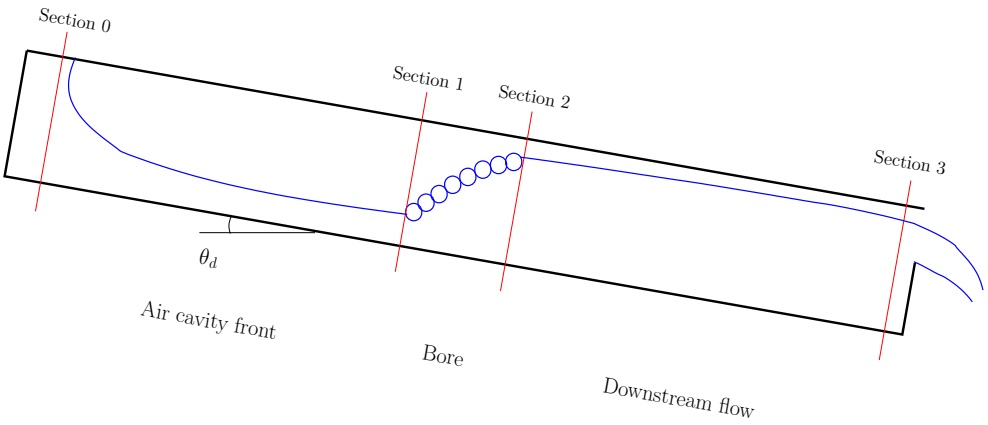

Figure 2.1: Sketch of an air cavity advancing in an inclined duct.

i.e., control volumes move with cavity or bore celerity. They are treated as fixed volumes, where relative velocities at inlet and outlet boundaries are considered. Nomenclature is $c_{()}$ and $c^*_{()}$ for absolute and relative celerities, respectively; and subscripts correspond to the sections shown in Figure 2.1. Integral form of mass and momentum conservation equations for moving control volumes is shown in Ref. [40] among others and they are reproduced in Appendix A.

2.1.1 Control Volume 1: Cavity

Control volume 1 starts at distance L_0 upstream the cavity stagnation point and ends before the bore (see Figure 2.2). In this control volume it is considered that flow is ideal, inlet and outlet velocity profiles are uniform and gas is at atmospheric pressure. In Fig. 2.2, P_0 is the pressure, d is the duct height and $\gamma^*{=}\rho g$ is the liquid specific weight. As control volume 1 moves with velocity c (positive sign indicates upstream direction) and fluid is at rest upstream the cavity, relative fluid velocities are $c^*_0{=}c$ and $c^*_1{=}c + c_1$, where c is the cavity celerity. Therefore, conservation equations for this control volume are,

- Mass conservation

$$c\, d = c^*_1\, h_1\ . \tag{2.1}$$

- Momentum conservation along the x-axis (see Fig. 2.2):

$$P_0\, d + \frac{d^2}{2}\gamma^* \cos\theta_d - \frac{h_1^2}{2}\gamma^* \cos\theta_d + V_c^{'}\gamma^* \sin\theta_d = c_1^{*2}\rho h_1 - c^2\rho d\ , \tag{2.2}$$

  where $V_c^{'}$ is the liquid volume between section 0 and 1.

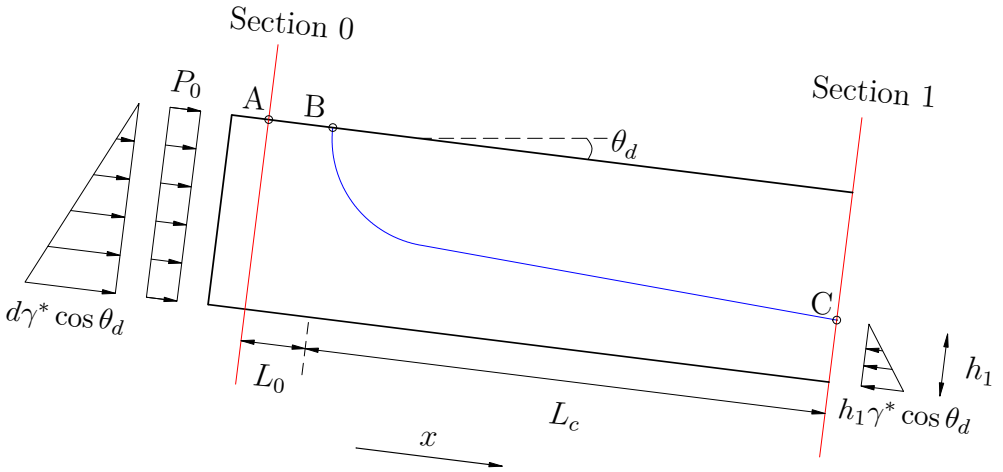

Figure 2.2: Control volume 1: air cavity

- Bernoulli equation along the streamline defined by points A and B:

$$P_0 = -\frac{c^2}{2}\rho - L_0\gamma^* \sin\theta_d \ . \tag{2.3}$$

- Bernoulli equation along the streamline defined by points B and C:

$$L_c \sin\theta_d + (d - h_1)\cos\theta_d = \frac{c_1^{*2}}{2g} \ . \tag{2.4}$$

Now, considering that $V_c^{'} = L_0 d + V_c$, (V_c is the liquid volume between section passing through B and Section 1 in Fig. 2.2), P_0 is cancelled out in Eqs. (2.3) and (2.2), and final set of equations is,

$$c\ d = c_1^*\ h_1 \ , \tag{2.5}$$

$$\frac{d^2 - h_1^2}{2}\gamma^* \cos\theta_d + V_c\gamma^* \sin\theta_d = \rho\left(c_1^{*2} h_1 - \frac{c^2}{2}d\right) \ , \tag{2.6}$$

$$L_c \sin\theta_d + (d - h_1)\cos\theta_d = \frac{c_1^{*2}}{2g} \ . \tag{2.7}$$

Reader can note that equations set has immediate solution for horizontal ducts ($\theta_d = 0$) because variables related to the cavity shape are no longer needed. In that case, it is obtained that $h_1{=}d/2$ and $c{=}c_1{=}\frac{1}{2}\sqrt{gd}$. These results match with T.B. Benjamin [8] and D.L. Wilkinson [81] without taking into account effects of surface tension and location of stagnation point.

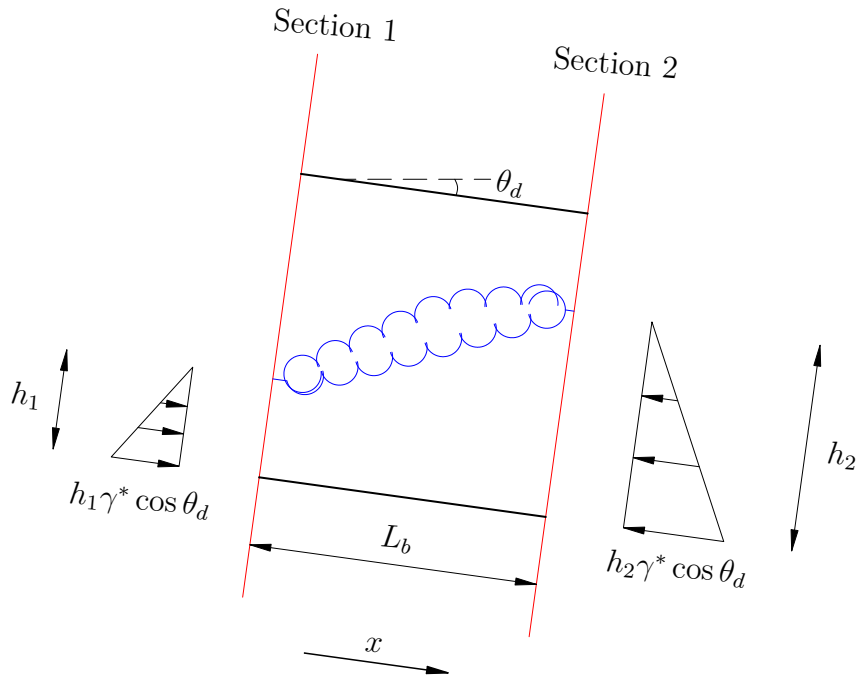

Figure 2.3: Control volume 2: bore

2.1.2 Control Volume 2: Bore

Figure 2.3 shows control volume 2, which embraces the bore. This part of the flow is highly rotational (ideal flow hypothesis is not valid) and it is assumed that energy loss due to ground friction is negligible and inlet and outlet velocity profiles are uniform. Bore and control volume 2 moves with velocity c_b, so relative fluid velocities at boundaries are $c_1^{**}{=}c_1 + c_b$ and $c_2^{*}{=}c_2 + c_b$. Because of energy loss in the bore is difficult to quantify, only mass and momentum conservation equations are considered,

$$c_1^{**}\, h_1 = c_2^{*}\, h_2 \ , \tag{2.8}$$

$$\frac{h_1^2 - h_2^2}{2}\gamma^* \cos\theta_d + V_b\gamma^* \sin\theta_d = c_2^{*2}\rho h_2 - c_1^{**2}\rho h_1 \ , \tag{2.9}$$

where V_b is the volume of the bore.

2.1.3 Control Volume 3: Discharge over Weir

Control volume 3 starts downstream the bore and ends upstream the weir, depicted in Figure 2.4. Here, velocity profile in section 2b is considered as uniform. In this case, the control volume is static, so velocities are absolute.

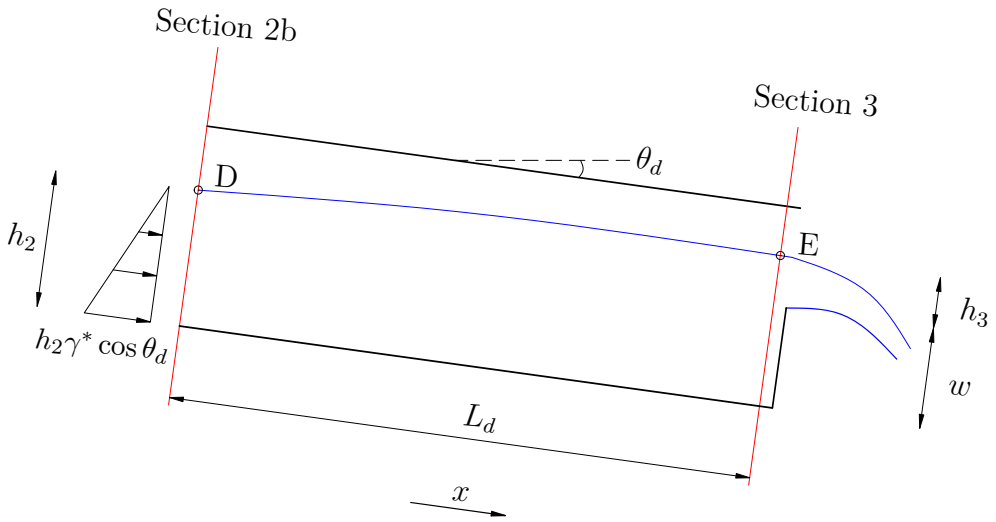

Figure 2.4: Control volume 3: Discharge over weir

Because of velocity and pressure profiles in section 3 are hard to quantify, only Bernoulli equation (between points D and E) is applied,

$$L_d \sin\theta_d + h_2 \cos\theta_d + \frac{c_2^2}{2g} = (w + h_3)\cos\theta_d + \frac{c_3^2}{2g} + \Delta E_3 \ . \tag{2.10}$$

Here, ΔE_3 is the energy loss due to friction between section 2b and 3. As velocities c_2 and c_3 are similar and small, equation (2.10) can be simplified as follows,

$$L_d \sin\theta_d + h_2 \cos\theta_d = (w + h_3)\cos\theta_d + \Delta E_3 \ . \tag{2.11}$$

Moreover, an equation related to the discharge over the weir can be raised,

$$q = \frac{2}{3} C_q \sqrt{2g} h_3^{3/2} \ , \tag{2.12}$$

where q is the unit discharge of water and $C_q = 0.611 + 0.075\frac{h_3}{w}$ is the discharge coefficient. Regarding mass conservation, this discharge of water is equal to the volume of air that enters in the duct per unit of time. Thus, next equation is obtained,

$$q = (c - c_b)(d - h_1) + c_b (d - h_2) \tag{2.13}$$

System of equations (2.5), (2.6), (2.7), (2.8), (2.9), (2.11) and (2.12) can be solved only if variables V_c, V_b, L_c, L_d and ΔE_3 are a priori known.

2.1.4 Special Case: Horizontal Duct

When duct is horizontal, weight of the fluid has no influence over its dynamics and problem becomes resolvable (see Refs. [8, 81]). Thus, equations (2.5), (2.6), (2.7), (2.8), (2.9), (2.11) and (2.12) turn into,

$$c\,d = c_1^*\,h_1\ , \tag{2.14}$$

$$\frac{d^2 - h_1^2}{2} g = c_1^{*2} h_1 - \frac{c^2}{2} d\ , \tag{2.15}$$

$$d - h_1 = \frac{c_1^{*2}}{2g}\ , \tag{2.16}$$

$$c_1^{**}\,h_1 = c_2^*\,h_2\ , \tag{2.17}$$

$$\frac{h_1^2 - h_2^2}{2} g = c_2^{*2} h_2 - c_1^{**2} h_1\ , \tag{2.18}$$

$$h_2 = w + h_3 + \Delta E_3\ , \tag{2.19}$$

$$q = (c - c_b)\,(d - h_1) + c_b\,(d - h_2) = \frac{2}{3} C_d \sqrt{2g} h_3^{3/2}\ , \tag{2.20}$$

where displacement of the stagnation point and surface tension effects [81] are not taken into account. For a simple study, only equations (2.14), (2.15), (2.16), (2.17) and (2.18) are considered in their non-dimensional form:

$$F = F_1^*\,H_1\ , \tag{2.21}$$

$$\frac{1 - H_1^2}{2} = F_1^{*2} H_1 - \frac{F^2}{2}\ , \tag{2.22}$$

$$1 - H_1 = \frac{F_1^{*2}}{2}\ , \tag{2.23}$$

$$F_1^{**}\,H_1 = F_2^*\,H_2\ , \tag{2.24}$$

$$\frac{H_1^2 - H_2^2}{2} = F_2^{*2} H_2 - F_1^{**2} H_1\ , \tag{2.25}$$

where $H_{()}{=}h_{()}/d$ and $F_{()}{=}c_{()}/\sqrt{gd}$. Non-dimensional variables F and $F_b = F_1^{**} - (F_1^* - F)$ are obtained by giving values to H_2 from zero to one. However, this premise is only valid when $F_b < F$ and flow is unsteady. At this stage, there are three regions that match with those studied in this section. On the other hand, when $F_b = F$, flow becomes steady and its behaviour is only governed by equations (2.21) and (2.22) (considering $H_1 = H_2$). This

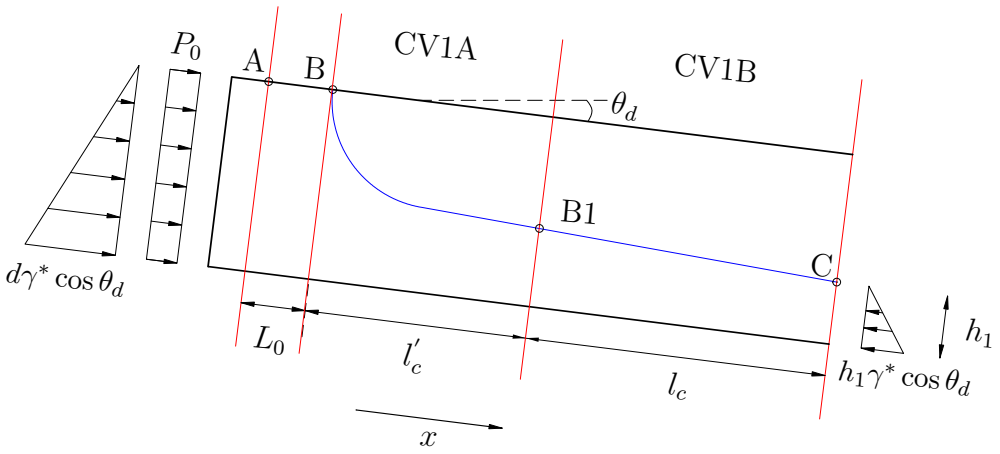

Figure 2.5: Modified control volume 1: air cavity

is because there is only one region, where energy loss is non-zero and unknown; in addition, cavity depth does not reach the value $h_1{=}\frac{d}{2}$. This stage occurs when $H_2 \gtrapprox 0.781$ (see Ref. [81]). Thus, if these equations are solved for different values of H_2, similar results to those shown by the dashed lines in Figure 1.10 can be obtained (there, surface tension and displacement of the stagnation point have been considered).

Finally, it is important to determine if air cavity closing (or gulping) is a feasible event in horizontal ducts. Firstly, because of energy conservation, it is not possible that cavity sealing occurs without adding energy to the system. Energy of a liquid particle at rest upstream the cavity is (dg); if gulping occurs, fluid at that point must have at least the same energy, but this hypothesis is not possible because energy losses are unavoidable between both points.

2.1.5 Simplified Numerical Solution for the Complete Problem

To construct a numerical solution for the set of equations, experimental results of W.D. Baines [1] are integrated in the algorithm. Thus, control volume 1 is divided in two parts (see Fig. 2.5), first one (designated as CV1A) starts at cavity stagnation point (point B) and ends where liquid flow is critical (i.e. $F_r{=}1$, point B1); second part (designated as CV1B) ends at bore beginning (point C). According to experimental observations [1], length of first part is $l'_c \approx d$. Now, cavity celerity is considered as known, whose value can be taken

from Ref. [1],

$$c \approx (0.46 + \frac{0.05}{0.14} S_0)\sqrt{gd}\,, \tag{2.26}$$

where S_0=tan (θ_d) is the duct slope. In this way, unknown V_c is not longer considered. Second issue to be discussed is the bore volume V_b, which can be circumvented by using the N. Rajaratnam equation for hydraulic jumps on slope [70],

$$\begin{gathered}\frac{h_2}{h_1} = \frac{1}{2}\left(\sqrt{1+8G^2}-1\right)\ , \\ G = K_1 F_1'\ , \\ K_1 = 10^{0.027\theta_d}\ , \\ \theta_d \text{ in degrees (duct slope)}\ ,\end{gathered}$$

where F_1'=$\frac{c_1+c_b}{\sqrt{gh_1}}$ is the Froude number upstream the bore. Then, proposed algorithm consists of following steps:

1. At initial time and for a given S_0 and w, c and initial value of $h_1^{'}$ (at the end of CV1A) are computed such that flow at point $B1$ is nearly critical, $\frac{c_1}{\sqrt{g\ h_1^{'}}} \gtrapprox 1$ (a value of 1.1 could be suitable). As previously stated, distance between point $B1$ and the stagnation point can be assumed as $l_c^{'}$=d.

2. Variables l_c and l_d are initialised, defined respectively as the CV1B length and the distance between the bore end and the weir. These variables are zero at first time step.

3. Obtain h_2, c_b and h_3 by solving the following system of equations,

$$\begin{gathered}\frac{h_2}{h_1} = \frac{1}{2}\left(\sqrt{1+8G^2}-1\right)\ , \\ l_d \sin\theta_d + h_2 = w + h_3\ , \\ (c-c_b)\,(d-h_1) + c_b\,(d-h_2) = \frac{2}{3} C_d \sqrt{2g} h_3^{3/2}\ .\end{gathered}$$

   Here, ΔE_3 is considered negligible because of the low flow velocity downstream the bore. Note that, if $w + h_3 \geq d$, cavity is sealed and computation must be stopped.

4. Calculate Δl_c, Δl_d and Δh_1,

$$\Delta l_c = \Delta t \, (c - c_b) \ ,$$
$$\Delta l_d = \Delta t \ c_b \ ,$$
$$\Delta h_1 = \Delta l_c \frac{S_0 - \left(\frac{n_m \, c_1}{h_1^{2/3}} \right)^2}{1 - \left(\frac{c_1}{\sqrt{g h_1}} \right)^2} \ ,$$

   where n_m is the Manning coefficient.

5. Update l_d and h_1, and c_1 by using Eq. (2.5), then return to step 3. If $l_d < 0$, bore is situated close to the weir and sealing is unlikely. In this case computation must be stopped.

This algorithm is only valid for low openings of the weir because, when gate height is large, bore moves faster than cavity and tends to fill it (thus air cavity and bore are coupled [1]). In this situation, flow cannot be described by previous one-dimensional equations.

2.1.6 Assessment

To assess semi-analytical model for air cavities propagation, a laboratory experiment performed in Ref. [1] is reproduced. This test consists of a square duct of height d=0.1 m filled with water, inclined at an angle of 1^o (S_0=0.017), and with a gate located at the lower end. At initial time, gate is opened up to a height of w=0.05 m, water starts to drain and an air pocket intrudes into the conduit. Manning coefficient is set as n_m=0.009 to simulate a plastic material similar to that employed in the laboratory. Obtained analytical results are showed in Fig. 2.6, where it is depicted values of relative bore celerity c_b/c, and non-dimensional water depth upstream the bore (h_1/d), downstream the bore (h_2/d) and at the gate ($(h_3 + w)/d$). Moreover, Figs. 2.7a-2.7c represent some sketches made from analytical outcomes. Besides, Fig. 2.8 shows laboratory outputs, where relative bore celerity was measured at three time steps: $c_b/c\,(t = 2.53s) = 0.812$, $c_b/c\,(t = 5.02s) = 0.621$ and $c_b/c\,(t = 7.71s) = 0.295$. As it can be seen, in both analytical and laboratory results, bore moves away from the weir with variable celerity and air cavity is finally sealed (see water depth at the weir in Figs. 2.6 and 2.8). However, significant deviations are appreciated in times where sealing is produced, as well as in the prediction of water depth upstream the bore. Reason of these discrepancies are mainly two: first, measured air cavity celerity is slightly lower than value given by Eq. (2.26); and second, it is assumed that air cavity is already formed

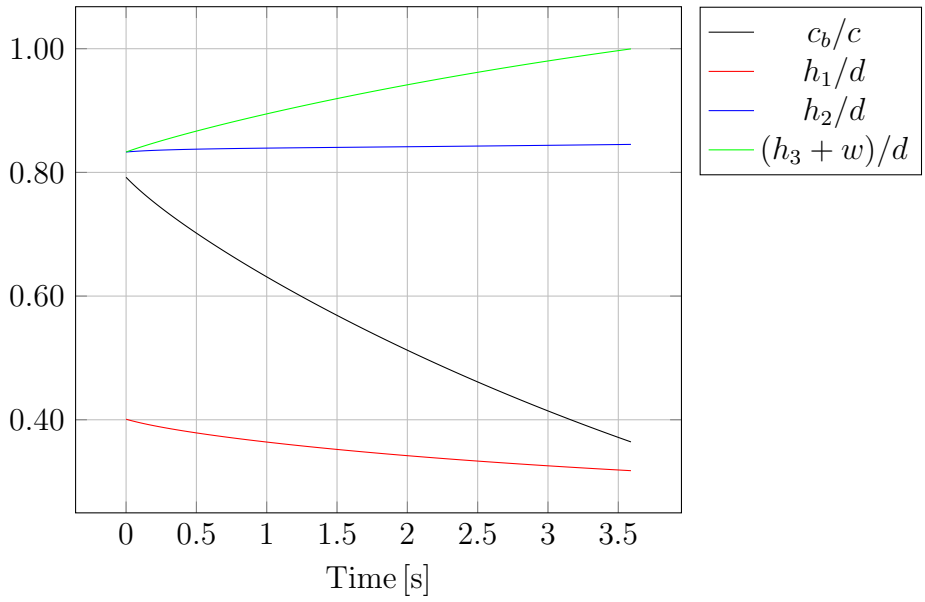

Figure 2.6: Air cavity propagation: analytical results

at t=0 in the analytical approach (see Fig. 2.7a). Nevertheless, bore celerity is fairly well captured, essential to predict the sealing of air pockets (values of c_b/d provided by analytical model are between 0.79 and 0.36 while real values are between 0.81 and 0.30 approximately).

Analytical approach is now employed to study combinations of duct slope and gate height that lead to a cavity shut. Theoretical results along with laboratory outputs of Ref. [1] are depicted in Fig. 2.9. In this figure, black colour indicates laboratory outputs, circles mark when sealing does not occur, while squares and crosses mean that cavity seals at irregular or regular intervals, respectively. Red denotes analytical results, crosses denote cavity sealing and circles denote open cavity. As in last experiment, conditions for sealing are well predicted, especially for slopes greater than 1^o. Hence, present analytical model can be useful to efficiently predict dynamics of air cavities and their eventual sealing in simple configurations.

2.2 Semi-Analytical Approach for Rising Elongated Bubbles and Geysering Phenomena

Effect of rising Taylor bubbles on the liquid free surface is studied in this section. Firstly it is examined the case with a single bubble; secondly, study is extended to N consecutive bubbles. In the analytical model presented in

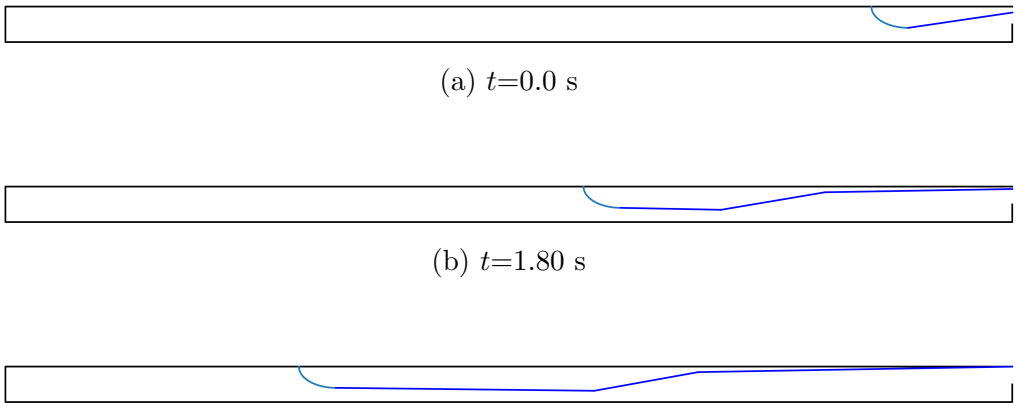

(a) t=0.0 s

(b) t=1.80 s

(c) t=3.58 s

Figure 2.7: Air cavity propagation: sketches from analytical results

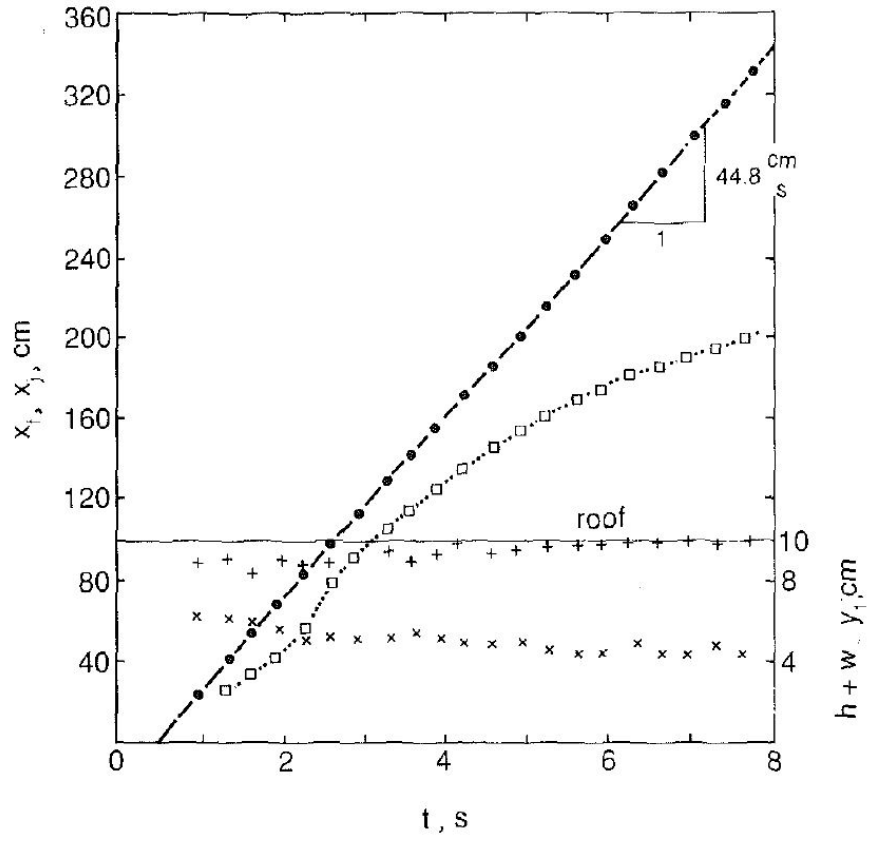

Figure 2.8: Air cavity propagation: laboratory outputs. • = position of air cavity front; □ = location of bore toe; + = water depth at weir; × = water depth at bore toe. Source: [1].

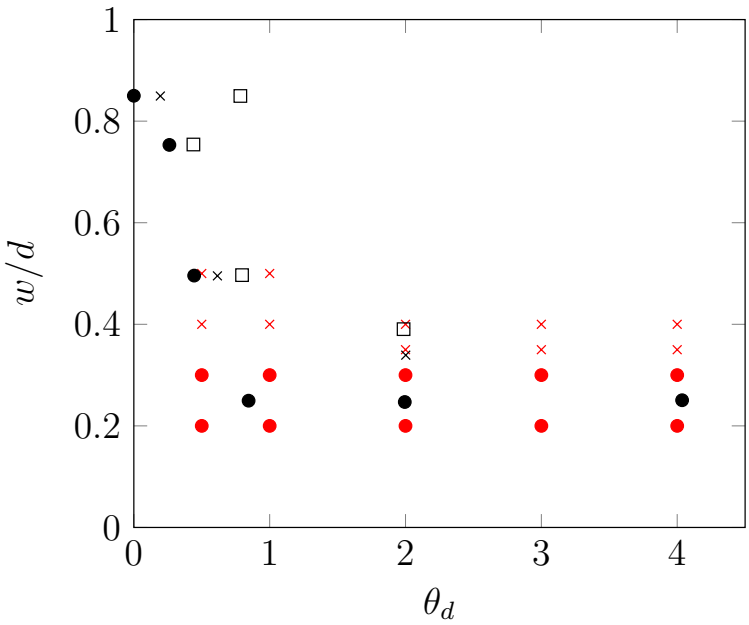

Figure 2.9: Cavity sealing as function of w/d and slope θ_d (in degrees). Comparison between experimental output [1] (black marks) and analytical results (red marks).

Ref. [79], bubble shape was simplified and drift velocity was imposed as initial bubble velocity. Here, a more realistic bubble shape is considered and drag and buoyancy forces along with gas expansion effects are taken into account to calculate bubble dynamics.

2.2.1 Bubble Geometry

Bubble geometry is defined according to Ref. [58]. Then, shape of a Taylor bubble rising in a vertical tube with diameter d is specified by the following three regions,

$$r(z) = \begin{cases} \frac{1}{2}\sqrt{z(3d-4z)} & if \quad z < z_1 \\ \frac{d}{2}\sqrt{1-\frac{U_\infty}{\sqrt{2gz}}} & if \quad z_1 \leq z \leq z_2 \\ \frac{d}{2} - \delta_\nu & if \quad z > z_2 \end{cases}, \tag{2.27}$$

where coordinates r and z are depicted in Fig. 2.10 and g is the gravity acceleration. First region has spherical shape with radius equal to $3d/8$. In second region, bubble shape is obtained under the premise of constant air pressure

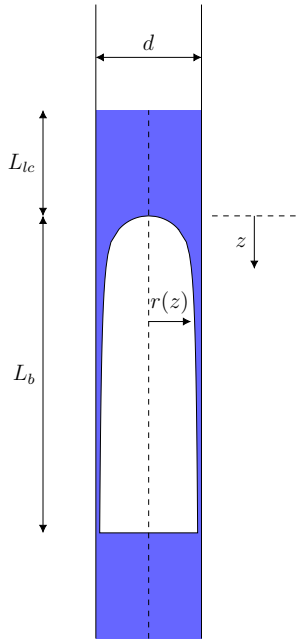

Figure 2.10: Sketch of a rising bubble

by applying mass conservation and Bernoulli equation to a stream line passing by the bubble nose. Besides, U_∞ is the bubble velocity in stagnant liquid defined as,

$$U_\infty = k\sqrt{gd}\,. \tag{2.28}$$

Here, k is a non-dimensional constant that was experimentally obtained in Refs. [24, 57] among others; k=0.345 is a commonly used value. Finally, third region is dominated by viscous forces, where δ_ν is the liquid film thickness between bubble and duct wall. Following Ref. [5], thickness δ_ν can be calculated from the equation,

$$U_\infty \pi \frac{d^2}{4} = \left(U_\infty + \frac{g\delta_\nu^2}{3\nu_l}\right) \cdot (\pi\delta_\nu(d-\delta_\nu))\ , \tag{2.29}$$

where ν_l is the kinematic viscosity of the liquid. Equation (2.29) establishes conservation of mass for a parabolic velocity profile across the liquid layer between bubble interface and solid wall with thickness $\delta_\nu \ll d/2$. On the other hand, z_1 can be attained by equating first and second shape forms of Eq. (2.10),

$$\frac{1}{2}\sqrt{z_1(3d-4z_1)} = \frac{d}{2}\sqrt{1-\frac{U_\infty}{\sqrt{2gz_1}}} \rightarrow z_1 = l_1(k)d\,, \tag{2.30}$$

where l_1=0.128484 if k=0.345. Finally, similar course of action is used to get z_2, resulting in

$$z_2 = \frac{1}{2g}\left(U_\infty + \frac{1}{3\nu_l} g\delta_\nu^2\right)^2 . \tag{2.31}$$

Once bubble shape is defined, gas volume is calculated,

$$V_1 = \int_0^{l_1 d} \frac{\pi}{4} z(3d - 4z)\mathrm{d}z = \frac{\pi}{4} d^3 l_1^2 \left(\frac{3}{2} - \frac{4}{3} l_1\right) , \tag{2.32}$$

$$V_2 = \int_{l_1 d}^{z_2} \pi \frac{d^2}{4}\left(1 - \frac{k\sqrt{gd}}{\sqrt{2gz}}\right)\mathrm{d}z = \frac{\pi d^2}{4}\left[(z_2 - l_1 d) - k\sqrt{2d}\left(\sqrt{z_2} - \sqrt{l_1 d}\right)\right] , \tag{2.33}$$

$$V_3 = \int_{z_2}^{L_b} \pi\left(\frac{d}{2} - \delta_\nu\right)^2 \mathrm{d}z = \pi\left(\frac{d}{2} - \delta_\nu\right)^2 (L_b - z_2) , \tag{2.34}$$

where L_b is the bubble length, and V_1, V_2 and V_3 are gas volumes of regions 1, 2 and 3, respectively, assuming that $L_b \geq z_2$. If $z_1 < L_b < z_2$, V_3=0 and

$$V_2 = \frac{\pi d^2}{4}\left[(L_b - l_1 d) - k\sqrt{2d}\left(\sqrt{L_b} - \sqrt{l_1 d}\right)\right] .$$

Moreover, surrounding liquid volume V_l (if $L_b \geq z_2$) is,

$$V_l = \frac{\pi d^2}{4} L_b - V_1 - V_2 - V_3 =$$
$$\frac{\pi d^2}{4}\left[l_1 d - l_1^2 d\left(\frac{3}{2} - \frac{4}{3} l_1\right) + k\sqrt{2d}\left(\sqrt{z_2} - \sqrt{l_1 d}\right)\right] + (L_b - z_2)\,\pi\delta_\nu\,(d - \delta_\nu) . \tag{2.35}$$

Finally, the derivative of the gas volume V_g confined in the bubble respect to the vertical coordinate z is

$$\frac{\mathrm{d}V_g}{\mathrm{d}z} = \begin{cases} \pi\frac{d^2}{4}\left(1 - \frac{k\sqrt{d}}{\sqrt{2z}}\right) & if \quad z_1 < L_b < z_2 \\ \pi\left(\frac{d}{2} - \delta_\nu\right)^2 & if \quad L_b \geq z_2 \end{cases} , \tag{2.36}$$

2.2.2 Compressibility Model

Liquid with density ρ_l surrounding the bubble is assumed incompressible, and gas compressions and expansions processes are considered adiabatic. Thus, gas density is defined as,

$$\rho_g = \left(\frac{P + P_{atm}}{C}\right)^{1/\gamma} ; \quad C = \frac{P_{atm}}{\rho_{g0}^\gamma} , \tag{2.37}$$

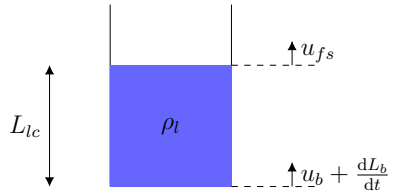

Figure 2.11: Control Volume 1

where P is the relative gas pressure of the bubble, P_{atm} is the atmospheric pressure, γ is the gas adiabatic index and ρ_{g0} is the gas density at atmospheric pressure.

2.2.3 Single Bubble: Control Volume Analysis

The case of a single Taylor bubble rising in a vertical conduit is now addressed. Formulation is accomplished by applying integral form of conservation equations to the bubble and to the liquid situated above the gas. Problem is considered as one-dimensional, by only taking into account the motion along vertical axis. Moreover, it is assumed that liquid column below the bubble is much greater than liquid column above the bubble; hence, gas expansions or compressions processes only have an effect on the upper region of the bubble. As final assumption, liquid flow rate between bubble and duct wall is constant and equal to $U_\infty \pi \frac{d^2}{4}$. As a consequence, free surface height variations ascribed to bubble rising celerity are considered much smaller than those ascribed to bubble velocity caused by gas expansion/compression (in agreement with conclusions of Ref. [72]).

Control Volume 1

First control volume includes the liquid column above the bubble nose (see Figs. 2.10 and 2.11). Control volume upper boundary velocity is $u_{fs}\mathbf{k}$, whereas lower boundary velocity is $\left(u_b + \frac{\mathrm{d}L_b}{\mathrm{d}t}\right)\mathbf{k}$. Here, $\mathbf{k}$ is the vertical unit vector and u_b is the velocity of the bubble bottom. Liquid velocity inside this control volume is constant with value $\mathbf{u}(\mathbf{x},t)=u_{fs}\mathbf{k}$. Mass conservation equation gives,

$$\frac{\mathrm{d}}{\mathrm{d}t}\left(\rho_l L_{lc}\frac{\pi d^2}{4}\right) + \rho_l \frac{\pi d^2}{4}\left[(u_{fs}-u_{fs}) - \left(u_{fs} - u_b - \frac{\mathrm{d}L_b}{\mathrm{d}t}\right)\right] = 0\,;$$

$$\frac{\mathrm{d}L_{lc}}{\mathrm{d}t} = u_{fs} - u_b - \frac{\mathrm{d}L_b}{\mathrm{d}t}\,, \tag{2.38}$$

where L_{lc} is the liquid column length. Regarding momentum conservation, gravity, pressure and wall friction are included as external forces,

$$\frac{\mathrm{d}}{\mathrm{d}t}\left(\rho_l L_{lc}\frac{\pi d^2}{4}u_{fs}\right)+\rho_l\frac{\pi d^2}{4}\left[u_{fs}\left(u_{fs}-u_{fs}\right)-u_{fs}\left(u_{fs}-u_b-\frac{\mathrm{d}L_b}{\mathrm{d}t}\right)\right]= \\ -\rho_l L_{lc}\frac{\pi d^2}{4}\left|g\right|+P_0\frac{\pi d^2}{4}-\frac{f}{8}L_{lc}\pi d\rho_l u_{fs}\left|u_{fs}\right| .$$

Insertion of Eq. (2.38) into last equation results in

$$\frac{P_0}{\rho_l}=L_{lc}\left[\frac{\mathrm{d}u_{fs}}{\mathrm{d}t}+\left|g\right|+\frac{f}{2}\frac{u_{fs}\left|u_{fs}\right|}{d}\right] , \tag{2.39}$$

where P_0 is the relative pressure at bubble nose position and f is the friction factor. In what follows, bubble pressure will be assumed constant over the entire gas volume and equal to the bubble nose pressure.

Control Volume 2

Second control volume includes the bubble and surrounding liquid (see Fig. 2.12). Upper boundary velocity is $\left(u_b+\frac{\mathrm{d}L_b}{\mathrm{d}t}\right)\mathbf{k}$ and lower boundary velocity is $u_b\mathbf{k}$. Liquid velocity in this control volume is not constant; on the upper boundary $\mathbf{u}(\mathbf{x},t)|_{z=0}{=}u_{fs}\mathbf{k}$, whereas on the lower boundary liquid velocity can be calculated from the flow rate between bubble and duct wall,

$$U_\infty\pi\frac{d^2}{4}=\left(-u|_{z=L_b}+U_\infty\right)\left[\pi\delta_\nu^*\left(d-\delta_\nu^*\right)\right] , \tag{2.40}$$

where $\delta_\nu^*{=}d/2-r\left(L_b\right)$. Note that liquid flow at the lower boundary is downward, so $u|_{z=L_b}<0$. Mass conservation law for this control volume is,

$$\frac{\mathrm{d}}{\mathrm{d}t}\left(\rho_g V_g+\rho_l V_l\right)+\rho_l\pi\frac{d^2}{4}\left(u_{fs}-u_b-\frac{\mathrm{d}L_b}{\mathrm{d}t}\right)- \\ \rho_l\left[\pi\delta_\nu^*\left(d-\delta_\nu^*\right)\right]\left(u|_{z=L_b}-u_b\right)=0 . \tag{2.41}$$

Inserting Eq. (2.40) into Eq. (2.41), and taking into account that gas mass is constant,

$$\frac{\mathrm{d}V_l}{\mathrm{d}t}=-\pi\frac{d^2}{4}\left(u_{fs}-u_b-\frac{\mathrm{d}L_b}{\mathrm{d}t}\right)-u_b\pi\delta_\nu^*\left(d-\delta_\nu^*\right)-U_\infty\left[\pi\frac{d^2}{4}-\pi\delta_\nu^*\left(d-\delta_\nu^*\right)\right] . \tag{2.42}$$

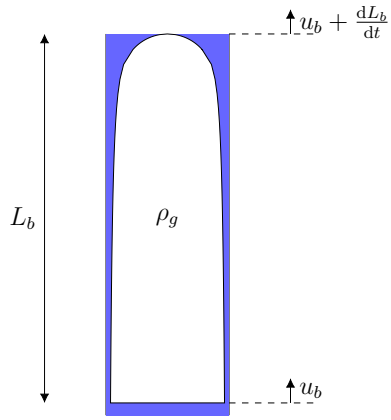

Figure 2.12: Control Volume 2

Besides, volumes derivatives are,

$$\frac{\mathrm{d}V_l}{\mathrm{d}t} = \frac{\mathrm{d}}{\mathrm{d}t}\left(\pi\frac{d^2}{4}L_b - V_g\right) = \frac{\mathrm{d}V_g}{\mathrm{d}t}\left(\psi - 1\right) , \tag{2.43}$$

$$\psi = \pi\frac{d^2}{4}\frac{\mathrm{d}L_b}{\mathrm{d}V_g} = \begin{cases} \left(1 - \frac{k\sqrt{gd}}{\sqrt{2gL_b}}\right)^{-1} & if \quad z_1 < L_b < z_2 \\ \frac{d^2}{4\left(\frac{d}{2}-\delta_\nu\right)^2} & if \quad L_b \geq z_2 \end{cases} , \tag{2.44}$$

where definition of ψ comes from Eq. (2.36). Definition of $\frac{\mathrm{d}V_g}{\mathrm{d}t}$ can be obtained by considering the gas mass conservation (M_g=$V_g\rho_g$),

$$\frac{\partial M_g}{\partial t} = 0 \rightarrow \frac{\mathrm{d}V_g}{\mathrm{d}t} = -\frac{V_g}{\rho_g}\frac{\mathrm{d}\rho_g}{\mathrm{d}t} ;$$

$$\frac{\mathrm{d}V_g}{\mathrm{d}t} = -\frac{V_g}{\rho_g}\frac{1}{\gamma C}\left(\frac{P_0 + Patm}{C}\right)^{1/\gamma-1}\frac{\mathrm{d}P_0}{\mathrm{d}t} . \tag{2.45}$$

As previously stated, bubble gas pressure is equal to $P_0(t)$, neglecting local variations inside the bubble. Finally, Eqs. (2.43), (2.44) and (2.45) are introduced into Eq. (2.42) to get an explicit equation for u_{fs},

$$u_{fs} = (u_b - U_\infty)\left(1 - \frac{\delta_\nu^*\left(d - \delta_\nu^*\right)}{d^2/4}\right) - \frac{4}{\pi d^2}\frac{V_g}{\rho_g}\frac{1}{\gamma C}\left(\frac{P_0 + Patm}{C}\right)^{1/\gamma-1}\frac{\mathrm{d}P_0}{\mathrm{d}t} . \tag{2.46}$$

Control Volume 3

For the third control volume, which only includes the bubble gas, momentum conservation equation is applied. To simplify the derivation, an average

bubble velocity of value u_b is considered. Therefore, it is assumed that those zones in the vicinity of bubble nose, where there are local velocity deviations due to gas expansion or compression processes, are small. Bubble momentum conservation equation is

$$\frac{\mathrm{d}}{\mathrm{d}t}\left[u_b\left(V_g\rho_g + K_M V_g \rho_l\right)\right] = |g|\,\rho_l V_g - \rho_l C_d \pi \frac{d^2}{4}\frac{u_b\,|u_b|}{2} \tag{2.47}$$

where K_M and C_d are the added mass and drag coefficients, respectively. Here, $K_M{=}\frac{\alpha\pi d^2 L_b}{4V_g}$ with $\alpha{=}0.32731$ (see Ref. [37]) and $C_d{=}\varepsilon\frac{V_g}{\pi(d/2)^3}$ (see Ref. [6]). Value of $\varepsilon{\approx}8.4$ corresponds to a nondimensional bubble velocity in stagnant liquid with $k{=}0.345$ (see Eq. (2.28)). Considering again Eqs. (2.43), (2.44) and (2.45), attained in the second volume, an equation for $\frac{\mathrm{d}u_b}{\mathrm{d}t}$ can be reached,

$$\beta\frac{\mathrm{d}u_b}{\mathrm{d}t} = u_b\alpha\rho_l\psi\frac{V_g}{\rho_g}\frac{1}{\gamma C}\left(\frac{P_0+Patm}{C}\right)^{1/\gamma-1}\frac{\mathrm{d}P_0}{\mathrm{d}t} + |g|\,\rho_l V_g - \rho_l\varepsilon V_g\frac{u_b\,|u_b|}{d}\,, \tag{2.48}$$

$$\beta = V_g\rho_g + \alpha\pi\frac{d^2}{4}L_b\rho_l\,.$$

Unknowns P_0, u_b, and u_{fs} can be computed by solving Eqs. (2.39), (2.46) and (2.48).

Discussion

In vertical momentum law (2.39) it can be assumed that $|g| \gg \frac{\mathrm{d}u_{fs}}{\mathrm{d}t}$ and $|g| \gg \frac{f}{2}\frac{u_{fs}|u_{fs}|}{d}$. Then, bubble pressure is,

$$P_0 = \rho_l L_{lc}\,|g|\,, \tag{2.49}$$

whose derivative, taking into account Eq. (2.38), is,

$$\frac{\mathrm{d}P_0}{\mathrm{d}t} = \rho_l\,|g|\left(u_{fs} - u_b - \frac{\mathrm{d}L_b}{\mathrm{d}t}\right)\,. \tag{2.50}$$

Moreover, first term on the right hand side of Eq. (2.48) can be considered as negligible respect to the others (this observation is substantiated by extensive analytical experiments (see section 4.3.3)); hence, for steady state conditions, $\frac{\mathrm{d}u_b}{\mathrm{d}t}{\to}0$, $u_b{\to}U_\infty$. Considering last hypothesis, Eq. (2.46) reduces to,

$$u_{fs} = -\frac{4}{\pi d^2}\frac{V_g}{\rho_g}\frac{1}{\gamma C}\left(\frac{P_0+Patm}{C}\right)^{1/\gamma-1}\frac{\mathrm{d}P_0}{\mathrm{d}t}\,. \tag{2.51}$$

Lastly, Eq. (2.51) is introduced into (2.50) to get the final equation for $\frac{\mathrm{d}P_0}{\mathrm{d}t}$,

$$\frac{\mathrm{d}P_0}{\mathrm{d}t} = \frac{-u_b}{\frac{1}{\rho_l|g|} - \frac{4(\psi-1)}{\pi d^2}\frac{V_g}{\rho_g}\frac{1}{\gamma C}\left(\frac{P_0+Patm}{C}\right)^{1/\gamma-1}}\,. \tag{2.52}$$

This result reveals a condition for a sudden bubble expansion and, consequently, for a significant free surface vertical acceleration. This condition can be written as

$$\rho_l\,|g|\,\frac{4\,(\psi-1)}{\pi d^2}\frac{V_g}{\rho_g}\frac{1}{\gamma C}\left(\frac{P_0+Patm}{C}\right)^{1/\gamma-1} \to 1\,. \tag{2.53}$$

Next it is studied the stage when free surface has reached the upper end of the duct; in this situation liquid column height only depends on bubble dynamics and Eq. (2.38) reduces to,

$$\frac{\mathrm{d}L_{lc}}{\mathrm{d}t} = -u_b - \frac{\mathrm{d}L_b}{\mathrm{d}t}\,. \tag{2.54}$$

Following the same procedure as above, new equation for time derivative of bubble pressure becomes,

$$\frac{\mathrm{d}P_0}{\mathrm{d}t} = \frac{-u_b}{\frac{1}{\rho_l|g|} - \frac{4\psi}{\pi d^2}\frac{V_g}{\rho_g}\frac{1}{\gamma C}\left(\frac{P_0+Patm}{C}\right)^{1/\gamma-1}}\,, \tag{2.55}$$

and the corresponding condition for a sudden expansion is,

$$\rho_l\,|g|\,\frac{4\psi}{\pi d^2}\frac{V_g}{\rho_g}\frac{1}{\gamma C}\left(\frac{P_0+Patm}{C}\right)^{1/\gamma-1} \to 1\,. \tag{2.56}$$

Note that the determining variable in Eqs. (2.53) and (2.56) is the relation between gas volume V_g and the square of duct diameter D^2. The remaining parameters are constants or suffer slight changes. From Eq. (2.44), ψ>1, and in case of elongated bubbles, ψ=$\mathcal{O}(1)$. Hence when free surface reaches the upper conduit end, a considerably smaller gas volume is needed to provoke a sudden bubble expansion (compare Eqs. (2.53) and (2.56)). Furthermore, once bubble nose arrives at upper end, V_g raises its maximum value, because compression originated from liquid column above the bubble has virtually vanished. In situ observations as well as numerical experiments (see section 4.3.6) provide evidences supporting that in this state a violent geyser may occur.

Semi-Analytical Solution Algorithm

Solution of equations (2.39), (2.46) and (2.48) gives P_0, u_b and u_{fs} at time level t^{n+1}. A straightforward temporal discretisation of these equations is,

$$\frac{P_0^{n+1}}{\rho_l} = L_{lc}\left[\left(\frac{\mathrm{d}u_{fs}}{\mathrm{d}t}\right)^{n+1} + |g| + \frac{f}{2}\frac{u_{fs}^{n+1}\left|u_{fs}^{n+1}\right|}{d}\right], \tag{2.57}$$

$$u_{fs}^{n+1} = \left(u_b^{n+1} - U_\infty\right)\left(1 - \frac{\delta_\nu^*\left(d-\delta_\nu^*\right)}{d^2/4}\right) - \frac{4}{\pi d^2}\frac{V_g}{\rho_g}\frac{1}{\gamma C}\left(\frac{P_0^{n+1}+Patm}{C}\right)^{1/\gamma-1}\left(\frac{\mathrm{d}P_0}{\mathrm{d}t}\right)^{n+1}, \tag{2.58}$$

$$\beta\left(\frac{\mathrm{d}u_b}{\mathrm{d}t}\right)^{n+1} = u_b^{n+1}\alpha\rho_l\psi\frac{V_g}{\rho_g}\frac{1}{\gamma C}\left(\frac{P_0^{n+1}+Patm}{C}\right)^{1/\gamma-1}\left(\frac{\mathrm{d}P_0}{\mathrm{d}t}\right)^{n+1} + |g|\,\rho_l V_g - \rho_l\varepsilon V_g\frac{u_b^{n+1}\left|u_b^{n+1}\right|}{d}. \tag{2.59}$$

Superscript $n+1$ indicates time level t^{n+1} and those variables without superscript are considered at time level t^n to facilitate the resolution. Derivative $(\mathrm{d}B/\mathrm{d}t)^{n+1}$ for a function $B(t)$ signifies,

$$\left(\frac{\mathrm{d}B}{\mathrm{d}t}\right)^{n+1} = \begin{cases} \frac{3B^{n+1}-4B^n+B^{n-1}}{2\Delta t} & if \quad n>0 \\ \frac{B^{n+1}-B^n}{\Delta t} & if \quad n=0 \end{cases}, \tag{2.60}$$

where $\Delta t = t^{n+1} - t^n$ and n=0 indicates initial time. Thus, solution algorithm consists of the following steps:

1. For a given duct geometry, gas mass and bubble position, initial bubble parameters and liquid column length are calculated (ρ_g^0, V_b^0, δ_ν^{*0}, ψ^0, L_b^0 and L_{lc}^0). At first time step, it is assumed that P_0^0=$L_{lc}^0\,|g|\,\rho_l$, u_{fs}^0=0 and u_b^0=0 or u_b^0=U_∞.

2. Computation of P_0^{n+1}, u_b^{n+1} and u_{fs}^{n+1} with Eqs. (2.57), (2.58), (2.59) and (2.60) for $n \geq 0$.

3. Free surface position updating,

$$h_{fs}^{n+1} = h_{fs}^n + u_{fs}^{n+1}\cdot\Delta t\,.$$

   Note that $h_{fs}^{n+1} \leq H$, where H is the duct upper end position (see e.g. Fig. 2.13, where H=0.610 m).

4. Updating of ρ_g and V_g,

$$\rho_g^{n+1} = \left(\frac{P_0^{n+1} + Patm}{C} \right)^{1/\gamma} ,$$
$$V_g^{n+1} = \frac{M_g}{\rho_g^{n+1}} .$$

5. Recalculate the bubble shape and get L_b^{n+1}, δ_ν^{*n+1}.

6. Updating of L_{lc},

$$L_{lc}^{n+1} = L_{lc}^n + \Delta t \left(u_{fs}^{n+1} - u_b^{n+1} - \frac{4\psi^{n+1}}{\pi d^2} \left(\frac{-V_g}{\rho_g} \right)^{n+1} \frac{1}{\gamma C} \left(\frac{P_0^{n+1} + Patm}{C} \right)^{1/\gamma - 1} \left(\frac{\mathrm{d}P_0}{\mathrm{d}t} \right)^{n+1} \right) ;$$

if free surface has reached the upper end of the duct, L_{lc} is computed as,

$$L_{lc}^{n+1} = L_{lc}^n + \Delta t \left(-u_b^{n+1} - \frac{4\psi^{n+1}}{\pi d^2} \left(\frac{-V_g}{\rho_g} \right)^{n+1} \frac{1}{\gamma C} \left(\frac{P_0^{n+1} + Patm}{C} \right)^{1/\gamma - 1} \left(\frac{\mathrm{d}P_0}{\mathrm{d}t} \right)^{n+1} \right) .$$

7. Calculation of bubble nose position h_b,

$$h_b^{n+1} = h_{fs}^{n+1} - L_{lc}^{n+1} .$$

8. Return to step 3 if $h_b^{n+1} < h_{fs}^{n+1}$.

Assessment

To validate the semi-analytical model, two experiments reported in Ref. [79] are reproduced. There, authors investigated the release of air and water through ventilation towers. Experiments consist of a vertical tube of length L_d=0.610 m having the top open to the atmosphere and connected below to a horizontal duct of diameter 0.094 m. Vertical duct is filled with water up to 0.254 m height and it has a diameter d=5.700·10^{-2} m (experiment 1) and d=1.269·10^{-2} m (experiment 2). A mass of air of M_g=4.642·10^{-3} kg introduced into the horizontal duct propagates towards the vertical tube base (see sketch in Fig. 2.13) and climbs up the vertical duct. Eventually, air mass causes geysering at the top of vertical tube. To adapt this experiment to the

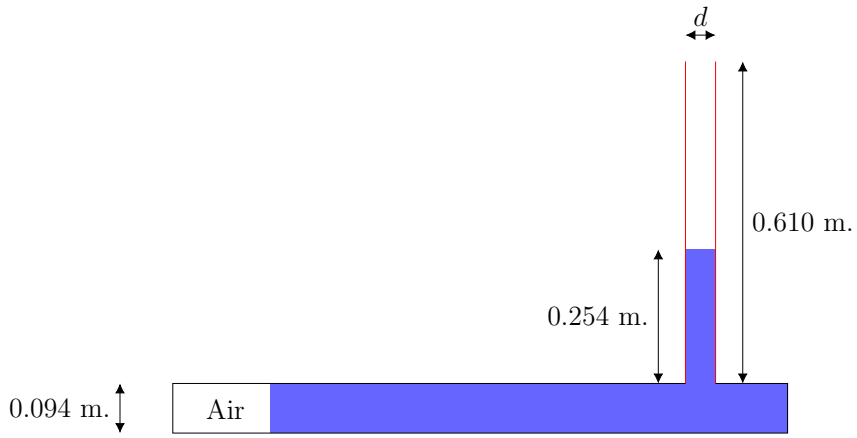

Figure 2.13: Sketch for analytical model assessment

analytical model, it is assumed that vertical tube has semi-infinite length with its upper end located at H=0.610 m (see red conduit in Fig. 2.13). Initial condition is considered when bubble reaches vertical pipe base; hence, h_b^0=0.0 m, h_{fs}^0=0.254 m and initial bubble pressure is P_0^0=0.254 meters of water column. Besides, ρ_l=1000 kg/m^3, ρ_{g0}=1.2 kg/m^3 and g=9.81 m/s^2. Non-dimensional results of three laboratory test repetitions and of analytical model are shown in Figs. 2.14 and 2.15 for experiments 1 and 2 respectively. Figures depict history of bubble head position h_b (Figs. 2.14a and 2.15a), free surface position h_{fs} (Figs. 2.14b and 2.15b) and bubble pressure h_p (Figs. 2.14c and 2.15c); where $\{h_b^*, h_{fs}^*, h_p^*\}=\{h_b, h_{fs}, h_p\}/L_d$, $h_p=P_0/(g\cdot\rho_l)$ and $t^*=t\sqrt{gd}/L_d$.

The model reproduces the quasi-constant bubble head celerity in test 1 (see Fig. 2.14a). However, gas expands faster under test 2 conditions, and bubble head has an apparent vertical acceleration (Fig. 2.15a). Left hand side value in sudden expansion condition (2.53) for case 1 is of 0.008; instead, for test 2 rises to 0.35. This fact gives an explanation of why flow is so different in both cases. Analytical model results have a good agreement with laboratory measurements in both tests. Free surface position is well captured in test 2 (Fig. 2.15b) and slightly underpredicted in test 1 (Fig. 2.14b), while oscillatory free surface behaviour shown in laboratory is adequately reproduced. It can be detected a (nearly) vanishing of oscillations in test 2, both in lab and model. This fact evinces a stage much closer to the formation of a high velocity vertical jet. Finally, analytical bubble pressure shows a good agreement with the three laboratory series in both tests (see Figs. 2.14c and 2.15c); in particular, amplitude and period of pressure oscillations in test 1 are very similar to laboratory observations (runs 1 and 2). The model introduced in Ref. [79] also reproduces bubble and free surface positions fairly

well; nonetheless, bubble pressure is more precisely replicated by the present model. Analytical results also show that bottom bubble velocity in both experiments remains quasi-constant along time with value $u_b \approx U_\infty$, proving that simplification of Eq. (2.48) performed in previous discussion section was valid.

2.2.4 Approach to Multiple Bubbles

In this section, N bubbles rising in a vertical duct are considered (see Fig. 2.16), where L_{bj} is the length of bubble j and L_{lcj} is the length of the liquid column above bubble j. Bubbles numbering starts from the lowest one, so that the nearest to free surface is the bubble N. Liquid columns between bubbles are considered long enough such that trailing bubble is not affected by the leading one. Thus, $L_{lcj} > 10d$ (see Ref. [76]) for $1 \leq j < N$. Each bubble pushes the above liquid column, including leading bubbles, with mean velocity u_{fsj}. Thus, bubble j velocity is,

$$u_{bj} = u^*_{bj} + C_I \cdot \sum_{i=1}^{j-1} u_{fsi} \tag{2.61}$$

where u^*_{bj} is the bubble relative velocity respect to the surrounding liquid. Parameter C_I takes into account deviation of maximum velocity from mean velocity in the profile ahead bubble $j-1$. This parameter is approximately 1.2 for turbulent flows and 2.0 for laminar flows [57]. Velocity u_{fsj} can be calculated in a similar way as Eq. (2.46),

$$u_{fsj} = \left(u^*_{bj} + (C_I - 1) \sum_{i=1}^{j-1} u_{fsi} - U_\infty \right) \left(1 - \frac{\delta^*_{\nu j} \left(d - \delta^*_{\nu j} \right)}{d^2/4} \right) - \frac{4}{\pi d^2} \frac{V_{gj}}{\rho_{gj}} \frac{1}{\gamma C} \left(\frac{P_{0j} + Patm}{C} \right)^{1/\gamma - 1} \frac{\mathrm{d}P_{0j}}{\mathrm{d}t}, \quad \text{for } 1 < j \leq N, \tag{2.62}$$

$$u_{fs1} = (u^*_{b1} - U_\infty) \left(1 - \frac{\delta^*_{\nu 1} (d - \delta^*_{\nu 1})}{d^2/4} \right) - \frac{4}{\pi d^2} \frac{V_{g1}}{\rho_{g1}} \frac{1}{\gamma C} \left(\frac{P_{01} + Patm}{C} \right)^{1/\gamma - 1} \frac{\mathrm{d}P_{01}}{\mathrm{d}t}. \tag{2.63}$$

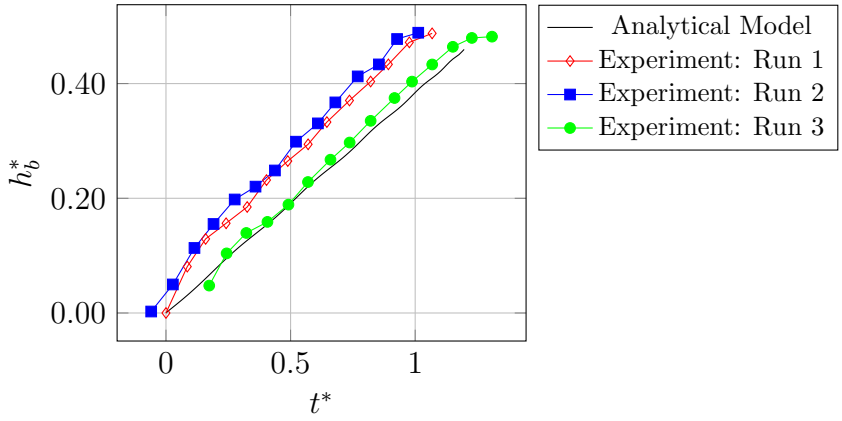

(a) Bubble position

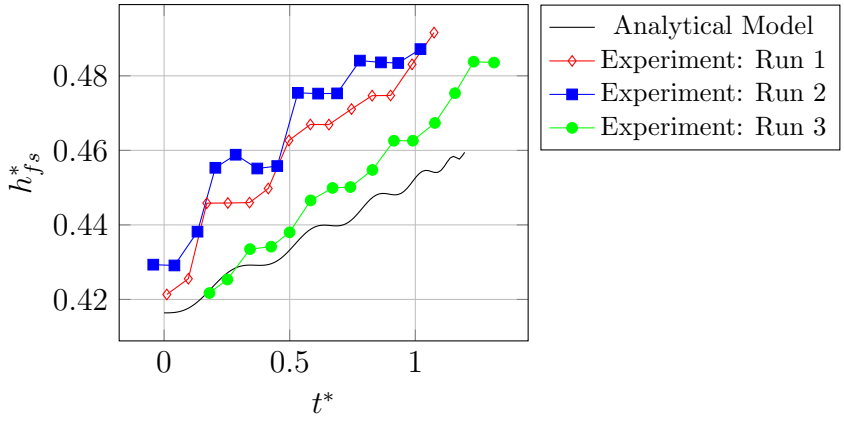

(b) Free surface position

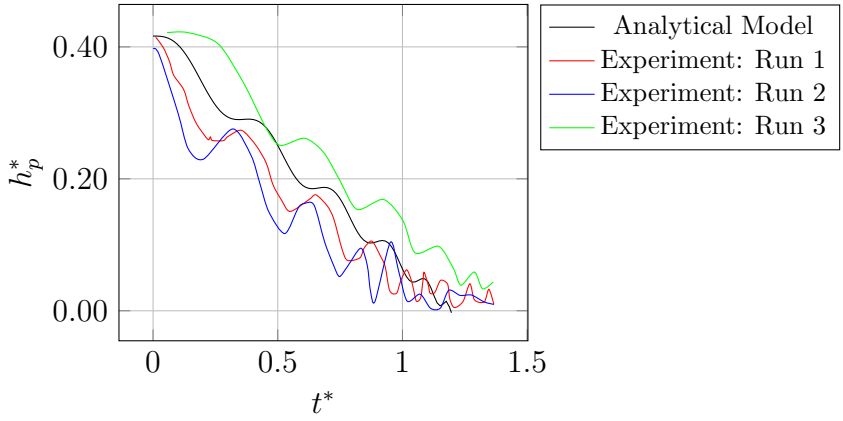

(c) Bubble pressure

Figure 2.14: Rising bubble, test 1: d=5.700 $\cdot$ 10^{-2} m. Comparison between semi-analytical model and experimental results [79].

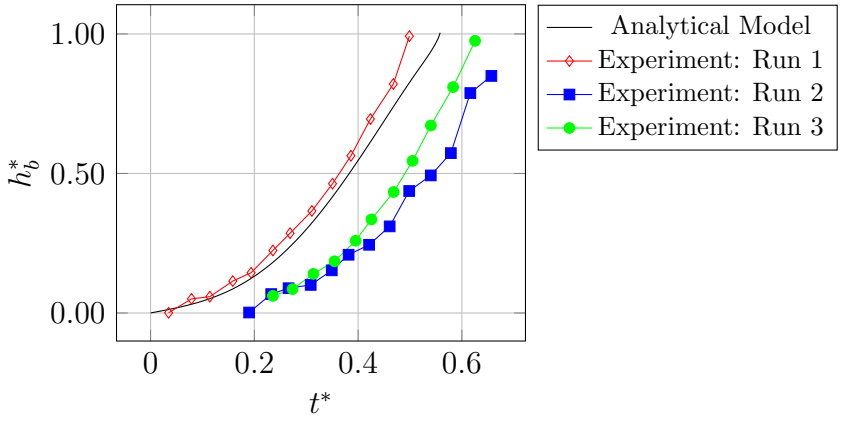

(a) Bubble position

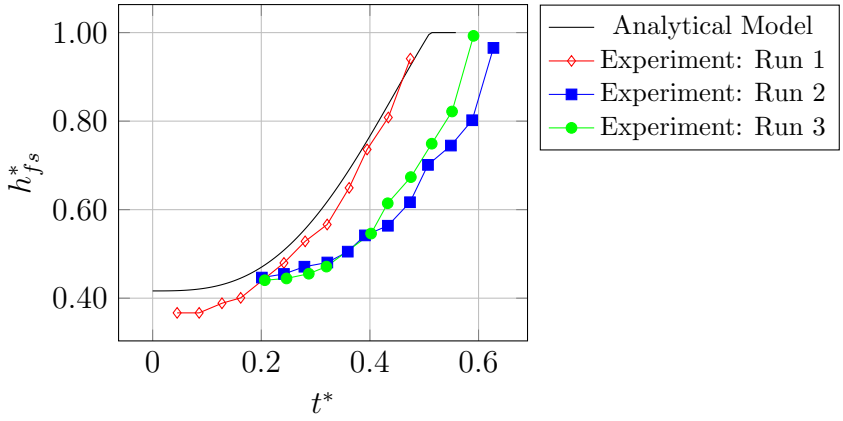

(b) Free surface position

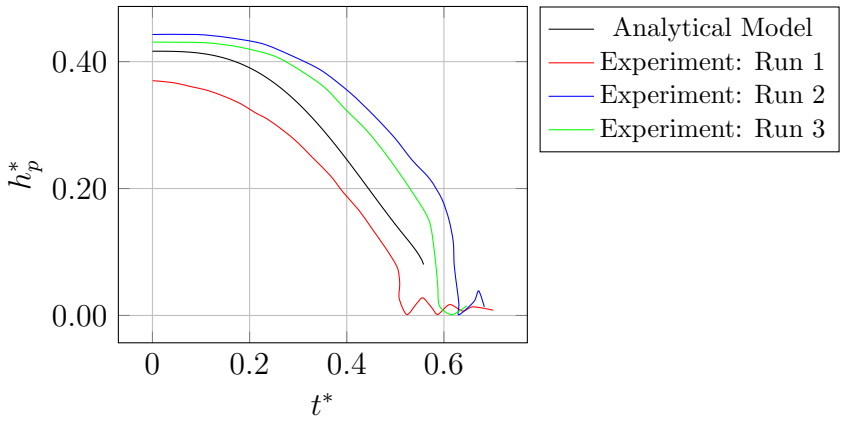

(c) Bubble pressure

Figure 2.15: Rising bubble, test 2: d=1.269 $\cdot$ 10^{-2} m. Comparison between semi-analytical model and experimental results [79].

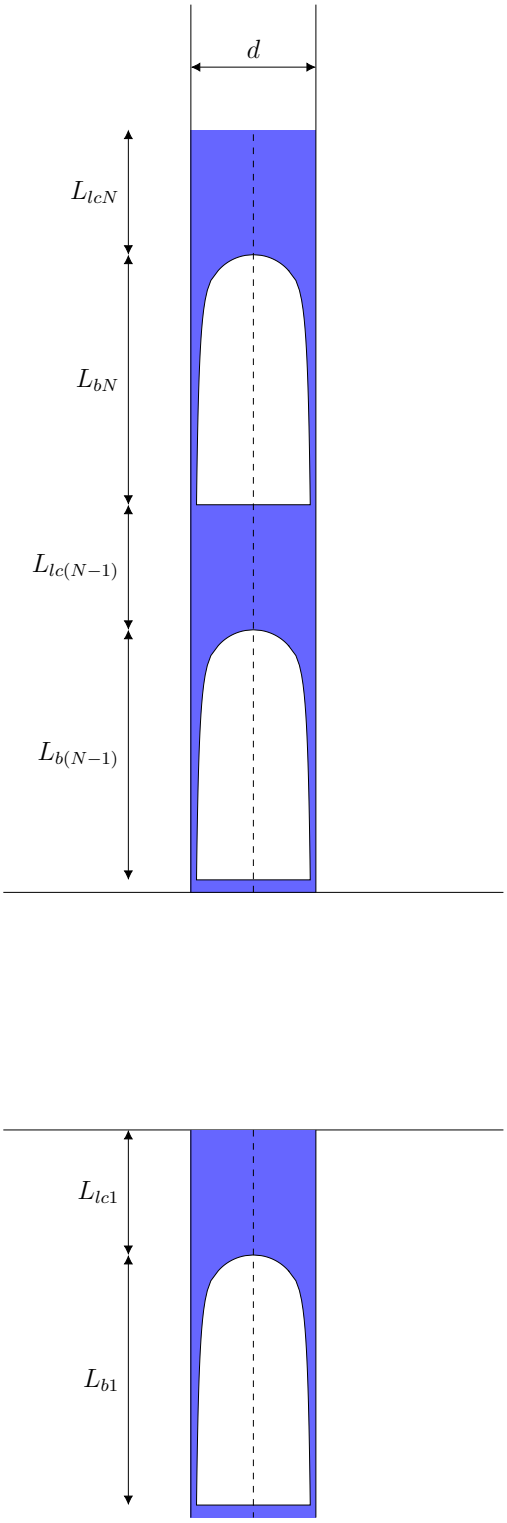

Figure 2.16: Sketch of multiple bubbles

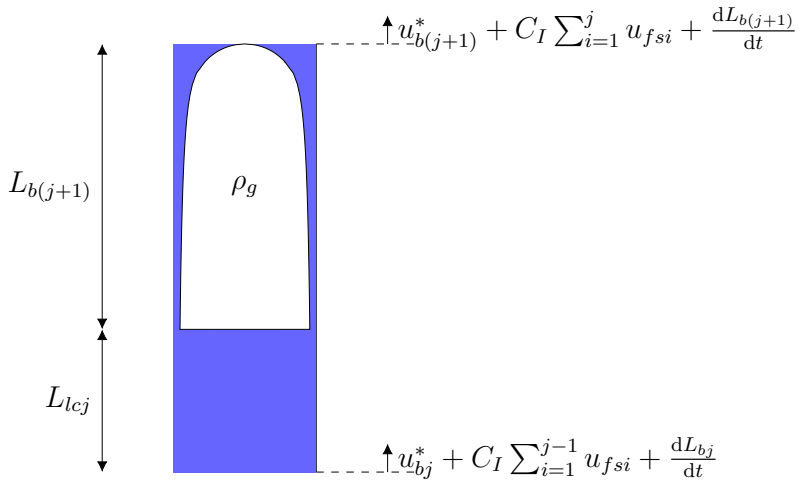

Figure 2.17: Control Volume 3

Likewise, equation for u^*_{bj} resembles calculation of u_b in Eq. (2.48),

$$\beta_j \frac{\mathrm{d}u^*_{bj}}{\mathrm{d}t} = u^*_{bj}\alpha\rho_l\psi_j \frac{V_{gj}}{\rho_{gj}} \frac{1}{\gamma C}\left(\frac{P_{0j}+Patm}{C}\right)^{1/\gamma-1} \frac{\mathrm{d}P_{0j}}{\mathrm{d}t} + |g|\,\rho_l V_{gj} - \rho_l \varepsilon V_{gj} \frac{u^*_{bj}\left|u^*_{bj}\right|}{d}\,. \quad (2.64)$$

$$\beta_j = V_{gj}\rho_{gj} + \alpha\pi\frac{d^2}{4} L_{bj}\rho_l\,.$$

To close the system, it is necessary additional equations for P_{0j}, $\frac{\mathrm{d}L_{lcj}}{\mathrm{d}t}$ and $\frac{\mathrm{d}L_{bj}}{\mathrm{d}t}$. Control volume of Fig. 2.17 is studied for that purpose, including bubble $j+1$ and liquid column j. Here, lower and upper boundaries move according to the nose of bubble j and $j+1$, respectively. Besides, liquid average velocities at lower and upper boundaries are $\sum_{i=1}^{j} u_{fsi}\mathbf{k}$ and $\sum_{i=1}^{j+1} u_{fsi}\mathbf{k}$. Mass conservation in the control volume results in

$$\frac{\mathrm{d}}{\mathrm{d}t}\left[\rho_l\left(L_{b(j+1)}+L_{lcj}\right)\pi\frac{d^2}{4} - V_{g(j+1)}\left(\rho_l-\rho_{g(j+1)}\right)\right] + \rho_l\pi\frac{d^2}{4}\left(\sum_{i=1}^{j+1} u_{fsi} - u^*_{b(j+1)} - C_I\sum_{i=1}^{j} u_{fsi} - \frac{\mathrm{d}L_{b(j+1)}}{\mathrm{d}t}\right) - \rho_l\pi\frac{d^2}{4}\left(\sum_{i=1}^{j} u_{fsi} - u^*_{bj} - C_I\sum_{i=1}^{j-1} u_{fsi} - \frac{\mathrm{d}L_{bj}}{\mathrm{d}t}\right) = 0\,,$$

$$\frac{\mathrm{d}L_{b(j+1)}}{\mathrm{d}t}+\frac{\mathrm{d}L_{lcj}}{\mathrm{d}t}-\frac{4}{\pi d^2}\frac{\mathrm{d}V_{g(j+1)}}{\mathrm{d}t}=-u_{fs(j+1)}+u^*_{b(j+1)}+ C_I u_{fsj}+\frac{\mathrm{d}L_{b(j+1)}}{\mathrm{d}t}-u^*_{bj}-\frac{\mathrm{d}L_{bj}}{\mathrm{d}t}\,,$$

$$\frac{\mathrm{d}L_{lcj}}{\mathrm{d}t}=-u_{fs(j+1)}+u^*_{b(j+1)}+C_I u_{fsj}-u^*_{bj}- \frac{\mathrm{d}L_{bj}}{\mathrm{d}t}+\frac{4}{\pi d^2}\frac{\mathrm{d}V_{g(j+1)}}{\mathrm{d}t}\,,\quad \text{for } 1\le j<N\,, \tag{2.65}$$

$$\frac{\mathrm{d}L_{lcN}}{\mathrm{d}t}=u_{fsN}-u^*_{bN}-\frac{\mathrm{d}L_{bN}}{\mathrm{d}t}-(C_I-1)\sum_{i=1}^{N-1}u_{fsi}\,, \tag{2.66}$$

and, if water has reached the top end of the duct,

$$\frac{\mathrm{d}L_{lcN}}{\mathrm{d}t}=-u^*_{bN}-\frac{\mathrm{d}L_{bN}}{\mathrm{d}t}-C_I\sum_{i=1}^{N-1}u_{fsi}\,. \tag{2.67}$$

Furthermore, to apply momentum conservation it is assumed that liquid moves with velocity $\sum_{i=1}^{j}u_{fsi}\mathbf{k}$, neglecting local bubble effects as well as gas momentum, given that normally $\frac{\rho_g}{\rho_l}\ll 1$. Thus, momentum conservation equation in vertical axis yields to,

$$\begin{aligned}
&\frac{\mathrm{d}}{\mathrm{d}t}\left(\sum_{i=1}^{j}u_{fsi}\right)\left[L_{b(j+1)}+L_{lcj}-\frac{4V_{g(j+1)}}{\pi d^2}\right]+\\
&\qquad\left(\sum_{i=1}^{j}u_{fsi}\right)\left[\frac{\mathrm{d}L_{b(j+1)}}{\mathrm{d}t}+\frac{\mathrm{d}L_{lcj}}{\mathrm{d}t}-\frac{4}{\pi d^2}\frac{\mathrm{d}V_{g(j+1)}}{\mathrm{d}t}\right]+\\
&\left(\sum_{i=1}^{j+1}u_{fsi}\right)\left(u_{fs(j+1)}-u^*_{b(j+1)}-(C_I-1)\sum_{i=1}^{j}u_{fsi}-\frac{\mathrm{d}L_{b(j+1)}}{\mathrm{d}t}\right)-\\
&\qquad\left(\sum_{i=1}^{j}u_{fsi}\right)\left(u_{fsj}-u^*_{bj}-(C_I-1)\sum_{i=1}^{j-1}u_{fsi}-\frac{\mathrm{d}L_{bj}}{\mathrm{d}t}\right)=\\
&\qquad-|g|\left(L_{b(j+1)}+L_{lcj}-\frac{4V_{g(j+1)}}{\pi d^2}\right)+\frac{P_{0(j)}-P_{0(j+1)}}{\rho_l}-\\
&\qquad\qquad\frac{f}{2d}\left(\sum_{i=1}^{j}u_{fsi}\left|\sum_{i=1}^{j}u_{fsi}\right|\right)\left(L_{b(j+1)}+L_{lcj}\right)\,,
\end{aligned}$$

$$\frac{\mathrm{d}}{\mathrm{d}t}\left(\sum_{i=1}^{j} u_{fsi}\right)\left[L_{b(j+1)} + L_{lcj} - \frac{4V_{g(j+1)}}{\pi d^2}\right] +$$
$$\left(\sum_{i=1}^{j} u_{fsi}\right)\left[\frac{\mathrm{d}L_{b(j+1)}}{\mathrm{d}t} - u_{fs(j+1)} + u^*_{b(j+1)} + C_I u_{fsj} - u^*_{bj} - \frac{\mathrm{d}L_{bj}}{\mathrm{d}t}\right] +$$
$$\left(\sum_{i=1}^{j} u_{fsi}\right)\left(u_{fs(j+1)} - u^*_{b(j+1)} - (C_I - 1)\sum_{i=1}^{j} u_{fsi} - \frac{\mathrm{d}L_{b(j+1)}}{\mathrm{d}t}\right) -$$
$$\left(\sum_{i=1}^{j} u_{fsi}\right)\left(u_{fsj} - u^*_{bj} - (C_I - 1)\sum_{i=1}^{j-1} u_{fsi} - \frac{\mathrm{d}L_{bj}}{\mathrm{d}t}\right) +$$
$$u_{fs(j+1)}\left(u_{fs(j+1)} - u^*_{b(j+1)} - (C_I - 1)\sum_{i=1}^{j} u_{fsi} - \frac{\mathrm{d}L_{b(j+1)}}{\mathrm{d}t}\right) =$$
$$-|g|\left(L_{b(j+1)} + L_{lcj} - \frac{4V_{g(j+1)}}{\pi d^2}\right) + \frac{P_{0(j)} - P_{0(j+1)}}{\rho_l} -$$
$$\frac{f}{2d}\left(\sum_{i=1}^{j} u_{fsi}\left|\sum_{i=1}^{j} u_{fsi}\right|\right)\left(L_{b(j+1)} + L_{lcj}\right),$$

$$\frac{\mathrm{d}}{\mathrm{d}t}\left(\sum_{i=1}^{j} u_{fsi}\right)\left[L_{b(j+1)} + L_{lcj} - \frac{4V_{g(j+1)}}{\pi d^2}\right] +$$
$$u_{fs(j+1)}\left(u_{fs(j+1)} - u^*_{b(j+1)} - (C_I - 1)\sum_{i=1}^{j} u_{fsi} - \frac{\mathrm{d}L_{b(j+1)}}{\mathrm{d}t}\right) =$$
$$-|g|\left(L_{b(j+1)} + L_{lcj} - \frac{4V_{g(j+1)}}{\pi d^2}\right) + \frac{P_{0(j)} - P_{0(j+1)}}{\rho_l} -$$
$$\frac{f}{2d}\left(\sum_{i=1}^{j} u_{fsi}\left|\sum_{i=1}^{j} u_{fsi}\right|\right)\left(L_{b(j+1)} + L_{lcj}\right),$$

$$\frac{P_{0j}}{\rho_l} = \frac{P_{0(j+1)}}{\rho_l} + \left[L_{b(j+1)} + L_{lcj} - \frac{4V_{g(j+1)}}{\pi d^2}\right]\left(\frac{\mathrm{d}}{\mathrm{d}t}\left(\sum_{i=1}^{j} u_{fsi}\right) + |g|\right) +$$
$$u_{fs(j+1)}\left(u_{fs(j+1)} - u^*_{b(j+1)} - (C_I - 1)\sum_{i=1}^{j} u_{fsi} - \frac{\mathrm{d}L_{b(j+1)}}{\mathrm{d}t}\right) +$$
$$\frac{f}{2d}\left(\sum_{i=1}^{j} u_{fsi}\left|\sum_{i=1}^{j} u_{fsi}\right|\right)\left(L_{b(j+1)} + L_{lcj}\right), \quad \text{for } 1 \le j < N, \quad (2.68)$$

$$\frac{P_{0N}}{\rho_l} = L_{lcN}\left[\frac{\mathrm{d}}{\mathrm{d}t}\left(\sum_{i=1}^{N} u_{fsi}\right) + |g| + \frac{f}{2d}\left(\sum_{i=1}^{N} u_{fsi}\left|\sum_{i=1}^{N} u_{fsi}\right|\right)\right] . \qquad (2.69)$$

Finally, time variation of bubble length and volume are,

$$\frac{\mathrm{d}L_{bj}}{\mathrm{d}t} = \frac{4\psi_j}{\pi d^2}\frac{\mathrm{d}V_{gj}}{\mathrm{d}t} ,$$
$$\frac{\mathrm{d}V_{gj}}{\mathrm{d}t} = -\frac{V_{gj}}{\rho_{gj}}\frac{1}{\gamma C}\left(\frac{P_{0j}+Patm}{C}\right)^{1/\gamma-1}\frac{\mathrm{d}P_{0j}}{\mathrm{d}t} .$$

Resolution algorithm is similar to that employed for one single bubble but, in this case, there are $3N$ unknowns and equations (Eqs. (2.62), (2.63), (2.64), (2.68) and (2.69)). Equations (2.65) and (2.66) (or Eq. (2.67) if free surface reaches the top end of the duct) update liquid columns length.

Discussion and Assessment

By following analogous assumptions to those discussed for one bubble dynamics, if u^*_{bj}=U_∞ and C_I=1, equations (2.62), (2.66) and (2.69) for bubble N reduce to,

$$u_{fsN} = -\frac{4}{\pi d^2}\frac{V_{gN}}{\rho_{gN}}\frac{1}{\gamma C}\left(\frac{P_{0N}+Patm}{C}\right)^{1/\gamma-1}\frac{\mathrm{d}P_{0N}}{\mathrm{d}t} , \qquad (2.70)$$

$$\frac{\mathrm{d}L_{lcN}}{\mathrm{d}t} = u_{fsN} - U_\infty - \frac{\mathrm{d}L_{bN}}{\mathrm{d}t} , \qquad (2.71)$$

$$\frac{P_{0N}}{\rho_l} = L_{lcN}\,|g| . \qquad (2.72)$$

Thus, when multiple bubbles are present, conditions for sudden expansion of top bubble are similar to those for one single bubble (see Eqs. (2.49)-(2.51)). Moreover, remaining bubbles are also affected by the sudden expansion of the top one (see Eq. (2.68)).

Test 2 of previous section is replicated, but considering propagation of two consecutive bubbles with M_{g1}=M_{g2}=4.642·10^{-3} kg and L_{lc1}=L_{lc2}=0.254 m (lengths of the liquid column above bubble 1 and 2, respectively). Duct has d=1.269·10^{-2} m. To elucidate the influence of lower bubble over the top one, non abridged equations with C_I=1.2 have been solved. Computations are performed for three setups: one single bubble with M_g= 4.642·10^{-3} kg (same as Fig. 2.15), two identical bubbles and one single bubble with M_g=9.284·10^{-3} kg. Analytical results are depicted in Fig. 2.18, where free surface position, top bubble position and pressure are shown. As can be seen in Figs. 2.18a and 2.18b, upper bubble and free surface velocities are sightly increased by

the presence of a second bubble. Otherwise, results also reveal that this increment is more relevant in case that both bubbles were joined (see results marked in green). In real cases, detachments among the three tests can be less significant. This is because solution overpredicts moderately velocities as it is assumed that all gas contained in each bubble has the same pressure, which may amplify expansion action for very large bubbles.

Finally, geysering caused by the rising of multiple bubbles is evaluated with analytical model. From experimental and real life observations, when a train of air pockets rises in a vertical pipe, first bubble seems to produce the weakest geyser in term of height and average velocity of the jet (see discussion in Ref. [44]). A reason for this can be the loss of expelled liquid during first geyser, which involves a sudden decrease of remaining bubbles pressure. A test, emulating laboratory experiment of Ref. [44], is performed trying to reproduce this phenomenon. Here it is considered a duct with d=0.152 m, two bubbles whose total volume is 1.7 m^3 at atmospheric pressure, L^0_{lc2}=6 m and L^0_{lc1}=4 m. In lab experiments, it seems that first bubble is smaller than the others (see Fig. 2.19), thus gas masses M_{g2}=0.36 kg and M_{g1}=1.68 kg are set. At initial time, free surface is located at the top end of the duct. Once nose of bubble 2 reaches the free surface, problem is solved by the system of equations for one single bubble with L_{lc} determined by

$$L_{lc} = L^{(n-1)}_{lc1} + \Omega \left(L^{(n-1)}_{b2} - \frac{4V^{(n-1)}_{g2}}{\pi d^2} \right) , \tag{2.73}$$

where variables with super-index $(n-1)$ represent values just before bubble 2 gets to the free surface and parameter Ω determines the percentage of liquid, previously located between bubble 2 and duct wall, remaining in the duct. In this test, it is assumed Ω=0.5.

Analytical model is able to reproduce laboratory observations despite the fact that the model does not consider the resulting diffuse air/water transition in the vertical duct when first bubble reaches the free surface. Figure 2.20 shows non-dimensional analytical results for free surface and bubbles position (Fig. 2.20a) and velocities (Fig. 2.20b), where $\{h^*_{fs}, h^*_{b2}, h^*_{b1}\} = \{h_{fs}, h_{b2}, h_{b1}\}/L^0_{lc2}$, $\{u'_{fs}, u'_{b1}, u'_{b2}\} = \{u_{fs}, u_{b1}, u_{b2}\}/\sqrt{gd}$ and t^*=$t\sqrt{gd}/L^0_{lc2}$. Variables u_{fs} and u_{bj} are the absolute velocity of free surface and bubble j nose respectively. When leading bubble reaches the free surface at t^*≈0.85, velocity of trailing bubble increases as can be seen in Fig. 2.20b (green line). This increment depends to some extent on the bubble pressure change, which is mainly determined by the amount of water expelled during first geyser. Hence, smaller values of Ω gives larger increases of trailing bubble velocity in analytical outputs. After first discharge, remaining water above trailing

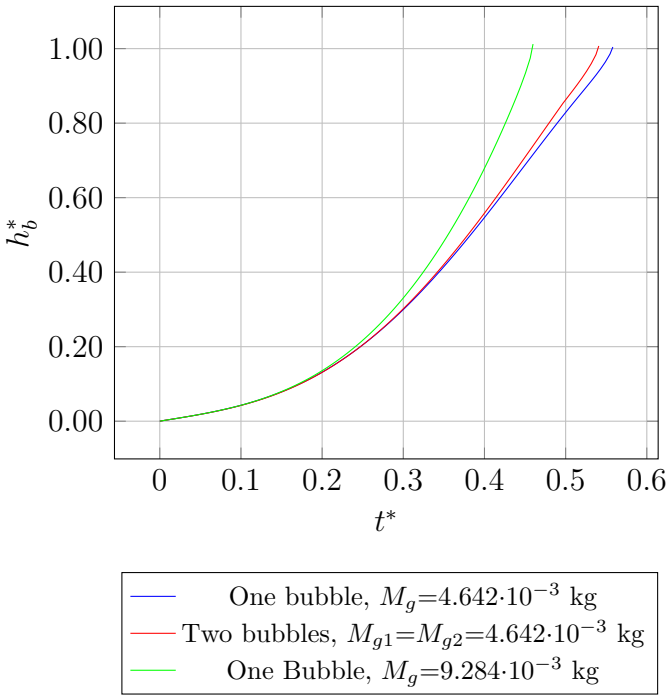

(a) Top bubble position

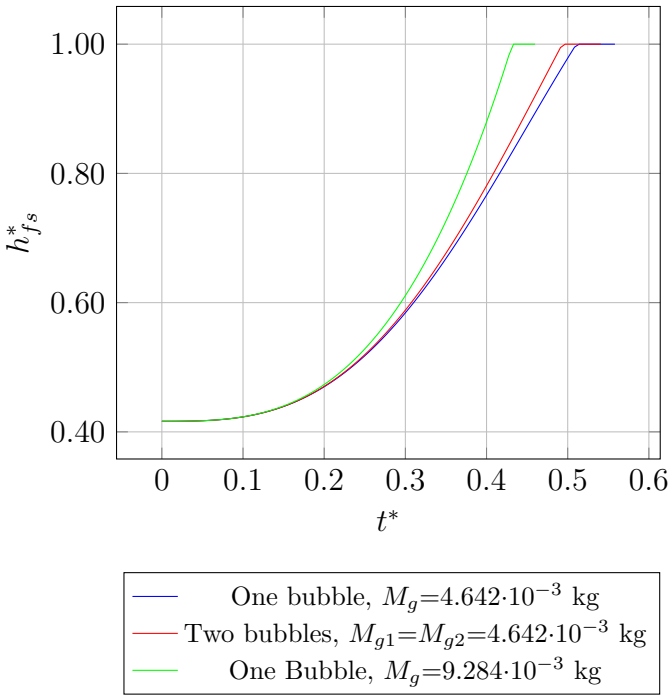

(b) Free surface position

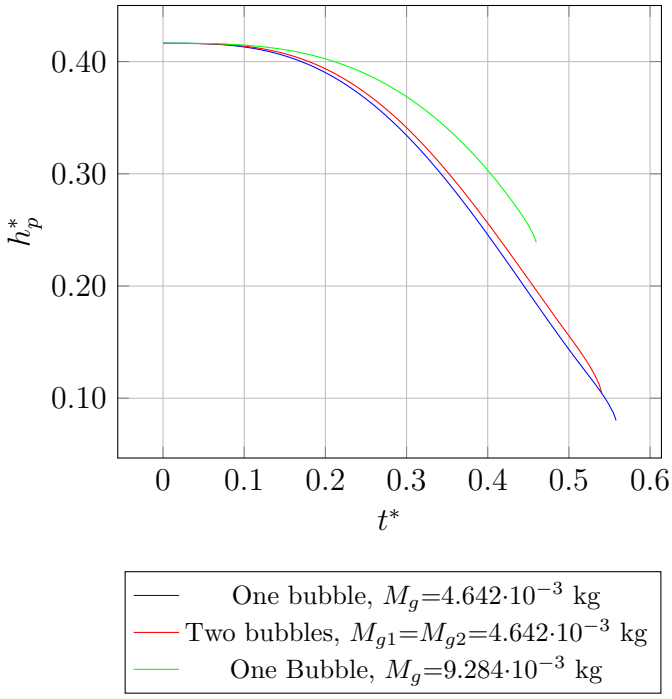

(c) Top bubble pressure

Figure 2.18: Comparison between one single bubble with different gas masses and two consecutive bubbles.

(a) First bubble

(b) Following bubble

Figure 2.19: Comparison between first and following bubbles in a laboratory experiment. Source: Fig. 7 of Ref. [44].

bubble is driven to the top end of the duct causing a second geyser. Violence of last eruption is greater than previous one as can be checked by comparing free surface velocity values at $t^*\approx 0.85$ and $t^*\approx 1.4$ in Fig. 2.20b. This state where second eruption is stronger than first one (also reported in Ref. [44]) is due to two reasons. First, relation between gas volume of trailing bubble and duct diameter is large enough; second, free surface arrives at the duct top end before bubble nose reaches the free surface. In this way, sudden expansion of gas is more likely to happen as in test 2 of previous section (see Fig. 2.15). Conversely, if water column ahead the trailing bubble is too large or bubble gas mass is small, momentum transferred from air to water may not be sufficient to propel violently the column of liquid. In that case, free surface position would oscillate as in test 1 of previous section (see Fig. 2.14).

Analytical solutions for air cavities propagation and rising Taylor bubbles have been reported in this chapter. Furthermore, both models have been assessed by comparing their answers with laboratory outputs. Results indicate that theoretical approaches, despite their limitations, reproduce fairly well the dynamics of open air cavities and rising pressurized bubbles propagating in ducts. Next chapter introduces numerical model for two-fluid flows, used to perform simulations involving these physical events.

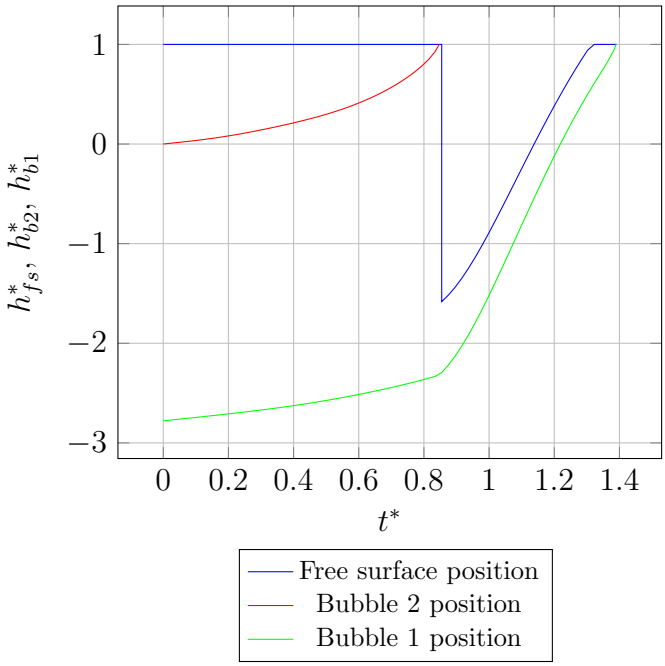

(a) Free surface and bubbles heights.

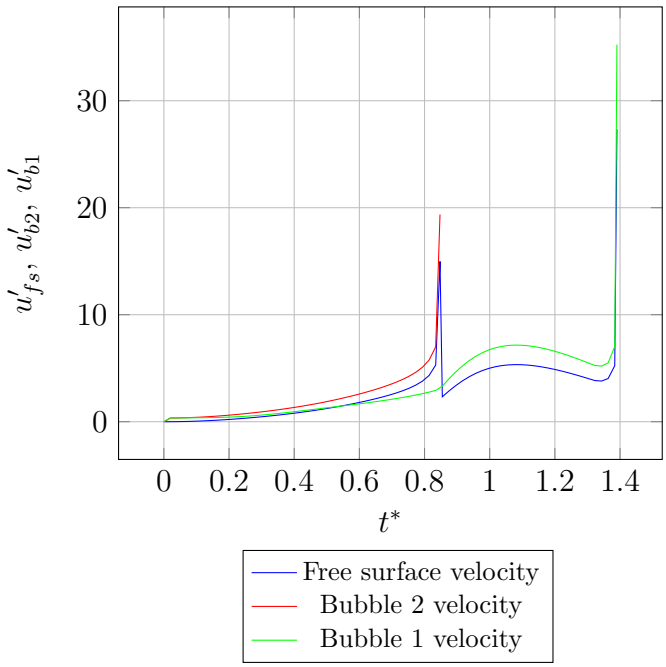

(b) Free surface and bubbles velocities

Figure 2.20: Geysering event due to two consecutive bubbles.

Chapter 3

Numerical Solutions for Interface Dynamics

Problems involving the formation and propagation of air cavities and rising elongated bubbles include several of the attributes that makes fluid interface numerical modelling a demanding subject. For example, cavities and Taylor bubbles develop an interface with regions where transition air/water is well defined (the front part) along with zones where transition is diffuse. Moreover, water and air determine a very low density ratio. In this situation, oscillations and overshoots in computed velocity field can appear in the neighbourhood of interfaces, creating nonphysical accelerations of the fluid with lower density [49]. Although incompressible assumption gives satisfactory results for cavity formation and propagation, this premise fails to reproduce adequately momentum transfer between phases for the bubble vertical motion, making necessary to implement a weakly compressible model.

Present numerical method computes solution of two fluids flow problems with given initial and boundary conditions. It consists of three stages. First step is the advection of a bounded phase function, whose value is zero in the lighter phase, one in the heavier phase and one half at interface. Second stage is the reinitialisation, which assures interface sharpness along the complete simulation. Last step is the update of velocity and pressure fields by the resolution of equations of motion, where density and viscosity are parametrically defined according to the phase function. These steps are repeated, in that order, every time step.

This chapter reports aforementioned numerical model for the calculation of two-phase flows solution. Section 3.1 introduces analytical set of equations for two incompressible and weakly compressible fluid flows. After that, section 3.2 details NFEM algorithm and limiting correction principles, which are employed in every stage of numerical model. NFEM requires both high and low order answers to build a final conservative solution with relevant

features as positivity (or monotonicity under certain conditions) and high order accuracy. Then, section 3.3 describes numerical solution for the advection equation, where NFEM is used to obtain a conservative squeme without unphysical phase function values. Here, high order solution is computed with the Characteristic-Galerkin method and low order answer is obtained with a first order upwind scheme. Reinitialisation is reported in section 3.4. Algorithm consists in the iterative solution of a parabolic equation, including a streamlined diffusivity balanced with an artificial compression. Flux corrections are integrated in this solution to preserve phase function bounds. Finally, hydrodynamics resolution is detailed in section 3.5, where NFEM and a customised flux correction procedure are integrated in the solution to reduce oscillations and velocity overshoots along the interface. In this stage, high order solution is calculated with the CBS method, while first order upwind FEM is again used for the low order solution.

The continuous discretisation of the variables, as well as the continuous interpolation of density across interface, give rise to a virtual stratification between phases. Under certain flow conditions, this artificial representation of the reality can lead to the amplification of high frequency perturbations related with Kelvin-Helmholtz instabilities. These perturbations could be stable for non-stratified flows but highly unstable for flows with high gradient transitions. Then, in section 3.6, it is examined stability of stratified flows, defined by density and velocity laws resembling numerical artificial distributions, as well as the effect of surface tension. To achieve a stable sharp interface resolution it is desirable a sufficient decrease of transition thickness between fluids. Some strategies are evaluated, being the interface refinement the most suitable. Hence, to seek band thickness decrease, a new dynamical mesh adaptation method is proposed in section 3.7. The procedure, based on nested grids, assures conservation and monotonicity of the variables in the refinement/unrefinement process and its computational cost is relatively low.

3.1 Continuous Solution for Two-Fluid Flows

Multiphase flows can be defined as motion involving two or more fluids with different physical properties in a way that the interaction between them significantly affects the dynamics of the resulting flow. In this section, mathematical model that describes motion of two phases flow and dynamics of the interface delimiting phases is reported.

Continuity and Navier-Stokes equations for one single phase are,

$$\frac{\partial \rho}{\partial t} + \nabla \cdot (\rho \mathbf{u}) = 0 \,, \tag{3.1}$$

$$\frac{\partial \rho \mathbf{u}}{\partial t} + \nabla \cdot (\rho \mathbf{u}\mathbf{u}) = -\nabla p + \mu \nabla^2 \mathbf{u} + \rho \mathbf{g} \,, \tag{3.2}$$

where $\mathbf{u}$ represents the velocity vector, $\mathbf{g}$ is the gravity acceleration vector, p is the pressure and ρ, μ are the fluid density and dynamic viscosity respectively. Equation (3.1) states that any change of mass in a domain is due to fluxes crossing the domain boundaries. On the other hand, Eq. (3.2) states that momentum changes (per unit volume) are caused by pressure, viscous and body forces, represented by first, second and third terms at right hand side respectively.

System of equations (3.1), (3.2) can also be applied to flows in domains where density is not constant (i.e. ρ=$\rho(\mathbf{x}, t)$). This fact allows the resolution of compressible or stratified fluids and, after some modifications, two-phase flows. Now, to distinguish between both fluids, an indicator function, also called phase function, is defined as $\phi = \phi(\mathbf{x}, t) \in [0, 1]$, whose value is zero or one in the domain occupied by the lightest and heaviest fluid respectively; moreover, at interface, value ϕ=1/2 is assumed. Thus, fluids' physical properties can be written as,

$$\rho = \rho_1 + \phi\,(\rho_2 - \rho_1) \quad \text{for} \quad \rho_1 < \rho_2 \,,$$

$$\mu = \mu_1 + \phi\,(\mu_2 - \mu_1) \,, \tag{3.3}$$

where subindexes 1 and 2 are referred to the lightest and heaviest phase respectively. Although previous density definition considers both fluids as incompressible, formulation for weakly compressible phases will be introduced at the end of this section. Then, density definition is inserted into Eq. (3.1) resulting in

$$(\rho_2 - \rho_1)\left(\frac{\partial \phi}{\partial t} + \nabla \cdot (\mathbf{u}\phi)\right) + \nabla \cdot (\rho_1 \mathbf{u}) = 0 \,,$$

which can be satisfied by imposing, $\frac{\partial \phi}{\partial t} + \nabla \cdot (\mathbf{u}\phi) = 0$ and $\nabla \cdot \mathbf{u} = 0$. These equations are the transport equation of the phase function and the continuity equation for an incompressible fluid.

Besides, it is necessary to include an additional term to the right hand side of Eq. (3.2) taking into account the surface tension. This tension can be defined as the necessary energy, due to intermolecular forces, to increase the surface of the fluid. Surface tension term is denoted as $\mathbf{T}$. Now, an

equivalent equation to Eq. (3.2) can be obtained by uncoupling terms at left hand side,

$$\rho\frac{\partial \mathbf{u}}{\partial t} + \rho\mathbf{u}\cdot\nabla\mathbf{u} + \mathbf{u}\left(\frac{\partial \rho}{\partial t} + \nabla\cdot(\rho\mathbf{u})\right) = -\nabla p + \mu\nabla^2\mathbf{u} + \rho\mathbf{g} + \rho\mathbf{T}\,,$$

where term between parenthesis is zero because of mass conservation. As a result, set of equations of motion for two fluids flow is the following,

$$\frac{\partial \phi}{\partial t} + \nabla\cdot(\mathbf{u}\phi) = 0\,, \tag{3.4}$$

$$\nabla\cdot\mathbf{u} = 0\,, \tag{3.5}$$

$$\frac{\partial \mathbf{u}}{\partial t} + \nabla\cdot(\mathbf{u}\mathbf{u}) = -\frac{1}{\rho}\nabla p + \frac{\mu}{\rho}\nabla^2\mathbf{u} + \mathbf{g} + \mathbf{T}\,, \tag{3.6}$$

$$\rho = \rho_1 + \phi\,(\rho_2 - \rho_1) \quad , \quad \mu = \mu_1 + \phi\,(\mu_2 - \mu_1)\ ,$$

in the domain Ω and time $t\ \in [t_0, T]$, where t_0 and T are initial and final times respectively.

Nearly incompressible hypothesis is formulated as follows. Flows are assumed isothermal and with a small density variation as a consequence of elastic deformation related to pressure change. Hence density is defined as

$$\rho = \rho_1 + (\rho_2 - \rho_1)\phi + \frac{p - p_0}{a_1^2 + (a_2^2 - a_1^2)\phi}\,, \tag{3.7}$$

where $a{=}\sqrt{\mathcal{K}/\rho}$ is the acoustic wave velocity, and $\mathcal{K}$ is the elastic bulk modulus. Celerity values a_1, a_2, are those corresponding to the reference densities ρ_1 and ρ_2 respectively, defined for a reference pressure p_0. Variation of viscosity due to pressure modification is assumed negligible. Thus, proceeding in the same way as for incompressible assumption, the set of equations for weakly compressible fluids is,

$$\frac{\partial \phi}{\partial t} + \nabla\cdot(\mathbf{u}\phi) = 0\,, \tag{3.8}$$

$$\frac{\partial}{\partial t}\left(\frac{p - p_0}{a_1^2 + (a_2^2 - a_1^2)\phi}\right) + \nabla\cdot\left(\rho^{'}\mathbf{u}\right) = 0\,, \tag{3.9}$$

$$\frac{\partial \mathbf{u}}{\partial t} + \nabla\cdot(\mathbf{u}\mathbf{u}) = -\frac{1}{\rho}\nabla p + \frac{\mu}{\rho}\nabla^2\mathbf{u} + \mathbf{g} + \mathbf{T} + \mathbf{Q}\,, \tag{3.10}$$

$$\rho = \rho_1 + (\rho_2 - \rho_1)\phi + \frac{p - p_0}{a_1^2 + (a_2^2 - a_1^2)\phi} \quad , \quad \mu = \mu_1 + \phi\,(\mu_2 - \mu_1)\ ,$$

in Ω, $t\ \in [t_0, T]$. Here, $\rho^{'}{=}\rho_1 + \dfrac{p - p_0}{a_1^2 + (a_2^2 - a_1^2)\phi}$ and $\mathbf{Q}{=}\mathbf{u}(\nabla\cdot\mathbf{u})$. Viscous terms depending on velocity divergence are neglected.

3.2 Non-Oscillatory Finite Element Method (NFEM)

In this work, a non-oscillatory finite element method is used in every solution step. The method was presented by P. Ortiz (see e.g. Refs.[61, 62]) and, as a main basis it integrates flux correction techniques (FCT). In this section, after reporting briefly FCT principles, the NFEM components and ad-hoc modifications to preserve mass conservation are introduced.

Flux correction method was originally developed by Boris and Book [10] and generalised by Zalesak [84, 85]. Extension for finite elements was introduced by Löhner et al. [48] and developed by Kuzmin [41], among others. The objective of FCT method is to find an accurate, high order and monotonic (or at least positive definite) solution for the advective-source transport equation and coupled equations such as equations of motion. In the following steps, advective-source transport scalar equation is used to report the principles. Algorithm is based on two schemes, a high order scheme (accurate but non-monotonic) and a low order predictor, generally diffusive, which satisfies the monotonicity condition. Final solution is obtained by the calculation of anti-diffusive fluxes, which are conveniently modified and added to the low order solution to obtain a final response satisfying previous requisites. First, advective-source transport equation is defined,

$$\frac{\partial B}{\partial t} + \nabla \cdot (\mathbf{u}B) + \mathcal{S} = 0 \ \text{ in } \Omega \ , t \in [t_0, T] \ , \tag{3.11}$$

with boundary conditions

$$B = \overline{B}(\mathbf{x}, t) \ \text{ on } \Gamma_B^- \qquad \text{(a)} \ ,$$
$$B\mathbf{u} \cdot \mathbf{n}_b = \overline{\mathbf{q}}_B(\mathbf{x}, t) \cdot \mathbf{n}_b \ \text{ on } \Gamma_q^- \qquad \text{(b)} \ ,$$
$$\Gamma^- = \Gamma_B^- \cup \Gamma_q^- \ , \quad \Gamma^- = \{\mathbf{x} \in \Gamma : (\mathbf{u} \cdot \mathbf{n}_b) \leq 0\} \ ,$$

and initial condition

$$B(\mathbf{x}, t_0) = \overline{B}_0(\mathbf{x}) \ \text{ in } \Omega \ ,$$

where B is the scalar transported by the advective velocity field $\mathbf{u}$, $\mathcal{S} = \mathcal{S}(B, \mathbf{x}, t)$ is a source, ($\mathbf{x}$=(x_l), l=1, D) and D is the number of space dimensions. Domain Ω in $\mathbf{R}^D$ is bounded by $\Gamma = \Gamma^- + \Gamma^+$, and $\overline{B}$, $\overline{B}_0$ and $\overline{\mathbf{q}}_B$ are known (the latter a vector) functions (from now on overline designates known values). Inflow boundary is denoted by Γ^- while Γ_q^- includes slip condition if suitable, $\Gamma^+ = \{\mathbf{x} \in \Gamma : (\mathbf{u} \cdot \mathbf{n}_b) > 0\}$ is the outflow boundary, $\mathbf{n}_b$ is the outward unit normal to the boundary and $[t_0, T]$ is the time interval.

Flux correction formulation starts by writing a finite element high order solution (HOS) of equation (3.11). Then, in matrix form the HOS is

$$\frac{1}{\Delta t}\mathbf{M}'_C \, \Delta\mathbf{B} = \mathbf{R}_H \ , \tag{3.12}$$

where $\mathbf{M}'_C$ is the left hand side matrix for the model problem. Next, a predictor-type monotonic (or positive definite) solution is introduced. In matrix form,

$$\frac{1}{\Delta t}\mathbf{M}'_L\Delta\mathbf{b} = \mathbf{R}_L \ , \tag{3.13}$$

where $\mathbf{M}'_L$ is a conservative diagonal matrix ensuring sign preservation of the scheme. The simplest predictor solution is a low order monotonic (or at least sign preserving) solution. This is referred as low order solution (LOS). Right hand sides $\mathbf{R}_H$, $\mathbf{R}_L$ correspond to the high order algorithm and to the predictor algorithm respectively, while $\mathbf{B}$ and $\mathbf{b}$ are the unknowns for high order method and for predictor method respectively. Hence, $\Delta\mathbf{B} = \mathbf{B}^{n+1} - \mathbf{B}^n$ and $\Delta\mathbf{b} = \mathbf{b}^{n+1} - \mathbf{B}^n$. If Eq. (3.12) is written as

$$\frac{1}{\Delta t}\mathbf{M}'_L\Delta\mathbf{B} = \mathbf{R}_H + \frac{1}{\Delta t}\left(\mathbf{M}'_L - \mathbf{M}'_C\right)\Delta\mathbf{B} \ , \tag{3.14}$$

by subtracting Eq. (3.13) from Eq. (3.14), it is got that

$$\frac{1}{\Delta t}\mathbf{M}'_L\left(\mathbf{B}^{n+1} - \mathbf{b}^{n+1}\right) = \mathbf{R}_H - \mathbf{R}_L + \frac{1}{\Delta t}\left(\mathbf{M}'_L - \mathbf{M}'_C\right)\left(\mathbf{B}^{n+1} - \mathbf{B}^n\right) \ . \tag{3.15}$$

The high order FEM solution can be written as a convenient identity by replacing original high and low order schemes (Eqs. (3.12) and (3.13) respectively) on the right hand side,

$$\mathbf{B}^{n+1} = \mathbf{b}^{n+1} + \sum_{j=1}^{E}(\mathbf{M}'_L)^{-1}\{(\mathbf{M}'_L)_j(\mathbf{B}^{n+1} - \mathbf{b}^{n+1})_j\} \ , \tag{3.16}$$

where the assembling of the product $(\mathbf{M}'_L)_j(\mathbf{B}^{n+1} - \mathbf{b}^{n+1})_j$ for each j element is explicitly written, and is extended over the total number of elements E. Element contribution (see Ref. [48]) is defined as,

$$\mathbf{A}_j = (\mathbf{M}'_L)^{-1}\{(\mathbf{M}'_L)_j(\mathbf{B}^{n+1} - \mathbf{b}^{n+1})_j\} \ ,$$

then the identity (3.16) for a node i is

$$B_i^{n+1} = b_i^{n+1} + \sum_{j=1}^{e}\mathbf{A}_j = b_i^{n+1} + \sum_{j=1}^{e}(\mathbf{A}_j^H - \mathbf{A}_j^L) \ , \tag{3.17}$$

where the sum of $\mathbf{A}_j$ extends over e, the total number of elements j surrounding i. High order solution B_i at time $(n+1)\Delta t$ results from updating the LO solution at time $(n+1)\Delta t$ by the sum of anti-diffusive contributions $\mathbf{A}_j$, that counterbalance the first order truncation error of the low order method.

Element contribution $\mathbf{A}_j$ is the difference between that obtained by the HOS, $\mathbf{A}_j^H$, and that obtained by the LOS, $\mathbf{A}_j^L$.

Equation (3.17) evinces a correction by limiting element contributions, resembling the original concept of flux correction [10]. Then it is constructed an improved solution $\tilde{B}_i$ as

$$\tilde{B}_i^{n+1} = b_i^{n+1} + \sum_{j=1}^{e} \tilde{\mathbf{A}}_j = b_i^{n+1} + \sum_{j=1}^{e} \mathbf{c}_j \mathbf{A}_j \ , \tag{3.18}$$

where the $\mathbf{c}_j$'s are elementwise correcting functions depending on nodal HOS, nodal LOS and element contributions to the node of the k variables; $\mathbf{c}_j$'s range is: $0 \leq c_{jk} \leq 1$, $c_{jk} \in \mathbf{c}_j$. Reader should notice that summation convention over repeated indexes is not used. For the scalar transport equation k=1, while for the two dimensional coupled transport equations, $1 \leq k \leq 3$.

These correcting functions must assure that solutions are bounded by nodal limits B_i^{max} and B_i^{min}. For the simplest case ($k = 1$), the condition is

$$B_i^{min} \leq b_i^{n+1} + \sum_{j=1}^{e} c_j A_j \leq B_i^{max} \ .$$

Now, if it is corrected positive and negative fluxes differently,

$$B_i^{min} \leq b_i^{n+1} + \frac{1}{2} \sum_{j=1}^{e} \left[c_j^+ \left(A_j + |A_j| \right) + c_j^- \left(A_j - |A_j| \right) \right] \leq B_i^{max} \ .$$

To fulfil the previous condition, it is sufficient that

$$B_i^{max} - b_i^{n+1} \geq \frac{c_i^+}{2} \sum_{j=1}^{e} A_j + |A_j| \ ,$$

$$b_i^{n+1} - B_i^{min} \geq \frac{c_i^-}{2} \sum_{j=1}^{e} |A_j| - A_j \ ,$$

where c_i^+ and c_i^- are nodal valued functions. These conditions can be expressed as follows

$$c_i^+ = \min \left[1, \frac{B_i^{max} - b_i^{n+1}}{\frac{1}{2} \sum_{j=1}^{e} \left(A_j + |A_j| \right) + \zeta} \right] \ , \tag{3.19}$$

$$c_i^- = \min \left[1, \frac{b_i^{n+1} - B_i^{min}}{\frac{1}{2} \sum_{j=1}^{e} \left(|A_j| - A_j \right) + \zeta} \right] \ , \tag{3.20}$$

where ζ is a small number to avoid the vanishing of the denominator. Nodal and element correcting functions are related as

$$c_j^+ = \min(c_i^+), \quad c_j^- = \min(c_i^-), \quad \forall \text{ nodes } i \in j \ . \tag{3.21}$$

For computation of B_i^{max} and B_i^{min}, the Zalesak idea (see Ref. [84]) is followed:

$$B_i^{max} = \max_{j=1,e} \left(B_i^n, B_p^n, b_i^{n+1}, b_p^{n+1} \right), \quad \forall \text{ (nodes } p \neq i) \in j \ , \tag{3.22}$$

$$B_i^{min} = \min_{j=1,e} \left(B_i^n, B_p^n, b_i^{n+1}, b_p^{n+1} \right), \quad \forall \text{ (nodes } p \neq i) \in j \ . \tag{3.23}$$

For coupled equations, there are several techniques to synchronise variables (see e.g. Refs. [48],[42],[62]). All strategies have a high degree of empiricism and, normally, their suitability depends on the case. In this work, it is defined nodal values of the correcting function as

$$c_i^+ = \min(c_{ik}^+), \quad c_i^- = \min(c_{ik}^-), \quad (1 \leq k \leq 3) \ . \tag{3.24}$$

Thus, final corrected solution is the following:

$$\tilde{B}_i^{n+1} = b_i^{n+1} + \sum_{j=1}^{e} \frac{1}{2} \left[c_j^+ (\mathbf{A}_j + |\mathbf{A}_j|) + c_j^- (\mathbf{A}_j - |\mathbf{A}_j|) \right] \ . \tag{3.25}$$

In the methodology proposed by R. Löhner [48], the LOS was the same as the high order solution with an added diffusion of the type $\mathcal{C}(\mathbf{M}_C - \mathbf{M}_L)$, where $\mathcal{C}$ is a diffusion coefficient that should be tuned to achieve sign-preservation. In that case, element contributions $\mathbf{A}_j$ were locally conservative and, to ensure mass conservation, element correcting functions must be equal for positive and negative fluxes, i.e. $c_j^+ = c_j^- = c_j = \min\left(c_j^+, c_j^-\right)$. However, in the Non-Oscillatory Finite Element Method (NFEM) proposed by P. Ortiz [61, 62], the HOS is obtained from the characteristic based method and LOS is constructed with an upwind monotone scheme, independent of the high order procedure, following the idea of selecting a scheme with the (nearly) minimum diffusion to assure positivity. Regarding high order solution, the characteristic based method after time discretisation for an scalar B (see Appendix B) is written as,

$$B^{n+1} = B^n - \Delta t \left\{ \left[\mathbf{u}^{n+1/2} - \frac{\Delta t}{2} \left(\mathbf{u}^{n+1/2} \cdot \nabla \right) \mathbf{u}^n \right] \cdot \nabla \right\} B^n + \frac{\Delta t^2}{2} \left(\mathbf{u}^{n+1/2} \cdot \nabla \right)^{(2)} B^n - \Delta t \left\{ Q^{n+1/2} - \frac{\Delta t}{2} \left(\mathbf{u}^{n+1/2} \cdot \nabla \right) Q^n \right\} \ , \tag{3.26}$$

where $Q = \mathcal{S} + B\,(\nabla \cdot \mathbf{u})$ and superscript $n+1/2$ for some variable is defined as $(\cdot)^{n+1/2} = \left((\cdot)^{n+1} + (\cdot)^{n}\right)/2$ (n and $n+1$ correspond to time levels $n\Delta t$ and $(n+1)\Delta t$ respectively). Operator $(\mathbf{f}\cdot\nabla)^{(2)}$ is

$$(\mathbf{f}\cdot\nabla)^{(2)} = \sum_{l_1=1}^{d}\sum_{l_2=1}^{d} f_{l_1} f_{l_2} \frac{\partial^2}{\partial x_{l_1}\partial x_{l_2}}$$

for a given vector field $\mathbf{f}$. Concerning low order approach, the scheme written as an equivalent differential equation after time discretisation is

$$b^{n+1} = B^{n} - \Delta t\,(\mathbf{u}\cdot\nabla b)^{n+1/2} - \Delta t Q^{n+1/2} + \Delta t\,[\nabla\cdot(\mathcal{K}\nabla b)]^{n+1/2}\ , \quad (3.27)$$

where $\mathcal{K}$ is an artificial diffusivity tensor such that

$$\mathcal{K}_{l_1 l_2} = \tilde{k}\ \frac{u_{l_1}u_{l_2}}{|\ \mathbf{u}\ |^2}, \quad (l_1, l_2 = 1, d)\ ,$$

and $\tilde{k}$ is a scalar depending on an element characteristic length in the streamline direction [13]. A standard split approach is assumed to compute values of $b^{n+1/2}$ for the LO scheme (see [62] and references therein), giving the following final computation of the unknown,

$$b^{n+1} = B^{n} - \Delta t\left(\mathbf{u}^{n+1/2}\cdot\nabla\left(B^{n} - \frac{\Delta t}{2}Q^{n}\right)\right) - \Delta t Q^{n+1/2} + \Delta t\left[\nabla\cdot\left(\mathcal{K}\nabla\left(B^{n} - \frac{\Delta t}{2}Q^{n}\right)\right)\right]\ . \quad (3.28)$$

For transport equation, element contributions $\mathbf{A}_j$ are not locally conservative because high order terms are not present at low order solution. This fact, independently of the choice of element correcting functions, lead a high order mass error. To clarify this issue, consider the combination of high order and low order solution in matrix form given by Eq. (3.15) to expand the correction given by Eq. (3.18) as

$$\tilde{\mathbf{B}}^{n+1} = \mathbf{b}^{n+1} + (\mathbf{M}'_L)^{-1}\sum_{j=1}^{E}\left\{\mathbf{c}\{\Delta t(\mathbf{R}_H - \mathbf{R}_L) + (\mathbf{M}'_L - \mathbf{M}'_C)\left(\mathbf{B}^{n+1} - \mathbf{B}^{n}\right)\}\right\}_j\ , \quad (3.29)$$

where low order solution $\mathbf{b}^{n+1}$ and high order solution $\mathbf{B}^{n+1}$ are global conservative solutions. If matrices involved in the calculation fulfil the conservation

property for each element j, a conservative corrected solution $\tilde{\mathbf{B}}^{n+1}$ is reached straightforwardly. For a symmetrical matrix $\mathbf{J}$ the conservation condition is

$$\sum_{k,k\neq i} \mathbf{J}_{ik} = -\mathbf{J}_{ii} \ . \tag{3.30}$$

Last term in the right hand side of Eq. (3.29) is a conservative anti-diffusion contribution, given that matrix $\mathbf{M}'_L - \mathbf{M}'_C$ verifies the conservation condition. After Galerkin spatial discretisation, terms on the right hand side of Eq. (3.26) that do not fulfil condition (3.30) agree with those on the right hand side of Eq. (3.28) that do not fulfil condition (3.30). These terms are

$$\begin{aligned} &-\Delta t \ \mathbf{u}^{n+1/2} \cdot \nabla B^n \quad \text{(a)} \ , \\ &-\Delta t Q^{n+1/2} \quad \text{(b)} \ , \\ &\frac{\Delta t^2}{2} \left(\mathbf{u}^{n+1/2} \cdot \nabla\right) Q^n \quad \text{(c)} \ . \end{aligned} \tag{3.31}$$

Despite the fact that all terms on the list (3.31) cancel each other once calculation of correction (3.29) is performed, high order global non-conservative residuals still can be created in calculation of $(\mathbf{R}_H - \mathbf{R}_L)$. The reason is twofold. Firstly, although definition of value of variables at $n + 1/2$ coincides for the methods given by Eqs. (3.26) and (3.27), interpolations do not have to match each other exactly (see details in Ref. [62]). Secondly, in the computation of the low order solution, results are essentially the same by median dual finite volume method or Galerkin linear finite elements with lumped mass approximation. Nevertheless, for an efficient computation, median dual cell based procedure is recommended, gathering the contribution to nodes in an elementwise manner to maintain the finite element structure, necessary for the calculation of the anti-diffusive fluxes. This practical procedure can produce high order residuals, given that its results are subtracted from results of typical Galerkin discretisation, kept from the terms on the list (3.31) corresponding to the high order algorithm.

Global mass error is substantially reduced by a modified antidiffusion term in [62] (see some stringent numerical experiments independent of boundary conditions). In this work a simple approach is proposed, by modifying the original formulation of the NFEM [61] in an intermediate step of the correction procedure. Once correcting functions have been evaluated, calculation of total positive and negative element contributions, M^+ and M^-

respectively, is performed as

$$M^+ = \sum_{i=1}^{N} \left[\sum_{j=1}^{e} \frac{c_j^+}{2} (A_j + |A_j|) \right]_i ,$$
$$M^- = \sum_{i=1}^{N} \left[\sum_{j=1}^{e} \frac{c_j^-}{2} (|A_j| - A_j) \right]_i ,$$

where N is the total number of nodes. Next, the global correction coefficients

$$c_c^+ = \min \left(1, \frac{M^-}{M^+} \right) , \tag{3.32}$$

$$c_c^- = \min \left(1, \frac{M^+}{M^-} \right) \tag{3.33}$$

are used to modify the corrected solution (3.25) as

$$\tilde{B}_i^{n+1} = b_i^{n+1} + \sum_{j=1}^{e} \frac{1}{2} \left[c_c^+ c_j^+ (\mathbf{A}_j + |\mathbf{A}_j|) + c_c^- c_j^- (\mathbf{A}_j - |\mathbf{A}_j|) \right] , \tag{3.34}$$

removing residuals from the correction procedure. Bounds (3.32) and (3.33) preserve nodal bounds B_i^{max} and B_i^{min}. As a result, conservation errors due to the limiting procedure are of the order of round-off values and errors in usual norms (see Chapter 4) does not show noticeable increase due to the proposed correction technique.

This method has proved to be effective for the resolution of problems involving interfaces. By one hand, it enhances interface capturing by providing a conservative, positive and non oscillatory phase field at advection and reinitialisation steps. On the other hand, it controls spurious velocity overshoots when it is used for the hydrodynamics solution step.

3.3 Solution for Transport Phase Advection

First stage of proposed two-phase flow method is the advection of a phase function, attained by solving next equation,

$$\frac{\partial \phi}{\partial t} + \nabla \cdot (\mathbf{u}\phi) = 0 \text{ in } \Omega \, , t \in [t_0, T] \tag{3.35}$$

with boundary conditions

$$\phi = \overline{\phi}(\mathbf{x}, t) \text{ on } \Gamma_\phi^- \quad \text{(a)} ,$$
$$\phi \mathbf{u} \cdot \mathbf{n}_b = \overline{\mathbf{q}}_\phi(\mathbf{x}, t) \cdot \mathbf{n}_b \text{ on } \Gamma_q^- \quad \text{(b)} ,$$
$$\Gamma^- = \Gamma_\phi^- \cup \Gamma_q^- \, , \quad \Gamma^- = \{ \mathbf{x} \in \Gamma : (\mathbf{u} \cdot \mathbf{n}_b) \leq 0 \} \, ,$$

and initial condition

$$\phi(\mathbf{x}, t_0) = \overline{\phi}_0(\mathbf{x}) \ \text{ in } \Omega \ .$$

For this step, the flux correction technique is employed, along with mass correction explained in previous section. High order solution is obtained with Eq. (B.21) by replacing R'=0 and B=ϕ. Thus, Galerkin spatial discretisation of Eq. (B.21) is stated in terms of the finite element spaces $\mathcal{W}^h$ and Φ^h defined as $\mathcal{W}^h \subset \mathcal{W} = \{w \in H^1(\Omega) \mid w = 0 \text{ on } \Gamma^-_\phi\}$, $\Phi^h \subset \Phi$=$\{\phi \in H^1(\Omega) \mid \phi = \overline{\phi} \text{ on } \Gamma^-_\phi\}$, and solution of phase function advection is formulated as: Find $\phi^h \in \Phi^h$ for all $t \in [t_o, T]$, such that

$$\begin{aligned}\left(w^h, \frac{\Delta\phi^h}{\Delta t}\right)_\Omega = \left(\mathbf{u}^{n+1/2} \cdot \nabla w^h, (\phi^h)^n\right)_\Omega - \\ \frac{\Delta t}{2}\Big\{\left\langle \nabla \cdot \left(w^h \left(\mathbf{u}^h\mathbf{u}^h\right)^{n+1/2}\right), \nabla(\phi^h)^n\right\rangle_{\Omega_I} - \\ \left\langle w^h \left((\mathbf{u}^h)^{n+1/2} \cdot \nabla(\mathbf{u}^h)^n\right), \nabla(\phi^h)^n\right\rangle_{\Omega_I} + \\ \left(\nabla \cdot w^h(\mathbf{u}^h)^{n+1/2}, \left(\phi^h \nabla \cdot \mathbf{u}^h\right)^n\right)_{\Omega_I}\Big\} - \\ \left[w^h, \phi^h\mathbf{u}\right]^n_{\Gamma^+} - \left[w^h, \overline{\mathbf{q}}_\phi\right]^n_{\Gamma^-_q} \ , \ \forall\ w^h \in \mathcal{W}^h \ , \end{aligned} \quad (3.36)$$

where

$$(v, w)_\Omega = \int_\Omega v\, w \, d\Omega \ , \ \ \langle \mathbf{v}, \mathbf{w}\rangle_\Omega = \int_\Omega (\mathbf{v} \cdot \mathbf{w}) \ d\Omega \ \text{ and } \ [v, \mathbf{c}]_\Gamma = \int_\Gamma v\, \mathbf{c} \cdot \mathbf{n}_b \, d\Gamma \ .$$

Here, Ω_I is the domain without elements with sides belonging to the boundary and $\Delta\phi^h = (\phi^h)^{n+1} - (\phi^h)^n$. Computation of $\mathbf{u}^{n+1/2}$ will be detailed in section 3.5. Matrix form of Eq. (3.36) can be inspected in Appendix C. Low order solution is a finite element upwind method computed in an edge-based manner for efficiency [2, 61]. From now on, notation $\mathcal{LO}(\,)$ indicates the low order operator comprising computation of upwind fluxes. Full derivation of the low order operator can be found in section 3.3 of Ref. [61] or, in a summarised form, in Appendix D. Then, low order method is defined as: Find ϕ^h_{LO} such that

$$\left(w^h_L, \frac{\Delta\phi^h_{LO}}{\Delta t}\right)_\Omega = \mathcal{LO}\left((\phi^h)^n, (\mathbf{u}^h)^n\right) \ , \quad (3.37)$$

where w^h_L corresponds to lumped mass matrix.

Final phase function solution $\tilde{\phi}^{n+1}$ is constructed by using flux correction through Eq. (3.34), then assuring its positivity (or its monotonicity under certain flow conditions), and avoiding high frequency oscillations in the vicinity of the interface as a consequence of dispersion error of the high order solution.

3.4 Reinitialisation

Reinitialisation of the phase function is necessary to preserve interface thickness or, in other words, to maintain the resolution of the contact discontinuity[1]. Reinitialisation of the phase function by the CLS algorithm is implemented once advection of phase function (Eq. (3.35)) is solved, and combines artificial compression and diffusion in a non-linear advection-diffusion equation (Eq. (7) of Ref. [60]) reproduced below,

$$\frac{\partial \hat{\phi}}{\partial \tau} + \nabla \cdot \left(\hat{\phi} \left(1 - \hat{\phi} \right) \mathbf{n} \right) = \nabla \cdot \left[\varepsilon \left(\nabla \hat{\phi} \cdot \mathbf{n} \right) \mathbf{n} \right] \ , \tag{3.38}$$

with initial condition

$$\hat{\phi}(\mathbf{x}, \tau = 0) = \phi(\mathbf{x}, t^{n+1}) \ . \tag{3.39}$$

Here, τ is a dummy time, $\hat{\phi}$ is the reconstructed phase function, and $\mathbf{n}$ is the interface normal, $\mathbf{n} = \dfrac{\nabla \phi}{|\nabla \phi|}$.

Artificial compression was born with the aim of fixing the spreading induced by numerical methods on discontinuities when they are advected in multidimensional problems. The essence of artificial compressibility method introduced by A. Harten [31] is to solve a modified advection equation. In one dimension, equation is

$$\frac{\partial B}{\partial t} + \frac{\partial}{\partial x} \left[f(B) + g(B) \right] = 0 \, ,$$

where additional function $g(B)$ must satisfy following properties,

$$\begin{gathered} g(B) = 0 \quad \text{for} \quad B \notin (B_L, B_R) \, , \\ g(B) \cdot \operatorname{sgn} \left[B_R - B_L \right] > 0 \quad \text{for} \quad B \in (B_L, B_R) \, , \end{gathered}$$

being B_L and B_R extreme values of the discontinuity. It can be proved that modified and original transport equations have the same analytical solution. However, numerically, both solutions are different: while numerical responses for original equation can spread out the interface, numerical solution of modified equation gives a well defined discontinuity. In current study, B_L=0 and B_R=1 and function $\phi \left(1 - \phi \right) \mathbf{n}$ satisfies both conditions. Further, the aim of diffusion term in Equation (3.38) is to achieve a solution with

[1] Contact discontinuities are surfaces delimiting regions with different density. In contrast, shocks are characterised by also presenting mass flows across the surface accompanied by abrupt pressure changes.

a controlled sharp interface without discontinuities allowing for high order accurate results. Thus, ε is a diffusivity coefficient defined to control the interface thickness [60]. Both artificial compression and diffusive fluxes are oriented along the interface normal. For this reason, neither tangential diffusion fluxes nor tangential compression fluxes to the contact discontinuity are allowed to grow during reinitialisation.

In this work, the continuous model proposed for reinitialisation step is an equation of the form

$$\frac{\partial \hat{\phi}}{\partial \tau} = \frac{\partial}{\partial \mathbf{n}} \left[\mathcal{D}(\hat{\phi}) \frac{\partial \hat{\phi}}{\partial \mathbf{n}} \right] , \tag{3.40}$$

merging both effects into the anisotropic diffusivity $\mathcal{D}(\hat{\phi})$ such that

$$\mathcal{D}(\hat{\phi}) = \varepsilon - \frac{\hat{\phi}\left(1-\hat{\phi}\right)}{\frac{\partial \hat{\phi}}{\partial \mathbf{n}} + \varsigma} , \tag{3.41}$$

where initial condition is that given by Eq. (3.39). Note that the diffusivity is not positive definite $\mathcal{D}(\hat{\phi}) \lesseqgtr 0$, therefore model (3.40) is a nonlinear anisotropic diffusion-anti-diffusion equation. Natural boundary condition and $\mathbf{n} \cdot \mathbf{n}_b = 0$ condition are assumed on boundaries. As Eq. (3.40) is nearly self-adjoint, standard Galerkin spatial discretisation is (in a sense) optimal [88]. To solve Eq. (3.40), a simple and efficient iterative method is constructed, based on the use of lumped mass matrix for dummy time discretisation and on explicit treatment of nonlinear diffusion terms. The choice of initial condition (3.39) gives a very fast convergence to reach steady state solution. Nevertheless, $\mathcal{D}(\hat{\phi}) \lesseqgtr 0$ leads to an enhanced solution $\hat{\phi}$ that does not preserve sign. To bound the reconstructed solution by the limits Φ_i^{min} and Φ_i^{max} of transport step, an ad-hoc correction of element contributions is introduced .

To achieve sign-preservation, the procedure defines D_j as the diffusive (or anti-diffusive) flux (element contribution) of j element to node i. Then, updated solution for node i at pseudo-time $(m+1)\Delta\tau$ is

$$\hat{\phi}_i^{m+1} = \hat{\phi}_i^m + \sum_{j=1}^{e} D_j^m \ .$$

Hence flux correction is embedded in the iterative method as

$$\hat{\phi}_i^{m+1} = \hat{\phi}_i^m + \sum_{j=1}^{e} c_j D_j^m \ ,$$

where elementwise correction coefficients c_j are chosen by

$$c_j = \min\left(c_k^+, c_k^-\right) \quad \forall \text{ nodes } k \in j \ ,$$

and for node i

$$c_i^+ = \min\left(1, \frac{\hat{\Phi}_i^{max} - \hat{\phi}_i^m}{\sum_{j=1}^e \frac{1}{2}\left(D_j + |D_j|\right) + \varsigma}\right) \ ,$$
$$c_i^- = \min\left(1, \frac{\hat{\phi}_i^m - \hat{\Phi}_i^{min}}{\sum_{j=1}^e \frac{1}{2}\left(|D_j| - D_j\right) + \varsigma}\right) \ .$$

Unlike advection step, in this case a single correction coefficient is used because fluxes D_j calculated from Eq. (3.40) are locally conservative. Hence, if positive and negative fluxes are corrected with different coefficients, mass conservation would not be preserved.

To allow reinitialisation to operate when interface is totally sharp (one or zero nodal values), an additional condition must be added to determine correcting functions such that

$$\text{if } \ \hat{\Phi}_i^{max} - \hat{\phi}_i^m = 0 \ \text{ and } \ \sum_{j=1}^e \frac{1}{2}\left(D_j + |D_j|\right) = 0 \ , \ \text{then } c_i^+ = 1 \ ,$$

and

$$\text{if } \hat{\phi}_i^m - \hat{\Phi}_i^{min} = 0 \ \text{ and } \ \sum_{j=1}^e \frac{1}{2}\left(|D_j| - D_j\right) = 0 \ , \ \text{then } c_i^- = 1 \ .$$

Finally, bounds are defined by

$$\hat{\Phi}_i^{max} = \max_{j=1,e}\left(\hat{\phi}_i^m, \hat{\phi}_k^m\right), \quad \forall \left(\text{nodes } k \neq i\right) \in j \ , \tag{3.42}$$

$$\hat{\Phi}_i^{min} = \min_{j=1,e}\left(\hat{\phi}_i^m, \hat{\phi}_k^m\right), \quad \forall \left(\text{nodes } k \neq i\right) \in j \ . \tag{3.43}$$

Improved solution after reconstruction is now bounded by $\Phi_i^{min} \leq \hat{\phi} \leq \Phi_i^{max}$.

Finite element discretisation of Eq. (3.40) is formulated as: find $\hat{\phi}^h \in \Phi^h$ such that

$$\left(w_L^h, \frac{\Delta\hat{\phi}^h}{\Delta\tau}\right)_\Omega = -\left(\frac{\partial w^h}{\partial \mathbf{n}}, \mathcal{D}(\hat{\phi})\frac{\partial\hat{\phi}^h}{\partial\mathbf{n}}\right)_\Omega^m + \left[w^h, \mathcal{D}(\hat{\phi})\frac{\partial\hat{\phi}^h}{\partial\mathbf{n}}\mathbf{n}\right]_\Gamma^m \ , \tag{3.44}$$

where w_L^h corresponds to the lumped mass matrix and $\mathcal{D}(\hat{\phi}) \lesseqgtr 0$. If $\mathbf{n} \cdot \mathbf{n}_b$=0 condition is assumed on boundaries, second term at right hand side

of Eq. (3.44) vanishes. In Eq. (3.44) diffusion is streamlined in the normal direction of the interface as in Eq. (3.38), and dummy time integration is carried out explicitly (superscript m indicates dummy time level τ^m).

A straightforward elementwise computation of interface normal $\mathbf{n}=\frac{\nabla\phi}{|\nabla\phi|}$ can produce indeterminacy far from interface, where phase function has nearly constant values. As a result, oscillations of phase function appear during reinitialisation [22]. Since normals at distant elements from the interface are not necessary, we propose to calculate normals only at few elements surrounding $\phi = \frac{1}{2}$ contour. Consider Fig. 3.1; the term *level* defines a layer of elements, such that elements belonging to *level* 1 of a specified element are all elements neighbouring it, *level* 2 embraces all elements adjacent to elements of *level* 1, and so on. For this study, three levels are sufficient to

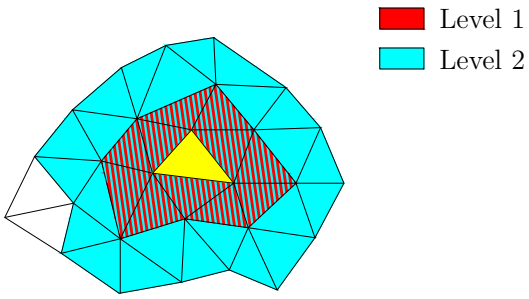

Figure 3.1: Definition of *level*

properly capture the entire interface[2]. To sort levels, a linked list algorithm [47] is implemented. Due to the static data involved, sorting has to be done only once, and data structure is called only once before dummy time iteration. In particular, additional static data stored is the distance between centroid of each element to all nodes covered by its level 3. These nodes are called *activated* nodes associated with the element.

Now, the method consists of the following steps,

1. Search for interface elements: elements containing $\phi = \frac{1}{2}$.

2. Calculation of interface elements normals: $\mathbf{n} = \dfrac{\nabla\phi}{|\nabla\phi|}$.

3. For each interface element: recover *activated* nodes associated with it.

[2]In numerical experiments (Chapter 4), maximum value of ε used is $\varepsilon\approx 0.83\delta$, interface thickness $\eta \approx 6\varepsilon$ (see [60], pp 796), then $\eta \approx 5\delta$, where δ is an average element size.

4. The normal corresponding to *activated* nodes is updated with value of normal for the nearest interface element.

5. Element normals are updated by the average of normal values for nodes belonging to the element.

Though this method has been developed for linear triangles, its implementation for tetrahedrons and other types of elements is straightforward. Improvement in reinitialisation stage achieved by enhanced normals calculation will be assessed in Chapter 4.

3.5 Flow Solver

High order solution for the set of equations (3.1) and (3.2) is attained by extending the continuous characteristic based split FEM to incorporate preservation of second order accuracy for transient advective field condition (see Appendix A in Ref. [61]). After time discretisation, the following form of split solution can be written,

$$\mathbf{u}^{n+1} = \mathbf{u}^n + \Delta\mathbf{u}^* + \Delta\mathbf{u}^{**} \ , \tag{3.45}$$

where velocity at time level $(n+1)\Delta t$ is computed as the sum of a predictor velocity $\mathbf{u}^*{=}\mathbf{u}^n + \Delta\mathbf{u}^*$, and a pressure correction velocity increment $\Delta\mathbf{u}^{**}$. First step is the calculation of predictor velocity, obtained by the Characteristic Galerkin method (see Appendix B, Eq. (B.22)), where $\mathbf{B}^{n+1}{=}\mathbf{u}^*$, and $\mathbf{R}{=}-\frac{\mu}{\rho}\nabla^2\mathbf{u} - \mathbf{g} - \mathbf{T} - \mathbf{u}\nabla\cdot\mathbf{u}$. Viscous force is specified as a source term to simplify notation. Viscous force, gravity force and surface force values are taken at $t{=}n\Delta t$. Hence, $\mathbf{R}^{n+1/2}{\approx}\mathbf{R}^n$ in Eq. (B.22). Then, finite element discretisation for velocity predictor is stated in terms of the finite element spaces $\mathcal{U}_i^h$ and $\mathcal{V}_i^h$ $(i = 1, D)$ defined as $\mathcal{V}_i^h \subset \mathcal{V}_i = \{v_i \in H^1(\Omega) \mid v_i = 0 \text{ on } \Gamma_q\}$, $\mathcal{U}_i^h \subset \mathcal{U}_i = \{u_i \in H^1(\Omega) \mid u_i = \overline{q}_i \text{ on } \Gamma_q\}$, being Γ_q is the portion of boundary with prescribed velocity, denoted as $\overline{\mathbf{q}}$. Solution is formulated as: Find $\Delta u_i^{*h} \in \mathcal{U}_i^h$ such that

$$\begin{aligned}\left(v_i^h, \frac{\Delta u_i^{*h}}{\Delta t}\right)_\Omega = &- \left(v_i^h, \nabla\cdot\left((\mathbf{u}^h)^{n+1/2}(u_i^h)^n\right)\right)_\Omega + \left(v_i^h, f_i^h\right)_\Omega^n \\ &+ \left(v_i^h, g_i\right)_\Omega^n - \frac{\Delta t}{2}\left\{\left\langle\nabla\cdot\left(v_i^h\left(\mathbf{u}^h\mathbf{u}^h\right)^{n+1/2}\right), \nabla(u_i^h)^n\right\rangle_{\Omega_I}\right. \\ &- \left\langle v_i^h\left((\mathbf{u}^h)^{n+1/2}\cdot\nabla(\mathbf{u}^h)^n\right), \nabla(u_i^h)^n\right\rangle_{\Omega_I} \\ &+ \left(\nabla\cdot v_i^h(\mathbf{u}^h)^{n+1/2}, \left(u_i^h\nabla\cdot\mathbf{u}^h\right)^n\right)_{\Omega_I} \\ &\left.+ \left(v_i^h, (\mathbf{u}^h)^{n+1/2}\cdot(\nabla(f_i^h + g_i))^n\right)_{\Omega_I}\right\} \ , \end{aligned} \tag{3.46}$$

where $\mathbf{f}=\frac{\mu}{\rho}\nabla^2\mathbf{u}+\mathbf{T}+\mathbf{u}\nabla\cdot\mathbf{u}$. Under the assumption of nearly incompressible flows, those viscous terms depending on velocity divergence are neglected. Supplemental integration by parts of viscous term (second term in the right hand side of Eq.(3.46)) is omitted for brevity. Hydrodynamic solution is performed after updating phase function and density and viscosity values given by parametrical definitions (3.3) or (3.7). Then, intermediate values $\rho^{n+1/2}$ and $\mu^{n+1/2}$ are incorporated. Next step is the pressure computation from the modified continuity equation (3.9) after following time discretisation,

$$\frac{\partial}{\partial t}\left(\frac{p-p_0}{a_1^2+(a_2^2-a_1^2)\phi}\right)+\nabla\cdot\left(\rho'\mathbf{u}^{n+\theta_1}\right)=0\,. \tag{3.47}$$

Taking into account that $\mathbf{u}^{n+\theta_1}=\mathbf{u}^n+\theta_1\left(\Delta\mathbf{u}^*+\mathbf{u}^{**}\right)$ and that $\Delta\mathbf{u}^{**}$ includes pressure terms,

$$\Delta\mathbf{u}^{**}=-\frac{\Delta t}{\rho}\nabla p^{n+\theta_2}+\frac{\Delta t^2}{2\rho}u_i^{n+1/2}\frac{\partial}{\partial x_i}\nabla p^{n+\theta_2}\,, \tag{3.48}$$

where $p^{n+\theta_2}=(1-\theta_2)p^n+\theta_2 p^{n+1}$, equation (3.47) remains as,

$$\frac{1}{(a^2)^{n+1/2}}\frac{\Delta p}{\Delta t}-\theta_1\frac{(\rho')^{n+1/2}}{\rho^{n+1/2}}\Delta t\nabla^2\left(p^{n+\theta_2}\right)=-\nabla\cdot\left((\rho')^n\mathbf{u}^n+\theta_1(\rho')^{n+1/2}\Delta\mathbf{u}^*\right)\,. \tag{3.49}$$

Second order terms in previous equation vanish if linear finite elements are employed. Thus, Galerkin spatial discretisation of Eq. (3.49) is stated in terms of finite element spaces $\mathcal{W}^h$ and $\mathcal{P}^h$, defined as $\mathcal{W}^h\subset\mathcal{W}=\{w\in H^1(\Omega)\mid w=0 \text{ on } \Gamma_p\}$, $\mathcal{P}^h\subset\mathcal{P}=\{p\in H^1(\Omega)\mid p=\overline{p} \text{ on } \Gamma_p\}$, where Γ_p specifies the portion of the boundary with prescribed pressure denoted as $\overline{p}$. Pressure solution is formulated as: Find $(p^h)^{n+1}\in\mathcal{P}^h$ for all $t\in[t_o,T]$, such that

$$\begin{aligned}\left(\frac{1}{(a^2)^{n+1/2}}w^h,\frac{\Delta p^h}{\Delta t}\right)_\Omega+\theta_1\theta_2\Delta t\left\langle\nabla w^h,\frac{(\rho')^{n+1/2}}{\rho^{n+1/2}}\nabla(\Delta p^h)\right\rangle_\Omega=\\ -\left(w^h,\nabla\cdot\left(\rho'\mathbf{u}^h\right)\right)_\Omega^n+\theta_1\left\langle\nabla w^h,(\rho')^{n+1/2}\Delta\mathbf{u}^{*h}\right\rangle_\Omega\\ -\theta_1\Delta t\left\langle\nabla w^h,\frac{\rho'}{\rho}\nabla p^h\right\rangle_\Omega^n-\theta_1\left[w^h,(\rho')^{n+1/2}\Delta\mathbf{u}^h\right]_\Gamma\,,\end{aligned} \tag{3.50}$$

where $\Delta\mathbf{u}^h=(\mathbf{u}^h)^{n+1}-(\mathbf{u}^h)^n$. In numerical experiments, integration parameters $\theta_1=\theta_2=1$ are employed unless otherwise stated. Reader can note that, if flow is assumed incompressible, first term of Eq. (3.50) vanishes and ρ' can be changed by 1. Equation (3.50) is solved by using a preconditioned conjugate gradient method. Once pressure increment is obtained, last step is

to update the velocity field through the calculation of $\Delta\mathbf{u}^{**}$. Finite element discretisation of Eq. (3.48) gives next equation,

$$\left(v_i^h, \frac{\Delta u_i^{**h}}{\Delta t}\right)_\Omega = -\left(\frac{1}{\rho^{n+1/2}} v_i^h, (\nabla p^h)_i^{n+\theta_2}\right)_\Omega - \frac{\Delta t}{2}\left(\frac{1}{\rho^{n+1/2}}\nabla\cdot\left(v_i^h(\mathbf{u}^h)^{n+1/2}\right), (\nabla p^h)_i^{n+\theta_2}\right)_{\Omega_I} . \quad (3.51)$$

Finally, new velocity and pressure values are $\mathbf{u}^{n+1}$=$\mathbf{u}^n$+$\Delta\mathbf{u}^*$+$\Delta\mathbf{u}^{**}$, p^{n+1}=p^n+Δp. Matrix forms of Eqs. (3.46), (3.50) and (3.51) are detailed in Appendix C. To compute velocities at $n+1/2$, required by Eqs. (3.36), (3.46) and (3.51), one level second order predictor-corrector procedure is proposed. Prior to outline the methodology, Eq. (3.46) is condensed by introducing the operator $\mathcal{G}$ such that

$$\left(v_i^h, \frac{\Delta u_i^{*h}}{\Delta t}\right)_\Omega = \mathcal{G}\left(\mathbf{u}^{n+1/2}, \mathbf{u}^n, \mathbf{f}^n, \mathbf{g}^n\right) . \quad (3.52)$$

Now, Eqs (3.45) and (3.52) are used to explicitly compute a predictor value $\widehat{\mathbf{u}}$=$\mathbf{u}^n + \Delta\widehat{\mathbf{u}}$ as

$$\left(v_i^h, \frac{\widehat{\Delta u_i^h}}{\Delta t}\right)_\Omega = \mathcal{G}\left(\mathbf{u}^n, \mathbf{u}^n, \mathbf{f}^n, \mathbf{g}^n\right) - \left(v_i^h, \frac{1}{\rho}(\nabla p^h)_i\right)_\Omega^n - \frac{\Delta t}{2}\left(\frac{1}{\rho}\nabla\cdot\left(v_i^h(\mathbf{u}^h)\right), (\nabla p^h)_i\right)_{\Omega_I}^n , \quad (3.53)$$

where values at $n+1/2$ were assumed as those corresponding at n. Then, values of $\mathbf{u}^{n+1/2}$ in Eq. (3.52) are calculated as $\mathbf{u}^{n+1/2}$=$\frac{1}{2}\left(\mathbf{u}^n + \widehat{\mathbf{u}}\right)$. Computation of $\mathbf{u}^{n+1/2}$ is performed before the phase function advection step, hence intermediate velocity field is ready to be used in Eq. (3.36) and to be reused in the hydrodynamics solution by Eqs. (3.46) and (3.51). Density $\rho^{n+1/2}$ is computed after solving Eq. (3.36) by using Eq. (3.7) but employing the value $\phi^{n+1/2}$=$\frac{1}{2}\left(\phi^n + \phi^{n+1}\right)$; accordingly, celerity $(a^2)^{n+1/2}$=$a_1^2 + (a_2^2 - a_1^2)\phi^{n+1/2}$ in Eq. (3.50). To compute ρ', pressure is approximated as $p \approx p^n$.

Low order solution is the next constituent of the NFEM method. Similarly to phase function advection, low order method is defined as: Find $(u_i^h)_{LO}^{n+1} \in \mathcal{U}_i^h$, $(i = 1, D)$ and $(p^h)_{LO}^{n+1} \in \mathcal{P}^h$ for all $t \in [t_o, T]$, such that

$$\left(v_{iL}^h, \frac{\Delta u_{iLO}^h}{\Delta t}\right)_\Omega = \left(v_{iL}^h, \frac{\Delta u_{iLO}^{*h}}{\Delta t}\right)_\Omega - \left(v_{iL}^h, \frac{1}{\rho}(\nabla p^h)_{iLO}\right)_\Omega^{n+1/2} , \ (i = 1, D), \quad (3.54)$$

where v_{iL}^h corresponds to the lumped mass matrix and LO subindex signifies low order solution. Low order intermediate velocity increment is calculated as

$$\left(v_{iL}^h, \frac{\Delta u_{iLO}^{*h}}{\Delta t}\right)_\Omega = \left(v_i^h, f_i^h\right)_\Omega^n + \left(v_i^h, g_i\right)_\Omega^n + \mathcal{LO}\left((u_i^h)^n, (\mathbf{u}^h)^n\right) . \tag{3.55}$$

Pressure solution is nearly identical to high order formulation (Eq. (3.50)) and is not reproduced for brevity. Computation of low order solutions of equations involving source terms is detailed in Appendix D.

Last fundamental ingredient in the NFEM is the flux correction strategy. Direct extension of the scalar computation developed in section 3.2 for each of the velocity components and pressure separately could result in inappropriate constrains for some of the variables, as observed in Ref. [85] for conservative variables in compressible flows. In this work, suitable synchronised antidiffusion is relevant to shrink oscillations and overshoots in velocity field in the vicinity of the contact discontinuity, and its benefits become evident for decreasing values of ρ_1/ρ_2. The construction of limiters to synchronise variables is significantly case dependent [48]. Among several coordination techniques tested (see e.g. [62]), the most effective is to act only on velocity components [48]. In this synchronisation, the correcting functions for a node i is defined by

$$c_i^+ = \min(c_{ik}^+) \ , \quad c_i^- = \min(c_{ik}^-) \ , \tag{3.56}$$

where k=1, D indicates velocity component; correcting function for element j is

$$c_j = \min(c_l^+, c_l^-), \quad \forall \text{ nodes } l \in j \ . \tag{3.57}$$

In other words, nodal correcting functions are calculated for each velocity component separately and it is selected the most restrictive candidate to correct antidiffusive fluxes for all velocity components. Application of the coordinated correction technique is performed by the conservative method proposed in Ref. [62]. The monolithic NFEM method stated above diminishes substantially wiggles near interface. However the semi-implicit algorithm requires the solution of two Poisson equations every timestep to build in the upcoming correction. To avoid this computational cost, a reduced NFEM is proposed. It consists in performing correction only for the predictor velocity field. All series of numerical tests have shown insignificant differences with monolithic NFEM (see section 4.2.2), retaining the capability to maintain interface resolution. Predictor velocity field is arbitrary, thus conservative correction formulated in section 3.2 is redundant. It is sufficient to get an improved solution by using original methodology (3.25), embedded

into the coordination procedure (3.56). Ensuing steps of CBS algorithm ensure mass conservation. Otherwise, conservation errors in momentum are negligible when compared with spurious momentum transmission between phases. Limiting techniques integrated into NFEM, either in the entire procedure or in the reduced version, do not get rid completely of spurious velocity jumps across interface. These nonphysical jumps can pollute severely results in interface neighbourhood, and in particular, can create nonphysical accelerations of the fluid with lower density, intensified for small ρ_1/ρ_2 values. Correction procedure does not fully filter artificial accelerations across the interface because the method defines bounds without identifying the presence of the interface. An enhanced bound estimation is introduced, picking out relevant information of the interface. To simplify, definitions are specified for the reduced procedure[3].

Bounds for k velocity component are given by the following approach. First, for each node i, nodes q surrounding i are identified such that,

$$\left|\phi_i^{n+1} - \phi_q^{n+1}\right| < \Upsilon \ .$$

Second, by calling p the total number of q nodes, bounds for node i are computed according to,

If $p > 0$,

$$\begin{aligned} u_{ik}^{max} &= \max_{q=1,p} \left(u_{ik}^n, (u_{LO}^*)_{ik}, u_{qk}^n, (u_{LO}^*)_{qk}\right) \ , \\ u_{ik}^{min} &= \min_{q=1,p} \left(u_{ik}^n, (u_{LO}^*)_{ik}, u_{qk}^n, (u_{LO}^*)_{qk}\right) \ . \end{aligned} \tag{3.58}$$

Else if p=0,

$$\begin{aligned} u_{ik}^{max} &= \max \left(u_{ik}^n, (u_{LO}^*)_{ik}\right) \ , \\ u_{ik}^{min} &= \min \left(u_{ik}^n, (u_{LO}^*)_{ik}\right) \ . \end{aligned} \tag{3.59}$$

Adequate value of parameter Υ=$\Upsilon(\delta, \varepsilon)$[4] prevents creation of undesired new limits across the interface.

Surface Tension

Surface tension force is calculated following the continuous model with finite thickness formulated in Ref. [11]. Equivalent volume force is

$$\mathbf{T} = \frac{2\sigma}{\rho_1 + \rho_2} \kappa \frac{\nabla \rho}{(\rho_2 - \rho_1)} \ , \tag{3.60}$$

[3]Extension of bounds calculation to the unabridged version of NFEM is straightforward, by taking into account Eqs. (42) and (43) in [62].

[4]A practical definition of Υ is Υ=$\delta/(100{\cdot}6\varepsilon)$.

where σ is the surface tension coefficient and $\kappa{=}-\nabla\cdot\frac{\nabla\phi}{|\nabla\phi|}$ is the interface curvature. To calculate the curvature, gradient of phase function is recovered at nodes employing improved interface normals attained by the procedure described in section 3.4. Particulars about this methodology can be found in Appendix C. Upper limit value for surface tension force is determined by the interface curvature, the interface thickness and the density profile across interface [11] (constructed in turn from the phase function). This limit is independent on densities' jump, hence Eq. (3.60) is well conditioned, even for flows with two fluids with close values of density.

3.6 Artificial fluid stratification

Several interface problems, such as air cavity intrusion in ducts, often involve two non-stratified fluids flow, identified by a lower fluid advancing in a specified direction, and an upper lighter fluid moving in the opposite way. Instabilities of this kind of problems are widely known as Kelvin-Helmholtz instabilities for non-stratified flows. If surface tension is taken into account, stability condition for horizontal interfaces (see e.g. Ref. [15]) is

$$g\left(\rho_2^2-\rho_1^2\right)+K^2\sigma(\rho_2+\rho_1)>K\rho_1\rho_2\left(u_2-u_1\right)^2\,, \tag{3.61}$$

where $K{=}2\pi/\lambda$ is the perturbation wave number, λ is the perturbation wavelength, and u_1, u_2 are the tangential velocity for upper fluid and lower fluid, respectively. Surface tension has an stabilising effect on non-stratified flows. However, last equation is not entirely appropriate to analyse instabilities in simulations because phases in numerical model are virtually stratified due to the parametrical definition of density (Eq. (3.3) or (3.7)) and to the continuous finite element discretisation of the variables. To examine stability of two phases flow with a diffused interface, an incompressible inviscid flow with density and velocity distributions is considered, given by

$$\rho(y)=\begin{cases}\rho_1+\frac{\rho_2-\rho_1}{2}\mathrm{e}^{-y/L_\rho} & if \quad y>0\\ \\ \rho_2+\frac{\rho_1-\rho_2}{2}\mathrm{e}^{y/L_\rho} & if \quad y<0\end{cases}\,, \tag{3.62}$$

$$u(y)=\begin{cases}u_1+\frac{u_2-u_1}{2}\mathrm{e}^{-y/L_u} & if \quad y>0\\ \\ u_2+\frac{u_1-u_2}{2}\mathrm{e}^{y/L_u} & if \quad y<0\end{cases}\,, \tag{3.63}$$

where interface is located at $y{=}0$ and L_ρ, L_u are parameters that control density and velocity gradients. In this section, y axis is the vertical one. Exponential density profile, also proposed in Ref. [51] for Rayleigh-Taylor

instabilities, is a reasonable assumption since density is defined in terms of the phase function and, because of reinitialisation step, phase function is the numerical solution of the parabolic equation (3.44). As can be seen, same transition profile is assumed for velocity, along the lines of Ref. [80]. Moreover, same transition thickness is considered in both density and velocity profiles, which, in the light of numerical test results, is a reasonable assumption. Hence, one parameter is used, $L_I{=}L_\rho{=}L_u$. Now, coordinate value y_b is introduced to indicate the position of a density iso-surface; thus, $\rho(y{=}y_b(x,t))$ is constant. Then, by designating as $\tilde{\rho}$, $\tilde{u}$, $\tilde{v}$, $\tilde{p}$, and $\tilde{y}_b$ the perturbed density, x and y velocity components, pressure, and density iso-surface position, respectively, the two-dimensional linearised equations governing the perturbation field can be written, following Ref. [15] as

$$\frac{\partial\tilde{\rho}}{\partial t}+u\frac{\partial\tilde{\rho}}{\partial x}=-\tilde{v}\frac{\partial\rho}{\partial y}\,, \tag{3.64}$$

$$\frac{\partial\tilde{u}}{\partial x}+\frac{\partial\tilde{v}}{\partial y}=0\,, \tag{3.65}$$

$$\rho\frac{\partial\tilde{u}}{\partial t}+\rho u\frac{\partial\tilde{u}}{\partial x}+\rho\tilde{v}\frac{\partial u}{\partial y}=-\frac{\partial\tilde{p}}{\partial x}\,, \tag{3.66}$$

$$\rho\frac{\partial\tilde{v}}{\partial t}+\rho u\frac{\partial\tilde{v}}{\partial x}=-\frac{\partial\tilde{p}}{\partial y}-g\tilde{\rho}+\sigma\frac{\partial^2\tilde{y}_b}{\partial x^2}\left[\left(\frac{\partial\rho}{\partial y}\frac{1}{\rho_1-\rho_2}\right)\frac{2\rho}{\rho_1+\rho_2}\right]_{y=y_b}\,, \tag{3.67}$$

$$\frac{\partial\tilde{y}_b}{\partial t}+u_b\frac{\partial\tilde{y}_b}{\partial x}=\tilde{v}_b\,. \tag{3.68}$$

Equation (3.64) is the mass conservation of the perturbed field, Eq. (3.65) is the solenoidal condition for the perturbed velocity field, Eqs. (3.66) and (3.67) are the x and y components of momentum equation for inviscid fluids, and Eq. (3.68) is the kinematic condition applied on a density iso-surface $y{=}y_b$. Variables with subscript b are evaluated at $y{=}y_b$ and σ is the surface tension coefficient value. Equation (3.67) includes the equivalent surface tension force of the continuous model defined in Eq. (3.60). Now, solutions of the form e^{iKx+st} are sought for perturbed variables in Eqs. (3.64)-(3.68), where $\mathrm{Re}(s)$ is the growth rate. In this way, previous set of equations becomes,

after replacement, as follows,

$$(s+iKu)\tilde{\rho} = -\tilde{v}\frac{\partial \rho}{\partial y}\,, \tag{3.69}$$

$$iK\tilde{u} = -\frac{\partial \tilde{v}}{\partial y}\,, \tag{3.70}$$

$$\rho(s+iKu)\tilde{u} + \rho\tilde{v}\frac{\partial u}{\partial y} = -iK\tilde{p}\,, \tag{3.71}$$

$$\rho(s+iKu)\tilde{v} = -\frac{\partial \tilde{p}}{\partial y} - g\tilde{\rho} - K^2\sigma\tilde{y}_b\left[\left(\frac{\partial \rho}{\partial y}\frac{1}{\rho_1-\rho_2}\right)\frac{2\rho}{\rho_1+\rho_2}\right]_{y=y_b}\,, \tag{3.72}$$

$$(s+iKu)\tilde{y}_b = \tilde{v}_b\,. \tag{3.73}$$

Next, $\tilde{u}$ is eliminated in Eq. (3.71) by means of Eq. (3.70), and $\tilde{\rho}$ and $\tilde{y}_b$ are eliminated in Eq. (3.72) by means of Eqs. (3.69) and (3.73). The resulting equations are

$$-\rho(s+iKu)\frac{\partial \tilde{v}}{\partial y} + iK\rho\tilde{v}\frac{\partial u}{\partial y} = K^2\tilde{p}\,, \tag{3.74}$$

$$\rho(s+iKu)\tilde{v} = -\frac{\partial \tilde{p}}{\partial y} + g\tilde{v}\frac{\partial \rho}{\partial y}\frac{1}{s+iKu} - K^2\sigma\frac{\tilde{v}}{s+iKu}\left(\frac{\partial \rho}{\partial y}\frac{1}{\rho_1-\rho_2}\right)\frac{2\rho}{\rho_1+\rho_2}\,. \tag{3.75}$$

Finally, by inserting Eq. (3.74) into Eq. (3.75), an equation dependent on vertical perturbed velocity is attained,

$$\frac{\partial}{\partial y}\left[-\rho(s+iKu)\frac{\partial \tilde{v}}{\partial y} + iK\tilde{v}\rho\frac{\partial u}{\partial y}\right] + K^2\rho(s+iKu)\tilde{v} - gK^2\tilde{v}\frac{\partial \rho}{\partial y}\frac{1}{(s+iKu)} + K^4\sigma\frac{\tilde{v}}{s+iKu}\left(\frac{\partial \rho}{\partial y}\frac{1}{\rho_1-\rho_2}\right)\frac{2\rho}{\rho_1+\rho_2} = 0\,. \tag{3.76}$$

Integration along vertical direction of Eq. (3.76) in the domain $(-\infty,\infty)$ can be written as (note that integration of first term in Eq. (3.76) is zero),

$$\int_{-\infty}^{\infty}\left((s+iKu)(K^2\rho\tilde{v}) - \frac{K^2 g}{s+iKu}\frac{\partial \rho}{\partial y}\tilde{v} + K^4\sigma\frac{\tilde{v}}{s+iKu}\left(\frac{\partial \rho}{\partial y}\frac{1}{\rho_1-\rho_2}\right)\frac{2\rho}{\rho_1+\rho_2}\right)\mathrm{d}y = 0\ . \tag{3.77}$$

Introducing density and velocity definition (Eqs. (3.62) and (3.63)) in previous equation, integration results in

$$
\begin{aligned}
-s^2K(\rho_1+\rho_2) - \frac{iK^2s}{(1+KL_I)(2+KL_I)}\left(\left(4+KL_I(3+KL_I)\right)\rho_1u_1+\right.\\
KL_I(3+KL_I)\rho_1u_2+\rho_2\left(4u_2+KL_I(3+KL_I)(u_1+u_2)\right))+\\
\frac{K}{4(1+KL_I)(2+KL_I)}\left(4gK(2+KL_I)(\rho_1-\rho_2)+\right.\\
K^2\left(8\rho_1u_1^2+8\rho_2u_2^2+K^2L_I\left(-4\sigma+L_I(\rho_1+\rho_2)(u_1+u_2)^2\right)+\right.\\
\left.\left.K\left(-8\sigma+3L_I(\rho_1+\rho_2)(u_1+u_2)^2\right)\right)\right)=0\,. \quad (3.78)
\end{aligned}
$$

In case of L_I=0 in Eq. (3.78), and Re(s)=0, stability condition for non-stratified two-fluid problem (3.61) is recovered.

To illustrate and to discuss results established by Eq. (3.78), it is useful to consider a particular case. It comprises a duct of height d, where water takes up the lower half, and air the upper half. Although proposed solution (3.78) is designed for an unbounded flow, it is adequate for this example as long as parameter L_I is small enough compared with d. At this point, transition thickness is defined as δ_I=$|y_1 - y_2|$, where $\rho(y_1)$=$0.99\rho_1$+$0.01\rho_2$ and $\rho(y_2)$=$0.01\rho_1$+$0.99\rho_2$; thus δ_I=$7.824L_I$. An upper limit $\delta_I \leq 0.2d$ is considered in this study to preserve the adequacy of the unbounded solution. Fluids velocities are u_1=$-1/2\sqrt{gd}$, u_2=$1/2\sqrt{gd}$, and density ratio is ρ_1/ρ_2=0.001. Figure 3.2 depicts the non-dimensional growth rate $\mathrm{Re}(s)\sqrt{d/g}$ as a function of non-dimensional transition thickness δ_I/d, for perturbation wavelengths values of λ/d = 0.25, 0.1, 0.05, 0.025. Growth rate is plotted for inviscid cases as solid lines when σ=0, and as dashed lines when non-dimensional surface tension coefficient $2\sigma/((\rho_1+\rho_2)gd^2)$=$1.426\cdot10^{-3}$. First conclusion is that, unlike Rayleigh-Taylor instabilities, stratification does not stabilise Kelvin-Helmholtz instabilities. Regarding cases without the action of surface tension, it can be derived from Eq. (3.61) that non-stratified flows are stable for perturbations with wavelengths $\lambda/d > 0.0063$. On the other hand, for stratified flows, it can be concluded that flows with high gradient transitions (i.e. small values of δ_I) are very unstable, particularly for short wavelength perturbations. Growth rate diminishes for lower gradient transitions because of the stabilising effect of velocity gradient, in opposition to the destabilising effect of the density gradient (see e.g. [80]). For sufficiently large values of δ_I, growth rate tends to zero.

Now, the action of the continuous surface tension is included (Eq. (3.60)). Its stabilising impact is present for all transitions thickness, and it is greater for short wavelength perturbations. For example, case corresponding to

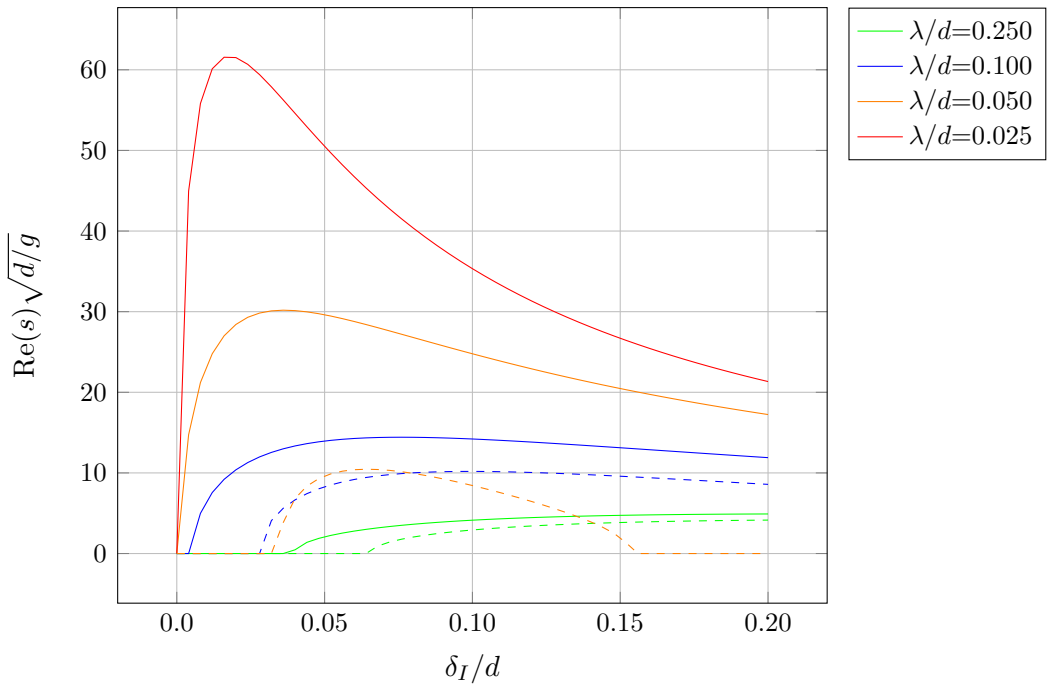

Figure 3.2: Non-dimensional growth rate $\mathrm{Re}(s)\sqrt{d/g}$ as a function of non-dimensional transition thickness δ_I/d. Solid and dashed lines are results without and with surface tension, respectively.

λ/d=0.025 is not distinguishable in Fig. 3.2 because flow is stable for all values of transition thickness, and the same occurs for shorter wavelengths. Amplification is discernible if $\delta_I/d \gtrapprox 0.03$ and $\lambda/d \geq 0.025$.

Finally, it is considered a transition band thin enough such that, although interface is diffuse, surface tension can be assumed to take action just at y=y_b=0. In this case surface tension term tends to its standard representation and Eq. (3.77) turns into

$$\int_{-\infty}^{\infty} \left((s+iKu)(K^2\rho\tilde{v}) - \frac{K^2 g}{s+iKu}\frac{\partial\rho}{\partial y}\tilde{v} + K^4\sigma\frac{\tilde{v}}{s+iKu}\delta_d(y) \right) \mathrm{d}y = 0 \tag{3.79}$$

since $\lim_{L_I\to 0}\left(\frac{\partial\rho}{\partial y}\frac{1}{\rho_1-\rho_2}\right)$=$\delta_d(y)$, and $2\rho(y{=}0)/(\rho_1+\rho_2)$=1, where δ_d is the Dirac-delta function. Integration of Eq. (3.79) yields to

$$\begin{aligned} -s^2K(\rho_1+\rho_2) - \frac{iK^2 s}{(1+KL_I)(2+KL_I)}\left((4+KL_I(3+KL_I))\,\rho_1u_1 + \right. \\ KL_I(3+KL_I)\rho_1u_2 + \rho_2\left(4u_2 + KL_I(3+KL_I)(u_1+u_2)\right)) + \\ \frac{K}{4(1+KL_I)(2+KL_I)}\left(4gK(2+KL_I)(\rho_1-\rho_2) + \right. \\ K^2\left(-4K^3L_I^2\sigma + 8\rho_1u_1^2 + 8\rho_2u_2^2 + \right. \\ K^2L_I\left(-12\sigma + L_I(\rho_1+\rho_2)(u_1+u_2)^2\right) + \\ \left.\left.\left. K\left(-8\sigma + 3L_I(\rho_1+\rho_2)(u_1+u_2)^2\right)\right)\right) = 0\,. \end{aligned} \tag{3.80}$$

Figure 3.3 shows results for this asymptotic state. In compare with previous responses, a reduction of growth rate is observed for all wavelengths. Also, Fig. 3.3 indicates an increase of the threshold value of δ_I/d whereupon growth rate starts to have non-zero values. Moreover, wavelength perturbation λ/d=0.050 is now completely stabilised when surface tension takes action. Notwithstanding, the overall response is similar to the continuous representation of surface tension.

Due to the continuous representation of the interface in numerical simulations, it is shown that some perturbations can be artificially activated. Nevertheless, there are some strategies to avoid these spurious Kelvin-Helmholtz instabilities. First, the most evident is to activate the surface tension and decrease the transition length to the extend that all perturbation wavelengths were stabilised (see Figs. 3.2 and 3.3). Some available strategies to decrease interface thickness can be appraised. Most direct technique is to reduce the diffusivity coefficient ε employed in reinitialisation (Eqs. (3.44) and (3.41)). Although a decrease of diffusion coefficient ε on interface improves resolution of the contact discontinuity, too small values of ε originate wiggles in phase

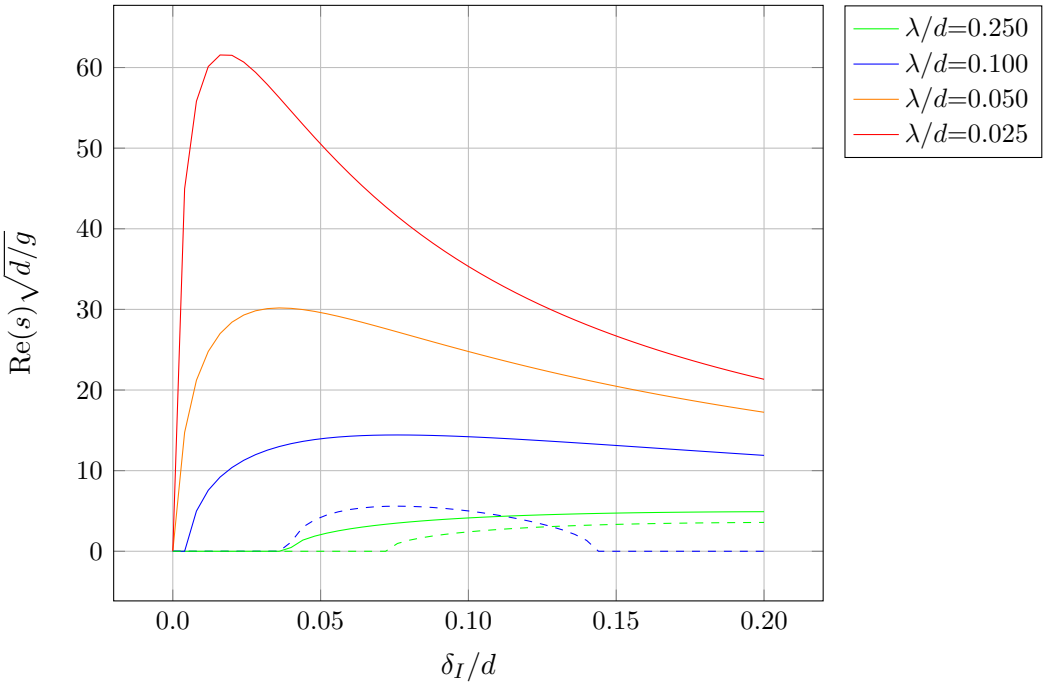

Figure 3.3: Non-dimensional growth rate $\mathrm{Re}(s)\sqrt{d/g}$ as a function of non-dimensional transition thickness δ_I/d for the asymptotic case: $\lim_{L_I \to 0}$. Solid and dashed lines are results without and with surface tension, respectively.

function [60]. Second strategy is to increase the transition thickness, however very large values of δ_I are necessary to be effective, enough to deteriorate significantly interface resolution and, therefore, the simulation accuracy.

A different course of action is to adjust original relation between density and phase function (Eq. (3.3)). In this case, modifications can have consequences in mass conservation. To scrutinise this option, it is considered here the incompressible limit and one alternative function to reduce band thickness. In the present model, density becomes a linear interpolation of phase function, $\rho(\phi)=\rho_1(1-\phi)+\rho_2\phi$. Then mass error is of round-off order if phase function is advected using a conservative method. As alternative function, it is examined the following interpolation proposed in Ref. [29],

$$\rho(\phi) = \begin{cases} \rho_1 & if \quad \phi < 1/2 - \vartheta \\ \rho_1 + (\phi - 1/2 + \vartheta)\frac{\rho_2-\rho_1}{2\vartheta} & if \quad 1/2 - \vartheta \leq \phi \leq 1/2 + \vartheta \\ \rho_2 & if \quad \phi > 1/2 + \vartheta \ , \end{cases} \tag{3.81}$$

where $\vartheta \leq 1/2$ controls the transition gradient. If $\vartheta=1/2$, present original interpolation is recovered, while for $\vartheta=0$ interpolation transforms into the Heaviside function. To estimate a mass error bound of this density interpolation, procedure introduced in Ref. [60] is followed. To this goal, it is defined the domain $\Omega=\Omega_1 \cup \Omega_2 \cup \Omega_3$, where $\{\phi = 0\} \cup \{\phi = 1\}$ in Ω_1, $\phi \in (0, 1/2-\vartheta)\cup(1/2+\vartheta, 1)$ in Ω_2, and $\phi \in [1/2-\vartheta, 1/2+\vartheta]$ in Ω_3. Mass error at time t^n is calculated by subtracting from the density function the original linear density interpolation with zero mass error, $\rho(\phi)=\rho_1(1-\phi)+\rho_2\phi$. Thus,

$$e(M) = \int_{\Omega_1+\Omega_2+\Omega_3} \left[\rho - \rho_1\,(1-\phi) - \rho_2\phi\right]\ \mathrm{d}\Omega \ . \tag{3.82}$$

Integrals for each subdomain are

$$\mathcal{I}_1 = \int_{\Omega_1} \left[\rho - \rho_1\,(1-\phi) - \rho_2\phi\right]\ \mathrm{d}\Omega_1 = 0 \ , \tag{3.83}$$

$$\mathcal{I}_2 = \int_{\Omega_2} \left[\rho - \rho_1\,(1-\phi) - \rho_2\phi\right]\ \mathrm{d}\Omega_2 = \\ (\rho_1 - \rho_2) \int_{\Omega_{2a}} \phi\ \mathrm{d}\Omega_{2a} + (\rho_2 - \rho_1) \int_{\Omega_{2b}} (1-\phi)\ \mathrm{d}\Omega_{2b} \ , \tag{3.84}$$

$$\mathcal{I}_3 = \int_{\Omega_3} \left[\rho_1 + (\phi - 1/2 + \vartheta)\frac{\rho_2 - \rho_1}{2\vartheta} - \rho_1\,(1-\phi) - \rho_2\phi\right]\,\mathrm{d}\Omega_3 = \frac{\rho_2 - \rho_1}{4\vartheta}\int_{\Omega_3}(2-4\vartheta)(\phi - 1/2)\,\mathrm{d}\Omega_3\ , \quad (3.85)$$

where Ω_{2a} and Ω_{2b} are sub-spaces of Ω_2 such that $\phi \in (0, 1/2-\vartheta)$ in Ω_{2a} and $\phi \in (1/2+\vartheta, 1)$ in Ω_{2b}. Now it is assumed a straight interface with length L_Γ, and an exponential phase function [60], $\phi(n)=\frac{1}{1+\mathrm{e}^{-n/\varepsilon}}$, where n is the signed distance measured along the interface normal. Then,

$$\mathcal{I}_2 = -L_\Gamma(\rho_2-\rho_1)\int_{-\infty}^{\varepsilon\log\left(\frac{1/2-\vartheta}{1/2+\vartheta}\right)}\phi(n)\,\mathrm{d}n + L_\Gamma(\rho_2-\rho_1)\int_{\varepsilon\log\left(\frac{1/2+\vartheta}{1/2-\vartheta}\right)}^{\infty}[1-\phi(n)]\,\mathrm{d}n\ , \quad (3.86)$$

$$\mathcal{I}_3 = L_\Gamma\frac{\rho_2-\rho_1}{4\vartheta}\int_{\varepsilon\log\left(\frac{1/2+\vartheta}{1/2-\vartheta}\right)}^{\varepsilon\log\left(\frac{1/2-\vartheta}{1/2+\vartheta}\right)}(2-4\vartheta)(\phi(n)-1/2)\,\mathrm{d}n\ . \quad (3.87)$$

Although $\mathcal{I}_1+\mathcal{I}_2+\mathcal{I}_3=0$ because analytical phase function is symmetrical respect to $\phi=1/2$, numerical results are not symmetrical. A mass error bound is established by computing integrals only for interval $n \in (0, \infty)$. Now,

$$\mathcal{I}_1+\mathcal{I}_2+\mathcal{I}_3 = L_\Gamma\frac{\rho_2-\rho_1}{4\vartheta}\int_{0}^{\varepsilon\log\left(\frac{1/2+\vartheta}{1/2-\vartheta}\right)}(2-4\vartheta)(\phi(n)-1/2)\,\mathrm{d}n + L_\Gamma(\rho_2-\rho_1)\int_{\varepsilon\log\left(\frac{1/2+\vartheta}{1/2-\vartheta}\right)}^{\infty}[1-\phi(n)]\,\mathrm{d}n\,, \quad (3.88)$$

resulting in the error bound

$$|e(M)| < \left|L_\Gamma(\rho_2-\rho_1)\varepsilon\left(\log\left(\frac{2}{1+2\vartheta}\right) + \frac{2\vartheta-1}{4\vartheta}\log\left((1+2\vartheta)(1-2\vartheta)\right)\right)\right|\ . \quad (3.89)$$

Error bound is proportional to interface length L_Γ and reinitialisation parameter ε. Maximum value is $|e(M)|_{\vartheta=0} < |L_\Gamma(\rho_2-\rho_1)\varepsilon\log(2)|$ for the Heaviside function, in agreement with Ref. [60] without considering $\mathcal{O}(\varepsilon^2)$ terms. For present numerical model $e(M)_{\vartheta=1/2}=0$.

In this work, an adaptive mesh refinement is proposed to diminish interface thickness. The method must preserve mass and keep bounds of primitive phase, velocity and pressure fields. To adapt the mesh to the demands of a moving interface problem, it is necessary a dynamic refinement to reduce band thickness and an unrefinement to recover previous mesh topology.

3.7 Mesh Refinement

This section reports the algorithm to the dynamical mesh refinement/unrefinement, without losing properties previously achieved. In general, conservation of a scalar field B in refinement and unrefinement processes [56] is carried out by finding a modified field $B_*^h \in V^h$ such that

$$\left(v^h, B_*^h\right)_\Omega = \left(v^h, B^h\right)_\Omega \,, \tag{3.90}$$

where $V^h \subset V = \{v \in H^1(\Omega)\}$ is the finite element space of the mesh after refinement (unrefinement) process and $B^h \in W^h$ is the initial scalar field defined in the finite element space of original mesh $W^h \subset W = \{w \in H^1(\Omega)\}$. However, solution B_* of Eq. (3.90) does not keep the bounds of original field B. Monotonicity is achieved by applying flux correction techniques. For that purpose, in addition to the high order solution B_*, it is necessary a low order approach that respects the bounds. In contrast with previous sections, where an upwind scheme was used to obtain the LOS, now it is employed a similar procedure to that proposed by J.R. Cebral and R. Löhner in Ref. [14]. In that work, they developed a conservative and monotone method, applied to fluid-solid interaction problems, to project the pressure field from fluid domain to structure domain. Unlike that work, here the required matrices can be easily calculated and incorporated a-priori in the code because primary and refined meshes are nested. Low order solution is obtained by multiplying the right hand side of Eq. (3.90) by the inverse of the lumped mass matrix of new mesh. Solution keeps the bounds without applying any additional amount of diffusion. To demonstrate this, LOS in matrix form is represented as

$$\mathbf{M}_{L*}\mathbf{b}_* = \mathbf{M}_C\mathbf{B}\,, \tag{3.91}$$

where $\mathbf{M}_{L*}=\left(v^h, 1\right)_\Omega$, $\mathbf{M}_C=\left(v^h, w^h\right)_\Omega$ and $\mathbf{B}$, $\mathbf{b}_*$ are vectors with nodal values of original and refined (unrefined) meshes, respectively. By nothing that $\sum_{j=1}^N \mathbf{M}_{C,ij}=\mathbf{M}_{L*,ii}$,

$$\sum_{j=1}^{N} \mathbf{M}_{C,ij} = \sum_{j=1}^{N} \int_\Omega v_i w_j \,\mathrm{d}\Omega = \int_\Omega v_i \sum_{j=1}^{N} w_j \,\mathrm{d}\Omega = \int_\Omega v_i \,\mathrm{d}\Omega = \mathbf{M}_{L*,ii}\,, \tag{3.92}$$

where N is the total number of nodes of the original mesh. Then, it is also true that $\mathbf{M}_{C,ij} \leq \mathbf{M}_{L*,ii} \;\; \forall \;\; 0 \leq j \leq N$ since $\mathbf{M}_{C,ij} \geq 0$. On the other hand, $\mathbf{b}_{*i}$ is calculated as

$$\mathbf{b}_{*i} = \sum_{j=1}^{N} \frac{\mathbf{M}_{C,ij}}{\mathbf{M}_{L*,ii}} \mathbf{B}_j\,, \tag{3.93}$$

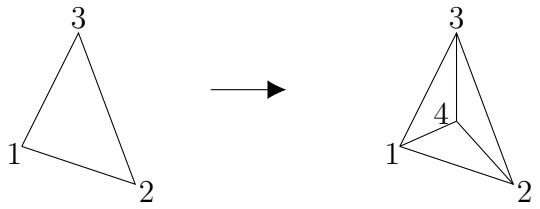

Figure 3.4: Refinement: Alternative 1

where terms $\frac{\mathbf{M}_{C,ij}}{\mathbf{M}_{L*,ii}} \leq 1$, $\frac{\mathbf{M}_{C,ij}}{\mathbf{M}_{L*,ii}} \geq 0$ and $\sum_{j=1}^{N} \frac{\mathbf{M}_{C,ij}}{\mathbf{M}_{L*,ii}} = 1$. Consequently $\mathbf{b}_*$ respects bounds of $\mathbf{B}$.

After getting LOS solution, anti-diffusive fluxes are calculated as

$$\mathbf{A}_j = \mathbf{M}_{L*}^{-1} \left\{ (\mathbf{M}_{L*} - \mathbf{M}_{C*}) \mathbf{B}_* \right\}_j \ ,$$

where $\mathbf{M}_{C*}$, $\mathbf{M}_{L*}$ are the consistent and lumped mass matrices of the refined (unrefined) mesh. Finally, improved field is constructed as,

$$\tilde{B}_{*i} = b_{*i} + \sum_{j=1}^{e} c_j A_j \ , \tag{3.94}$$

where b_{*i} is the nodal LOS, e is the total number of surrounding elements to node i and c_j are element limiters, whose equation is detailed in [61]. Nodal bounds are calculated considering primitive field B. Last procedure is applied to the phase, velocity and pressure fields, and candidates for refinement are all elements contained in Level 3 of interface elements (those which contain ϕ=1/2).

Two refinement strategies based on nested grids are inspected. First option is the division sketched in Fig. 3.4. In this situation, the modified field after refinement is calculated straightforwardly, and procedure described above is only necessary for unrefinement stage. Second option is the division sketched in Fig. 3.5, by adding middle edge nodes. Here, both refinement and unrefinement need the conservative projection. Although first option is cheaper to a limited extent, second option sometimes yields to more regular meshes in the vicinity of the current interface. Numerical experiments reveals that both strategies give similar results. Matrix forms of system (3.90) for both methodologies are detailed in Appendix E.

Present chapter has described the numerical finite element model for the solution of two-phase flows with moving interfaces. After a brief report about principles of the NFEM and flux correction techniques, the three stages of the numerical method were detailed. These are: phase function advection,

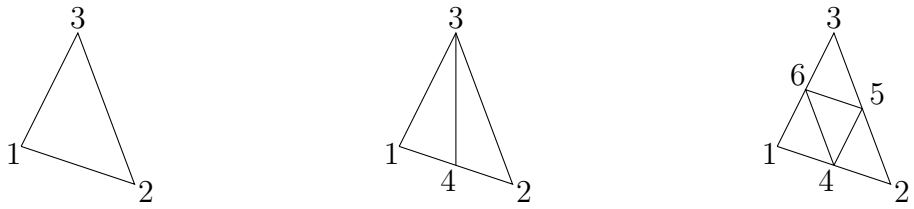

Figure 3.5: Refinement: Alternative 2

reinitialisation step and hydrodynamics resolution. Moreover, problems arising from the continuous interface discretisation in simulations with Kelvin-Helmholtz instabilities were studied, and a new mesh refinement strategy based on nested-grids has been proposed to ameliorate its negative effects. Next chapter collects simulations performed with numerical model, including benchmark tests and experiments of air cavities propagation and rising Taylor bubbles.

Chapter 4

Numerical Experiments

This chapter reports numerical experiments and consists of three sections. Section 4.1 focuses on the advection algorithm assessment. After checking the convergence order of the NFEM, some stringent transport tests are reproduced. Firstly, accuracy of the model is evaluated by simulating rotating disks in stationary and time-dependent flows. Then, to discuss coalescence among nearby interfaces, it is performed an experiment composed by four disks advected by a Gaussian vortex distribution. Last two experiments of this section appraise the efficiency of the three dimensional extension of presented model. Section 4.2 presents the evaluation of the complete numerical model (including the phase function transport and hydrodynamics solution). First series of experiments involves Rayleigh-Taylor instabilities, where several physical parameters are tested to scrutinise spurious momentum transfers. Then, two versions of the dam break experiment are carried out: one version in a 2D domain without obstacle and the other one in a 3D domain with obstacle. Finally, experiments related with air pockets and geysering phenomena are detailed in section 4.3. First and second subsections scrutinise propagation of air cavities by combining partial closure of the gate with horizontal and inclined ducts to validate current numerical model. Third subsection concerns the study of conditions under which air cavities intrude in ducts with a weir located across its open end. In fourth subsection a laboratory experiment, previously employed to assess the analytical approach (see section 2.2.3), is now reproduced by numerical model to evaluate its performance with rising Taylor bubbles simulations. Limits of semi-analytical approach to multiple bubbles dynamics are estimated in fifth subsection, by comparing theoretical predictions with numerical outputs. In last subsection it is simulated the momentum transfer between an horizontal duct with an air cavity and a vertical duct with still water, the rising Taylor bubble formed in the vertical duct and the final geysering event. By this sequence of tests, numerical study covers the comparison with laboratory

experiments concerning propagation of air cavity [8, 81], emergence of closed cavities [1], vertical propagation of bubbles in vertical tubes [79] and the geyser on top of the conduit.

Simulations and assessment tests have been executed in a server with a CPU Intel Core i7-6800K and 32GB of RAM.

4.1 Advection Assessment Simulations

4.1.1 Advection of a Gaussian profile. An assessment of convergence

This test (also published in Ref. [61]) investigates the recovery of second order accuracy when corrections are active by comparing rates of convergence. Each experiment is performed with nearly constant Courant-Friedrichs-Lewy (CFL) number and with uniform advection velocity. A Gaussian cone of height 4 is placed at initial time with its centre at (-2,-2) of a domain [-50,50]×[-50,50], then initial condition is prescribed as

$$\overline{\phi}_0(\mathbf{x}) = 4\,\exp\left(-\frac{1}{2}\left\{\left(\frac{(x+2)}{2}\right)^2 + \left(\frac{(y+2)}{2}\right)^2\right\}\right),$$

where scalar function is denoted as the phase function, and $\mathbf{u}$=(2.4,2.4). Four unstructured meshes were generated with average element side length[1] $\overline{\delta}$ values of 0.221, 0.44, 0.89, 1.81; comprising 367616, 91636, 22764, 5606 linear triangular elements, and 184613, 46223, 11587, 2908 nodes, respectively. CFL=0.9 and 0.5 are specified for all meshes, while final time of the experiment corresponds to 16, 8, 4 and $2\Delta t$ for the four grids, respectively.

The solution was calculated by the high order FEM method (Eq. (3.36)) and by the NFEM. The $e(L_1)$ and $e(L_2)$ errors were computed for the HO-FEM and for the NFEM for each mesh and for each CFL, to observe recovery of accuracy once the correction operates. Figures 4.1 and 4.2 depict errors in terms of average element size for CFL=0.9 and 0.5 respectively. Second order accuracy of the HO-FEM is approximately preserved by NFEM for both CFL numbers. HO-FEM and NFEM methods are always over second order rate, except for values measured in the two coarsest meshes for CFL=0.9. For this condition, the NFEM has $\varrho\approx1.95$ while the HO-FEM has $\varrho\approx2.06$ (errors in L_2 norm). Similar rates of convergence were obtained by doubling the final time of the experiments.

[1]Average element side length for 2D unstructured meshes is defined as $\overline{\delta} = \frac{1}{E}\sum_{j=1}^{E}\sqrt{(\overline{\Delta x})_j^2 + (\overline{\Delta y})_j^2}$.

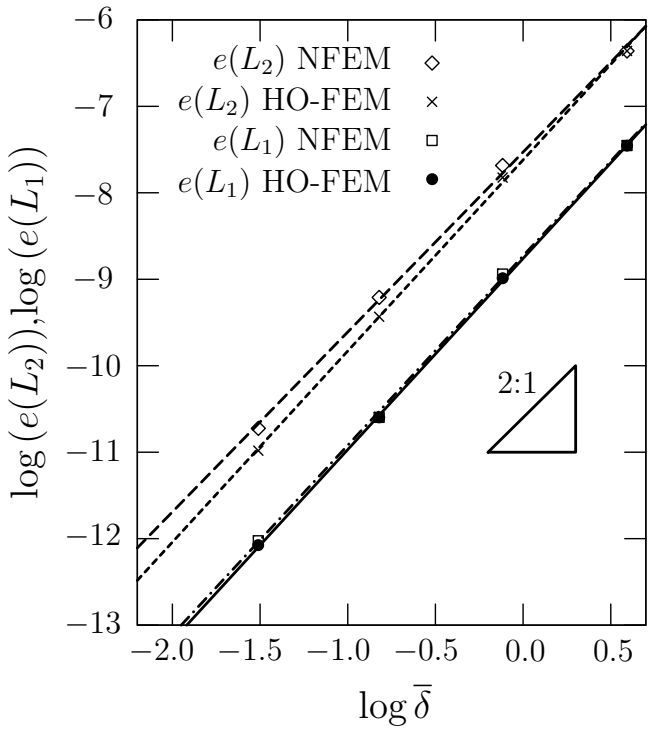

Figure 4.1: Gaussian cone test. Convergence for 4 unstructured meshes and CFL$\approx$ 0.9. $e(L_1)$: L_1 error, $e(L_2)$: L_2 error. NFEM: new method. HO-FEM: Characteristic based FEM.

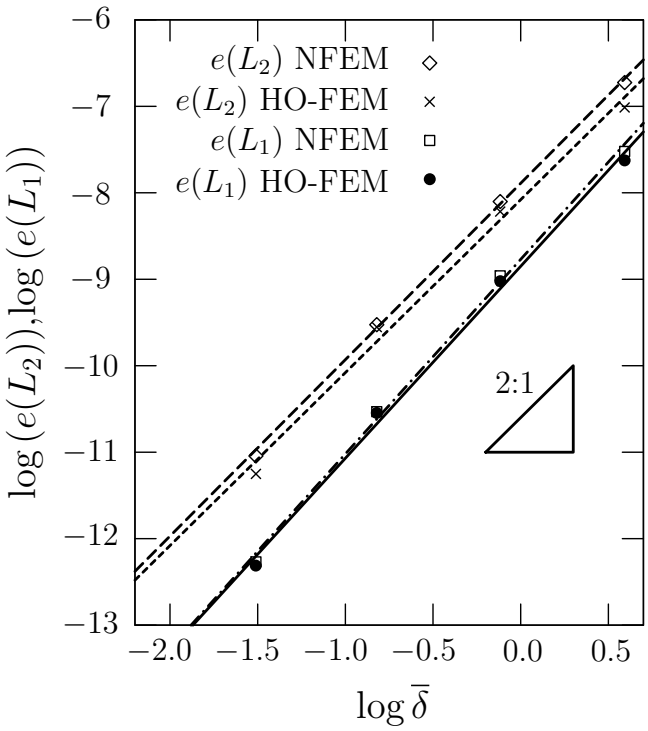

Figure 4.2: Gaussian cone test. Convergence for 4 unstructured meshes and CFL$\approx$ 0.5. $e(L_1)$: L_1 error, $e(L_2)$: L_2 error. NFEM: new method. HO-FEM: Characteristic based FEM.

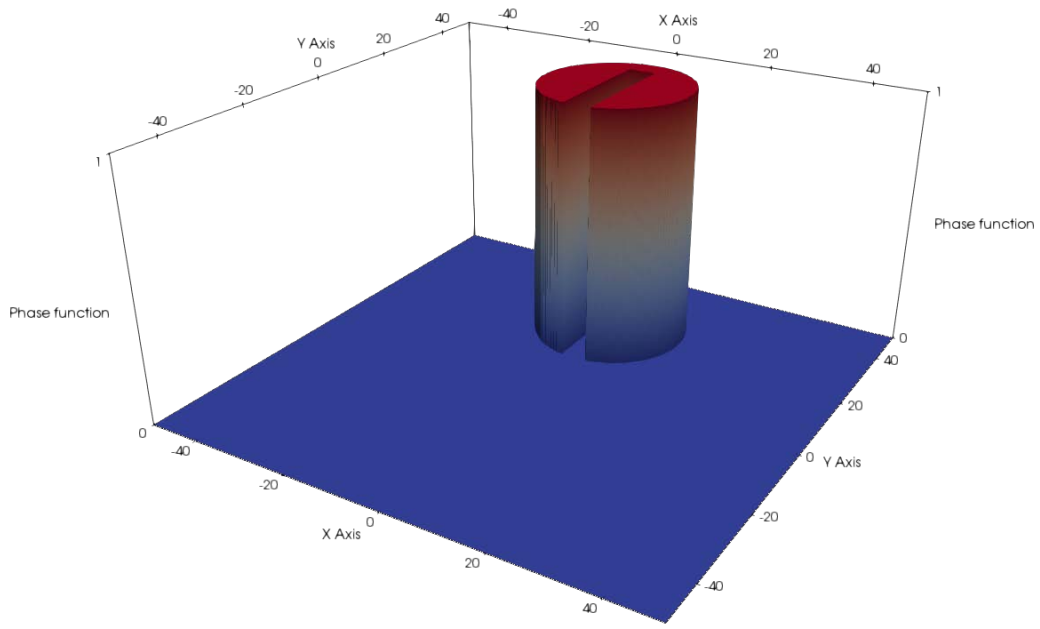

Figure 4.3: Slotted cylinder in a rotating flow. Initial condition

4.1.2 Slotted cylinder in a rotating flow

In this section the accuracy of the transport model to capture interfaces is evaluated (see section 3.3), by reproducing the stringent test proposed by Zalesak in Ref. [84]. The simulation is defined by a discontinuous initial profile sketched in Fig. 4.3. The slotted disk of Fig. 4.3 has radius 15 and height 1, and the slot has width 5 and length 25. The disk at initial time is centred at (0,25) in a $[-50, 50] \times [-50, 50]$ region. As a result of an advective velocity field $\mathbf{u}=(\omega y, -\omega x)$, $\mathbf{u}=\mathbf{0}$ on Γ, $\omega=0.1$, the cylinder moves clockwise until completion of one rotation. Two and ten rotations are also reviewed. Three structured grids of linear triangular elements are employed, element side length δ[2] and total number of time steps are $\left\{\sqrt{2}, 1030\right\}$, $\left\{\frac{\sqrt{2}}{2}, 2060\right\}$, and $\left\{\frac{\sqrt{2}}{4}, 4120\right\}$, respectively. Reinitialisation step parameters are, $\varepsilon=0.83\Delta l$, and $\Delta\tau=\alpha\frac{\Delta l^2}{8\varepsilon}$ (dummy timestep), where Δl is the maximum triangle height, and $\alpha=0.1$.

In addition to standard errors $e(L_1)$, $e(L_2)$, and total mass error, test utilises the interface error measure [74] and the enclosed volume error mea-

[2]Element side length in 2D structures meshes is $\delta = \sqrt{\Delta x^2 + \Delta y^2}$.

sure, defined as

$$e(L_1^I) = \frac{1}{L}\sum_{i=1}^{N}\left\{\left|H\left(\hat{\phi}_i - \frac{1}{2}\right) - H\left(\phi_i - \frac{1}{2}\right)\right|(\mathbf{M}'_L)_i\right\}, \tag{4.1}$$

$$A^e_{0.5}(t^n) = \frac{A_{0.5}(t^n) - A_{0.5}(t_0)}{A_{0.5}(t_0)}. \tag{4.2}$$

In previous equations, $H(\cdot)$ is the Heaviside function, L is the interface length, N is the total number of nodes, $(\mathbf{M}'_L)_i$ is the lumped mass matrix element corresponding to node i, $\hat{\phi}$ indicates the numerical solution (after reinitialisation, unless stated otherwise), ϕ is the analytical (ideal) phase function solution and $A_{0.5}$ is the enclosed volume. Interface length is given by initial conditions in this experiment, and its value is L=143.80. The enclosed volume is computed as the area contained by the closed ϕ=0.5 contour, tracked by reconstructing the interface through elementwise linear interpolation.

Results of the series of experiments after one and two rotations are summarised in Tables 4.1 and 4.2. First column of Table 4.1 indicates the method, either original NFEM scheme, as proposed in Ref. [61] (Eq. (3.25)), or modified NFEM with mass correction proposed in section 3.2 (see Eq. (3.34)). Columns 2 to 7 indicate average element side length, errors $e(L_1^I)$, $e(L_1)$, $e(L_2)$, $A^e_{0.5}$ [%], and mass error, respectively. The five columns of Table 4.2 display:

1. Methods: present method, finite element method and finite volume method in Ref. [29].

2. Dimensionless element side length written as $\Delta x/l = \delta/(l\sqrt{2})$ to be consistent with data in Ref. [29].

3. Number of rotations.

4. Dimensionless interface error $e(L_1^I)/l$.

5. Enclosed volume error, where l is the characteristic length of the domain (here, l=100).

Table 4.1 shows results without computing reinitialisation step, to focus on transport. Further, prescribed advective velocity field for these experiments avoids mass errors originated on boundaries. Errors are essentially the same in the original method and when mass correction is activated. Therefore redistribution of antidiffusion arising from the global correction functions is inconsequential in terms of errors in standard norms, as well as errors in

Table 4.1: Slotted cylinder in a rotating flow. Interface error $e(L_1^I)$, errors $e(L_1)$, $e(L_2)$, enclosed volume error $A_{0.5}^e$ [%] and mass error after one rotation, for original NFEM (Eq. (3.25)), and for NFEM with embedded global mass correction (Eq. (3.34))

	δ	$e(L_1^I)$	$e(L_1)$	$e(L_2)$	$A_{0.5}^e$ [%]	Mass error
Original Eq. (3.25)	$\sqrt{2}$	3.8942E-01	2.1206E-02	8.3295E-02	1.281	2.022E-02
	$\frac{\sqrt{2}}{2}$	1.5299E-01	1.1418E-02	5.8962E-02	-0.567	5.3E-04
	$\frac{\sqrt{2}}{4}$	7.6493E-02	6.4900E-03	4.4255E-02	-0.274	1.62E-03
Mass Correction Eq. (3.34)	$\sqrt{2}$	3.7551E-01	2.1950E-02	8.4983E-02	-0.757	-7.0E-15
	$\frac{\sqrt{2}}{2}$	1.5472E-01	1.1534E-02	5.9233E-02	-0.512	-6.71E-14
	$\frac{\sqrt{2}}{4}$	7.3450E-02	6.5382E-03	4.4400E-02	-0.118	-2.09E-13

Table 4.2: Slotted cylinder in a rotating flow. Dimensionless interface error $e(L_1^I)/l$, and enclosed volume error $A_{0.5}^e$ [%] after one rotation and after two rotations; l: characteristic length of the domain. Comparisons with finite element method and finite volume method in Ref. [29]

Method	$\Delta x/l$	Rotations	$e(L_1^I)/l$	$\lvert A_{0.5}^e \rvert$ [%]
Present	1.00E-2	1	5.146E-03	0.645
		2	1.001E-02	0.598
	5.00E-3	1	5.911E-04	0.363
		2	5.911E-04	0.354
	2.50E-3	1	2.521E-04	0.093
		2	2.868E-04	0.093
Q1 Finite Element [29]	1.25E-2	1	4.259E-03	2.021
		2	4.446E-03	0.741
	6.25E-3	1	1.750E-03	0.153
		2	2.010E-03	0.441
Finite Volume [29]	1.000E-2	1	-	0.086
		2	-	0.191
	4.95E-3	1	-	0.027
		2	-	0.044
	2.49E-3	1	-	0.019
		2	-	0.026

interface quality. However mass adjustment stated in Eq. (3.34) removes completely high order mass errors ascribable to correction procedure (see seventh column, rows 5 to 7 in Table 4.1, where mass errors are of the order of round-off).

To scrutinise the reinitialisation algorithm (section 3.4), its results are condensed in Table 4.2 and they are compared with those attained in Ref. [29], where a modified conservative level set method by antidiffusion techniques has some comparable spatial and temporal discretisation features with the present model. Reduction of interface error $e(L_1^I)$ usually involves an increase in enclosed volume error $A_{0.5}^e$, and vice versa; that is, reducing $A_{0.5}^e$ through a significant decrease of diffusion in reinitialisation step normally provokes oscillations in the phase field and, consequently, a rise in $e(L_1^I)$ [60]. Interface error decreases for finer grids, and increases according to the number of cycles, as expected. Present model has a performance competitive with Q1 finite element model in Ref. [29] for intermediate mesh size. It is interesting to observe the considerable decrease in error reached when a moderate refinement of mesh is produced, from the finer Q1 finite elements mesh in Ref. [29] ($\Delta x/l$=6.25E-3) to the intermediate mesh in the present model ($\Delta x/l$=5.0E-3). For $\Delta x/l$=2.5E-3 error diminishes considerably. The behaviour of enclosed volume error is not as evident, showing some high frequency wiggles in time. This is apparent for some meshes with higher $A_{0.5}^e$ values after one rotation than values after two rotations. Nevertheless, $A_{0.5}^e$ decreases by refining grid size. Enclosed volume error results for NFEM are again competitive with Q1 finite element model in Ref. [29], showing better results for coarser meshes. It is remarkable the good enclosed volume conservation property achieved by the finite volume method in Ref. [29], improving $A_{0.5}^e$ in compare with responses for finer meshes with other methods. However this trend is not distinguished for the transient velocity field case (section 4.1.3).

Finally, the long term answer of current scheme is studied, exploring in particular the reinitialisation. Experiments were carried out for ten complete rotations. Results are condensed in Table 4.3 and in Fig. 4.4. Columns in Table 4.3 indicate $e(L_1^I)$, $e(L_1)$, $e(L_2)$, and $A_{0.5}^e$ [%] errors, respectively, for the unaltered NFEM, the NFEM with reinitialisation, and the NFEM with reinitialisation and local calculation of normals (see section 3.4), and for three meshes with δ values of $\sqrt{2}$, $\sqrt{2}/2$, and $\sqrt{2}/4$. Figure 4.4 depicts final shape of cylinder area after 10 rotations for the three procedures mentioned above, and for meshes with delta values of $\sqrt{2}/2$ (Figs. 4.4a, 4.4b, 4.4c), and $\sqrt{2}/4$ (Figs. 4.4d, 4.4e, 4.4f).

Error $e(L_1^I)$ measures the quality of interface position. Reinitialisation process often produces adjustments of interface placing, and consequently,

Table 4.3: Slotted cylinder in a rotating flow. Ten rotations. Interface error $e(L_1^I)$, $e(L_1)$, $e(L_2)$, and enclosed volume error $A^e_{0.5}$ [%] for NFEM, NFEM + Reinitialisation step without local calculation of normals, and with local calculation of normals.

Method	δ	$e(L_1^I)$	$e(L_1)$	$e(L_2)$	$A^e_{0.5}$ [%]
NFEM	$\sqrt{2}$	1.0779E-00	3.5493E-02	1.1446E-01	10.758
	$\frac{\sqrt{2}}{2}$	2.3295E-01	1.9254E-02	7.7951E-02	-1.517
	$\frac{\sqrt{2}}{4}$	1.4038E-01	1.1000E-02	5.8235E-02	-0.345
NFEM + Reinitialisation	$\sqrt{2}$	1.4395E-00	2.5985E-02	1.2854E-01	-0.633
	$\frac{\sqrt{2}}{2}$	3.3552E-01	1.0503E-02	6.1525E-02	0.005
	$\frac{\sqrt{2}}{4}$	2.7772E-01	8.2987E-03	5.5314E-02	-0.265
Local Calculation of Normals	$\sqrt{2}$	1.2865E-00	2.3750E-02	1.1953E-01	-0.462
	$\frac{\sqrt{2}}{2}$	3.1292E-01	9.7879E-03	6.0358E-02	-0.196
	$\frac{\sqrt{2}}{4}$	1.7472E-01	5.2347E-03	4.6201E-02	-0.069

difficulties arise to reduce interface error during this process. Further, interface error values can deteriorate, as discussed in paragraphs above: for instance, compare $e(L_1^I)$ for NFEM (transport) with NFEM+Reinitialisation in Table 4.3. The subsequent new computation of normals mitigates the deterioration during reinitialisation, and removes efficiently interface wiggles created by the reconstruction. This enhancement is manifest in Fig. 4.4 by comparing Fig. 4.4b with Fig. 4.4c, and Fig. 4.4e with Fig. 4.4f, respectively. Table 4.3 also shows a considerable reduction of $e(L_1^I)$ once local calculation is performed, particularly for the finer mesh. Enclosed area error diminishes consistently by the successive application of reinitialisation and local normals regularisation. An increase of $A^e_{0.5}$ from the intermediate grid to the fine grid is detected if local calculation of normals is not performed, and is ascribable to the evolving nature of high frequency wiggles present in $A^e_{0.5}$, as reported previously. Errors $e(L_1)$ and $e(L_2)$ do not deteriorate after reconstruction procedures, and even decrease for intermediate and fine grids, specially in the L_1 norm. On the other hand, some error indicators for the coarser mesh (δ=$\sqrt{2}$) suggest that this characteristic element length is not sufficient to reach minimum size for a competent usage of reinitialisation tools in long term calculations. Responses of very high order schemes for this test [16] reveal that the intermediate grid size (δ=$\frac{\sqrt{2}}{2}$) is sufficient to achieve same order of errors as high order scheme in Ref. [16] with the coarse mesh (δ=$\sqrt{2}$).

Reinitialisation step demands a burden of around 20% CPU time. Nonetheless, local calculation of normals does not add extra cost. The reason is twofold; first, the use of static data about neighbourhood of activated nodes

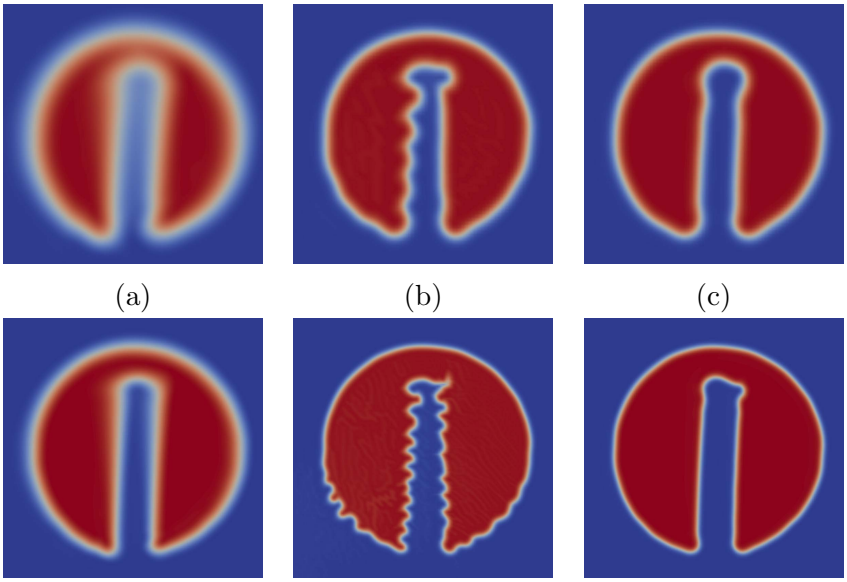

Figure 4.4: Slotted cylinder in a rotating flow. Phase field ϕ after 10 rotations. $\delta = \frac{\sqrt{2}}{2}$: (a) NFEM, (b) NFEM + Reinitialisation, (c) local calculation of normals; $\delta = \frac{\sqrt{2}}{4}$: (d) NFEM, (e) NFEM + Reinitialisation, (f) local calculation of normals.

associated with the interface elements; second, the remarkable acceleration of convergence for the reinitialisation step once regularised normals are integrated in the calculation. Sign of phase function is strictly preserved and, in addition, monotonicity is achieved. This is due to the fact that advective velocity field is independent of transported phase function, determining the monotonicity of the low order scheme.

4.1.3 Circle in a time dependent swirling deformation flow

This experiment imposes severe conditions to the model, taking into account that filaments smaller that element side length could appear as a consequence of the very large deformation suffered by the initial phase field function. The advective velocity field $\mathbf{u}$ is a time dependent swirling flow with the following Cartesian components,

$$u(\mathbf{x},t) = 100\sin^2\left(\frac{\pi\,(x+50)}{100}\right)\sin\left(\frac{2\pi\,(y+50)}{100}\right)\cos\left(\frac{\pi t}{T}\right)\,,$$
$$v(\mathbf{x},t) = -100\sin^2\left(\frac{\pi\,(y+50)}{100}\right)\sin\left(\frac{2\pi\,(x+50)}{100}\right)\cos\left(\frac{\pi t}{T}\right)\,,$$

where T=8. Initial phase function shape is a circle of diameter 30 with its centre at (0,25) in a $[-50, 50] \times [-50, 50]$ domain (Fig. 4.5a). Element side length and value of timestep for the three structured meshes of linear triangular elements implemented are $\{\sqrt{2}, 0.004\}$, $\{\frac{\sqrt{2}}{2}, 0.002\}$, and $\{\frac{\sqrt{2}}{4}, 0.001\}$, respectively. To achieve a better resolution of thin filaments, ε=0.70Δl is set, whereas $\Delta\tau$=$\alpha\frac{\Delta l^2}{8\varepsilon}$ is the same as previous test.

Tables 4.4 and 4.5 have the same format and definitions as Tables 4.3 and 4.2, respectively. Results represented in Tables 4.4 and 4.5 correspond to the final time of simulation T=8. Legends 'NFEM+Reinitialisation' in Table 4.4, and 'Present' in Table 4.5 signify NFEM plus complete reinitialisation process, including regularisation of normals. Now, in Table 4.5 it is added the P1 Finite element model of Ref. [29] to the methods included in Table 4.2. Figures 4.5b-4.5g illustrate the shape of phase function for the three meshes at t=$T/2$=4, when the circle has the largest deformation, and at the end of the cycle t=T=8, when circle recovers the initial position.

Tables 4.4 and 4.5 show similar error measure features to previous test. This experiment confirms that the coarsest mesh has not enough resolution to catch properly the behaviour of the deforming circle. Even so, this fact is not evident from inspection of errors in Table 4.4, but it is evident by inspecting Fig. 4.5b and 4.5c. The coarse mesh is not capable to preserve the smallest filaments because reinitialisation tends to produce small isolated droplets (see Fig. 4.5b). At the end of the cycle these dissociations lead to a completely corrupted interface (Fig. 4.5c). Instead, intermediate mesh (Figs. 4.5d and 4.5e), and fine mesh (Figs. 4.5f and 4.5g) are able to retain fibres and thus, final interface is sufficiently accurate. Comparison of results with those of Ref. [29] reveals same order of magnitude for error $e(L_1^I)$, although bigger to some extent for the same discretisation. In the case of $A_{0.5}^e$ error measure, current model results have lower error values than finite volume and P1 finite element in [29] for the intermediate and fine grids, but of the same order and larger than Q1 finite elements. As outlined in section 4.1.2, finite volume method has remarkable enclosed volume conservation property, but in this transient advective experiment this characteristic is not longer present (Table 4.5).

4.1.4 Gaussian Vortex Test

Now interaction and coalescence among adjacent interfaces is discussed by means of a demanding distribution of a scalar function transported by a time dependent Gaussian vortex flow. The test is defined by four disks of radius 15 and height 1, centred at (-25,0), (25,0), (0,-25) and (0,25), respectively, in a $[-50, 50] \times [-50, 50]$ region (see sketch in Fig. 4.6). The advective velocity

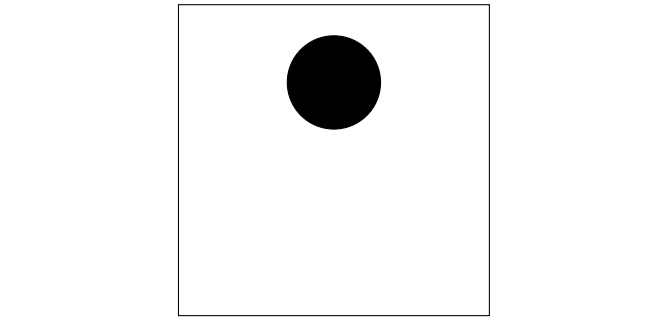

(a) t=0

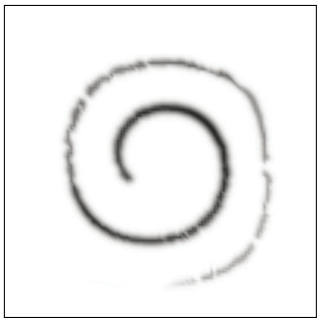

(b) δ=$\sqrt{2}$. t=4

(c) δ=$\sqrt{2}$. t=8

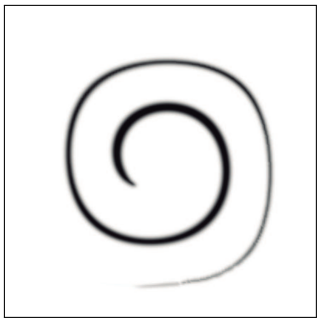

(d) δ=$\frac{\sqrt{2}}{2}$. t=4

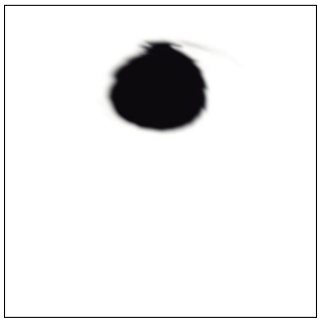

(e) δ=$\frac{\sqrt{2}}{2}$. t=8

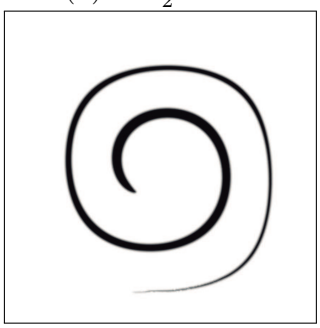

(f) δ=$\frac{\sqrt{2}}{4}$. t=4

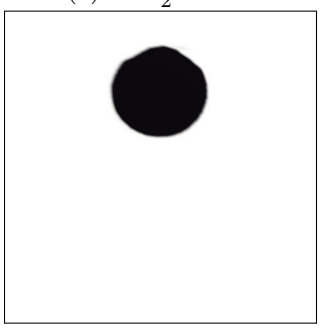

(g) δ=$\frac{\sqrt{2}}{4}$. t=8

Figure 4.5: Circle in a time dependent swirling flow. Phase field ϕ at t=0, t=4, and t=8, for δ=$\sqrt{2}$, δ=$\sqrt{2}/2$, and $\sqrt{2}/4$

Table 4.4: Circle in a time dependent swirling flow. Interface error $e(L_1^I)$, $e(L_1)$, $e(L_2)$, and enclosed volume error $A_{0.5}^e$ [%] at t=T=8, for NFEM and NFEM + Reinitialisation

Method	δ	$e(L_1^I)$	$e(L_1)$	$e(L_2)$	$A_{0.5}^e$ [%]
NFEM	$\sqrt{2}$	3.7984E-00	7.2051E-02	1.6624E-01	-50.489
	$\frac{\sqrt{2}}{2}$	6.3660E-01	4.2338E-02	1.1784E-01	-5.219
	$\frac{\sqrt{2}}{4}$	1.3727E-01	2.1159E-02	7.9945E-02	-0.354
NFEM+ Reinitialisation	$\sqrt{2}$	2.546E-00	3.5987E-02	1.3029E-01	0.730
	$\frac{\sqrt{2}}{2}$	1.1167E-00	1.4358E-02	8.6543E-02	-1.680
	$\frac{\sqrt{2}}{4}$	4.6618E-01	5.9939E-03	5.6459E-02	-0.287

Table 4.5: Circle in a time dependent swirling flow. Dimensionless interface error $e(L_1^I)/l$, and enclosed volume error $A_{0.5}^e$ [%] at t=8; $\Delta x/l$=$\delta/(l\sqrt{2})$, l: characteristic length of the domain (l=100). Comparisons with finite volume method, P1 finite element method, and Q1 finite element method by [29]

Method	$\Delta x/l$	$e(L_1^I)/l$	$\lvert A_{0.5}^e \rvert$ [%]
Present	1.000E-2	2.55E-2	0.73
	5.000E-3	1.12E-2	1.68
	2.500E-3	4.66E-3	0.29
Finite Volume [29]	1.000E-2	8.70E-3	16.00
	4.950E-3	4.08E-3	4.82
	2.488E-3	2.04E-3	1.38
P1 Finite Element [29]	1.000E-2	8.61E-3	11.48
	6.250E-3	3.32E-3	4.18
	3.125E-3	1.29E-3	0.84
Q1 Finite Element [29]	1.000E-2	1.15E-2	9.80
	5.000E-3	3.85E-3	0.81
	2.500E-3	2.01E-3	0.16

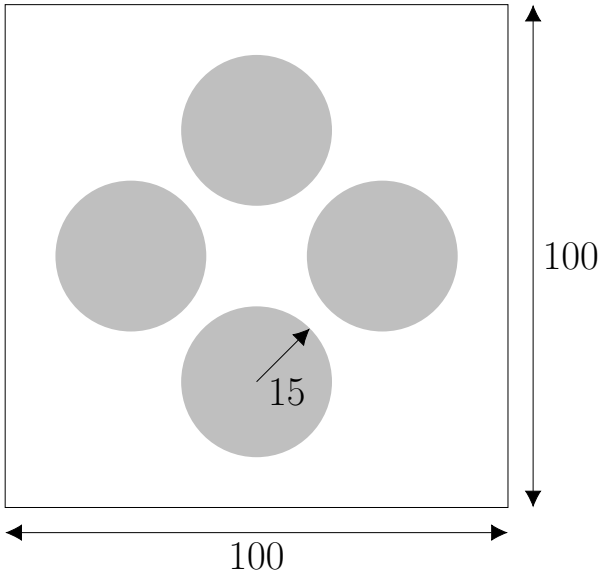

Figure 4.6: Gaussian Vortex: Initial configuration.

field has the following Cartesian components:

$$u(\mathbf{x},t) = -1747\frac{y}{r^2}\cdot\left(1-e^{-\frac{r^2}{\beta^2}}\right)\cdot\cos\left(\frac{\pi t}{T}\right)$$
$$v(\mathbf{x},t) = 1747\frac{x}{r^2}\cdot\left(1-e^{-\frac{r^2}{\beta^2}}\right)\cdot\cos\left(\frac{\pi t}{T}\right)$$

where $r{=}\sqrt{x^2+y^2}$, $\beta{=}22.303$ and $T{=}10$, producing maximum velocity $|\mathbf{u}|_{max}$ value of 50 at $r{=}25$. Four structured meshes of linear triangular elements are employed with element size lengths and time step values of $\left\{\sqrt{2}, 0.005\right\}$, $\left\{\frac{\sqrt{2}}{2}, 0.0025\right\}$, $\left\{\frac{\sqrt{2}}{4}, 0.00125\right\}$ and $\left\{\frac{\sqrt{2}}{8}, 0.000625\right\}$, respectively. Reinitialisation step parameters are $\varepsilon{=}0.83\Delta l$ and $\Delta\tau{=}\alpha\frac{\Delta l^2}{8\varepsilon}$ (dummy time step), where $\alpha{=}0.1$. Simulation stops at the end of a cycle ($t{=}T$).

Results of the experiments for the four grids are summarised in Table 4.6, where first column indicates the method, either NFEM, or NFEM including reinitialisation, or NFEM including reinitialisation and local calculation of normals. Columns two to seven indicate average element side length δ, errors $e(L_1^I)/l$, $e(L_1)$, $e(L_2)$, $|A_{0.5}^e|$ %, and total mass error, respectively. Interface length is computed at initial time and its value is 120π.

As can be expected, errors $e(L_1)$ and $e(L_2)$ diminish when finer meshes are used (Table 4.6) for NFEM solution of transport equation (Figs. 4.7a-4.7h). Convergence order is lower than two mainly due to the presence of several

Table 4.6: Gaussian Vortex. Errors at $t = T$.

Method	Mesh (δ)	$e(L_1^l)/l$	$e(L_1)$	$e(L_2)$	$\lvert A^e_{0.5}\rvert$ [%]	Mass Error
NFEM	$\sqrt{2}$	1.682E-02	1.414E-01	2.329E-01	16.124	4.009E-15
	$\frac{\sqrt{2}}{2}$	8.647E-03	8.280E-02	1.700E-01	7.037	-1.644E-14
	$\frac{\sqrt{2}}{4}$	1.532E-03	4.642E-02	1.208E-01	0.383	-1.481E-13
	$\frac{\sqrt{2}}{8}$	6.068E-04	2.410E-02	8.461E-02	0.145	-8.923E-13
NFEM + Reinitialisation	$\sqrt{2}$	2.684E-02	1.207E-01	2.681E-01	6.197	-5.291E-15
	$\frac{\sqrt{2}}{2}$	1.121E-02	4.894E-02	1.723E-01	1.579	-1.999E-14
	$\frac{\sqrt{2}}{4}$	3.084E-03	1.742E-02	9.116E-02	0.021	-1.653E-13
	$\frac{\sqrt{2}}{8}$	2.926E-04	5.979E-03	4.211E-02	0.000	-7.203E-13
Local Calculation of Normals	$\sqrt{2}$	2.761E-02	1.133E-01	2.792E-01	0.935	3.367E-15
	$\frac{\sqrt{2}}{2}$	1.199E-02	5.199E-02	1.794E-01	1.328	-1.628E-14
	$\frac{\sqrt{2}}{4}$	3.307E-03	1.898E-02	9.430E-02	0.072	-1.669E-13
	$\frac{\sqrt{2}}{8}$	3.046E-04	6.400E-03	4.219E-02	0.017	-1.197E-12

quasi-discontinuities, as in previous experiments. Interface error decreases once mesh is refined but convergence order shows an irregular behaviour as it can be noted if it is compared results of $\delta=\frac{\sqrt{2}}{2}$ and $\delta=\frac{\sqrt{2}}{4}$ with the others. Nevertheless, interface error lessens monotonically when element side length is reduced. A reason of this erratic behaviour arises from the use of the Heaviside function in the error definition. Enclosed volume error oscillates, although it is bounded and decreases with finer meshes. This response is in accordance with discussion in Ref. [60] where enclosed volume error is related with value of ε. Hence enclosed volume error depends on the value of the maximum element size on the interface.

Errors behave in a similar manner when reinitialisation is active (see Fig. 4.8a-4.8h and second row of Table 4.6). Decrease in $e(L_1)$ and $e(L_2)$ is noticeable in fine grids, up to four times. However, reinitialisation process is not efficient for low mesh resolution: reader can observe in Table 4.6 that $e(L_2)$ for the coarsest mesh is higher when reinitialisation is used. Although now interface error is marginally higher for coarse meshes, for the finest mesh this error diminishes substantially. Besides, enclosed volume errors with reinitialisation exhibit values nearly an order of magnitude lower for all the resolutions. This enhancement is due to the artificial compression effect in the reconstruction, reducing extra diffusion originated in the transport step. Local computation of normals does not introduce relevant further amelioration because interfaces are too close, and there are not regions in the vicinity of interfaces with (approximately) constant values of the phase function. Overall results reveal that coarsest mesh ($\delta=\sqrt{2}$) has not sufficient resolution for a competent usage of reinitialisation tools in long term

Table 4.7: Slotted sphere in a rotating flow. Dimensionless interface error $e(L_1^I)/l$, $e(L_1)$, $e(L_2)$, and enclosed volume error $A^e_{0.5}$ [%] after one rotation; $\Delta x/l{=}\delta_{3D}/(l\sqrt{3})$, l: characteristic length of the domain (l=100). Comparison with finite volume method in [29]

Method	$\Delta x/l$	$e(L_1^I)/l$	$e(L_1)$	$e(L_2)$	$\lvert A^e_{0.5}\rvert$ [%]
Present	1.000E-2	2.971E-03	4.473E-03	3.781E-02	5.959
	5.000E-3	5.923E-04	2.048E-03	2.409E-02	1.332
Finite Volume [29]	1.000E-2	3.22E-03	-	-	4.60
	5.000E-3	1.17E-03	-	-	1.32

calculation for this severe test (see Figs. 4.7b and 4.8b). Without reinitialisation, finest resolution is needed ($\delta{=}\sqrt{2}/8$) to avoid spurious coalescence of disks (see Fig. 4.7h). Instead, for NFEM plus reinitialisation, $\delta{=}\sqrt{2}/4$ (see Fig. 4.8f) is enough to prevent merging of disks.

4.1.5 Slotted sphere in a rotating flow

This test is the three-dimensional extension of the slotted cylinder experiment. Here, initial profile is a sphere of radius 15 whose centre is placed at $(0, 25, 0)$ in a $[-50, 50] \times [-50, 50] \times [-50, 50]$ domain. The slot has width 5 and length 25 (see Fig. 4.9). Velocity field $\mathbf{u}{=}(-\omega y, \omega x, 0)$ and reinitialisation parameters are $\varepsilon{=}0.67\Delta l$, $\tau{=}\alpha\frac{\Delta l^2}{8\varepsilon}$, where $\omega{=}0.1$, Δl is the maximum tetrahedral height and $\alpha{=}0.1$. It is employed two structured meshes of linear tetrahedral finite elements with element size lengths δ_{3D} [3] and total number of time steps $\left\{\sqrt{3}, 1030\right\}$ and $\left\{\frac{\sqrt{3}}{2}, 2060\right\}$, respectively. Interface area is $L{\approx}3.9 \cdot 10^3$. Results are shown in Fig. 4.9, while error measures after one rotation are detailed in Table 4.7, whose arrangement is the same as Table 4.2. Results reveal same trends as observed in the two dimensional case. Use of the finest mesh implies errors reduction, significant for interface and enclosed volume errors, and are of the same order of those reported in Ref. [29]. Accuracy of NFEM to preserve slot shape and dimensions shown by NFEM for slotted cylinder is kept for the three dimensional extension (Fig. 4.9).

4.1.6 Sphere in a transient swirling deformation flow

This experiment was proposed by Leveque [45]. A sphere of diameter 30 is placed at initial time with its centre at $(-15, -15, -15)$ in a $[-50, 50] \times$

[3] Element size length in structured three dimensional meshes is $\delta_{3D}{=}\sqrt{\Delta x^2 + \Delta y^2 + \Delta z^2}$, where Δx, Δy and Δz are size lengths of a cube composed by five tetrahedral cells.

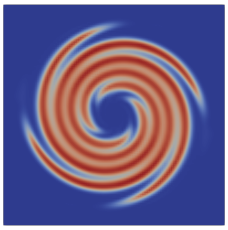

(a) $t{=}T/2$, $\delta{=}\sqrt{2}$

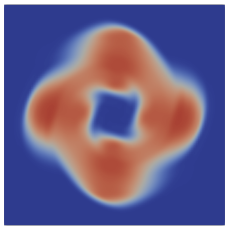

(b) $t{=}T$, $\delta{=}\sqrt{2}$

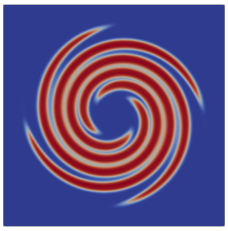

(c) $t{=}T/2$, $\delta{=}\frac{\sqrt{2}}{2}$

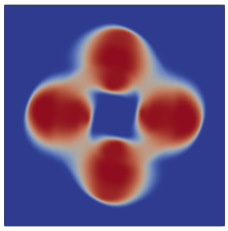

(d) $t{=}T$, $\delta{=}\frac{\sqrt{2}}{2}$

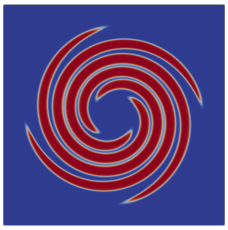

(e) $t{=}T/2$, $\delta{=}\frac{\sqrt{2}}{4}$

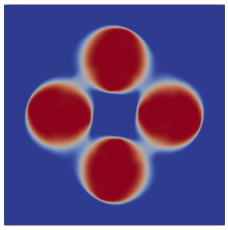

(f) $t{=}T$, $\delta{=}\frac{\sqrt{2}}{4}$

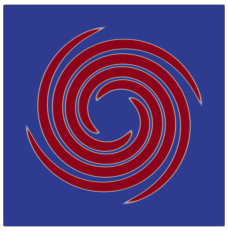

(g) $t{=}T/2$, $\delta{=}\frac{\sqrt{2}}{8}$

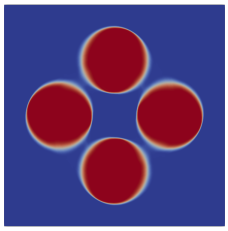

(h) $t = T$, $\delta = \frac{\sqrt{2}}{8}$

Figure 4.7: Gaussian Vortex Test. Phase field ϕ. NFEM results.

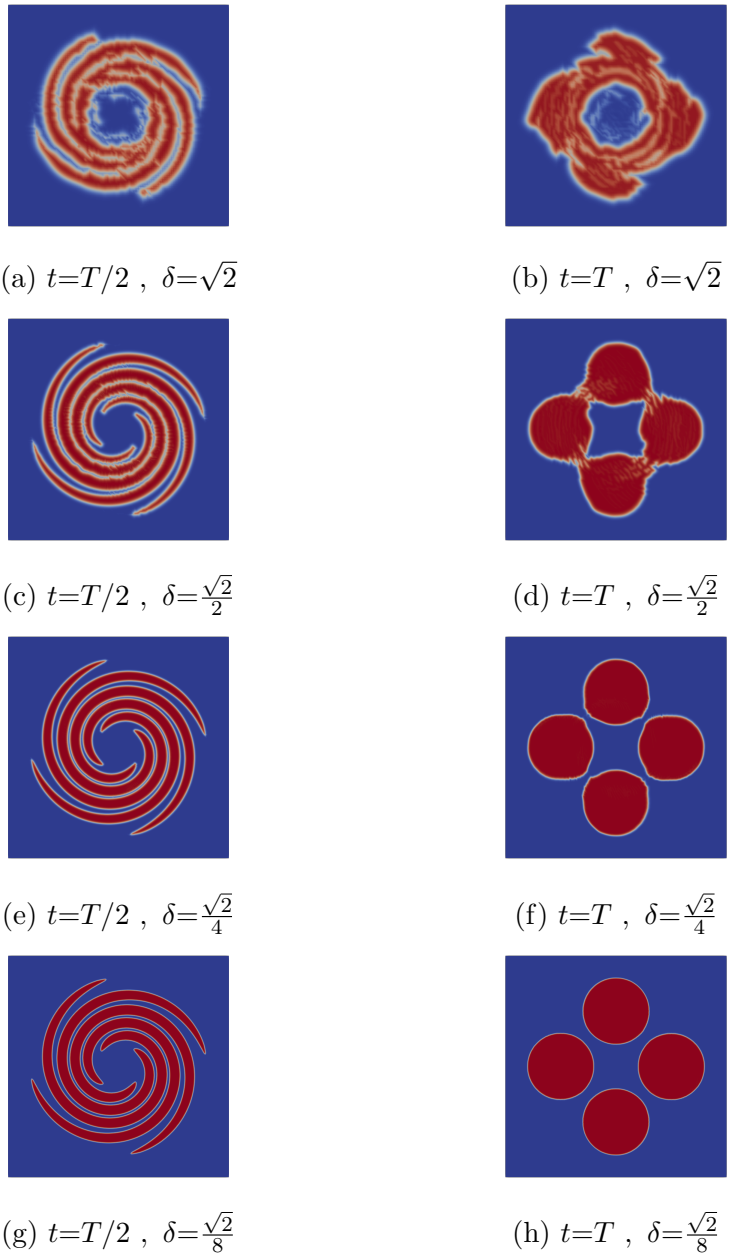

(a) $t{=}T/2$, $\delta{=}\sqrt{2}$ (b) $t{=}T$, $\delta{=}\sqrt{2}$

(c) $t{=}T/2$, $\delta{=}\frac{\sqrt{2}}{2}$ (d) $t{=}T$, $\delta{=}\frac{\sqrt{2}}{2}$

(e) $t{=}T/2$, $\delta{=}\frac{\sqrt{2}}{4}$ (f) $t{=}T$, $\delta{=}\frac{\sqrt{2}}{4}$

(g) $t{=}T/2$, $\delta{=}\frac{\sqrt{2}}{8}$ (h) $t{=}T$, $\delta{=}\frac{\sqrt{2}}{8}$

Figure 4.8: Gaussian Vortex Test. Phase field ϕ. NFEM+Reinitialisation results.

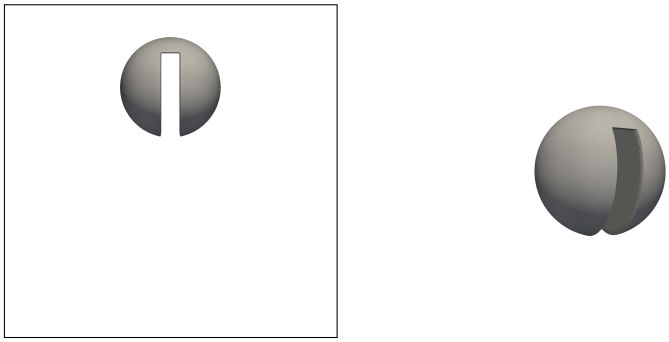

(a) Initial condition

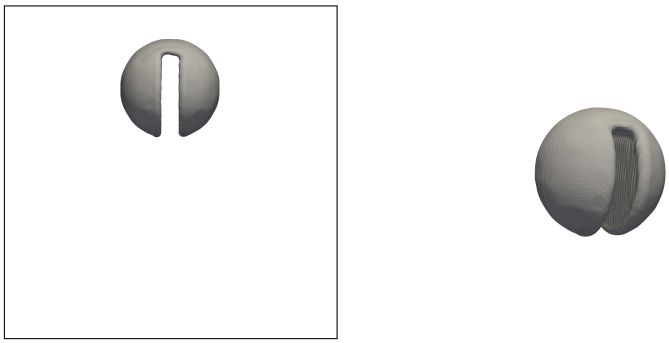

(b) After one rotation

Figure 4.9: Slotted sphere in a rotating flow. Iso-surface ϕ=0.5. δ_{3D}=$\sqrt{3}$/2.

Table 4.8: Sphere in a transient swirling deformation flow. Errors at t=T.

Method	δ_{3D}	$e(L_1^I)/l$	$e(L_1)$	$e(L_2)$	$\lvert A^e_{0.5}\rvert$ [%]
NFEM	$\sqrt{3}$	9.332E-03	9.694E-03	5.632E-02	13.950
	$\frac{2\sqrt{3}}{3}$	5.397E-03	6.826E-03	4.597E-02	5.191
	$\frac{\sqrt{3}}{2}$	3.786E-03	5.338E-03	4.015E-02	2.954
NFEM + Reinitialisation	$\sqrt{3}$	8.995E-03	6.029E-03	4.416E-02	12.238
	$\frac{2\sqrt{3}}{3}$	5.663E-03	4.377E-03	3.603E-02	7.062
	$\frac{\sqrt{3}}{2}$	4.069E-03	3.497E-03	3.093E-02	4.509
Local Calculation of Normals	$\sqrt{3}$	6.729E-03	4.214E-03	3.874E-02	3.849
	$\frac{2\sqrt{3}}{3}$	3.945E-03	2.838E-03	3.059E-02	2.407
	$\frac{\sqrt{3}}{2}$	2.748E-03	2.359E-03	2.582E-02	1.750
Guermond et al., [29]	$\sqrt{3}$	6.943E-02	-	-	4.179
	$\frac{\sqrt{3}}{2}$	6.329E-03	-	-	0.481

$[-50,50]\times[-50,50]$ domain. The periodic advective velocity field has the following Cartesian components

$$u(\mathbf{x},t) = 200\sin\left(\frac{\pi(x+50)}{100}\right)^2\sin\left(\frac{2\pi(y+50)}{100}\right)\sin\left(\frac{2\pi(z+50)}{100}\right)\cos\left(\frac{\pi t}{T}\right),$$

$$v(\mathbf{x},t) = -100\sin\left(\frac{2\pi(x+50)}{100}\right)\sin\left(\frac{\pi(y+50)}{100}\right)^2\sin\left(\frac{2\pi(z+50)}{100}\right)\cos\left(\frac{\pi t}{T}\right),$$

$$w(\mathbf{x},t) = -100\sin\left(\frac{2\pi(x+50)}{100}\right)\sin\left(\frac{2\pi(y+50)}{100}\right)\sin\left(\frac{\pi(z+50)}{100}\right)^2\cos\left(\frac{\pi t}{T}\right),$$

where T=3. The largest deformation of the sphere takes place at t=$T/2$ (Fig. 4.10b), while at t=T the sphere recovers the initial state. It is used three structured meshes of four nodes tetrahedral elements with element size length and time step $\left\{\sqrt{3}, 0.002\right\}$, $\left\{\frac{2\sqrt{3}}{3}, 0.001333\right\}$, and $\left\{\frac{\sqrt{3}}{2}, 0.001\right\}$, respectively. To achieve sufficient resolution of thin filaments, ε=$0.50\Delta l$, and $\Delta\tau$=$\alpha\frac{\Delta l^2}{8\varepsilon}$, where α=0.1. Interface area is L=900π.

Table 4.8 shows errors at t=T, (l=100), with the same arrangement as Table 4.6. Results from Ref. [29] are added, where a modified conservative level set method by antidiffusion techniques has some comparable spatial and temporal discretisation features with the present model. For results given in Ref. [29], the resulting equivalent element size lengths are indicated in second column for a proper comparison, given that discretisations do not match exactly. Reinitialisation diminishes $e(L_1)$ and $e(L_2)$ as in previous tests. Regularisation of normals improves the performance. For instance, with the intermediate mesh (δ_{3D}=$2\sqrt{3}/3$) and local calculation of normals (see Table 4.8, ninth row) results are better than with the fine mesh (δ_{3D}=$\sqrt{3}/2$) with

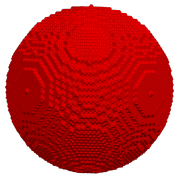

(a) t=0 , δ=$\sqrt{3}$/2.

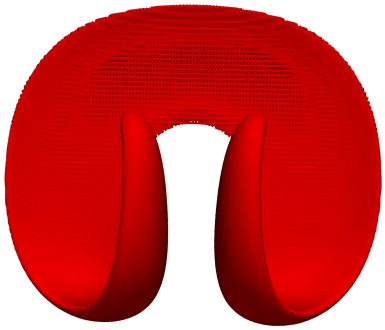

(b) t=T/2 , δ=$\frac{\sqrt{3}}{2}$, with reinitialisation.

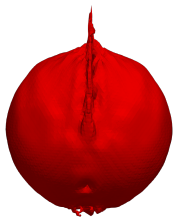

(c) t=T , δ=$\frac{\sqrt{3}}{2}$, with reinitialisation.

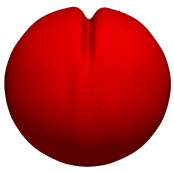

(d) t=T , δ=$\frac{\sqrt{3}}{2}$, without reinitialisation.

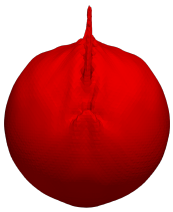

(e) t=T , δ=$\frac{\sqrt{3}}{2}$, improved normals.

Figure 4.10: Sphere in a transient swirling deformation flow. Surface ϕ=1/2. (b) and (c): with reinitialisation. (d) without reinitialisation. (e) local calculation of normals

standard normal usage (see Table 4.8, seventh row). Interface error and enclosed volume error decrease once local calculation of normals is active (see Table 4.8, third, sixth and ninth rows). Besides, this tool reduces $e(L_1)$ and $e(L_2)$ attained by reinitialisation. Sharp interfaces are not as close as in Gaussian Vortex experiment, hence action of normal local calculation avoids the indeterminacy far from the interface in a more efficient way, and reduces wiggles of phase function in the vicinity of interfaces. Interface error is smaller in compare with Ref. [29] for the coarse and intermediate mesh, and results are marginally better for the coarse mesh in terms of enclose volume error. Enclosed volume error diminishes substantially for intermediate mesh and fine mesh, although somewhat higher than finite volume results from Ref. [29]; nevertheless in this test the model reported in [29] does not preserve sign.

To capture the thinnest pattern of the deformed state (Fig. 4.10b) it is necessary the finest mesh. Slight oscillations on the interface (Fig. 4.10c) are significantly reduced by the beneficial effect of local calculation of normals (Fig. 4.10e). Notwithstanding, at the end of the cycle some kind of crest attached to the sphere appears, ascribable to a secondary effect of the reinitialisation, which moves the interface artificially. This anomaly can also be observed in other models (see e.g. Ref. [38]), but was not detected in other experiments of this work. In fact these deviations, as well as wiggles, do not appear for transport equation solution without reconstruction (see Fig. 4.10d).

4.2 Hydrodynamics Assessment Simulations

4.2.1 Rayleigh-Taylor Instability

Present test consists on two fluid layers with the heavier one situated above. Due to gravity action, the heavier fluid penetrates into the lighter one and process continues until lighter fluid is entirely situated above. This experiment has been used in several works (e.g. Ref. [67]) and set-up consists of a domain $[-0.5, 0.5] \times [-2.0, 2.0]$ m^2; $|\mathbf{g}|$=9.81 m/s^2, ρ_1=0.1694 kg/m^3, ρ_2=1.225 kg/m^3, and μ_1=μ_2=3.13·10^{-3} kg/(ms) (see Fig. 4.11). Fluids are considered incompressible with a density ratio ρ_1/ρ_2=0.138 and the average Reynolds number is $\mathcal{R}$=$d\sqrt{dg}/\nu$=698, where d in this case is the channel width, and ν=$(\mu_1+\mu_2)/(\rho_1+\rho_2)$. Position of the interface at t=0 is defined by

$$y = -0.05\cos(2\pi x)\ , \tag{4.3}$$

to introduce a small perturbation in the onset (see Fig. 4.11). Because of the high value of density ratio and the relatively low value of $\mathcal{R}$, CBS technique

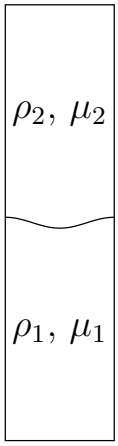

Figure 4.11: Rayleigh-Taylor Instability. Initial condition

can be used without correction to reach a sufficiently accurate solution for hydrodynamics. Parameters for reinitialisation are $\varepsilon = 0.83\Delta l$ and $\Delta\tau = \alpha\frac{\Delta l^2}{8\varepsilon}$, with α=0.1 as in previous tests. Linear triangular structured mesh has $\delta=\frac{\sqrt{2}}{128}$ m, and $\Delta t=10^{-4}$s. Interface has a thickness of $2\Delta x$ at t=0 to attain a better definition of initial perturbation (4.3). To be consistent with preceding reports (e.g. Ref. [9]), slip boundary condition is prescribed on vertical walls and no-slip condition on horizontal walls.

Figure 4.12 illustrates the evolution of the instability. Phase field is represented at t=0.3 s, t=0.6 s, t=0.9 s, and t=1.2 s. At early stages, amplification of initial perturbation is observed (Fig 4.12a). In subsequent states, interface takes a typical mushroom shape (Fig. 4.12b), and then starts to elongate and to form thin filaments which finally detaches, creating isolated filaments and bubbles (Figs. 4.12c and 4.12d). A manifest symmetry is detected in Figures 4.12a, 4.12b and 4.12c, violated at ensuing times by aforementioned thin filaments (see Figure 4.12d, t=1.2 s). Figure 4.13 displays lowest position of the jet, $s(t)$, by the current numerical method, by a numerical solution in Ref. [9], and by the theoretical solution for inviscid flows without surface tension [15],

$$s = s_0 \cosh(\Psi t) \ ,$$
$$\Psi = \sqrt{g\frac{2\pi}{W}\frac{\rho_2-\rho_1}{\rho_2+\rho_1}} \ ,$$

where initial position of the front is denoted as s_0, and its value is 0.05 m. Numerical solution has a close agreement with theoretical solution for inviscid flows at early stages of motion, when non-linearity is weak and perturbation amplitude is much smaller than its wavenumber. In addition, an acceptable

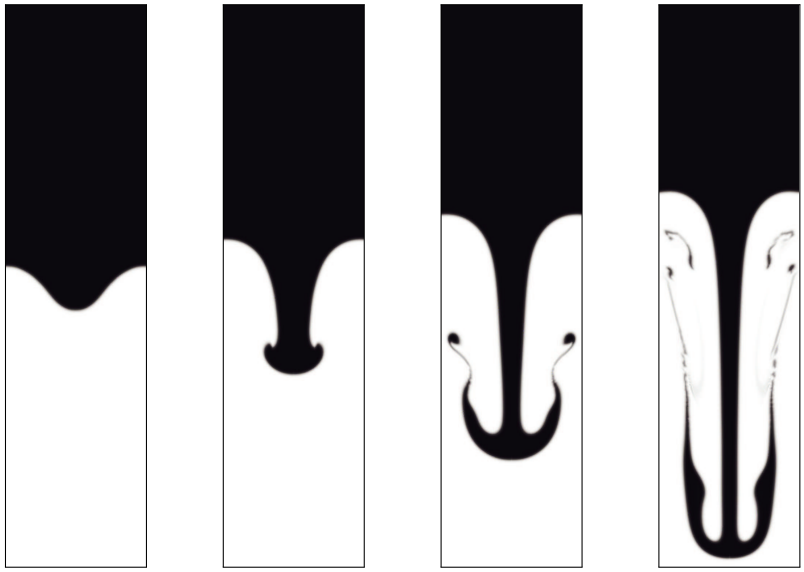

(a) $t = 0.3$s (b) $t = 0.6$s (c) $t = 0.9$s (d) $t = 1.2$s

Figure 4.12: Rayleigh-Taylor Instability. Phase field at different times. Darker shades indicate higher ϕ values

agreement is extended up to $t{\approx}0.3$ s, consistent with the symmetry, still clearly identified. On the other hand, present results match with outcomes of Ref. [9], both in qualitative description (Fig. 4.12), and in quantitative form (Fig. 4.13).

Rayleigh-Taylor instability. Air-helium and xenon-hydrogen interface

In order to show the benefits of the complete method for hydrodynamics as reported in section 3.5, two new combinations of gases are selected such that average Reynolds number increases considerably and density ratio decreases. In addition to new fluid densities, real viscosities are employed, substantially different than values used previously. Although results of this test can only be qualitatively evaluated, it is shown that solutions reported by the method used in previous Rayleigh-Taylor test produces significant momentum transfers between phases, while complete NFEM method for interfaces avoids momentum jumps. It is important to note that in these tests, velocity jumps between phases could be physically meaningful. Purpose of the experiments is to illustrate the efficacy of the method assuming the hypothesis of preceding experiment.

Air-helium and xenon-hydrogen combinations are simulated. Domain is the same as in preceding test for both cases; for air-helium: ρ_1=0.178 kg/m^3,

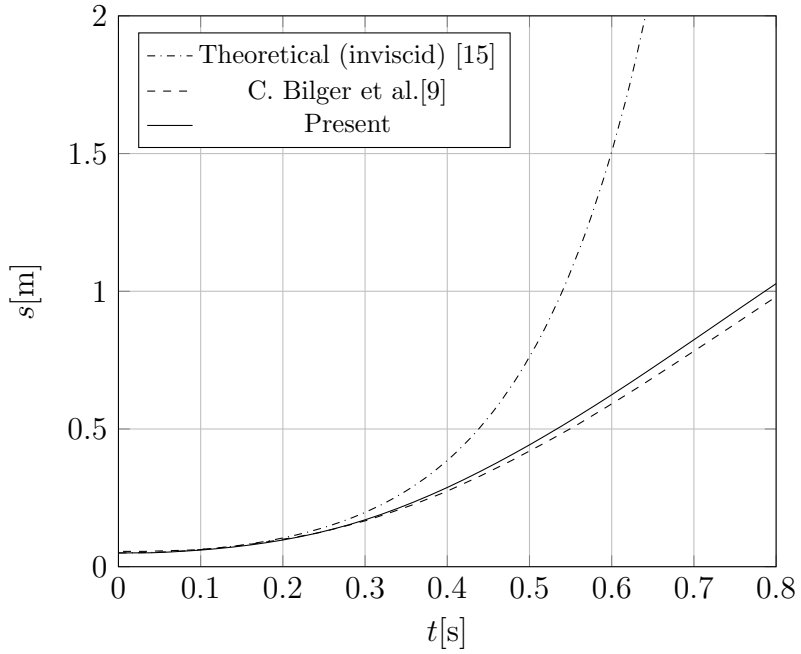

Figure 4.13: Rayleigh-Taylor Instability. Amplitude growth, comparison with theoretical results [15], and with numerical model in [9]

μ_1=1.88·10^{-5} kg/(ms), ρ_2=1.293 kg/m^3, μ_2=1.73·10^{-5} kg/(ms), and $\rho_1/\rho_2 \approx$ 0.178, $\mathcal{R}$=127626. For xenon-hydrogen: ρ_1=0.09 kg/m^3, μ_1=8.4·10^{-6} kg/(ms), ρ_2=5.86 kg/m^3, μ_2=2.12 · 10^{-5} kg/(ms), and $\rho_1/\rho_2 \approx$0.015, $\mathcal{R}$=629593. In both cases, parameters corresponds to absolute temperature value of 273.15 K, and initial interface is given by $y=-0.10\cos(2\pi x)$. Space and time discretisation of first experiment was used.

Secondary vortexes emerge along interface, and symmetry is lost at much earlier stages than foregoing test. Figures 4.14a-4.14f feature the transformation of the instability for air-helium. Subfigures 4.14a and 4.14b depict results by CBS. At t=0.35 s overshoots in velocity field causes severe distortions in the interface (see Fig. 4.14b). At upcoming states, interface spreads completely. Subfigures 4.14c-4.14f show evolution of the interface for t=0.25 s, t=0.50 s, t=0.75 s, and t=1.00 s, respectively, applying the complete algorithm. Velocity jumps are effectively controlled, and experiment remains stable even at very advanced stages, when interface is largely twisted. In the case of xenon-hydrogen, interface descends much faster and its shape tends to change from a mushroom kind to a jet kind[4]. Figures 4.15a-4.15d depict

[4]This regime is frequently characterised by high values of Atwood number. Atwood number is defined as $At=(\rho_2 - \rho_1)/(\rho_2 + \rho_1)$; At(air-helium)=0.76; At(xenon-

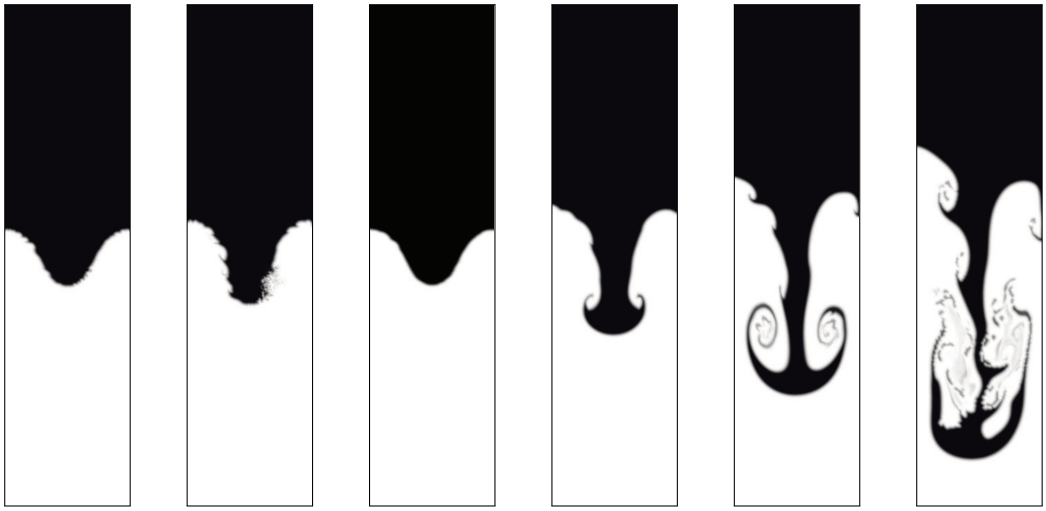

(a) (b) (c) (d) (e) (f)

Figure 4.14: Rayleigh-Taylor Instability for Air-Helium. Comparison between CBS and NFEM. Darker shades indicate higher ϕ values. (a) CBS. t=0.25s; (b) CBS. t=0.35s; (c) NFEM. t=0.25s; (d) t=0.50s; (e) t=0.75s; (f) t=1.00s

evolution of Rayleigh-Taylor instability for xenon-hydrogen by the complete scheme, plotting series of times: t=0.25 s, t=0.50 s, t=0.75 s, and t=1.00 s. In this experiment results from CBS become completely distorted in earlier stages than in preceding combination of gases.

4.2.2 DamBreak problem

The dambreak flow in a horizontal channel is simulated. At initial time, a steady volume of water (ρ_2=998 kg/m^3, μ_2=1.003·10^{-3} kg/(ms)) of height b=0.05715 m and length b (see sketch in Fig. 4.16) is released over a dry channel of length 5b and height 1.25b. Ambient fluid is air (ρ_1=1.205 kg/m^3, μ_1=1.808·10^{-5} kg/(ms)), so density ratio is ρ_1/ρ_2=1.2·10^{-3}. Both fluids are assumed incompressible and surface tension is neglected. Linear triangular structured mesh has $\delta=\frac{1.25\sqrt{2}b}{80}$, and Δt=10^{-4} s. Slip boundary condition is imposed on walls.

Main goal of this simulation is to explore further the answer of the model when density ratio is very low. For this purpose, two options of the model are compared: first option is the complete algorithm, without including the enhanced bound estimation; second option is the complete algorithm includ-

hydrogen)=0.97.

Figure 4.15: Rayleigh-Taylor Instability for Xenon-Hydrogen by NFEM. Darker shades indicate higher ϕ values. (a) t=0.25s; (b) t=0.50s; (c) t=0.75s; (d) t=1.00s

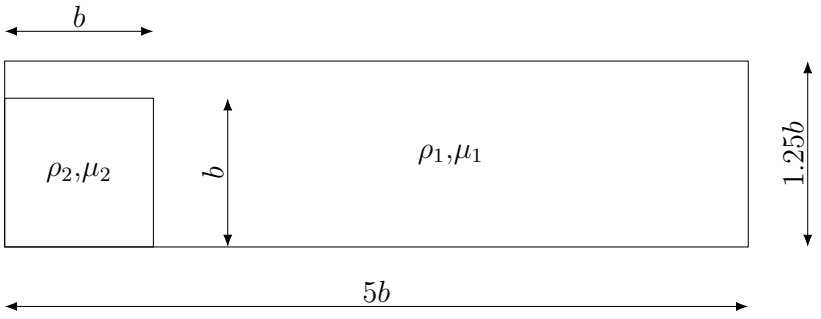

Figure 4.16: Dam Break: initial configuration

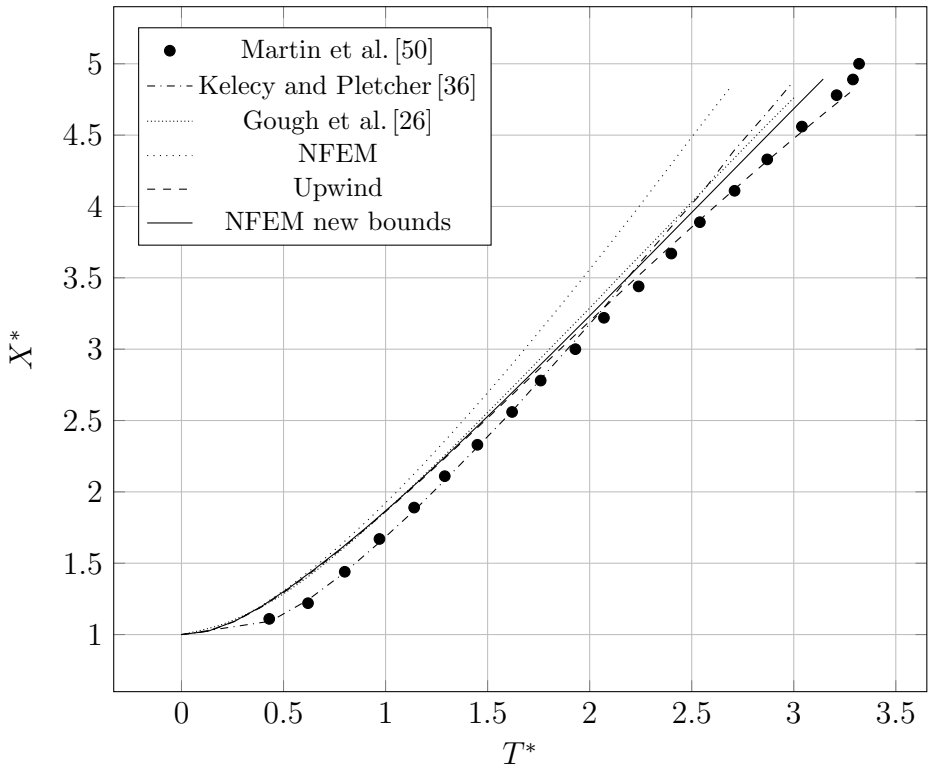

Figure 4.17: Surge front position over time. $T^*=t\sqrt{g/b}$, $X^*=X/b$

ing enhanced bound estimation (Eqs. (3.58) and (3.59)). To illustrate some details of the responses, upwind FEM is also included.

Figures 4.17 and 4.18 depict wave front location measured on bottom wall (X), and height of water on left wall (H), respectively, in terms of time, for the three aforementioned alternatives. In Figs. 4.17 and 4.18 coordinates are dimensionless: time $T^*=t\sqrt{g/b}$, height $H^*=H/b$, and distance $X^*=X/b$, respectively. Moreover, numerical solutions shown in Refs. [26, 36] and experimental results of Ref. [50] are superimposed to present numerics for the three alternatives.

Well-known overdiffusive answer of upwind FEM solution can be verified in Fig. 4.17, by comparing the given wave celerity from $T^*\approx 2$ with experimental data. The NFEM, integrating transport and reinitialisation techniques, has a satisfactory capture of interface, but still have some inadequacies, perceptible in an overestimated celerity value in compare with experimental and other results in the literature (see Fig. 4.17). Deviation is attributed to spurious velocity discontinuities across interface originated during wave propagation. The NFEM is not able to remove completely these accelera-

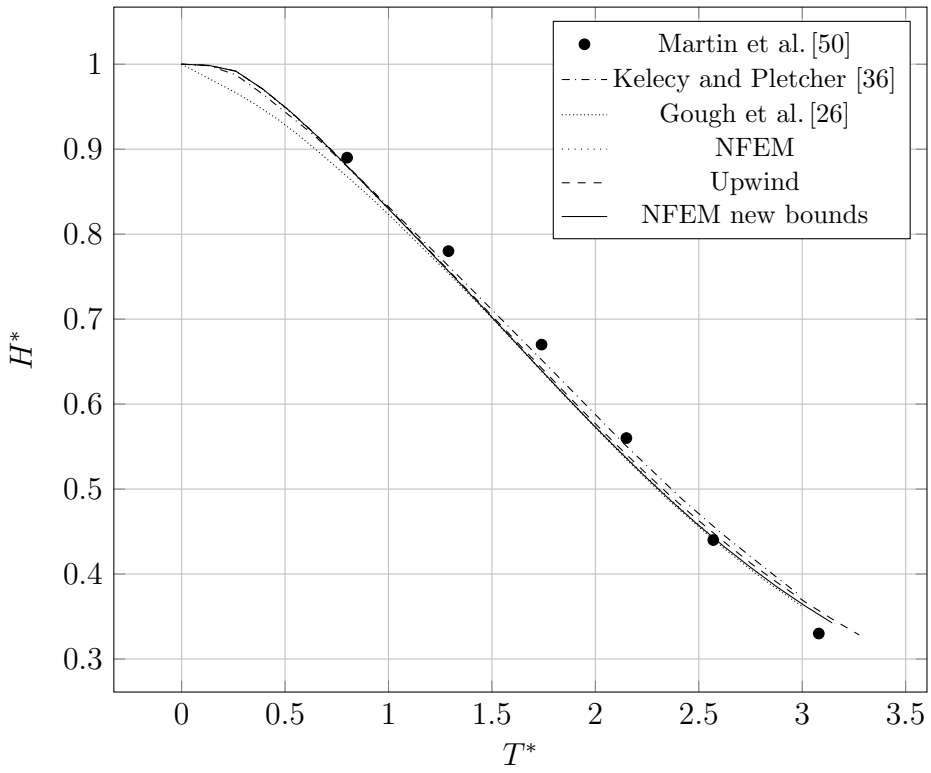

Figure 4.18: Height (left wall) over time. $T^*=t\sqrt{g/b}$, $H^*=H/b$

(a) NFEM. T^*=2.75

(b) Upwind. T^*=2.75

(c) NFEM new bounds. T^*=2.75

(d) NFEM new bounds. T^*=4.26

Figure 4.19: Dam Break problem. Water phase at T^*=2.75 for NFEM, Upwind FEM, and NFEM with new bounds calculation. Water phase at T^*=4.26 for NFEM. Darker shades indicate higher ϕ values

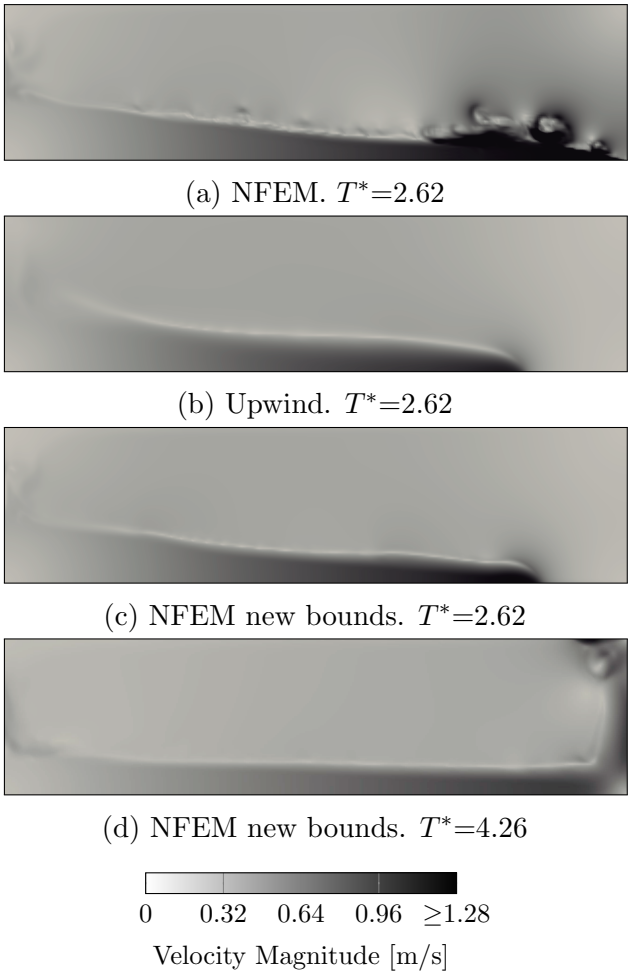

(a) NFEM. T^*=2.62

(b) Upwind. T^*=2.62

(c) NFEM new bounds. T^*=2.62

(d) NFEM new bounds. T^*=4.26

Figure 4.20: Dam Break problem. Velocity field at T^*=2.75 for NFEM, Upwind FEM, and NFEM with new bounds calculation. Velocity field at T^*=4.26 for NFEM with new bounds.

tions for two-phase flows with very low density ratios as in this experiment (see phase function at T^*=2.75 in Fig. 4.19a, and absolute velocity values at T^*=2.62 for NFEM in Fig. 4.20a as illustrations). In particular, Fig. 4.19a shows a shift to the right in front position (compare with other subfigures). Otherwise, results for height evolution of expansion wave on left wall nearly agree with experimental (Fig. 4.18). Once new restrictions are imposed to limiters in NFEM, results in the interface neighbourhood have a significant improvement, resulting in more precise front location (see Fig. 4.17), and in more effective interface capture. Improvements can also be recognised by comparing results in Figs. 4.19c and 4.20c (using NFEM with bounds depending on interface position), with results plotted in Figs. 4.19a and 4.20a, respectively. Figure 4.20a displays a notable pattern of vortexes in air domain initiated by accelerations across interface during propagation, while in Fig. 4.20b, this pattern is completely removed due to diffusion introduced by Upwind FEM. Figure 4.20c shows an enhancement of the good behaviour of upwind FEM in terms of celerity (Figs. 4.19b-4.19c and 4.20b-4.20c) and reveals the close match with experimental data for front position, detected in Fig. 4.17. Slight discrepancies in celerity between laboratory and numerics appear at initial stages (Fig. 4.17), also present in Refs. [26, 19, 20]. In Ref. [19], authors found that this lag diminishes to zero by assigning a high viscosity to the water. Discrepancies are probably ascribed to imprecise front definition during transient states ensued from gate release.

Simulation has been extended to more advanced computational times to prove the ability of the proposed method to model strong interface deformations. Experiment has been extended up to final time T^*=4.26, when water wave reflects on the right wall (see Figs. 4.19d and 4.20d).

To verify the performance of reduced NFEM for Navier-Stokes equations solution discussed in section 3.5, error estimators were computed in the L_2 norm for phase function, pressure, and velocity, and in the L_1 norm for front position. Values are per timestep, and assuming reduced solution as an approximation of complete NFEM solution. Error values are, $e(\phi)$=1.004E-5, $e(p)$=7.38E-4, $e(|\mathbf{u}|)$=1.27E-5, and $e(X)$=1.346E-5, respectively. Moreover, ratio of CPU time between massive computation and reduced is 2.1. These results prove that reduced algorithm gives almost same output that monolithic alternative with half of the computational cost.

4.2.3 Dam Break with Obstacle

This experiment is the three dimensional extension of previous test and was firstly explored by K.M.T. Kleefsman et al. [39]. It is performed in a tank of 3.22m $\times$ 1m $\times$ 1m, where a closed gate retains a steady vol-

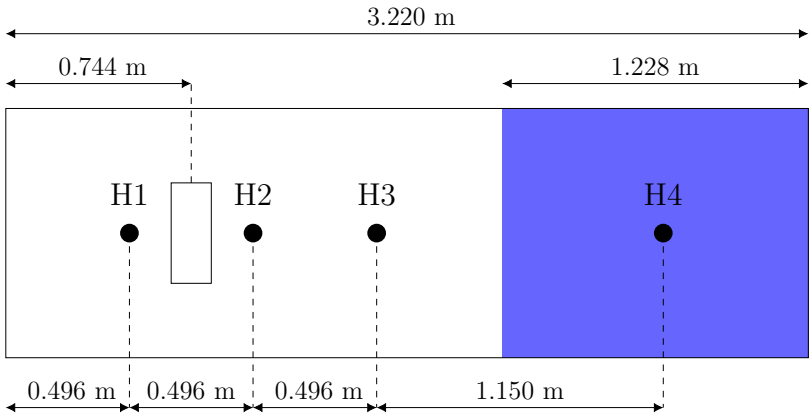

Figure 4.21: Dam break with obstacle. Set up

ume of water of 1.228m × 1m × 0.55m (0.6754 m^3). A fixed brick of size 0.161m × 0.403m × 0.161m is placed with its centroid at 1.248 m downstream of the gate axis. Test starts by releasing the water almost instantaneously. Figures 4.21, 4.22 and 4.23a sketch the geometry and initial condition. Figure 4.21 also indicates as H1, H2, H3, and H4 the positions of height measurements, while Fig. 4.22 depicts the brick and the positions of pressure gauges, indicated as P1 to P8. In the numerical test a structured grid of linear tetrahedrons with 202 × 64 × 63 nodes is employed. Slip boundary condition was prescribed on the boundaries. Time increment is Δt=0.001 s, $\Upsilon=\Delta l/(11\varepsilon)$ and $\varepsilon=0.67\Delta l$. Hence, two levels are used for the computation of regularised normals. Fluids are incompressible with density ratio ρ_1/ρ_2=0.001 and surface tension coefficient σ=0.07 N/m; viscosity ratio value is assumed as μ_1/μ_2=0.01, to be consistent with results of other models (see e.g. Ref. [35]).

Figures 4.23a–4.23e show some interesting snapshots of the simulation at times t=0 (initial), 0.4 s, 0.6 s, 1.1 s and 2.0 s, respectively. In Fig. 4.23b it is seen the propagation of the initial wave over the dry bed before the impact against the brick, while in Fig. 4.23c it is recognised when the discharge overflows the block, and is advancing towards the left wall, reaching it at time of around 0.8 s. After the impact on the left wall the reflected wave travels back and, at the same time, relevant momentum transfer from horizontal to vertical occurs in the obstacle (see Fig. 4.23d). Figure 4.23e depicts backing wave submerging the obstacle at t=2.0 s.

Figures 4.24, 4.25, 4.26, 4.27, 4.28 and 4.29 plot the history $p(t)$ (pressure) at the points P1, P3, P5, and P7, and the history $h(t)$ (height of water) at the points H2 and H4, respectively, for experimental measurements and computed values. First pressure peak at point P1 is accurately captured in

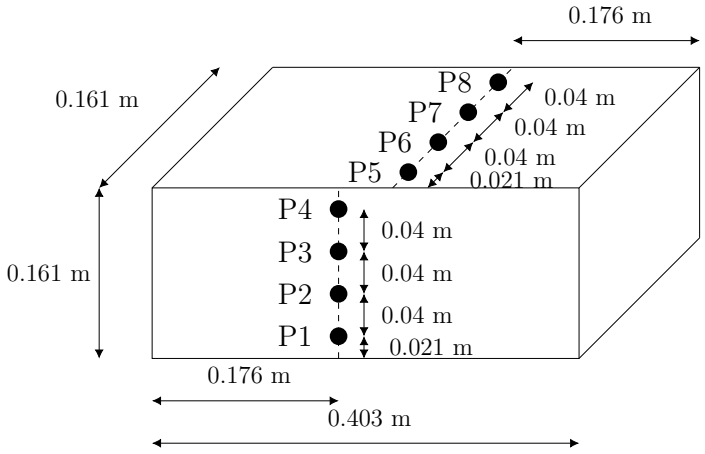

Figure 4.22: Dam break with obstacle. Geometry of the obstacle

phase and amplitude (Fig. 4.24). Pressure computation at point P3 is also very precise in phase, but amplitude is somewhat underpredicted, mainly due to limitation of the grid resolution to simulate a proper momentum transfer from horizontal to vertical in the vicinity of the brick wall. It is interesting to note that this reduction of pressure is also observed in other works (e.g. Refs. [39, 35]). Computation matches with experimental for P1 and P3 up to t=4.5s, covering a complete travel of primary and secondary waves, and a relevant part of the second travel after reflection on the right wall. A small delay appears in the second impact ($t\approx$5 s) (as in models referenced above); despite this fact, amplitude is again well captured. Pressure computations over the brick (points P5 and P7, see Figs. 4.26, 4.27) are adequate, although the first peak is slightly overpredicted. However, at the top of the obstacle an intense mixing of water/air occurs, yielding a foreseeable detachment of numerical calculations from local pressure measurements. Some oscillations in the pressure, existing in the physics (see Figs. 4.26 and 4.27), and in water heights (Fig. 4.28) are amplified to a limited degree by the numerical solution. These deviations from real oscillations are attributed to an insufficient interface resolution in the vicinity of the obstacle, where also an intense and diffuse water/air mixing occurs when water collides the brick (see e.g. Fig. 4.23e). In the case of measurement points P5 and P7, the vortex shedding created on the brick edge also contributes to spread water in the vicinity of the brick.

Water height results show good agreement with measurements in terms of celerity of the wave travelling on a dry bed (first peak is again precisely caught (see Fig. 4.28)), and in terms of elevations in the expansion wave region (see Fig. 4.29). Peaks are very accurately detected in the first travel.

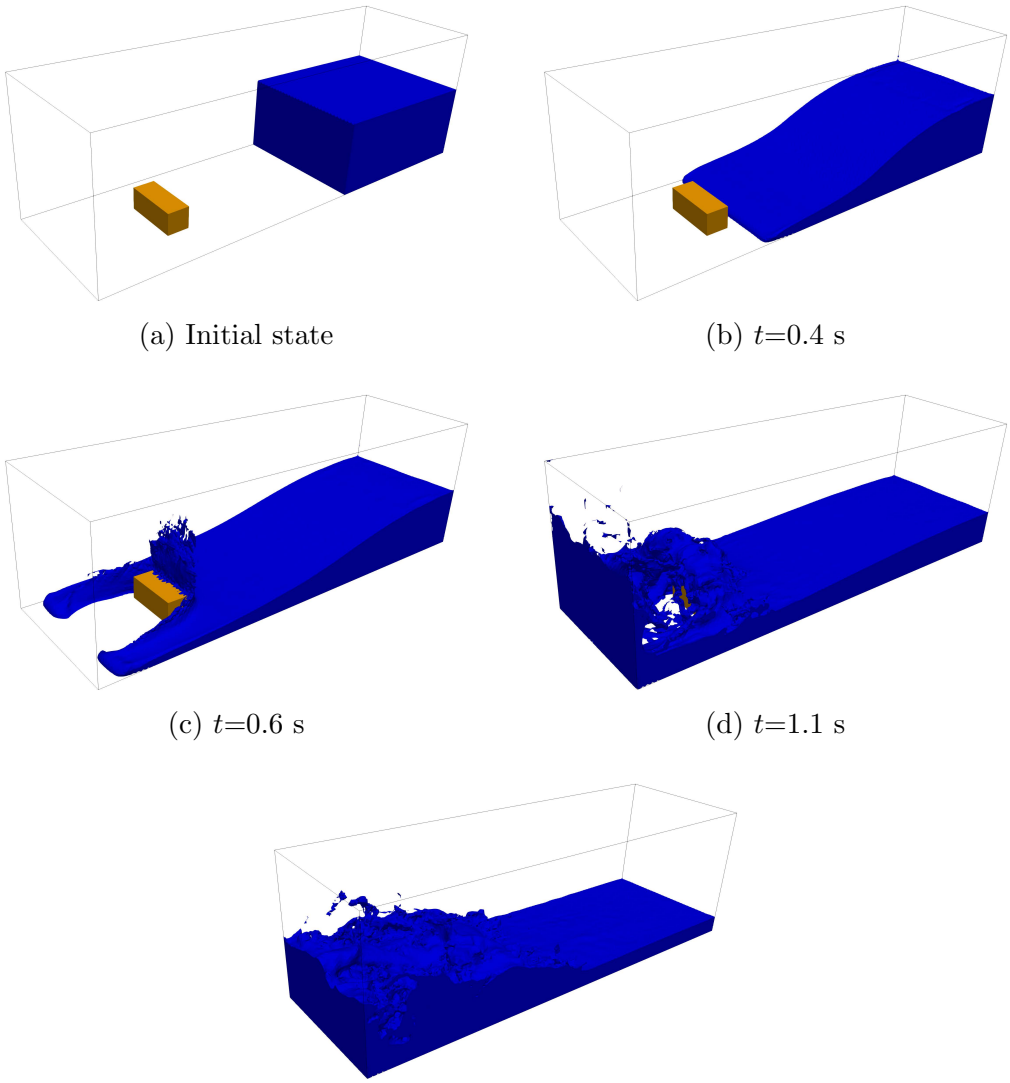

(a) Initial state

(b) t=0.4 s

(c) t=0.6 s

(d) t=1.1 s

(e) t=2.0 s

Figure 4.23: Dam break with obstacle

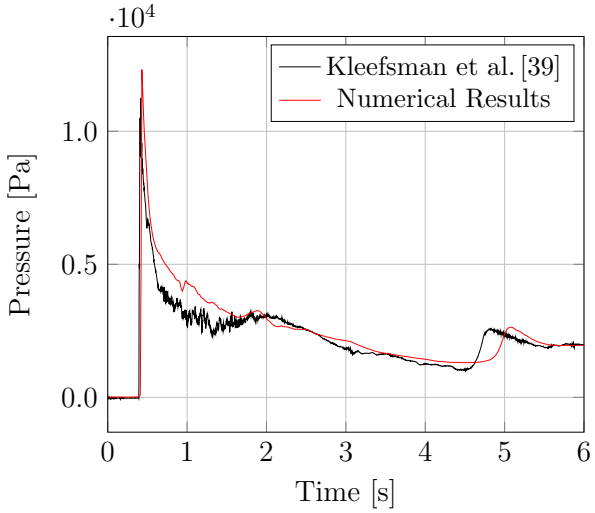

Figure 4.24: Dambreak with obstacle. Pressure at P1

Of course, a small delay in the second peak appears, consistent with pressure outputs. Reader can observe the good capture of the returning wave front at H4 (at around t=2.7 s) in Fig. 4.29. Water heights computed by a NFEM depth integrated model [63] are remarkable close (see output in [62], pp 66-67). Nevertheless, although some phase and amplitude errors at peaks are lower, pressure computation is not sufficiently accurate in the neighbourhood of the block for the depth integrated model, as might be expected.

4.3 Intrusion and Propagation of Air Cavities and Geysering

4.3.1 Air cavities in horizontal ducts

Aim of present and next section is to report the simulation of air cavities intrusion and propagation, comparing numerical results with existing laboratory observations and scrutinising effects of surface tension and interface refinement on outputs. First, special cases with horizontal ducts are examined. Numerical domain is the same as in section 4.3.3 (see Fig. 4.35) but inlet velocity at left boundary is set to zero and chamber is slightly shifted downward. As in previous test, duct is filled with water and gate is locked as initial conditions. At t=0, gate is suddenly unlocked up to a partial opening by moving it down. Then water starts to drain and air fills the evacuated water volume. Both fluids are assumed incompressible, ρ_1/ρ_2=0.001, μ_1/μ_2=0.01, $|\mathbf{g}|$=9.81 m/s^2, and σ=0.07 N/m. Tests were conducted for gate

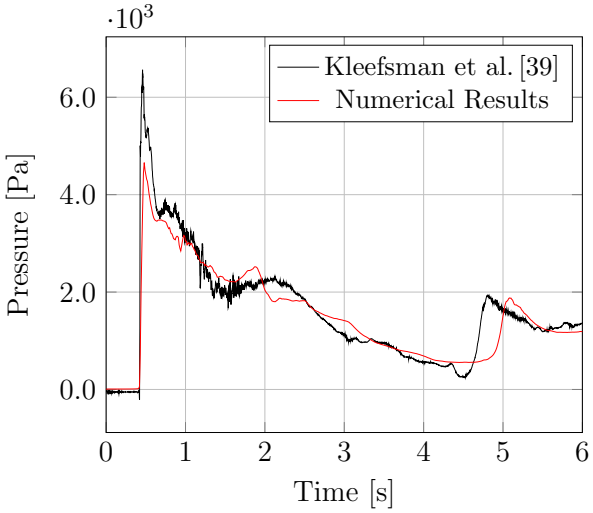

Figure 4.25: Dambreak with obstacle. Pressure at P3

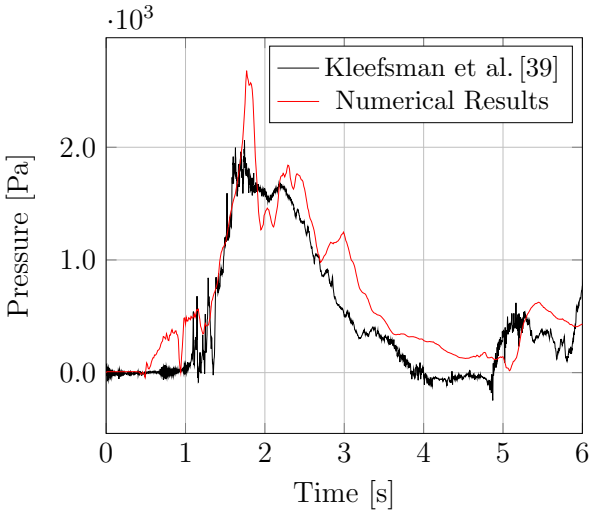

Figure 4.26: Dambreak with obstacle. Pressure at P5

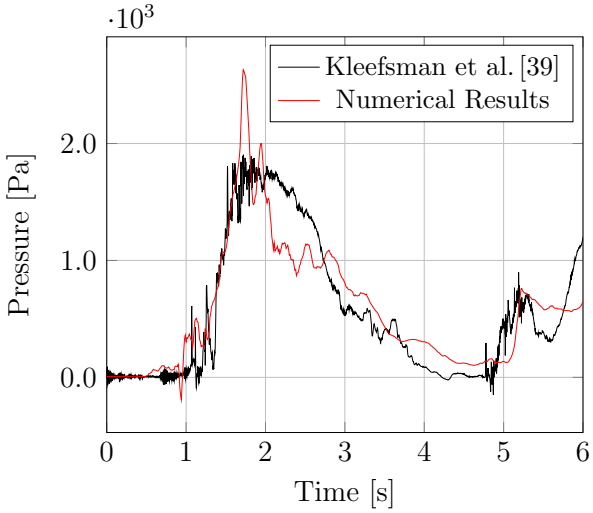

Figure 4.27: Dambreak with obstacle. Pressure at P7

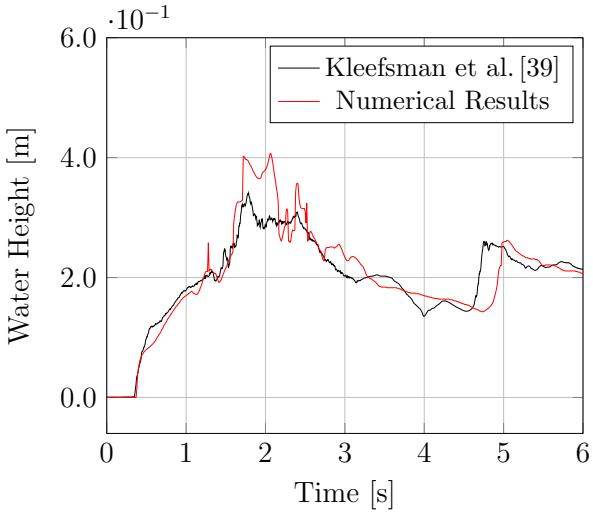

Figure 4.28: Dambreak with obstacle. Water height at H2

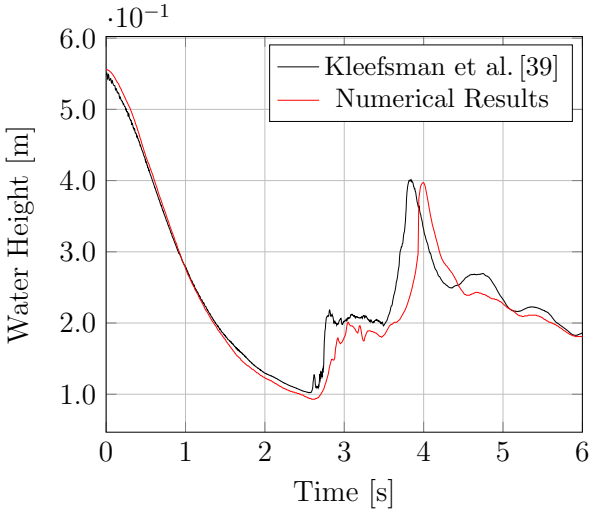

Figure 4.29: Dambreak with obstacle. Water height at H4

heights w/d=0, 0.2, 0.3, 0.4, 0.5, 0.6 and 0.7. Average element length for the grid in the series is δ=0.002$\sqrt{2}$ m and Δt=1.0 $\cdot$ 10^{-4} s. Simulations stop at 3 s. Reinitialisation parameters are ε=0.83Δl and $\Delta\tau$=0.1$\Delta l^2/(8\varepsilon)$.

When the gate is partially closed, a bore is developed downwind the front of the cavity (see e.g. Fig. 4.30). Cases considered in numerical tests, in section 2.1, and in the laboratory [81], have a bore formation with low (supercritical) Froude number, with jumps going from prejump type, to undular type and to transition regime. For these Froude number ranges, free surface in the subcritical region is highly oscillating. These oscillations can be artificially amplified as it was explained in section 3.6. However, grids do not include interface refinement because surface tension is sufficient to obtain a stable free surface (see illustration in Fig. 4.30). Surface tension can reduce cavity celerity and can affect slightly the shape of the front (see e.g. Ref. [81] and references therein), but its overall impact is not significant. The resolution parameter is chosen with the value Υ=$\Delta l/(30\varepsilon)$. Very low values of Υ originate an overestimation of bore celerity. Nevertheless, cavity celerity appears to be independent of resolution parameter. This is probably due to the behaviour of the cavity in the supercritical region, close to a potential flow.

Figure 4.31 depicts normalised cavity celerity F=$c/\sqrt{gd}$, where c is the cavity celerity, and normalised bore celerity F_b=$c_b/\sqrt{gd}$, where c_b is the bore celerity, in terms of downstream water depth ratio H_2=h_2/d; the depth h_2 is measured downstream the bore. Black marks indicate experimental measurements in Ref. [81], and red marks indicate numerical output; cross sign

(a) Without Surface Tension

(b) With Surface Tension

Figure 4.30: Air cavity simulation for an horizontal duct with w=0.5d. Phase function at t=3 s.

corresponds to bore celerity, while circle sign corresponds to cavity celerity. Finally, solid line represents the historical theoretical results by Benjamin [8], and dashed lines represent theoretical results in Ref. [81], taking into account surface tension and stagnation point position effects. Cavity front location and bore location were tracked each 0.5 s in the interval $[0, 3]$ s. Discrepancies between experimental results and numerics are small for values of bore celerity. Numerical results are slightly higher than measurements, but these differences are always less than 5% when compared with laboratory results. Besides, for unsteady regime (i.e. when bore and cavity have different celerities), bore celerity model results are in good agreement with measurements.

4.3.2 Air cavities in sloping ducts

Two series of experiments for ducts with slope and partial opening of the final gate are conducted. First series is defined by w/d=0.2, 0.3, 0.4, and slopes 2%, 5% and 7%; second series is defined by w/d=0.5, 0.6, 0.7, and slopes 1%, 2% and 3%. For the second series, interface is close to the top of the pipe and high air velocity yields very unstable interfaces. For both situations, Υ=$\Delta l/(300\varepsilon)$ and local mesh refinement is implemented. Figure 4.32 illustrates the effect of reducing interface thickness by refinement. Without refinement, a fictitious sealing of the cavity takes place due to nonphysical amplification of perturbations along the free surface; sealing does not occur in laboratory experiments for this set-up (see Ref. [1]). In this experiment, mesh is updated every two time steps on average, and the extra cost value is of around 30% with respect to the experiments with same grid and without adaptivity.

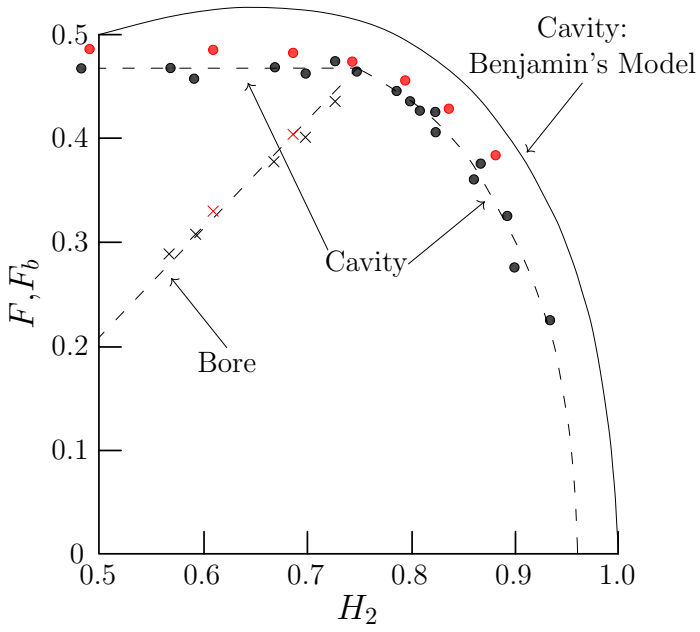

Figure 4.31: Cavity and bore normalised celerities as function of downstream water depth ratio. Red marks: numerical results; black marks: experimental [81]. Solid line: theoretical [8]; dashed line: theoretical [81]. $F{=}c/\sqrt{gd}$, $F_b{=}c_b/\sqrt{gd}$, $H_2{=}h_2/d$, c_b is the bore celerity and h_2 is the flow depth downstream the bore.

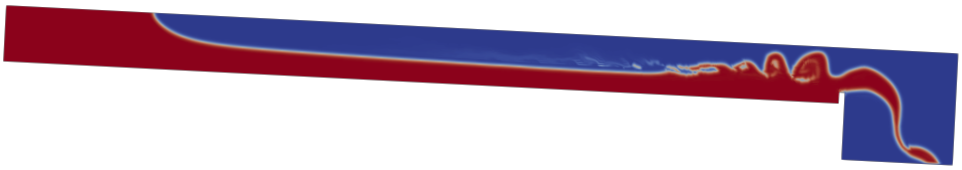

(a) Without interface refinement

(b) With interface refinement

Figure 4.32: Air cavity simulation results for a duct with 5% slope and w=0.2d. Phase function at t=2.5 s.

Numerical and experimental results are shown in Fig. 4.33. Black colour indicates laboratory output, circles mark when sealing does not occur, while squares and crosses mean that cavity seals at irregular or regular intervals, respectively. Red denotes numerics, crosses denote cavity sealing, and circles denote open cavity. A special experiment is pointed out by diamond sign. In this case, a splash of water touches the top of the duct, occurring just after state depicted in Fig. 4.34a. Though resulting air bag is isolated from atmosphere, it cannot be considered as a meta-stable state. Triangles show those cases in which the bore advances away the outflow end of the conduit. Here, downstream flow depths continue to rise (see Fig. 4.34b). Although duct length is not long enough to capture the sealing for configurations denoted by the triangles, sealing occurrence is assured for longer ducts. Finally, dotted black line in Fig. 4.33 is an interpolation of both experimental and numerical outputs. Line displays limiting conditions for sealing in terms of gate opening and slope. Expression of previous interpolation is $(w/d)_L = 0.435 \cdot \theta_d^{-0.405}$, where $(w/d)_L$ indicates the limit weir height that produces a cavity sealing and $\theta_d \in [0.15^o, 4.0^o]$ (in degrees). It is noted that numerical results for sealing development are fairly close to those observed in the laboratory.

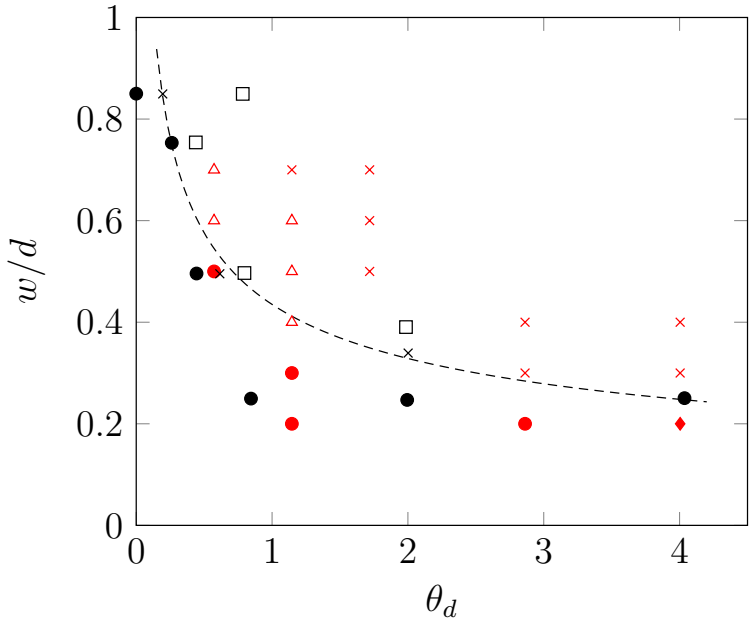

Figure 4.33: Cavity sealing as function of w/d and slope θ_d (in degrees). Comparison between experimental output [1] (black marks) and numerical results (red marks).

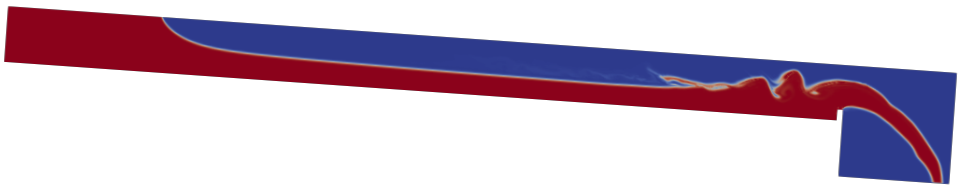

(a) Air cavity simulation results for a duct with 7% slope and w=0.2d. Phase function at t=2.45 s.

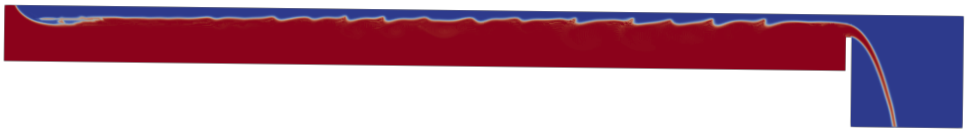

(b) Air cavity simulation results for a duct with 1% slope and w=0.6d. Phase function at t=3.45 s.

Figure 4.34: Air cavity simulation results for a duct with 7% slope and 1% slope

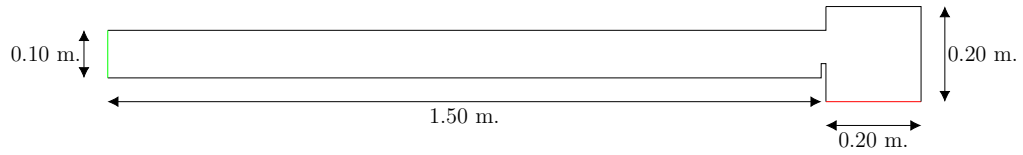

Figure 4.35: Domain for air cavities simulations. Black colour boundary: slip condition; green colour boundary: inlet condition; red colour boundary: inlet/outlet condition.

4.3.3 Air cavities intrusion conditions

Intrusion of air cavities in ducts is a phenomenon deeply studied during last years (see e.g. Ref. [8, 81, 1]); however, fluid inside the duct is normally considered at rest when air propagates. Although these configurations are beneficial to compare analytical and numerical results with laboratory observations, they do not consider cases imitating real floods. Here it is taken into consideration these real states by regarding a downward fluid flow while air cavity intrudes, and flow conditions under which air is not allowed to enter inside the conduit are explored.

For this purpose, a series of tests is conducted with the numerical model reported in Chapter 3. The domain consists of a rectangular duct of length 1.50 m and height d=0.10 m, a gate of variable height situated at the lower end, and a chamber of 0.20×0.20 m placed after the weir to drain the water (see Fig. 4.35). Water and air are assumed nearly-incompressible, air has ρ_1=1.205 kg/m^3, μ_1=1.808 $\cdot$ 10^{-5} kg/ms and a_1^2=1.0 $\cdot$ 10^5 m^2/s^2, whereas physical parameters of water are ρ_2=998 kg/m^3, μ_2=1.0$\cdot$10^{-3} kg/ms and a_2^2=2.2 $\cdot$ 10^6 m^2/s^2. Besides, gravity $|\mathbf{g}|$=9.81 m/s^2 and surface tension parameter σ=0.07 N/m. The structured linear triangular finite element grid has an average element length δ=1.67$\sqrt{2}\cdot 10^{-3}$ m; and time step $\Delta t \in [1\cdot10^{-4}, 1\cdot10^{-5}]$ s, depending on each case. Reinitialisation parameters are ε=0.83Δl and $\Delta\tau$=0.1$\Delta l^2/(8\varepsilon)$, and Υ=$\Delta l/(600\varepsilon)$. Regarding boundary conditions, slip condition is applied on solid walls (black in Fig. 4.35). On inlet/outlet boundary (red in Fig. 4.35) velocity is free, p=0, $\frac{\partial p}{\partial \mathbf{n}_b}$=0, and ϕ=0; hence, water can drain and, if $\mathbf{u}\cdot\mathbf{n}_b < 0$, air flows into the domain. Phase function ϕ=1, $\frac{\partial p}{\partial \mathbf{n}_b}$=0 and velocity is prescribed on inlet boundary (green in Fig. 4.35) to reproduce water inflow. As initial condition, duct is filled up with still water in all cases. Simulations are specified by varying weir height w and the duct slope θ_d. For each pair w,θ_d several inlet velocities are tested during a computational time of 3 seconds. To calculate the threshold inflow velocity u_L from which air does not enter in the duct, the strategy is as follows: first, selection of those simulations such that air is present inside the

duct at last time step; second, calculation of mean gas inflow rate over the whole computational time; third, computation of inlet velocity limit value for which gas inflow rate is zero by linear regressions (a sound method, based on test comparisons). Experiments were performed for $w/d = 0.0$, 0.1, 0.2, 0.3, 0.4, 0.5, 0.6, 0.7; and slopes $\theta_d = 2\%$, 5%, 7%, 10%, 14%.

Results are shown in Fig. 4.36, where non-dimensional inflow velocity limit value is represented as function of weir height w/d for the slopes selected. As can be seen, duct slope has a very limited influence over u_L for moderate slopes ($\theta_d \leq 14\%$). Analytical solutions of cavity and bore propagation celerities in stagnant fluid are reported section 2.1; these solutions can be recalculated in a simple manner in case of an existing uniform liquid flow in the conduit with average velocity u_w. Results indicate that, if flow velocity equals analytical cavity celerity in stagnant fluids, u_w=c, where c=$0.464\sqrt{gd}$ (see Ref. [81]), then air pocket does not propagate inside the duct. This straightforward theory is only valid for low weir heights (see red line in Fig. 4.36 representing simplified theory, and compare it with numerical (points)). For weirs in higher positions (w/d >0.1), limit inflow velocity is determined by the flow rate for which the duct is able to drain, assuming that water level is touching the upper wall. This value is calculated as,

$$q = \frac{2}{3} C_q \sqrt{2g}\,(d-w)^{3/2}\ , \tag{4.4}$$

where q is the flow rate per unit width and C_q is the discharge constant. Hence, if $u_w \cdot d \geq q$, air flow rate is zero, so non-dimensional limit velocity is determined as

$$u_L/\sqrt{gd} = \frac{2}{3} C_q \sqrt{2}(1-w/d)^{3/2}\,. \tag{4.5}$$

Equation (4.5) is plot in Fig. 4.36 as the orange curve, with C_q=0.611. It is apparent that numerical model accommodates accurately to solutions for the whole range of weir openings.

4.3.4 Bubble rising in a vertical duct

The dynamics of free surface ascension of large air bubbles along a vertical duct requires a three-dimensional simulations. In Refs. [21, 25] authors substantiate this requisite by computing the non-dimensional rising velocity of purely inertial Taylor bubbles for plane and axisymmetric cases. Results reveal a significant difference between both premises: values of velocities are $w_b/\sqrt{gd}$=0.240 for plane bubbles, and 0.345 for axisymmetric ones, much closer to experimental observations; w_b is the rising velocity and d is the vertical duct diameter (axisymmetric case) or the distance between parallel

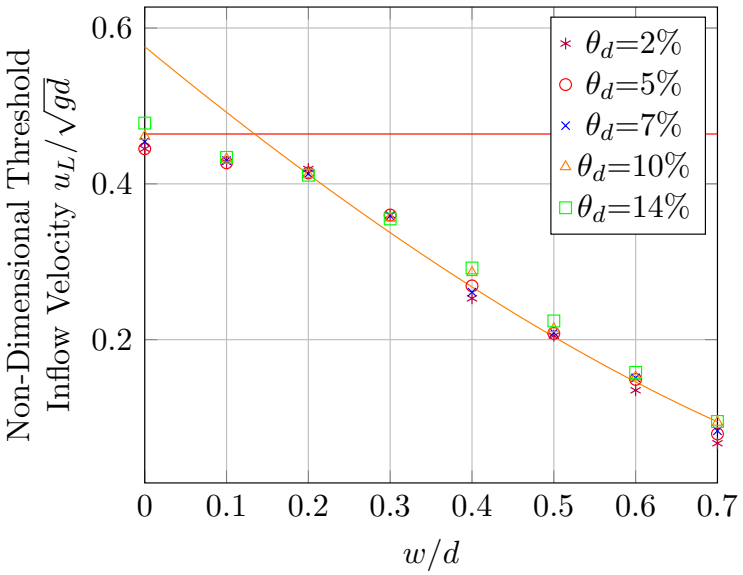

Figure 4.36: Inflow velocity limit value as a function of weir height w and slope θ_d. Red line is the velocity of a cavity unaffected by the bore (see Ref. [81]). Orange line is $u_L/\sqrt{gd} = 0.611 \cdot \frac{2}{3} \cdot \sqrt{2} \cdot (1 - w/d)^{3/2}$.

planes (planar case). This test focuses on the coupling of the bubble head and the free surface progression, without the need of details in geometrical features of the bubble provided by the full three-dimensional procedure. Hence, problem is assumed as axisymmetric and numerical model outlined in Appendix F is applied. Nevertheless, for completeness, a full 3D case of the problem has been performed and discussed at the end of this chapter.

As it was stated in section 1.2, bubble dynamics is mainly governed by three elements, the imbalance between air pressure and water column height, the water film attached to the duct wall, and the air compression/expansion due to the surrounding water [79]. To simulate adequately internal air pressure, compressible model is activated. If the model operates on the assumption that fluids are incompressible, initial air pressure is automatically overwritten by hydrostatic pressure of the liquid phase, and the bubble acquires a low rising velocity because air expansion is not taken into account. Thus free surface keeps nearly static as a consequence of the resulting weak momentum transfer, contradicting laboratory and in-situ observations.

Now, the experiment of Ref.[79] (also used in section 2.2.3) is reproduced by the numerical model. Experiment consists of a vertical tube of diameter d=0.057 m and length L_d=0.610 m connected below to an horizontal duct of 0.094 m diameter. The initial time is considered when air reaches entrance of

the vertical pipe (zero height). At this initial stage, vertical duct is filled of water up to a height of 0.254 m, while horizontal duct is filled with air with a relative pressure of 2452.5 Pa (0.25 meters of water column). The test is repeated three times in the laboratory. Numerical domain for this simulation is depicted in Fig. 4.37. It has two chambers, the upper one allows air to enter and leave the vertical duct, and the lower one contains necessary gas to originate the air bubble. Lower chamber has a height of 0.1 m. Although this value is close to the diameter of the horizontal tube in the laboratory experiment, it is not relevant to the test to replicate exactly laboratory size of the horizontal tube, as long as air mass is approximately the same as laboratory set-up. Initial conditions for the simulation are established as follows. Water reaches level z=0.254 m, and lower water/air interface is an arch of circle with radius of 0.07 m and its centre situated at z=-0.055 m. This shape is imposed to help bubble genesis, avoiding indeterminacy at initial steps. Reference densities are ρ_1=1.225 kg/m^3, ρ_2=1000 kg/m^3, viscosities are μ_1=$1.8 \cdot 10^{-5}$ kg/(ms), μ_2=$1 \cdot 10^{-3}$ kg/(ms), surface tension coefficient is σ=0.07 N/m, and $|\mathbf{g}|$=9.81 m/s^2. Celerity values are a_1^2=$1.0 \cdot 10^5$ m^2/s^2 and a_2^2=$2.2 \cdot 10^6$ m^2/s^2. It is employed a structured mesh with δ=$1.14 \cdot 10^{-3}\sqrt{2}$ m and a time step Δt=$1.25 \cdot 10^{-5}$ s. Reinitialisation parameters are ε=$0.83\Delta l$ and $\Delta\tau$=$0.1\Delta l^2/(8\varepsilon)$, and Υ=$\Delta l/(1200\varepsilon)$. This value of Υ proves to be adequate to alleviate spurious momentum transfers between air and the thin water layer attached to the vertical duct wall. Boundary marked with red in Fig. 4.37 has inlet/outlet boundary condition, as described in previous sections; remaining boundaries have slip condition. No additional conditions are necessary for boundaries coinciding with axisymmetry axis.

Numerical, analytical and experimental non-dimensional results for the three runs are superimposed on Fig. 4.38. Figure depicts history of bubble head position h_b (Fig. 4.38a), free surface height h_{fs} (Fig. 4.38b), and bubble pressure h_p (measured in height of water column) (Fig. 4.38c), where $\{h_b^*, h_{fs}^*, h_p^*\}$=$\{h_b, h_{fs}, h_p\}/L_d$, and t^*=$t\sqrt{gd}/L_d$. There are appreciable differences among laboratory series due to fluctuations in the valve opening at early stages of experiments. After initial transients during bubble formation, numerical output shows a quasi-constant bubble celerity, with a good agreement with the three laboratory series (Fig. 4.38a). Experimental tests also evince a strong dependency of free surface vertical displacement on initial conditions, particularly on the phase of its oscillations. This uncertainty makes difficult a proper comparison with numerics. Nevertheless free surface numerical solutions show a proper capture of its history, coinciding almost always with Run 3 (Fig. 4.38b). Furthermore, bubble release in the laboratory is consequential in inner bubble pressure fluctuations [79]. Fluctuations are visible in model results (Fig. 4.38c), suggesting a realistic coupling between

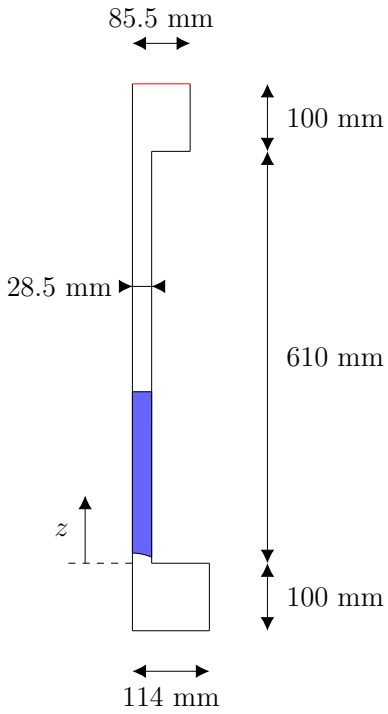

Figure 4.37: Geysering Test. Sketch and dimensions

fluids due to the weakly compressible premise. Numerical results are again in the range of experimental results. Analytical results also match well with numerical and laboratory outputs, although it indicates a slight underprediction in bubble celerity and free surface position. Conversely, theoretical pressure values are in the range of laboratory data.

4.3.5 Two bubbles rising in a vertical duct

Now the semi-analytical approach for multiple bubbles dynamics (see Section 2.2.4) is assessed by comparing it with the numerical model. Experiment incorporates a vertical duct of length L_d=2.0 m and diameter d=0.05 m filled with water up to z=0.75 m (origin of z coordinate is at half the height of the tube). Two air bubbles are inside the duct with their noses situated at z=0.4 m and at z=-0.41 m; both bubbles have a length L_b=0.305 m (see Fig. 4.40a). At initial time fluids are at rest, and bubbles air pressure values are 0.35 m and 1.16 m of water column respectively. Same initial conditions are applied for both the analytical and numerical models. For numerical simulation, axisymmetric version of the numerical model is used. Physical parameters values are the same as in section 4.3.3. Average element length

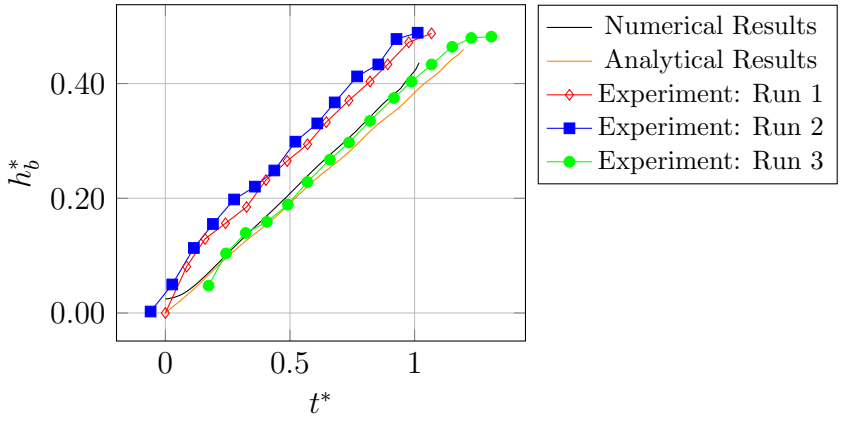

(a) Bubble position

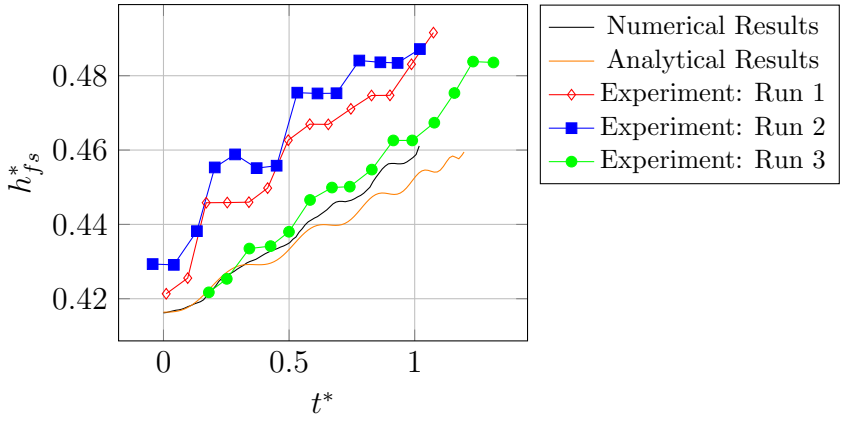

(b) Free surface position

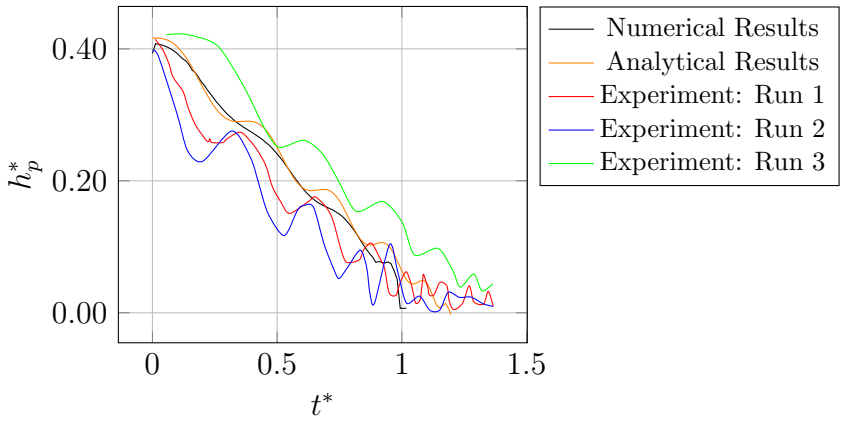

(c) Bubble Pressure

Figure 4.38: Taylor bubble emergence. Comparison between axisymmetric model and experimental results [79].

of axisymmetric mesh is δ=6.25$\sqrt{2} \cdot 10^{-4}$ m, Δt=$4 \cdot 10^{-5}$ s, reinitialisation parameters are ε=0.83Δl, $\Delta\tau$=0.1$\Delta l^2/(8\varepsilon)$, and parameter Υ=$\Delta l/(6000\varepsilon)$. Slip condition is applied on all boundaries except on the upper one, where inlet/outlet condition is used to allow the air to inflow/outflow. Gas expansion effect is not as consequential as in tests performed in section 2.2.3, nevertheless it is relevant to compare analytical and numerical approaches to scrutinise constraints of the theoretical model.

History of free surface position h_{fs} and bubbles nose positions h_{b1}, h_{b2} are plotted in Fig. 4.39, where analytical and numerical outputs are marked with dashed and solid lines, respectively. Free surface position is specified as the highest point on tube axis with $\phi > 0.5$, and position of each bubble nose is specified as highest position with $\phi < 0.5$. Numerical results at different times are depicted in Figs. 4.40b-4.40e. Free surface and bubbles head positions are well captured by the analytical model for $t < 1.6$ s, although a slight overprediction of upper bubble position is observed between t=0.8 s and t=1.6 s. This is probably due to detached secondary small bubbles (see Figs. 4.40b-4.40c), only attained by the numerical algorithm. The detachment reduces gas mass and bubble length, altering gas expansion effect and bubble velocity. Furthermore, effect of downstream wakes emergence during pocket rising is not considered in the analytical approach. Once upper bubble reaches free surface, analytical solution predicts a sudden decrease in free surface level because the entire gas mass is assumed to be released at the same time. Instead, free surface in numerical simulation is transformed into a diffuse air/water interface because of previously detached bubbles (see Figs. 4.39, 4.40d and 4.40e), seemingly, a more realistic event. Due to this reason, numerical model can not capture free surface location precisely. Nonetheless both solutions tend to converge over time (see results in Fig. 4.39, e.g. at t≈3.1 s). Lastly, trailing bubble position is accurately foretold by analytical. The slight underprediction from t≈2 s on is attributed to the leading bubble wake, altering dynamics of trailing bubble.

4.3.6 Geysering Experiments

This section gives an account of two experiments reproducing the physical process leading to a geysering event. While first test simulates last stage, where Taylor bubble is developed and ascends generating the geyser, second one computes a closed air cavity propagation, the air and momentum transfer from nearly horizontal to vertical conduits, the resulting rising Taylor bubble and final geysering event. Experiments set-up are the following. First test consists on a vertical conduit of 4.0 m length and 0.5 m diameter filled of water up to a height of 3.90 m. This duct has two chambers connected to

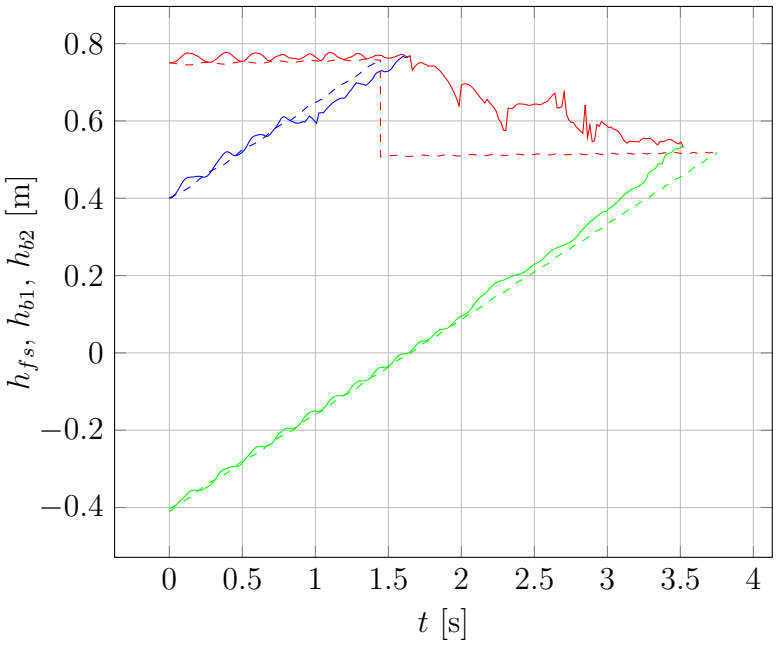

Figure 4.39: Two bubbles rising in a vertical duct, analytical and numerical results for free surface and bubbles positions as a function of time. Solid and dashed lines represent numerical and analytical results respectively. Red lines depict free surface position and blue and green lines show leading and trailing bubbles position respectively.

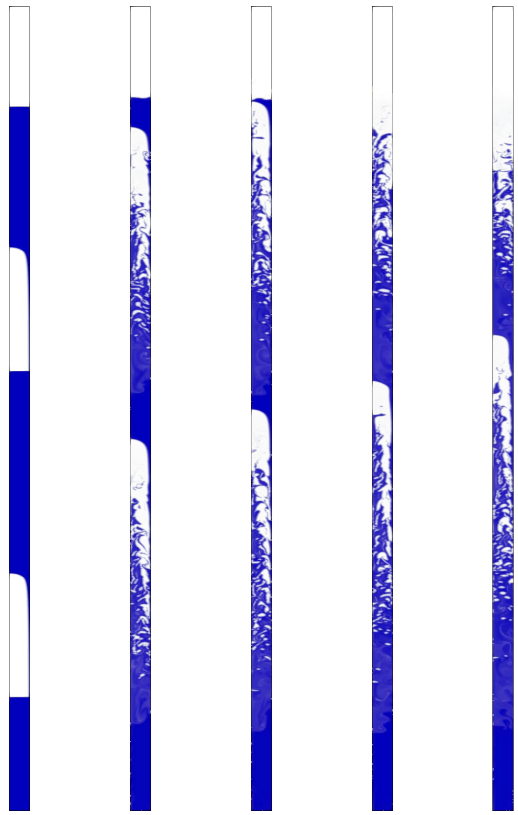

Figure 4.40: Two bubbles rising in a vertical duct, numerical results at times (a)0.00s, (b)1.28s, (c)1.60s, (d)1.92s and (e)2.24s. Horizontal axis is scaled by 2.

its upper and lower ends with the same objective as in experiment of section 4.3.4 (see Fig. 4.41). This test is performed with axisymmetric and full three dimensional models. For axisymmetric simulation, the grid is structured with δ=0.01$\sqrt{2}$ m, and time step is 1.2·10^{-5} s; hydrodynamics solution parameter $\Upsilon=\Delta l/(12000\varepsilon)$, to properly capture flow at the moment when entrapped air is explosively released to the atmosphere. For the full complete simulation, an unstructured tetrahedral mesh with average element length[5] of δ_{3D}=1.42 · 10^{-2} m is generated, Δt=5.0 · 10^{-5} s, and $\Upsilon=\Delta l/(6\varepsilon)$. Second experiment consists on an air bag entrapped in an inclined duct connected to ground level by a saturated vertical shaft (Fig. 4.42). Main duct has a diameter of 1.5 m, a length of 17 m, and an inclination of 5^o with respect to the horizontal. Vertical conduit has a diameter of 0.5 m, a length of 4.207 m, and joins main duct at a distance of 5.0 m from main duct left end. Moreover, a $4 \times 4 \times 5$ m chamber with its basis on ground level (see Fig. 4.42) allows water to leave the domain and air to outflow/inflow. Average element length is δ_{3D}=1.71 · 10^{-2} m, Δt=2.0 · 10^{-4} s and $\Upsilon=\Delta l/(600\varepsilon)$. Slip boundary condition is applied on solid walls (black lines in Fig. 4.42) and inlet/outlet condition is used on chamber upper boundary (red line in Fig. 4.42). At initial time, water level is situated at 0.1 m below ground level, and air occupies approximately last 8 meters of the inclined duct. Initial air volume is about 14 m^3 and air pressure is 5.5 m of water column. Fluids are assumed nearly-incompressible in both cases. Physical parameters are ρ_1=1.225 kg/m^3, μ_1=1.8·10^{-5} kg/ms, a_1^2=10^5 m^2/s^2 (air), ρ_2=1000 kg/m^3, μ_2=10^{-3} kg/ms, a_2^2=2.2 · 10^6 m^2/s^2 (water), σ=0.07 N/m and $|\mathbf{g}|$=9.81 m/s^2.

Aim of first experiment is to compare results of axisymmetric and complete models. Concerning axisymmetric simulation, water starts to emerge from the duct at t=0.51 s, when air cavity head is situated at a height of 0.8 m. Selected results at subsequent times are shown in Fig. 4.43. Figure 4.43a depicts the water phase at time 1.38 s. At this time, air cavity head is still travelling inside the duct and free surface has a twofold shape. Along with the radial propagation of a shallow layer of water, a volume of water with mushroom shape raise, in agreement with observations (see first frame of Fig. 4.46, captured from a real footage). When air bubble head reaches ground level, water and air are expelled upwards in the form of a high velocity jet (see second frame of Fig. 4.46). Figure 4.43c shows a slice of the numerical results, highlighting the mixing of phases (blue signifies ϕ=1 and white corresponds to ϕ=0). Although the model does not cover all the subtle details of the highly complex mixing, it achieves a good agreement with the

[5]Average element length for 3D unstructured meshes is $\delta_{3D}=\sqrt[3]{\frac{\sum_1^N V_i}{N}}$, where V_i is the volume of tetrahedron i and N is the total number of tetrahedrons.

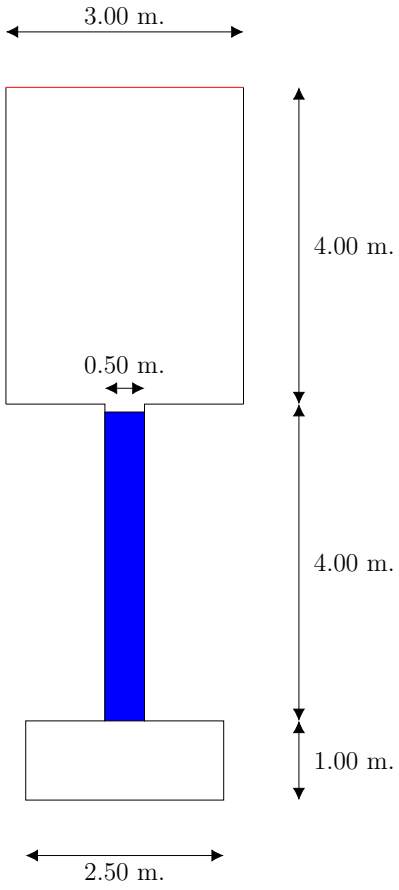

Figure 4.41: Domain for geysering simulation 1. Black colour boundary: Slip condition; red colour boundary: inlet/outlet condition. Blue colour indicates regions occupied by water at initial time step.

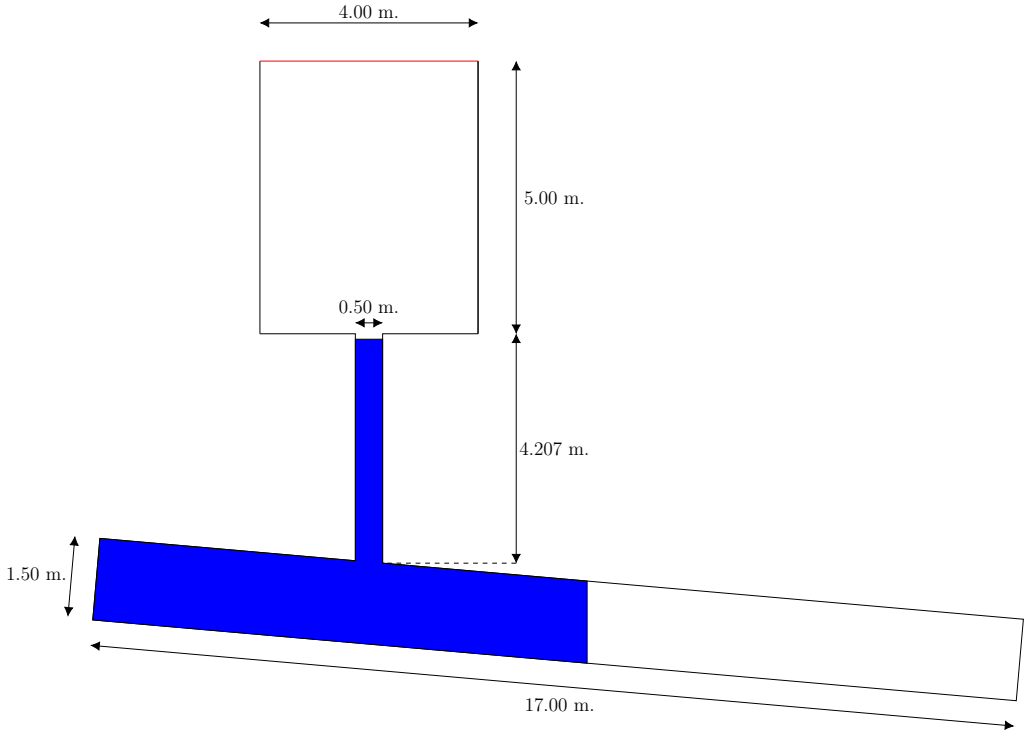

Figure 4.42: Domain for geysering simulation 2. Black colour boundary: Slip condition; red colour boundary: inlet/outlet condition. Blue colour indicates regions occupied by water at initial time step.

general topology of the phenomenon. The distribution shows, both in real and numerical cases, a shallow radial flux, two central widening of the jet, and a sharp front propagating in vertical direction.

Solution given by the full three dimensional model shows that air bubble reaches the top of the duct at t=1.554 s, while in axisymmetric solution this time is 1.434 s. This lag is ascribed to a small overprediction of bubble velocity by the axisymmetric model when bubble's head is close to the free surface. Overall flow pattern is almost axisymmetric and full 3D model results are very similar to outputs obtained with the simplified model until bubble head reaches street level (see Fig. 4.43b). Although three dimensional simulation differs from axisymmetric once water and air are expelled, main topological features remains very similar (compare Figs. 4.43c and 4.43d). In this case it is also evident that resolution of the three dimensional mesh is not enough to capture the spray flow.

Regarding second experiment, numerical results are shown in Figs. 4.44 and 4.45. At initial propagation stage, entrapped air expands because pressure is discontinuous across air/water interface; as a consequence, free surface in vertical shaft rises as can be seen in Fig. 4.44a. Cavity reaches the basis of vertical duct at $t\approx$1.63 s and starts to ascend. Bubble nose position is plotted in Fig. 4.47 superimposed to analytical solution. Although both solutions show same trend, in numerical simulation bubble velocity is higher when pocket starts to rise. This is due to the extra momentum picked up during the cavity propagation along the inclined duct, which is partially transferred to vertical component (e.g. at the state plot in Fig. 4.44b). Both numerical and analytical bubble velocities are much higher than U_∞=0.764 m/s (see section 2.2.1) because gas expansion effects are significant. As air pocket travels along vertical tube, water free surface also shows typical mushroom (see Figs. 4.44b-4.44d and Fig. 4.45a). Bubble reaches ground level at $t\approx$2.58 s, and then water is ejected upwards, resulting in a geyser that reaches a height of 4.0 m over the ground level (see sequence 4.44e-4.44g and Fig. 4.45b). Although again mesh resolution is not enough to capture the waterspray expelled from the duct, flow pattern (almost axisymmetric) is similar to real geyser events (compare Fig. 4.45b and second frame of Fig. 4.46).

This chapter has collected simulations performed with the numerical method for two-phase flows with interfaces. Assessment tests indicate that model captures accurately the interface and dynamics of both fluids, preventing oscillations in phase function and spurious momentum transfers between fluids. Furthermore, experiments of air cavities propagation and rising Taylor bubbles prove that numerical method is suitable to predict and evaluate these phenomena, as well as geysering events, occurring in sewer systems. Next chapter contains conclusions of the Thesis.

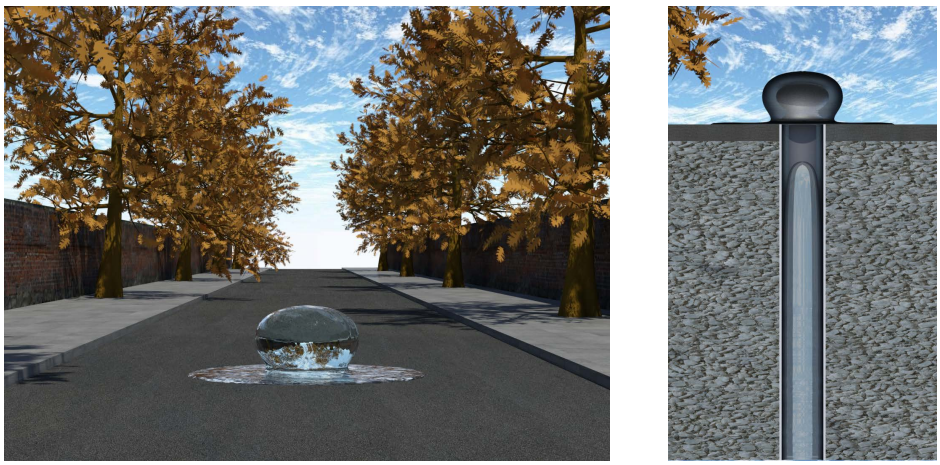

(a) Axisymmetric numerical results at t=1.380 s

(b) Three dimensional numerical results at t=1.440 s

Figure 4.43: Geysering simulation 1

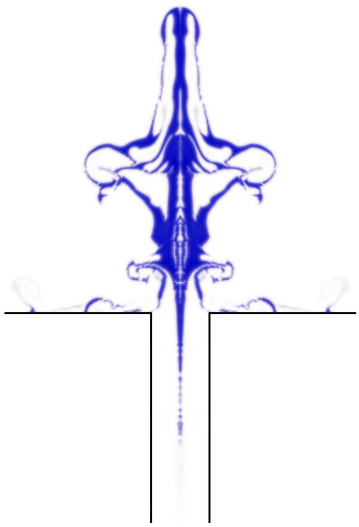

(c) Slice for axisymmetric numerical results at t=1.578 s

(d) Three dimensional numerical results at t=1.848 s

Figure 4.43: Geysering simulation 1 (cont.)

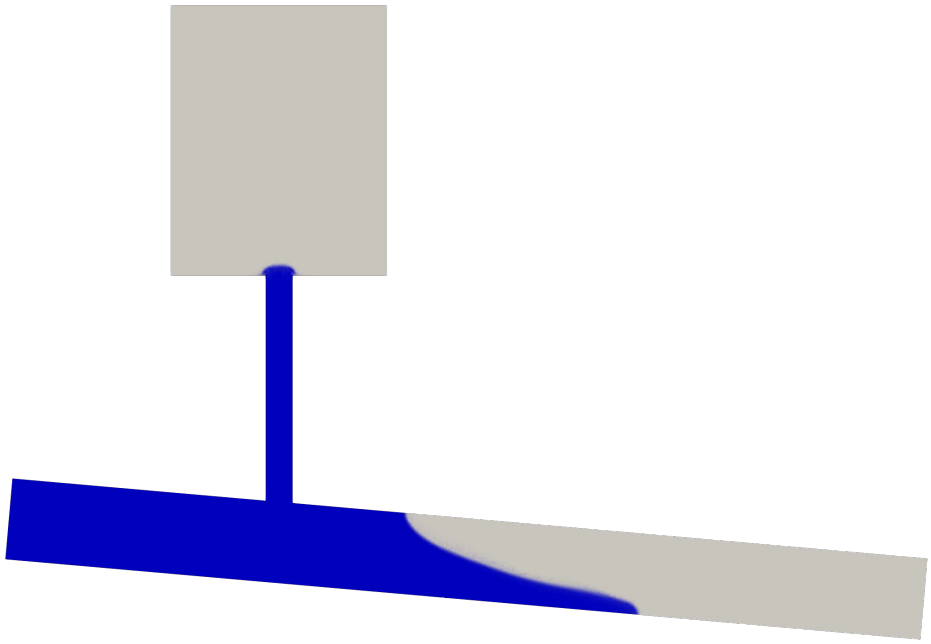

(a) t=0.75 s.

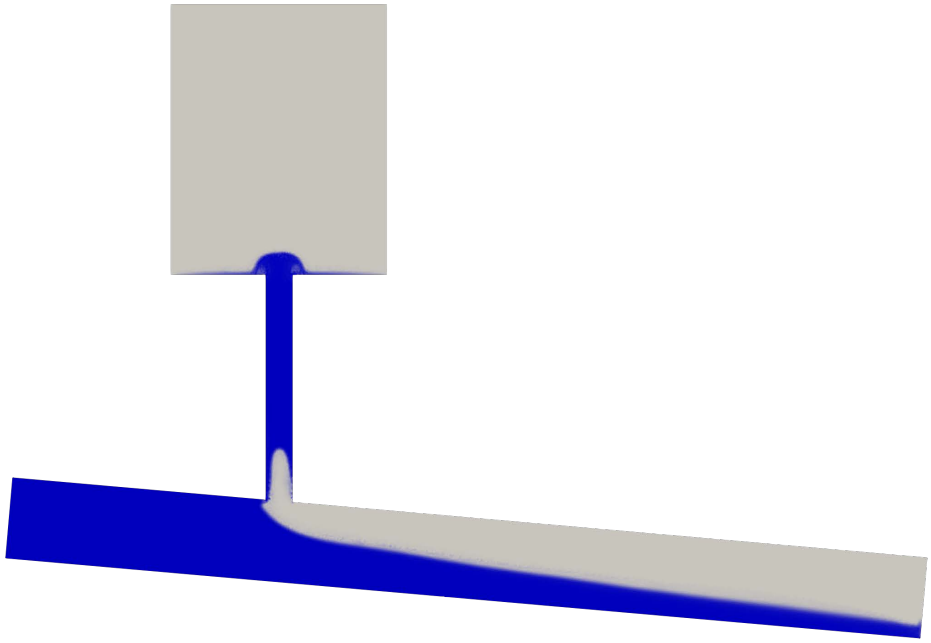

(b) t=2.00 s.

Figure 4.44: Geysering experiment 2, phase function results.

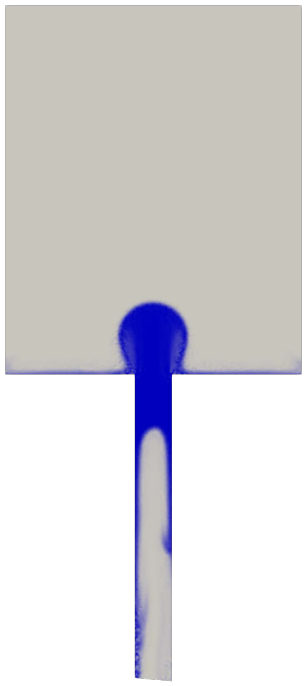

(c) t=2.50 s.

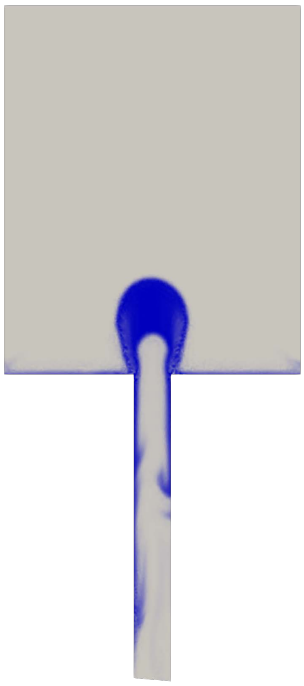

(d) t=2.625 s.

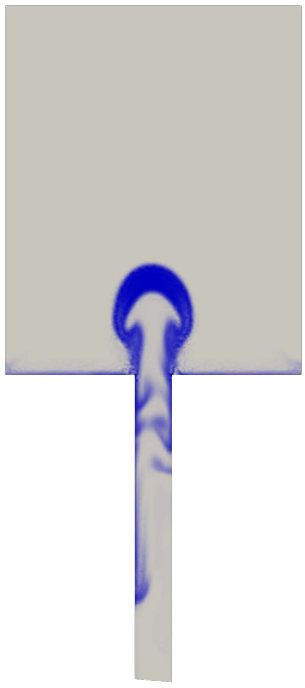

(e) t=2.675 s.

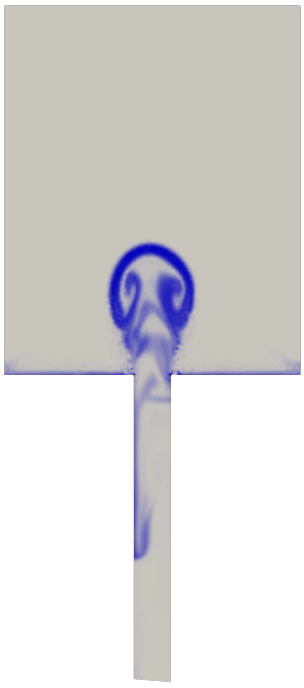

(f) t=2.725 s.

Figure 4.44: Geysering experiment 2, phase function results (cont.).

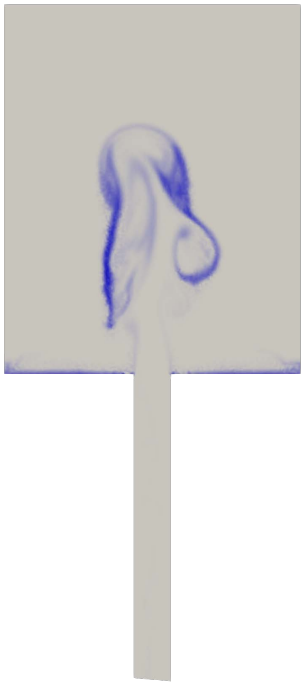

(g) t=2.850 s.

Figure 4.44: Geysering experiment, phase function results (cont. 2).

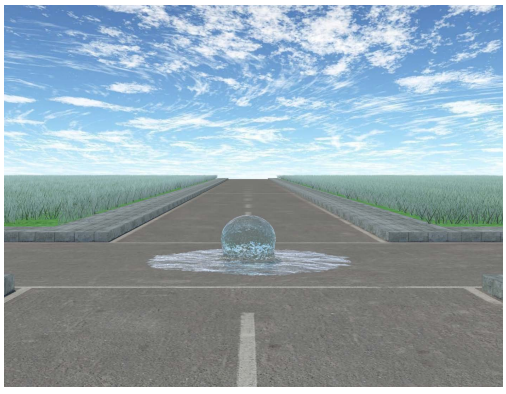

(a) t=2.375 s.

(b) t=2.875 s.

Figure 4.45: Geysering experiment 2, HD plots.

Figure 4.46: Frames from a footage of a geyser (https://www.youtube.com/watch?v=dM2L9EHNM5o).

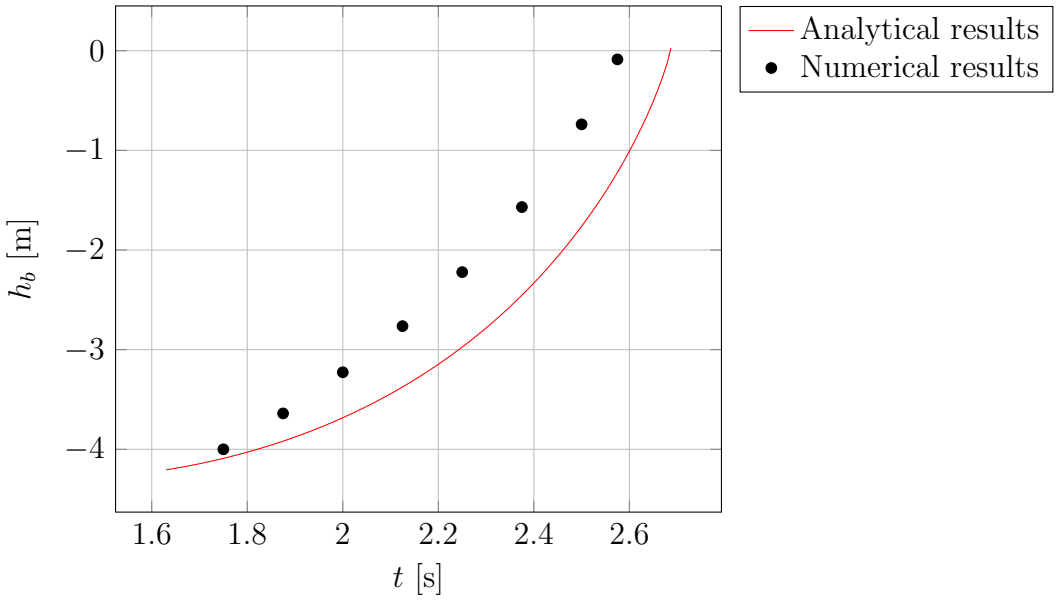

Figure 4.47: Geysering experiment 2. Numerical and analytical results for bubble position in vertical duct.

Chapter 5

Conclusions

This Thesis has reported a new numerical model for the simulation of two-phase flows with moving interfaces, and then it has been applied to scrutinise intrusion and propagation of air cavities in ducts and geysering events. This dynamics was also explored with analytical solutions based on control volume analysis. The numerical model was constructed on the basis of the Non-Oscillatory Finite Element Method, including effective customised extensions of flux correction techniques in the three stages of the resolution procedure. Solution of phase function transport equation needs the computation of two conservative approaches, a high order solution obtained with the Characteristic Galerkin algorithm and an independent positive definite low order solution calculated with an upwind scheme, which introduces the (nearly) minimum diffusion to achieve positivity. However, original limiting methodology introduces high order mass residuals because of the use of different discrete fluxes computation. To amend this issue, it has been proposed a modification of the correction algorithm by computing two additional global coefficients, in terms of total positive and negative element contributions, that counteract mass residuals. Performed benchmarks tests have shown that final answers, attained after applying modified flux correction procedures, preserves sign (or monotonicity under certain flow conditions). Regarding conservation property, mass error is reduced to round-off order in all performed tests. Comparison between errors in usual norms and ad-hoc interface capture error measures before and after the activation of new corrections proves that additional mass rebalancing does not worsen accuracy of original algorithm. Despite the good performance of new correction functions, an improved version without the adjustment of the mass distribution indiscriminately in the entire grid will be considered for future investigations.

After advection, reinitialisation step reconstructs the phase function to preserve numerical representation of the interface. This stage requires an equilibrium between the amount of artificial compressibility and the amount

of artificial diffusion to maintain stability and accuracy of the simulation. Too large diffusion could give spurious answers of the flow dynamics, while a too low diffusion can produce oscillations in the phase field. In this work, it has been introduced a novel reinitialisation procedure based on a non-linear anisotropic diffusion equation that accommodates both aforementioned effects. Unlike original reinitialisation, computation of this diffusion equation gives locally conservative fluxes, making straightforward the implementation of flux correction techniques. Then, resulting phase field after reinitialisation, calculated by an efficient and iterative explicit process, is conservative and monotone respect to advection solution. Numerical tests have shown that this new reinitialisation procedure enhances interface definition, since errors in standard norms and enclosed volume error substantially decrease. Moreover, the higher mesh resolution, the better effect of reinitialisation. Nevertheless, as reinitialisation could adjust the discontinuity location, interface error slightly increases for the most part of examined cases. To amend this problem, accuracy of reconstruction can be powered thanks to an improved calculation of interface normals. Proposed procedure, only involving static data, constrains normal calculation to a few elements surrounding the interface and extends normal direction values from the nearest element containing the border between phases. Effectiveness of this new strategy is higher in simulations without too close interfaces, reaching a substantial reduction in every measured error. Besides, these errors are generally of the same order or better than those provided by existing models of similar class. Drawback of last improvement lies in its use for extensive three dimensional simulations, where a huge amount of memory (RAM) has to be dedicated to store necessary static data for normals computation. An interesting issue to investigate in the future is the upgrading of reinitialisation to diminish interface artificial displacements. One possible solution could be the incorporation of a new term proportional to $|\phi - 0.5|$ in the diffusion equation.

Solution of two incompressible or weakly compressible fluid flows by continuous numerical models needs for any treatment (especially in convective acceleration terms) to avoid spurious momentum transfers between phases. In this work, the Non-Oscillatory Finite Element Method was implemented to control this pathology because low order solution of hydrodynamics (calculated with an upwind finite element scheme) almost entirely eliminates velocity overshoots due to its high diffusivity. However, the final solution obtained after adding anti-diffusive fluxes to low order solution did not preserve this quality, especially for very small density ratios. The reason is that standard flux limiting procedure did not take into account interface location. Thus, bounds for a node situated at one phase were computed with velocity values of the other phase. Hence, an enhanced bounds estimation strategy

has been proposed, including a parametric dependence on interface location into the bounds calculation. By means of this procedure, it is favoured, in some way, the prevalence of low order solution at those nodes close to the interface. Accomplished numerical experiments involving two fluids with very different density values (e.g. air-water) have shown a noticeable reduction of velocity peaks once enhanced bounds are used. Notwithstanding, an alternative strategy that does not require to tune additional parameters is an attractive idea to scrutinise in future research. It is worth noting that limiting procedure is just applied to the velocity predictor field, thus avoiding the computation of two complete hydrodynamics solutions each time step. While this course of action gives almost identical results that monolithic approach, its computational cost is nearly a half.

Continuous numerical representation of the contact discontinuity and parametrical definition of density gives rise to a virtual stratification between phases that can provoke false amplifications in problems including Kelvin-Helmholtz instabilities. Stability analysis demonstrates the beneficial effect of an active equivalent surface tension force to attenuate high frequency wiggles, and determines the necessity of reducing the interface thickness to some extent to avoid spurious amplifications. After considering some strategies to reduce transition thickness, the most suitable solution is an adaptive mesh refinement in the interface neighbourhood, thus preserving original density interpolation. Grid adaptivity method proposed assures conservation and monotonicity of variables in refinement/unrefinement processes by means of a procedure founded on flux correction techniques. Moreover, used nested grids enable an undemanding dynamic computation. Simulations of two fluids advancing in opposite directions have exhibited a substantial reduction of artificially exited perturbations when local refinement is activated. In addition, extra computational cost was about 30%, a much lower value than simulations with a complete refined mesh.

A relevant portion of of this Thesis has been dedicated to study dynamics of air cavities and geysering events either by analytical approaches or by the numerical approximations. Proposed analytical model takes into account gas expansion effects and free surface position to accurately predicts dynamics of rising Taylor bubbles and of liquid column situated above them. Although the theoretical model filters some local details of flow as the detachment of small bubbles, comparison with laboratory experiments reveals that main characteristics as time evolution of air cavity and free surface positions, or bubble pressure, are correctly reproduced. Besides, it was obtained a theoretical solution, whose principal parameter is the relation between bubble gas volume and the square of duct diameter, able to predict sudden decompressions of the bubble. It has been proved by existing experiments

and numerical simulations that, when this condition is near to be fulfilled, bubble and free surface velocities heavily increase, provoking a strong geysering event. Thus, despite its constraints, theoretical model may constitute an efficient tool to evaluate risk of geysering events in simple sewer system configurations. Furthermore, from analytical solution of consecutive rising bubbles, liquid expelled in first geyser is the principal reason why following air pockets cause stronger eruptions. This is because pressure of subsequent bubbles instantly decrease when part of above water leaves the duct, then air bags expand and drive remainder liquid to the conduit upper end with a higher strength. Nonetheless, strength of succeeding geysers also depends on bubbles gas volume and the liquid column remainder inside the duct.

Two-dimensional, axisymmetric and full three dimensional versions of numerical model were used to perform simulations involving air cavities and geysering events. Firstly, numerical method assessed air cavities propagating in straight and inclined ducts. Results indicate that cavity and bore celerities are accurately predicted with errors lower than 5% respect to experimental results. Besides, conditions for air cavity entrapment in inclined ducts due to partially open weirs match fairly well with laboratory outputs. Additionally, minimum necessary flow rate under which air is not allowed to intrude in ducts was determined. While duct inclination appears to be inconsequential (at least for moderate slopes), weir position plays the most important role. For low gate heights, velocity of liquid flowing in the duct has to be close to real air cavities celerity (i.e. close to $0.464\sqrt{gd}$). Conversely, for higher gate positions, threshold is related to the admissible flow rate over the weir, that can be calculated with a simple equation. Strategy to determine these conditions has proved to be effective for a realistic configuration and its future application for more complex geometries of sewer and stormwater storage systems is encouraging. Results accomplished can be useful to avoid geysering events by forcing a water inflow in the conduit or by controlling a gate situated at the lower end of the system, to prevent air intrusion. On the other hand, if emergence of air cavities is unavoidable, depressurisation could be beneficial to avert the geyser. This preventive action should be located at those critical locations that promote the cavity sealing (e.g. section changes or obstacles).

Last series of tests involved rising Taylor bubbles in vertical conduits and geysering events. In these cases, accuracy of capture of momentum exchanges between bubble and liquid column above is critical to determine the geyser strength, making imperative the use of weak-compressibility assumption and three dimensional simulations (or, at least, axisymmetric for circular conduits). In the case of multiple bubbles simulations, numerical model has supplemented to a large degree available outputs of analytical approach by

providing details of the dynamics not well reproduced by theoretical procedure. As an example, it was captured the effect of downstream wakes over trailing bubble, which alters moderately the expected bubble velocity given by analytical model. Finally, for geysering experiments, axisymmetric and full three dimensional numerical approaches provided main topological features of the flow once water and air were expelled from the vertical duct. In qualitative terms, obtained geysers were similar to real events occurring in sewer systems. A challenging issue to be developed will be the coupling of present model with shallow water flow models to simulate street level surface flows for integrated studies of urban floodings. Moreover, future applications of present numerical method for interfaces in other fields will be explored. Some targets are sediment transport processes and fluid-structure interaction problems.

Appendix A

Integral Form of Conservation Equations

The integral form of Conservation Laws are written as:

- Mass conservation:

$$\frac{\mathrm{d}}{\mathrm{d}t}\int_{\Omega(t)}\rho(\mathbf{x},t)\,\mathrm{d}\Omega+\int_{\Gamma(t)}\rho(\mathbf{x},t)(\mathbf{u}(\mathbf{x},t)-\mathbf{b})\cdot\mathbf{n}_b\,\mathrm{d}\Gamma=0 \qquad \text{(A.1)}$$

- Momentum conservation:

$$\frac{\mathrm{d}}{\mathrm{d}t}\int_{\Omega(t)}\rho(\mathbf{x},t)\mathbf{u}(\mathbf{x},t)\,\mathrm{d}\Omega+\int_{\Gamma(t)}\rho(\mathbf{x},t)\mathbf{u}(\mathbf{x},t)(\mathbf{u}(\mathbf{x},t)-\mathbf{b})\cdot\mathbf{n}_b\,\mathrm{d}\Gamma= \int_{\Omega(t)}\rho(\mathbf{x},t)\mathbf{g}\,\mathrm{d}\Omega+\int_{\Gamma(t)}\mathbf{f}(\mathbf{n}_b,\mathbf{x},t)\,\mathrm{d}\Gamma \qquad \text{(A.2)}$$

- Energy conservation for flows with constant internal energy and without heat fluxes:

$$\frac{\mathrm{d}}{\mathrm{d}t}\int_{\Omega(t)}\rho(\mathbf{x},t)\frac{|\mathbf{u}(\mathbf{x},t)|^2}{2}\,\mathrm{d}\Omega+\int_{\Gamma(t)}\rho(\mathbf{x},t)\left[\frac{|\mathbf{u}(\mathbf{x},t)|^2}{2}\left(\mathbf{u}(\mathbf{x},t)-\mathbf{b}\right)\right]\cdot\mathbf{n}_b\,\mathrm{d}\Gamma = \int_{\Omega(t)}\rho(\mathbf{x},t)\mathbf{g}\cdot\mathbf{u}(\mathbf{x},t)\,\mathrm{d}\Omega+\int_{\Gamma(t)}\mathbf{f}(\mathbf{n}_b,\mathbf{x},t)\cdot\mathbf{u}(\mathbf{x},t)\,\mathrm{d}\Gamma\,, \qquad \text{(A.3)}$$

where Ω represents a control volume bounded by Γ, $\mathbf{n}_b$ is the normal unit vector to the control volume boundary, $\mathbf{b}$ is the boundary velocity and $\mathbf{f}$ represents external forces applied on control volume boundary.

Appendix B

Characteristic-Galerkin Formulation

Characteristic-Galerkin formulation for transport equation is reported in Ref. [61]. Here, steps to obtain final forms are reproduced for completeness.

Transport equation of a scalar field B is,

$$\frac{\partial B}{\partial t} + \mathbf{u} \cdot \nabla B + R^{'} = 0\,, \tag{B.1}$$

$$R^{'} = R + B\nabla \cdot \mathbf{u}\,, \tag{B.2}$$

where R comprises source terms. As $\frac{\partial x_j}{\partial t}{=}u_j$, Eq. (B.1) can be rewritten as,

$$\frac{dB}{dt} = -R^{'}\,, \tag{B.3}$$

where $\frac{d}{dt}$ represents the material derivative. Consider Fig. B.1, where both the temporal and spatial dimensions are represented. Quantity $B(P)$ is determined by $B(Q)$ and velocity field at both points. The aim is to obtain an expression to get $B(P)$ in function of values at the same spatial position, i.e. $B(K)$ and $u_j(K)$. Firstly, Eq. (B.3) is discretized along the characteristics to obtain $B(P)$ and $B(Q)$,

$$B(P) = B(Q) + \Delta t \left.\frac{dB}{dt}\right|_{t(Q)} + \frac{\Delta t^2}{2} \left.\frac{d^2B}{dt^2}\right|_{t(Q)+\theta\Delta t} \tag{B.4}$$

$$B(Q) = B(P) - \Delta t \left.\frac{dB}{dt}\right|_{t(P)} + \frac{\Delta t^2}{2} \left.\frac{d^2B}{dt^2}\right|_{t(P)-\theta\Delta t}\,, \tag{B.5}$$

where $\Delta t{=}t^{n+1} - t^n$ and $\theta \in [0, 1]$. Next, operating with Eqs. (B.4) and (B.5) and taking $\theta{=}1/2$,

$$B(P) - B(Q) = \frac{\Delta t}{2}\left(\left.\frac{dB}{dt}\right|_{t(Q)} + \left.\frac{dB}{dt}\right|_{t(P)}\right) = -\frac{\Delta t}{2}\left(\left.R^{'}\right|_{t(Q)} + \left.R^{'}\right|_{t(P)}\right). \tag{B.6}$$

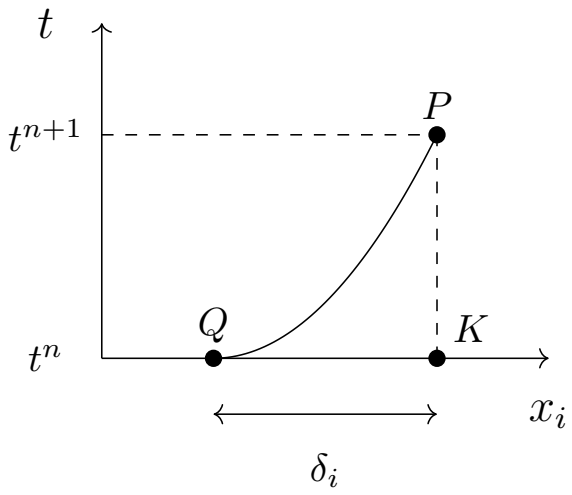

Figure B.1: Characteristic-Galerkin scheme

On the other hand, following the same procedure, next equations can be obtained,

$$x_j(P) = x_j(Q) + \Delta t \left.\frac{\partial x_j}{\partial t}\right|_{t(Q)} + \frac{\Delta t^2}{2} \left.\frac{\partial^2 x_j}{\partial t^2}\right|_{t(Q)+\theta\Delta t}, \tag{B.7}$$

$$x_j(Q) = x_j(P) - \Delta t \left.\frac{\partial x_j}{\partial t}\right|_{t(P)} + \frac{\Delta t^2}{2} \left.\frac{\partial^2 x_j}{\partial t^2}\right|_{t(P)-\theta\Delta t}, \tag{B.8}$$

$$x_j(P) - x_j(Q) = \delta_j = \frac{\Delta t}{2}\left(u_j|_{t(Q)} + u_j|_{t(P)}\right). \tag{B.9}$$

Now, an equation of $B(Q)$ in function of $B(K)$ is constructed as follows,

$$B(Q) = B(K) - \delta_i \left.\frac{\partial B}{\partial x_i}\right|_{t^n} + \frac{\delta_i\delta_j}{2} \left.\frac{\partial^2 B}{\partial x_i \partial x_j}\right|_{t^n}; \tag{B.10}$$

which is reformulated by introducing Eq. (B.9) into Eq. (B.10),

$$B(Q) = B(K) - \frac{\Delta t}{2}\left(u_i|_{t(Q)} + u_i|_{t(P)}\right) \left.\frac{\partial B}{\partial x_i}\right|_{t^n} + \frac{\Delta t^2}{8}\left(u_i|_{t(Q)} + u_i|_{t(P)}\right)\left(u_j|_{t(Q)} + u_j|_{t(P)}\right) \left.\frac{\partial^2 B}{\partial x_i \partial x_j}\right|_{t^n}. \tag{B.11}$$

It is interesting to eliminate values at Q from previous equations, for that

purpose next expressions are taken into account,

$$u_i|_{t(Q)} = u_i|_{t^n} - \delta_j \left.\frac{\partial u_i}{\partial x_j}\right|_{t^n} + \frac{\delta_j\delta_k}{2} \left.\frac{\partial^2 u_i}{\partial x_j \partial x_k}\right|_{t^n}, \tag{B.12}$$

$$\left.R'\right|_{t(Q)} = \left.R'\right|_{t^n} - \delta_j \left.\frac{\partial R'}{\partial x_j}\right|_{t^n} + \frac{\delta_j\delta_k}{2} \left.\frac{\partial^2 R'}{\partial x_j \partial x_k}\right|_{t^n}. \tag{B.13}$$

$$u_i|_{t(Q)} = u_i|_{t^n} - \frac{\Delta t}{2}\left(u_j|_{t(Q)} + u_j|_{t(P)}\right) \left.\frac{\partial u_i}{\partial x_j}\right|_{t^n} + \frac{\Delta t^2}{8}\left(u_j|_{t(Q)} + u_j|_{t(P)}\right)\left(u_k|_{t(Q)} + u_k|_{t(P)}\right) \left.\frac{\partial^2 u_i}{\partial x_j \partial x_k}\right|_{t^n}, \tag{B.14}$$

$$\begin{aligned} u_i|_{t(Q)} = u_i|_{t^n} - & \\ \frac{\Delta t}{2}\left(u_j|_{t^n} - \delta_l \left.\frac{\partial u_j}{\partial x_l}\right|_{t^n} + \frac{\delta_l\delta_m}{2} \left.\frac{\partial^2 u_j}{\partial x_l \partial x_m}\right|_{t^n} + u_j|_{t(P)}\right) \left.\frac{\partial u_i}{\partial x_j}\right|_{t^n} + & \\ \frac{\Delta t^2}{8}\left(u_j|_{t^n} - \delta_l \left.\frac{\partial u_j}{\partial x_l}\right|_{t^n} + \frac{\delta_l\delta_m}{2} \left.\frac{\partial^2 u_j}{\partial x_l \partial x_m}\right|_{t^n} + u_j|_{t(P)}\right) & \\ \left(u_k|_{t^n} - \delta_l \left.\frac{\partial u_k}{\partial x_l}\right|_{t^n} + \frac{\delta_l\delta_m}{2} \left.\frac{\partial^2 u_k}{\partial x_l \partial x_m}\right|_{t^n} + u_k|_{t(P)}\right) \left.\frac{\partial^2 u_i}{\partial x_j \partial x_k}\right|_{t^n}, & \end{aligned} \tag{B.15}$$

where Eqs. (B.14) and (B.15) are obtained by introducing Eq. (B.9) into Eq. (B.12) and Eq. (B.12) into Eq. (B.14) respectively. Neglecting third order terms from previous equation, next equation is obtained

$$u_i|_{t(Q)} = u_i|_{t^n} - \frac{\Delta t}{2}\left(u_j|_{t^n} + u_j|_{t(P)} - \delta_l \left.\frac{\partial u_j}{\partial x_l}\right|_{t^n}\right) \left.\frac{\partial u_i}{\partial x_j}\right|_{t^n} + \frac{\Delta t^2}{8}\left(u_j|_{t^n} + u_j|_{t(P)}\right)\left(u_k|_{t^n} + u_k|_{t(P)}\right) \left.\frac{\partial^2 u_i}{\partial x_j \partial x_k}\right|_{t^n}. \tag{B.16}$$

Then, replacing again Eq. (B.9) into Eq. (B.16) and neglecting third order terms, next equation is achieved

$$u_i|_{t(Q)} = u_i|_{t^n} - \frac{\Delta t}{2}\left(u_j|_{t^n} + u_j|_{t(P)} - \frac{\Delta t}{2}\left(u_k|_{t^n} + u_k|_{t(P)}\right) \left.\frac{\partial u_j}{\partial x_l}\right|_{t^n}\right) \left.\frac{\partial u_i}{\partial x_j}\right|_{t^n} + \frac{\Delta t^2}{8}\left(u_j|_{t^n} + u_j|_{t(P)}\right)\left(u_k|_{t^n} + u_k|_{t(P)}\right) \left.\frac{\partial^2 u_i}{\partial x_j \partial x_k}\right|_{t^n}. \tag{B.17}$$

Similar equation is obtained for Eq. (B.13),

$$R^{'}\Big|_{t(Q)} = R^{'}\Big|_{t^n} - \frac{\Delta t}{2}\left(u_j|_{t^n} + u_j|_{t(P)} - \frac{\Delta t}{2}\left(u_k|_{t^n} + u_k|_{t(P)}\right)\frac{\partial u_j}{\partial x_l}\Big|_{t^n}\right)\frac{\partial R^{'}}{\partial x_j}\Big|_{t^n} + \frac{\Delta t^2}{8}\left(u_j|_{t^n} + u_j|_{t(P)}\right)\left(u_k|_{t^n} + u_k|_{t(P)}\right)\frac{\partial^2 R^{'}}{\partial x_j \partial x_k}\Big|_{t^n} . \quad \text{(B.18)}$$

Now, Eqs. (B.17) and (B.9) are introduced into Eq. (B.11),

$$B(Q) = B(K) - \frac{\Delta t}{2}\left(u_i|_{t^n} + u_i|_{t(P)} - \frac{\Delta t}{2}\left(u_j|_{t^n} + u_j|_{t(P)}\right)\frac{\partial u_i}{\partial x_j}\Big|_{t^n}\right)\frac{\partial B}{\partial x_i}\Big|_{t^n} + \frac{\Delta t^2}{8}\left(u_i|_{t^n} + u_i|_{t(P)}\right)\left(u_j|_{t^n} + u_j|_{t(P)}\right)\frac{\partial^2 B}{\partial x_i \partial x_j}\Big|_{t^n} , \quad \text{(B.19)}$$

and Eq. (B.18) into Eq. (B.6),

$$B(P) = B(Q) - \frac{\Delta t}{2}\left(R^{'}\Big|_{t^n} + R^{'}\Big|_{t(P)} - \frac{\Delta t}{2}\left(u_j|_{t^n} + u_j|_{t(P)}\right)\frac{\partial R^{'}}{\partial x_j}\Big|_{t^n}\right) . \quad \text{(B.20)}$$

Third order terms have been neglected in last two equations. Finally, by introducing Eq. (B.19) into Eq. (B.20) and recalling $\frac{(\cdot)|_{t^n}+(\cdot)|_{t(P)}}{2}=(\cdot)^{n+1/2}$, $B(P)=B^{n+1}$ and $B(K)=B^n$, final equation is obtained,

$$B^{n+1} = B^n - \Delta t u_i^{n+1/2}\frac{\partial B}{\partial x_i}\Big|_{t^n} - \Delta t R'^{n+1/2} + \frac{\Delta t^2}{2}u_j^{n+1/2}\frac{\partial u_i}{\partial x_j}\Big|_{t^n}\frac{\partial B}{\partial x_i}\Big|_{t^n} + \frac{\Delta t^2}{2}u_i^{n+1/2}u_j^{n+1/2}\frac{\partial^2 B}{\partial x_i \partial x_j}\Big|_{t^n} + \frac{\Delta t^2}{2}u_i^{n+1/2}\frac{\partial R^{'}}{\partial x_i}\Big|_{t^n} , \quad \text{(B.21)}$$

or, replacing $R^{'}=R+B\frac{\partial u_i}{\partial x_i}$,

$$B^{n+1} = B^n - \Delta t\left[u_i^{n+1/2}\frac{\partial B}{\partial x_i}\Big|_{t^n} + B^{n+1/2}\frac{\partial u_k}{\partial x_k}\Big|_{t^n} + R^{n+1/2}\right] + \frac{\Delta t^2}{2}\left[u_i^{n+1/2}\frac{\partial u_j}{\partial x_i}\Big|_{t^n}\frac{\partial B}{\partial x_j}\Big|_{t^n} + u_i^{n+1/2}u_j^{n+1/2}\frac{\partial^2 B}{\partial x_i \partial x_j}\Big|_{t^n} + u_i^{n+1/2}\frac{\partial}{\partial x_i}\left(B^n\frac{\partial u_k}{\partial x_k}\Big|_{t^n}\right) + u_i^{n+1/2}\frac{\partial R}{\partial x_i}\Big|_{t^n}\right] . \quad \text{(B.22)}$$

Appendix C

Matrix Formulation

This appendix reports the matrix form of finite element discretisation of solved equations. Here linear shape functions for triangular elements are used for clarity. Note that equations for linear tetrahedrons (3D formulation) can be straightforward constructed. Following equations are calculated for a single element, and full system of equations is built by the suitable assembling of individuals matrices.

C.1 Transport Equation

Phase function transport equation is obtained by replacing $B^{n+1/2}{\approx}B^n$, $B{=}\phi$, and $R{=}0$ in Eq. (B.22). Then, standard Galerkin procedure, calling N^l to shape function of node l, over one element Ω gives

$$\overbrace{\int_\Omega N^l \Delta\phi \,\mathrm{d}\Omega}^{1} = -\Delta t \overbrace{\int_\Omega N^l \frac{\partial\left(\phi^n u_i^{n+1/2}\right)}{\partial x_i}\,\mathrm{d}\Omega}^{2} + \frac{\Delta t^2}{2}\left[\left(\overbrace{\int_\Omega N^l u_i^{n+1/2}\frac{\partial u_j^n}{\partial x_i}\frac{\partial \phi^n}{\partial x_j}\,\mathrm{d}\Omega}^{3}\right) + \left(\overbrace{\int_\Omega N^l u_i^{n+1/2}\frac{\partial}{\partial x_i}\left(\phi^n\frac{\partial u_k^n}{\partial x_k}\right)\,\mathrm{d}\Omega}^{4}\right) + \left(\overbrace{\int_\Omega N^l u_i^{n+1/2}u_j^{n+1/2}\frac{\partial^2\phi^n}{\partial x_i\partial x_j}\,\mathrm{d}\Omega}^{5}\right)\right]. \quad \text{(C.1)}$$

Integral 1

$$\int_\Omega N^l \Delta\phi \, \mathrm{d}\Omega = \frac{A}{12}\left(\Delta\phi^l + \Delta\phi^a + \Delta\phi^b + \Delta\phi^c\right) \quad \text{for } l = a, b, c\,, \tag{C.2}$$

where A is the area of element Ω and super-indexes a, b and c indicate values of the three nodes of the triangle. Integral evaluation for each node is obtained by replacing l=a, b, c respectively.

Integral 2

$$\int_\Omega N^l \frac{\partial\left(\phi^n u_i^{n+1/2}\right)}{\partial x_i}\,\mathrm{d}\Omega = \overbrace{-\int_\Omega \frac{\partial N^l}{\partial x_i}\phi^n u_i^{n+1/2}\,\mathrm{d}\Omega}^{2a} + \overbrace{\int_\Gamma N^l \phi^n\left(u_i^{n+1/2}\cdot n_{b,i}\right)\,\mathrm{d}\Omega}^{2b} \quad \text{for } l = a, b, c\,. \tag{C.3}$$

In last equation, Γ represents the domain boundary and $n_{b,i}$ is the i component of the boundary normal. Note that last integral is only calculated at those elements with any edge belonging to the boundary.

Integral 2a

$$-\int_\Omega \frac{\partial N^l}{\partial x_i}\phi^n u_i^{n+1/2}\,\mathrm{d}\Omega = -\frac{A}{3}\left[\frac{\partial N^l}{\partial x_i}\left(\left(\phi^a\right)^n\left(u_i^a\right)^{n+1/2} + \left(\phi^b\right)^n\left(u_i^b\right)^{n+1/2} + \left(\phi^c\right)^n\left(u_i^c\right)^{n+1/2}\right)\right] \quad \text{for } l = a, b, c\,. \tag{C.4}$$

Integral 2b

$$\int_\Gamma N^l \phi^n\left(u_i^{n+1/2}\cdot n_{b,i}\right)\,\mathrm{d}\Omega = \frac{L_\Gamma}{6}\left[\left(\left(\phi^l\right)^n\left(u_i^l\right)^{n+1/2} + \left(\phi^a\right)^n\left(u_i^a\right)^{n+1/2} + \left(\phi^b\right)^n\left(u_i^b\right)^{n+1/2}\right) n_{b,i}\right] \quad \text{for } l = a, b\,, \tag{C.5}$$

where L_Γ is the length of the boundary edge joining nodes a and b.

Integral 3

$$\int_\Omega N^l u_i^{n+1/2} \frac{\partial u_j^n}{\partial x_i} \frac{\partial \phi^n}{\partial x_j} \, \mathrm{d}\Omega = \frac{A}{12} \left(u_i^l + u_i^a + u_i^b + u_i^c\right)^{n+1/2} \left(\frac{\partial u_j^n}{\partial x_i} \frac{\partial \phi^n}{\partial x_j}\right) \quad \text{for } l = a, b, c \,, \tag{C.6}$$

where derivatives are calculated as

$$\begin{aligned} \frac{\partial u_i}{\partial x_j} &= \frac{\partial N^a}{\partial x_j} u_i^a + \frac{\partial N^b}{\partial x_j} u_i^b + \frac{\partial N^c}{\partial x_j} u_i^c \,, \\ \frac{\partial \phi}{\partial x_j} &= \frac{\partial N^a}{\partial x_j} \phi^a + \frac{\partial N^b}{\partial x_j} \phi^b + \frac{\partial N^c}{\partial x_j} \phi^c \,. \end{aligned}$$

Integral 4

$$\int_\Omega N^l u_i^{n+1/2} \frac{\partial}{\partial x_i} \left[\left(\phi \frac{\partial u_k}{\partial x_k}\right)^n\right] \, \mathrm{d}\Omega = \overbrace{- \int_\Omega \frac{\partial}{\partial x_i} \left(N^l u_i^{n+1/2}\right) \left(\phi \frac{\partial u_k}{\partial x_k}\right)^n \, \mathrm{d}\Omega}^{4a} + \overbrace{\int_\Gamma N^l \left(\phi \frac{\partial u_k}{\partial x_k}\right)^n \left(u_i^{n+1/2} \cdot n_{b,i}\right) \, \mathrm{d}\Gamma}^{4b} \,. \tag{C.7}$$

Integral 4a

$$- \int_\Omega \frac{\partial}{\partial x_i} \left(N^l u_i^{n+1/2}\right) \left(\phi \frac{\partial u_k}{\partial x_k}\right)^n \, \mathrm{d}\Omega \approx - A \left[\overline{\phi}^n \left(\frac{\partial u_k}{\partial x_k}\right)^n \left(\overline{u}_i^{n+1/2} \frac{\partial N^l}{\partial x_i}\right)\right] \quad \text{for } l = a, b, c \,. \tag{C.8}$$

In last equation, overlined terms are calculated as $\overline{u_i} = \dfrac{u_i^a + u_i^b + u_i^c}{3}$ and $\overline{\phi} = \dfrac{\phi^a + \phi^b + \phi^c}{3}$.

Integral 4b

$$\int_\Gamma N^l \left(\phi \frac{\partial u_k}{\partial x_k}\right)^n \left(u_i^{n+1/2} \cdot n_{b,i}\right) \, \mathrm{d}\Gamma \approx \frac{L_\Gamma}{12} \left[\left(\phi^a + \phi^b\right)^n \left(\frac{\partial u_k^n}{\partial x_k}\right)\right] \left[\left(u_i^a + u_i^b + u_i^l\right)^{n+1/2} \cdot n_{b,i}\right] \quad \text{for } l = a, b \text{ respectively}. \quad \text{(C.9)}$$

Integral 5

$$\int_\Omega N^l u_i^{n+1/2} u_j^{n+1/2} \frac{\partial^2 \phi^n}{\partial x_i \partial x_j} \, \mathrm{d}\Omega = \overbrace{-\int_\Omega \frac{\partial}{\partial x_i}\left(N^l u_i^{n+1/2} u_j^{n+1/2}\right) \frac{\partial \phi^n}{\partial x_j} \, \mathrm{d}\Omega}^{5a} + \overbrace{\int_\Gamma N^l u_j^{n+1/2} \frac{\partial \phi^n}{\partial x_j}\left(u_i^{n+1/2} \cdot n_{b,i}\right) \, \mathrm{d}\Gamma}^{5b}. \quad \text{(C.10)}$$

Integral 5a

$$-\int_\Omega \frac{\partial}{\partial x_i}\left(N^l u_i^{n+1/2} u_j^{n+1/2}\right) \frac{\partial \phi}{\partial x_j} \, \mathrm{d}\Omega \approx -A \left(\frac{\partial N^l}{\partial x_i} \overline{u}_i^{n+1/2}\right) \left(\frac{\partial \phi^n}{\partial x_j} \overline{u}_j^{n+1/2}\right) \quad \text{for } l = a, b, c. \quad \text{(C.11)}$$

Integral 5b

$$\int_\Gamma N^l u_j^{n+1/2} \frac{\partial \phi^n}{\partial x_j}\left(u_i^{n+1/2} \cdot n_{b,i}\right) \, \mathrm{d}\Gamma \approx \frac{L_\Gamma}{12} \left[\left(u_j^a + u_j^b\right)^{n+1/2} \frac{\partial \phi^n}{\partial x_j}\right] \left[\left(u_i^a + u_i^b + u_i^l\right)^{n+1/2} \cdot n_{b,i}\right] \quad \text{for } l = a, b. \quad \text{(C.12)}$$

C.2 Hydrodynamics Solution - Velocity Predictor

First step of hydrodynamics solution is the calculation of velocity predictor $\mathbf{u}^*$. Equations for both velocity predictor components are attained by

replacing $B{=}u_m$ and

$$R = -\frac{1}{\rho}\frac{\partial \mathcal{T}_{mj}}{\partial x_j} - g_m - \mathbf{T}_m - u_m \nabla \cdot \mathbf{u}\,,$$

for $m{=}1, D$, where $\mathcal{T}$ is the viscous stress tensor and $\mathbf{T}$ is the surface tension term. Here, $R^{n+1/2} \approx R^n$ is assumed to obtain a full explicit discretisation. As in previous section, standard Galerkin method over one single element Ω gives

$$\begin{aligned}
\overbrace{\int_\Omega N^l \Delta u_m^* \,\mathrm{d}\Omega}^{1} = -\Delta t \overbrace{\int_\Omega N^l \frac{\partial u_m^n u_i^{n+1/2}}{\partial x_i}\,\mathrm{d}\Omega}^{2} + \Delta t \overbrace{\int_\Omega N^l \frac{1}{\rho}\frac{\partial \mathcal{T}_{mj}^n}{\partial x_j}\,\mathrm{d}\Omega}^{3} \\
+ \Delta t \overbrace{\int_\Omega N^l g_m \,\mathrm{d}\Omega}^{4} + \Delta t \overbrace{\int_\Omega N^l \mathbf{T}_m^n \,\mathrm{d}\Omega}^{5} + \Delta t \overbrace{\int_\Omega N^l u_m^n \frac{\partial u_k^n}{\partial x_k}\,\mathrm{d}\Omega}^{6} \\
+ \frac{\Delta t^2}{2}\left[\left(\overbrace{\int_\Omega N^l u_i^{n+1/2}\frac{\partial u_j^n}{\partial x_i}\frac{\partial u_m^n}{\partial x_j}\,\mathrm{d}\Omega}^{7}\right)\right. \\
+ \left(\overbrace{\int_\Omega N^l u_i^{n+1/2}\frac{\partial}{\partial x_i}\left(-\frac{1}{\rho}\frac{\partial \mathcal{T}_{mj}^n}{\partial x_j} - g_m - \mathbf{T}_m^n\right)\,\mathrm{d}\Omega}^{8}\right) \\
\left. + \left(\overbrace{\int_\Omega N^l u_i^{n+1/2} u_j^{n+1/2}\frac{\partial^2 u_m^n}{\partial x_i \partial x_j}\,\mathrm{d}\Omega}^{9}\right)\right] \quad \text{for } m = 1, D. \quad \text{(C.13)}
\end{aligned}$$

In last equation, $\Delta u_m^*{=}u_m^* - u_m^n$ and integrals 1, 2, 7 and 9 can be obtained from Eqs. (C.2), (C.3), (C.6) and (C.10) by replacing ϕ with u_m. Summation convention is not applied to subindex m in previous and following equations.

Integral 3

$$\int_\Omega N^l \frac{1}{\rho}\frac{\partial \mathcal{T}_{mj}^n}{\partial x_j}\,\mathrm{d}\Omega \approx \overbrace{-\frac{1}{\overline{\rho}}\int_\Omega \frac{\partial N^l}{\partial x_j}\mathcal{T}_{mj}^n\,\mathrm{d}\Omega}^{3a} + \overbrace{\frac{1}{\overline{\rho}}\int_\Gamma N^l \mathcal{T}_{mj}^n \cdot n_{b,j}\,\mathrm{d}\Gamma}^{3b}\,, \qquad \text{(C.14)}$$

where

$$\mathcal{T}_{mj} = \overline{\mu}\left(\frac{\partial N^a}{\partial x_j}u_m^a + \frac{\partial N^b}{\partial x_j}u_m^b + \frac{\partial N^c}{\partial x_j}u_m^c + \frac{\partial N^a}{\partial x_m}u_j^a + \frac{\partial N^b}{\partial x_m}u_j^b + \frac{\partial N^c}{\partial x_m}u_j^c\right),$$

$$\overline{\rho} = \frac{\rho^a + \rho^b + \rho^c}{3},$$

$$\overline{\mu} = \frac{\mu^a + \mu^b + \mu^c}{3}.$$

Integral 3a

$$-\frac{1}{\overline{\rho}}\int_\Omega \frac{\partial N^l}{\partial x_j}\mathcal{T}_{mj}^n \,\mathrm{d}\Omega = -\frac{A}{\overline{\rho}}\left(\frac{\partial N^l}{\partial x_j}\mathcal{T}_{mj}\right)^n \text{ for } l = a, b, c, \tag{C.15}$$

Integral 3b

$$\frac{1}{\overline{\rho}}\int_\Gamma N^l \mathcal{T}_{mj}^n \cdot n_{b,j} \,\mathrm{d}\Gamma = \frac{L_\Gamma}{2\overline{\rho}}\left(\mathcal{T}_{mj}^n \cdot n_{b,j}\right) \quad \text{for nodes } a, b. \tag{C.16}$$

Integral 4

$$\int_\Omega N^l g_m \,\mathrm{d}\Omega = \frac{A}{3}g_m \quad \text{for nodes } a, b, c. \tag{C.17}$$

Integral 5

$$\int_\Omega N^l \mathbf{T}_m^n \,\mathrm{d}\Omega = \frac{A}{3}\mathbf{T}_m^n \quad \text{for nodes } a, b, c. \tag{C.18}$$

Surface tension term $\mathbf{T}$ is calculated by element in the following way,

1. Calculation of nodal values of $\nabla\phi^n$ by using Eq. (D.4) and improved normals (see section 3.4),
2. Calculation of interface curvature by using shape functions and nodal values of $\nabla\phi$,

$$\kappa^n = -\nabla\cdot\frac{\nabla\phi^n}{|\nabla\phi^n|} = -\left[\frac{\partial N^a}{\partial x_1}\left(\frac{\nabla\phi^n}{|\nabla\phi^n|}\right)_1^a + \frac{\partial N^b}{\partial x_1}\left(\frac{\nabla\phi^n}{|\nabla\phi^n|}\right)_1^b + \frac{\partial N^c}{\partial x_1}\left(\frac{\nabla\phi^n}{|\nabla\phi^n|}\right)_1^c + \frac{\partial N^a}{\partial x_2}\left(\frac{\nabla\phi^n}{|\nabla\phi^n|}\right)_2^a + \frac{\partial N^b}{\partial x_2}\left(\frac{\nabla\phi^n}{|\nabla\phi^n|}\right)_2^b + \frac{\partial N^c}{\partial x_2}\left(\frac{\nabla\phi^n}{|\nabla\phi^n|}\right)_2^c\right].$$

3. Calculation of surface tension term,

$$\mathbf{T}_m^n \approx \frac{2\sigma}{(\rho_1+\rho_2)(\rho_2-\rho_1)}\kappa^n \frac{\partial \rho}{\partial x_m} ,$$

$$\frac{\partial \rho}{\partial x_m} = \frac{\partial N^a}{\partial x_m}\rho^a + \frac{\partial N^b}{\partial x_m}\rho^b + \frac{\partial N^c}{\partial x_m}\rho^c .$$

Integral 6

$$\int_\Omega N^l u_m^n \frac{\partial u_k^n}{\partial x_k}\,\mathrm{d}\Omega = \frac{A}{12}\left(\frac{\partial u_k^n}{\partial x_k}\right)\left(u_m^l + u_m^a + u_m^b + u_m^c\right)^n \quad \text{for } l = a,b,c\,. \quad \text{(C.19)}$$

Integral 8

$$\int_\Omega N^l u_i^{n+1/2}\frac{\partial}{\partial x_i}\left(-\frac{1}{\rho}\frac{\partial \mathcal{T}_{mj}^n}{\partial x_j} - g_m - \mathbf{T}_m^n\right)\,\mathrm{d}\Omega = \overbrace{-\int_\Omega \frac{\partial}{\partial x_i}\left(N^l u_i^{n+1/2}\right)\left(-\frac{1}{\rho}\frac{\partial \mathcal{T}_{mj}^n}{\partial x_j} - g_m - \mathbf{T}_m^n\right)\,\mathrm{d}\Omega}^{8a} + \overbrace{\int_\Gamma N^l\left(-\frac{1}{\rho}\frac{\partial \mathcal{T}_{mj}^n}{\partial x_j} - g_m - \mathbf{T}_m^n\right)\left(u_i^{n+1/2}\cdot n_{b,i}\right)\,\mathrm{d}\Gamma}^{8b} . \quad \text{(C.20)}$$

Integral 8a

$$-\int_\Omega \frac{\partial}{\partial x_i}\left(N^l u_i^{n+1/2}\right)\left(-\frac{1}{\rho}\frac{\partial \mathcal{T}_{mj}^n}{\partial x_j} - g_m - \mathbf{T}_m^n\right)\,\mathrm{d}\Omega \approx -A\left[\left(-g_m - \mathbf{T}_m^n\right)\left(\overline{u}_i^{n+1/2}\frac{\partial N^l}{\partial x_i}\right)\right] \quad \text{for } l = a,b,c\,. \quad \text{(C.21)}$$

Integral 8b

$$\int_\Gamma N^l \left(-\frac{1}{\rho}\frac{\partial \mathcal{T}^n_{mj}}{\partial x_j} - g_m - \mathbf{T}^n_m\right)\left(u_i^{n+1/2}\cdot n_{b,i}\right)\,\mathrm{d}\Gamma \approx \frac{L_\Gamma}{6}\left(-g_m - \mathbf{T}^n_m\right)\left(\left(u_i^a + u_i^b + u_i^l\right)\cdot n_{b,i}\right)^{n+1/2} \quad \text{for } l = a, b\,. \quad \text{(C.22)}$$

C.3 Hydrodynamics Solution - Pressure Calculation

Second step of hydrodynamics solution is the calculation of pressure increment. Equation (3.47) can be written as

$$\frac{\partial}{\partial t}\left(\frac{p-p_0}{a_1^2+(a_2^2-a_1^2)\phi}\right) + \theta_1\nabla\cdot\left(\rho'\Delta\mathbf{u}^{**}\right) = -\nabla\cdot\left(\rho'\mathbf{u}^n\right) - \theta_1\nabla\cdot\left(\rho'\Delta\mathbf{u}^{*}\right)\,, \quad \text{(C.23)}$$

where $\rho'=\rho_1 + \frac{p-p_0}{a_1^2+(a_2^2-a_1^2)\phi}$, density values are calculated after solving phase function transport equation and reinitialisation, and $\Delta\mathbf{u}^{**}$ includes pressure terms (see Eq. (3.48)). Now, a forward Euler time discretisation is employed and weighted residual method is applied to the resulting equation over one single element Ω,

$$\int_\Omega N^l \frac{1}{a^2}\frac{\Delta p}{\Delta t}\,\mathrm{d}\Omega - \Delta t\theta_1\theta_2\int_\Omega N^l\nabla\cdot\left(\frac{\rho'}{\rho}\nabla(\Delta p)\right)\,\mathrm{d}\Omega = -\int_\Omega N^l\nabla\cdot\left(\rho'\mathbf{u}^n\right)\,\mathrm{d}\Omega - \theta_1\int_\Omega N^l\nabla\cdot\left(\rho'\Delta\mathbf{u}^*\right)\,\mathrm{d}\Omega + \Delta t\theta_1\int_\Omega N^l\nabla\cdot\left(\frac{\rho'}{\rho}\nabla p^n\right)\,\mathrm{d}\Omega\,.$$

Note that pressure second order term vanishes because linear finite elements are used. Next, integration by parts is applied over some integrals,

$$\overbrace{\int_\Omega N^l \frac{1}{a^2}\frac{\Delta p}{\Delta t}\,\mathrm{d}\Omega}^{1} + \Delta t\theta_1\theta_2 \frac{\overline{\rho}'}{\overline{\rho}} \overbrace{\int_\Omega \frac{\partial N^l}{\partial x_i}\frac{\partial\,(\Delta p)}{\partial x_i}\,\mathrm{d}\Omega}^{2} =$$

$$\overbrace{-\int_\Omega N^l \nabla\cdot\left(\rho^{'}\mathbf{u}^n\right)\,\mathrm{d}\Omega}^{3} + \theta_1\overline{\rho}^{'}\overbrace{\int_\Omega \frac{\partial N^l}{\partial x_i}\Delta u_i^*\,\mathrm{d}\Omega}^{4}$$

$$-\Delta t\theta_1\frac{\overline{\rho}'}{\overline{\rho}}\overbrace{\int_\Omega \frac{\partial N^l}{\partial x_i}\frac{\partial p^n}{\partial x_i}\,\mathrm{d}\Omega}^{5} - \theta_1\overline{\rho}'\overbrace{\int_\Gamma N^l\left(\Delta u_i^* - \frac{1}{\overline{\rho}}\frac{\partial p^{n+\theta_2}}{\partial x_i}\right)\cdot n_{b,i}\,\mathrm{d}\Gamma}^{6}\,. \quad \text{(C.24)}$$

$$a^2 = a^2(\phi) = a_1^2 + (a_2^2 - a_1^2)\phi\,,$$

$$\overline{\rho}' = \frac{\rho'^a + \rho'^b + \rho'^c}{3}\,.$$

For clarity, integrals 1 and 2 will be expressed in matrix form because they constitute the coefficients matrix of the equations system.

Integral 1

$$\int_\Omega N^l \frac{1}{a^2}\frac{\Delta p}{\Delta t}\,\mathrm{d}\Omega = \frac{1}{\overline{a}^2\Delta t}\frac{A}{12}\begin{pmatrix} 2 & 1 & 1\\ 1 & 2 & 1\\ 1 & 1 & 2\end{pmatrix}\begin{pmatrix}\Delta p^a\\ \Delta p^b\\ \Delta p^c\end{pmatrix}\,, \quad \text{(C.25)}$$

$$\overline{a}^2 = \frac{(a^2)^a + (a^2)^b + (a^2)^c}{3}\,.$$

Integral 2

$$\int_\Omega \frac{\partial N^l}{\partial x_i}\frac{\partial\,(\Delta p)}{\partial x_i}\,\mathrm{d}\Omega =$$

$$A\begin{pmatrix} \left(\frac{\partial N^a}{\partial x_1}\right)^2 + \left(\frac{\partial N^a}{\partial x_2}\right)^2 & \frac{\partial N^a}{\partial x_1}\frac{\partial N^b}{\partial x_1} + \frac{\partial N^a}{\partial x_2}\frac{\partial N^b}{\partial x_2} & \frac{\partial N^a}{\partial x_1}\frac{\partial N^c}{\partial x_1} + \frac{\partial N^a}{\partial x_2}\frac{\partial N^c}{\partial x_2}\\ \frac{\partial N^b}{\partial x_1}\frac{\partial N^a}{\partial x_1} + \frac{\partial N^b}{\partial x_2}\frac{\partial N^a}{\partial x_2} & \left(\frac{\partial N^b}{\partial x_1}\right)^2 + \left(\frac{\partial N^b}{\partial x_2}\right)^2 & \frac{\partial N^b}{\partial x_1}\frac{\partial N^c}{\partial x_1} + \frac{\partial N^b}{\partial x_2}\frac{\partial N^c}{\partial x_2}\\ \frac{\partial N^c}{\partial x_1}\frac{\partial N^a}{\partial x_1} + \frac{\partial N^c}{\partial x_2}\frac{\partial N^a}{\partial x_2} & \frac{\partial N^c}{\partial x_1}\frac{\partial N^b}{\partial x_1} + \frac{\partial N^c}{\partial x_2}\frac{\partial N^b}{\partial x_2} & \left(\frac{\partial N^c}{\partial x_1}\right)^2 + \left(\frac{\partial N^c}{\partial x_2}\right)^2 \end{pmatrix}\begin{pmatrix}\Delta p^a\\ \Delta p^b\\ \Delta p^c\end{pmatrix}\,, \quad \text{(C.26)}$$

Integral 3

$$-\int_\Omega N^l \nabla \cdot (\rho' \mathbf{u}^n)\ \mathrm{d}\Omega \approx -\overline{\rho}' \frac{A}{3} \left(\frac{\partial u_k^n}{\partial x_k} \right) \text{ for nodes } a, b, c. \tag{C.27}$$

Integral 4

$$\int_\Omega \frac{\partial N^l}{\partial x_i} \Delta u_i^*\ \mathrm{d}\Omega = A \left(\frac{\partial N^l}{\partial x_i} \overline{\Delta u_i^*} \right) \quad \text{for } l = a, b, c\,, \tag{C.28}$$

$$\overline{\Delta u_i^*} = \frac{(\Delta u_i^*)^a + (\Delta u_i^*)^b + (\Delta u_i^*)^c}{3}\,.$$

Integral 5

$$\int_\Omega \frac{\partial N^l}{\partial x_i} \frac{\partial p^n}{\partial x_i}\ \mathrm{d}\Omega = A \left(\frac{\partial N^l}{\partial x_i} \frac{\partial p^n}{\partial x_i} \right) \quad \text{for } l = a, b, c\,, \tag{C.29}$$

$$\frac{\partial p}{\partial x_i} = \frac{\partial N^a}{\partial x_i} p^a + \frac{\partial N^b}{\partial x_i} p^b + \frac{\partial N^c}{\partial x_i} p^c\,.$$

Integral 6

$$\int_\Gamma N^l \left(\Delta u_i^* - \frac{1}{\overline{\rho}} \frac{\partial p^{n+\theta_2}}{\partial x_i} \right) \cdot n_{b,i}\ \mathrm{d}\Gamma \approx \frac{L_\Gamma}{2} \left[\left(\frac{(\Delta u_i^*)^a + (\Delta u_i^*)^b + (\Delta u_i^*)^l}{3} - \frac{1}{\overline{\rho}} \frac{\partial p^n}{\partial x_i} \right) \cdot n_{b,i} \right] \text{ for } l = a, b\,. \tag{C.30}$$

Note that last integral vanishes on boundaries with wall or slip conditions.

C.4 Hydrodynamics Solution - Velocity Calculation

Final step is the computation of $\mathbf{u}^{n+1}=\mathbf{u}^n+\Delta\mathbf{u}^*+\Delta\mathbf{u}^{**}$. Standard Galerkin method for Eq. (3.48) gives over one single element Ω,

$$\overbrace{\int_\Omega N^l \Delta u_m^{**}\,\mathrm{d}\Omega}^{1} = -\Delta t \overbrace{\int_\Omega N^l \frac{1}{\rho}\frac{\partial p^{n+\theta_2}}{\partial x_m}\,\mathrm{d}\Omega}^{2} + \frac{\Delta t^2}{2}\overbrace{\int_\Omega N^l u_i^{n+1/2}\frac{\partial}{\partial x_i}\left(\frac{1}{\rho}\frac{\partial p^{n+\theta_2}}{\partial x_m}\right)\,\mathrm{d}\Omega}^{3}, \quad \text{(C.31)}$$

where $p^{n+\theta_2}=p^n+\theta_2\Delta p$ and integral 1 can be obtained from Eq. (C.2) by replacing ϕ with Δu_m^{**}.

Integral 2

$$\int_\Omega N^l \frac{1}{\rho}\frac{\partial p^{n+\theta_2}}{\partial x_m}\,\mathrm{d}\Omega \approx \frac{1}{\overline{\rho}}\frac{A}{3}\frac{\partial p^{n+\theta_2}}{\partial x_m} \quad \text{for nodes } a,b,c\,. \quad \text{(C.32)}$$

Integral 3

$$\int_\Omega N^l u_i^{n+1/2}\frac{\partial}{\partial x_i}\left(\frac{1}{\rho}\frac{\partial p^{n+\theta_2}}{\partial x_m}\right)\,\mathrm{d}\Omega = \overbrace{-\int_\Omega \frac{\partial}{\partial x_i}\left(N^l u_i^{n+1/2}\right)\left(\frac{1}{\rho}\frac{\partial p^{n+\theta_2}}{\partial x_m}\right)\,\mathrm{d}\Omega}^{3a} + \overbrace{\int_\Gamma N^l\left(\frac{1}{\rho}\frac{\partial p^{n+\theta_2}}{\partial x_m}\right)\left(u_i^{n+1/2}\cdot n_{b,i}\right)\,\mathrm{d}\Gamma}^{3b}. \quad \text{(C.33)}$$

Integral 3a

$$-\int_\Omega \frac{\partial}{\partial x_i}\left(N^l u_i^{n+1/2}\right)\left(\frac{1}{\rho}\frac{\partial p^{n+\theta_2}}{\partial x_m}\right)\,\mathrm{d}\Omega \approx -\frac{A}{\overline{\rho}}\left[\frac{\partial p^{n+\theta_2}}{\partial x_m}\left(\overline{u}_i^{n+1/2}\frac{\partial N^l}{\partial x_i}\right)\right] \quad \text{for } l=a,b,c\,. \quad \text{(C.34)}$$

Integral 3b

$$\int_\Gamma N^l \left(\frac{1}{\rho}\frac{\partial p^{n+\theta_2}}{\partial x_m}\right) u_i^{n+1/2} \cdot n_{b,i}\, \mathrm{d}\Gamma \approx \frac{L_\Gamma}{6}\frac{1}{\overline{\rho}}\left(\frac{\partial p^{n+\theta_2}}{\partial x_m}\right)\left[\left(u_i^a + u_i^b + u_i^l\right)^{n+1/2} \cdot n_{b,i}\right] \quad \text{for } l = a, b\,. \quad \text{(C.35)}$$

Appendix D

First Order Upwind Scheme

D.1 Advection Equation

The proposed low order approach is an upwind monotone scheme independent of the high order solution. Procedure to construct the low order response was reported in Ref. [61], where it was demonstrated that standard Galerkin discretisation of an advective equation plus an added numerical diffusion has an equivalent discretisation on median dual grids (where bounds pass through the centroid of the elements and midside of edges). A similar conclusion can be found in Ref. [2]. Now consider Fig. D.1, where G is the centroid of triangle Ω, ab, bc and ca are the middle points of edges a-b, b-c and c-a respectively, and $\mathbf{n}_{abG}$, $\mathbf{n}_{bcG}$ and $\mathbf{n}_{caG}$ are the normals to the segments G-ab, G-bc and G-ca respectively. Then, according to aforementioned premise, next equation is satisfied,

$$
\begin{aligned}
&\int_\Omega \frac{\partial N^l}{\partial x_i} B^n u_i^n \,\mathrm{d}\Omega - \int_\Omega \frac{\partial N^l}{\partial x_i} \mathcal{K}_{ij} \frac{\partial B^n}{\partial x_j} \,\mathrm{d}\Omega = \\
&\quad - \left[\frac{1}{2}\left(u^{ab} + \left|u^{ab}\right|\right) L_{abG} B_a^n + \frac{1}{2}\left(u^{ab} - \left|u^{ab}\right|\right) L_{abG} B_b^n\right] + \\
&\left[\frac{1}{2}\left(u^{ca} + |u^{ca}|\right) L_{caG} B_c^n + \frac{1}{2}\left(u^{ca} - |u^{ca}|\right) L_{caG} B_a^n\right] \quad \text{if} \quad l = a\,, \\
&\quad - \left[\frac{1}{2}\left(u^{bc} + \left|u^{bc}\right|\right) L_{bcG} B_b^n + \frac{1}{2}\left(u^{bc} - \left|u^{bc}\right|\right) L_{bcG} B_c^n\right] + \\
&\left[\frac{1}{2}\left(u^{ab} + \left|u^{ab}\right|\right) L_{abG} B_a^n + \frac{1}{2}\left(u^{ab} - \left|u^{ab}\right|\right) L_{abG} B_b^n\right] \quad \text{if} \quad l = b\,, \quad \text{and} \\
&\quad - \left[\frac{1}{2}\left(u^{ca} + |u^{ca}|\right) L_{caG} B_c^n + \frac{1}{2}\left(u^{ca} - |u^{ca}|\right) L_{caG} B_a^n\right] + \\
&+ \left[\frac{1}{2}\left(u^{bc} + \left|u^{bc}\right|\right) L_{bcG} B_b^n + \frac{1}{2}\left(u^{bc} - \left|u^{bc}\right|\right) L_{bcG} B_c^n\right] \quad \text{if} \quad l = c\,.
\end{aligned}
\tag{D.1}
$$

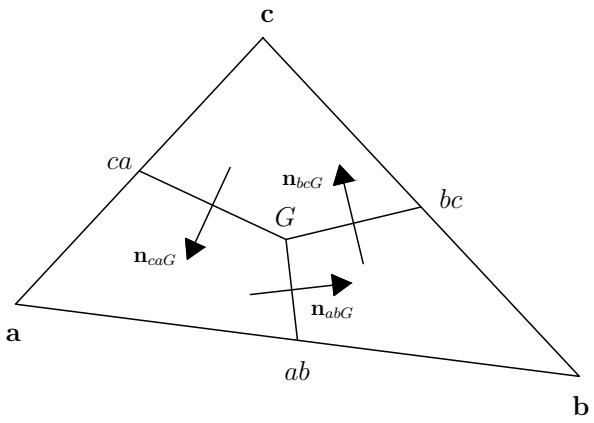

Figure D.1: Element Ω from a discretised domain.

In last equations, N^l is the shape function of node l, $\mathcal{K}_{ij}$ is an artificial diffusivity tensor, L_{pq} is the length of segment p-q and

$$u^{ab} = \left[\frac{\mathbf{u}^a + \mathbf{u}^b}{2} \cdot \mathbf{n}_{abG}\right]^n ,$$
$$u^{bc} = \left[\frac{\mathbf{u}^b + \mathbf{u}^c}{2} \cdot \mathbf{n}_{bcG}\right] ,$$
$$u^{ca} = \left[\frac{\mathbf{u}^c + \mathbf{u}^a}{2} \cdot \mathbf{n}_{caG}\right] .$$

Then, the resulting LO scheme for a node p after a forward Euler discretisation in time is,

$$\Delta b^p_{LO} = \frac{\Delta t}{\mathbf{M}_{L,pp}} \left(\sum^{e} F_{\text{Inflow}} - \sum^{e} F_{\text{Outflow}} \right) , \tag{D.2}$$

where Δb^p_{LO}=$(b^p)^{n+1}_{LO} - (B^p)^n$ ($\mathbf{b}_{LO}$ is the LO answer), $\mathbf{M}_{L,pp}$ is the lumped mass matrix element corresponding to node p, e is the total number of surrounding elements connected with node p and F_{Inflow}, F_{Outflow} can be computed from equation (D.1).

D.2 Source Terms Integration

Now a transport equation with source term Q is considered. If it is assumed that source values are known per node, final solution (D.2) can be modified

as follows,

$$\Delta b_{LO}^{p} = \frac{\Delta t}{\mathbf{M}_{L,pp}} \left(\sum^{e} F_{\text{Inflow}} - \sum^{e} F_{\text{Outflow}} \right) + \Delta t Q_p \,. \tag{D.3}$$

However, if source term involves derivatives, these are obtained per element in the FE domain. In this case, source term can be reconstructed from element values to nodal values in the following way,

$$Q_p = \frac{1}{\mathbf{M}_{L,pp}} \sum_{q=1}^{e} Q_q \mathbf{M}_{L,p}^{q} \,. \tag{D.4}$$

In last equation, subindexes p and q indicate values per node and per element respectively, and $\mathbf{M}_{L,p}^{q}$ is the term corresponding to node p of the individual lumped mass matrix of finite element q. Hence, for linear triangles $\mathbf{M}_{L,p}^{q}$=$A_q/3$, and for bilinear quadrilateral $\mathbf{M}_{L,p}^{q}$=$A_q/4$, where A_q is the area of finite element q.

Appendix E

Matrices for Refinement

Two refinement methodologies are designed, the first one divides each triangle into three triangles by introducing an additional node at the triangle centre (see Fig. E.1). In this case, for refinement, new node values can be calculated as

$$B^4 = \frac{B^1 + B^2 + B^3}{3},$$

which conserves the element mass and respects the bounds. However, for unrefinement process, it must be employed the procedure proposed in section 3.7. System (3.90) for unrefinement process of a single element is

$$\frac{\Omega}{12}\begin{bmatrix} 2 & 1 & 1 \\ 1 & 2 & 1 \\ 1 & 1 & 2 \end{bmatrix}\begin{bmatrix} B_*^1 \\ B_*^2 \\ B_*^3 \end{bmatrix} = \frac{\Omega}{108}\begin{bmatrix} 14 & 5 & 5 & 12 \\ 5 & 14 & 5 & 12 \\ 5 & 5 & 14 & 12 \end{bmatrix}\begin{bmatrix} B^1 \\ B^2 \\ B^3 \\ B^4 \end{bmatrix}$$

Second alternative divides the element into four triangles by adding nodes at edges middle points. Thus, there are three types of elements shown in Fig. E.2. For this kind of refinement, new nodal values can not be calculated as the average of edge nodal values because resulting field is not always conservative. Specifically, it is not possible when it is transformed an element previously divided in two triangles into an element divided in four triangles.

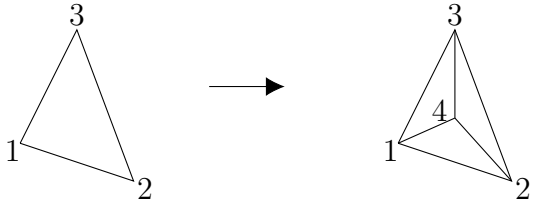

Figure E.1: Refinement: Alternative 1

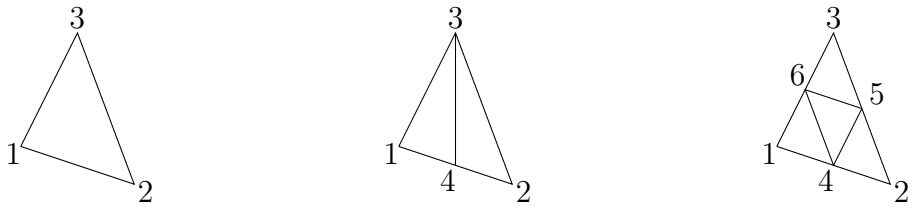

Figure E.2: Refinement: Alternative 2

In this manner, there are seven different cases of refinement or unrefinement. For each option, system (3.90) for a single element is:

1. From two triangles to one triangle (unrefinement), see Fig. E.3:

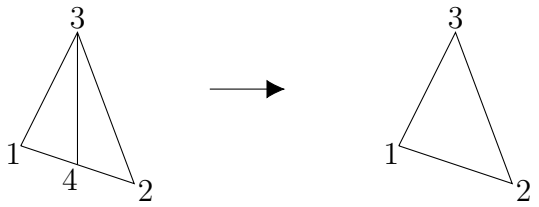

Figure E.3: Two triangles to one triangle

$$\frac{\Omega}{12}\begin{bmatrix}2 & 1 & 1\\ 1 & 2 & 1\\ 1 & 1 & 2\end{bmatrix}\begin{bmatrix}B^1_*\\ B^2_*\\ B^3_*\end{bmatrix} = \frac{\Omega}{48}\begin{bmatrix}5 & 1 & 4 & 6\\ 1 & 5 & 4 & 6\\ 2 & 2 & 8 & 4\end{bmatrix}\begin{bmatrix}B^1\\ B^2\\ B^3\\ B^4\end{bmatrix}$$

2. From four triangles to one triangle (unrefinement), see Fig. E.4:

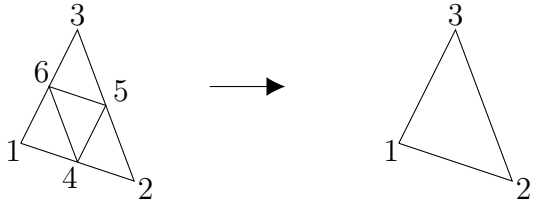

Figure E.4: Four triangles to one triangle

$$\frac{\Omega}{12}\begin{bmatrix}2&1&1\\1&2&1\\1&1&2\end{bmatrix}\begin{bmatrix}B_*^1\\B_*^2\\B_*^3\end{bmatrix}=\frac{\Omega}{96}\begin{bmatrix}6&1&1&10&4&10\\1&6&1&10&10&4\\1&1&6&4&10&10\end{bmatrix}\begin{bmatrix}B^1\\B^2\\B^3\\B^4\\B^5\\B^6\end{bmatrix}$$

3. From four triangles to two triangles (unrefinement), see Fig. E.5:

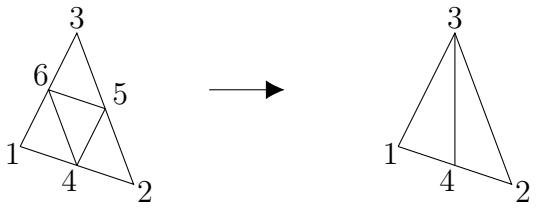

Figure E.5: Four triangles to two triangle

$$\frac{\Omega}{24}\begin{bmatrix}2&0&1&1\\0&2&1&1\\1&1&4&2\\1&1&2&4\end{bmatrix}\begin{bmatrix}B_*^1\\B_*^2\\B_*^3\\B_*^4\end{bmatrix}=\frac{\Omega}{192}\begin{bmatrix}10&0&1&7&1&13\\0&10&1&7&13&1\\2&2&12&8&20&20\\4&4&2&26&14&14\end{bmatrix}\begin{bmatrix}B^1\\B^2\\B^3\\B^4\\B^5\\B^6\end{bmatrix}$$

4. Change edge, see Fig. E.6:

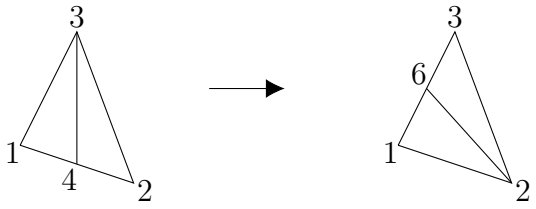

Figure E.6: Change edge

$$\frac{\Omega}{24}\begin{bmatrix}2&1&0&1\\1&4&1&2\\0&1&2&1\\1&2&1&4\end{bmatrix}\begin{bmatrix}B_*^1\\B_*^2\\B_*^3\\B_*^6\end{bmatrix}=\frac{\Omega}{144}\begin{bmatrix}10&1&3&10\\3&15&12&18\\1&4&15&4\\10&4&18&16\end{bmatrix}\begin{bmatrix}B^1\\B^2\\B^3\\B^4\end{bmatrix}$$

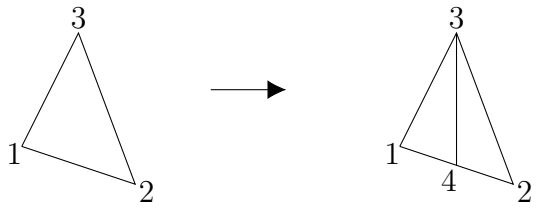

Figure E.7: One triangle to two triangles

5. From one triangle to two triangles (refinement), see Fig. E.7:

$$\frac{\Omega}{24}\begin{bmatrix}2&0&1&1\\0&2&1&1\\1&1&4&2\\1&1&2&4\end{bmatrix}\begin{bmatrix}B_*^1\\B_*^2\\B_*^3\\B_*^4\end{bmatrix}=\frac{\Omega}{48}\begin{bmatrix}5&1&2\\1&5&2\\4&4&8\\6&6&4\end{bmatrix}\begin{bmatrix}B^1\\B^2\\B^3\end{bmatrix}$$

6. From one triangle to four triangles (refinement), see Fig. E.8:

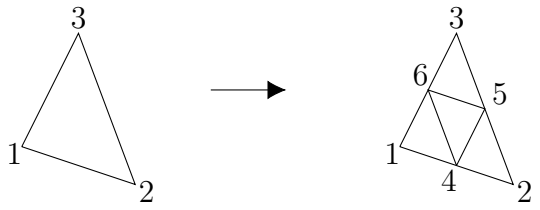

Figure E.8: One triangle to four triangles

$$\frac{\Omega}{48}\begin{bmatrix}2&0&0&1&0&1\\0&2&0&1&1&0\\0&0&2&0&1&1\\1&1&0&6&2&2\\0&1&1&2&6&2\\1&0&1&2&2&6\end{bmatrix}\begin{bmatrix}B_*^1\\B_*^2\\B_*^3\\B_*^4\\B_*^5\\B_*^6\end{bmatrix}=\frac{\Omega}{96}\begin{bmatrix}6&1&1\\1&6&1\\1&1&6\\10&10&4\\4&10&10\\10&4&10\end{bmatrix}\begin{bmatrix}B^1\\B^2\\B^3\end{bmatrix}$$

7. From two triangles to four triangles (refinement), see Fig. E.9:

$$\frac{\Omega}{48}\begin{bmatrix}2&0&0&1&0&1\\0&2&0&1&1&0\\0&0&2&0&1&1\\1&1&0&6&2&2\\0&1&1&2&6&2\\1&0&1&2&2&6\end{bmatrix}\begin{bmatrix}B_*^1\\B_*^2\\B_*^3\\B_*^4\\B_*^5\\B_*^6\end{bmatrix}=\frac{\Omega}{192}\begin{bmatrix}10&0&2&4\\0&10&2&4\\1&1&12&2\\7&7&8&26\\1&13&20&14\\13&1&20&14\end{bmatrix}\begin{bmatrix}B^1\\B^2\\B^3\\B^4\end{bmatrix}$$

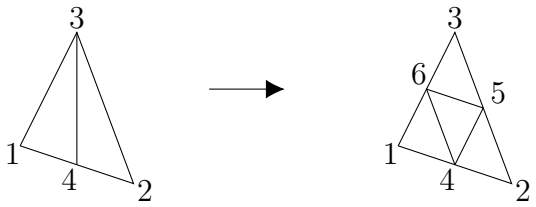

Figure E.9: Two triangles to four triangles

Appendix F

Axisymmetric Model

Axisymmetric formulation is obtained from conservation equations in cylindrical coordinates (see e.g. Appendix B of Ref. [40]), by neglecting terms in the azimuthal direction and derivatives respect to the azimuthal coordinate. Thus, transport and Navier-Stokes equations are,

$$\frac{\partial \phi}{\partial t} + \nabla_o \cdot (\mathbf{u}_o \phi) = 0\,, \tag{F.1}$$

$$\frac{\partial}{\partial t}\left(\frac{p - p_0}{a_1^2 + (a_2^2 - a_1^2)\phi}\right) + \nabla_o \cdot \left(\rho' \mathbf{u}_o\right) = 0\,, \tag{F.2}$$

$$\frac{\partial \mathbf{u}_o}{\partial t} + \nabla_o \cdot (\mathbf{u}_o \mathbf{u}_o) = -\frac{1}{\rho}\nabla_o p + \frac{1}{\rho}\nabla_o \cdot \tau_o + \mathbf{g} + \mathbf{T} + \mathbf{Q}_o\,, \tag{F.3}$$

where $\mathbf{u}_o{=}(u_r, u_z)$, u_r, u_z are radial and axial velocity components, $\nabla_o \cdot \tau_o{=}\mu\left(\nabla_o^2 u_r - \frac{u_r}{r^2}\right)\mathbf{r}{+}\mu\left(\nabla_o^2 u_z\right)\mathbf{z}$, $\mathbf{Q}_o{=}\mathbf{u}_o(\nabla_o{\cdot}\mathbf{u}_o)$ and operators $\nabla_o^2 f = \frac{1}{r}\frac{\partial}{\partial r}\left(r\frac{\partial f}{\partial r}\right){+}\frac{\partial^2 f}{\partial z^2}$, $\nabla_o f{=}\frac{\partial f}{\partial r}\mathbf{r} + \frac{\partial f}{\partial z}\mathbf{z}$, $\nabla_o \cdot \mathbf{f}_o{=}\frac{1}{r}\frac{\partial (r f_r)}{\partial r} + \frac{\partial f_z}{\partial z}$, r and z are the radial and axial coordinates, f is a scalar field and $\mathbf{f}_o$ is a vector field.

Now, taking into account that differential volume is $2\pi r \mathrm{d}\Omega$, discretisation according to characteristic Galerkin method of previous equations are:

- Solution of phase function is defined by the finite element spaces $\mathcal{W}^h \subset \mathcal{W} = \{w \in H^1(\Omega) \mid w = 0 \text{ on } \Gamma_\phi^-\}$ and $\Phi^h \subset \Phi{=}\{\phi \in H^1(\Omega) \mid \phi =$

$\overline{\phi}$ on $\Gamma_\phi^-\}$, and it is formulated as: Find $\phi^h \in \Phi^h$ such that

$$\left(rw^h, \frac{\Delta\phi^h}{\Delta t}\right)_\Omega = \left(\mathbf{u}_o^{n+1/2} \cdot \nabla_o w^h, r(\phi^h)^n\right)_\Omega - \frac{\Delta t}{2}\left\{\left\langle r\nabla_o \cdot \left(w^h \left(\mathbf{u}_o^h \mathbf{u}_o^h\right)^{n+1/2}\right), \nabla_o(\phi^h)^n\right\rangle_{\Omega_I} - \left\langle rw^h \left((\mathbf{u}_o^h)^{n+1/2} \cdot \nabla_o(\mathbf{u}_o^h)^n\right), \nabla_o(\phi^h)^n\right\rangle_{\Omega_I} + \left(r\nabla_o \cdot \left(w^h(\mathbf{u}_o^h)^{n+1/2}\right), \left(\phi^h \nabla_o \cdot \mathbf{u}_o^h\right)^n\right)_{\Omega_I}\right\} - \left[w^h, r\phi^h \mathbf{u}_o\right]_{\Gamma^+}^n - \left[w^h, r\overline{\mathbf{q}}_\phi\right]_{\Gamma_q^-}^n \ , \ \forall\ w^h \in \mathcal{W}^h \ . \quad \text{(F.4)}$$

- Find $(p^h)^{n+1} \in \mathcal{P}^h$ for all $t \in [t_o, T]$, such that

$$\left(\frac{r}{(a^2)^{n+1/2}} w^h, \frac{\Delta p^h}{\Delta t}\right)_\Omega + \frac{\theta\Delta t}{2}\left\langle \nabla_o w^h, \frac{(\rho')^{n+1/2}}{\rho^{n+1/2}} r\nabla_o(\Delta p^h)\right\rangle_\Omega = -\left(rw^h, \nabla_o \cdot \left(\rho' \mathbf{u}_o^h\right)\right)_\Omega^n + \frac{1}{2}\left\langle \nabla_o w^h, (\rho')^{n+1/2} r\Delta\mathbf{u}_o^{*h}\right\rangle_\Omega - \frac{\Delta t}{2}\left\langle \nabla_o w^h, \frac{\rho'}{\rho} r\nabla_o p^h\right\rangle_\Omega^n - \frac{1}{2}\left[w^h, (\rho')^{n+1/2} r\Delta\mathbf{u}_o^h\right]_\Gamma \ , \quad \forall\ v_i^h \in \mathcal{V}_i^h, \ \ w^h \in \mathcal{W}^h \ , \quad \text{(F.5)}$$

- Find $(u_i^h)^{n+1} \in \mathcal{U}_i^h$, $(i = r, z)$ for all $t \in [t_o, T]$, such that

$$\left(rv_i^h, \frac{\Delta u_i^{*h}}{\Delta t}\right)_\Omega = -\left(rv_i^h, \nabla_o \cdot \left((\mathbf{u}_o^h)^{n+1/2}(u_i^h)^n\right)\right)_\Omega + \left(rv_i^h, f_i^h\right)_\Omega^{n+1/2} + \left(rv_i^h, g_i\right)_\Omega^n - \frac{\Delta t}{2}\left\{\left\langle r\nabla_o \cdot \left(v_i^h \left(\mathbf{u}_o^h \mathbf{u}_o^h\right)^{n+1/2}\right), \nabla_o(u_i^h)^n\right\rangle_{\Omega_I} - \left\langle rv_i^h \left((\mathbf{u}_o^h)^{n+1/2} \cdot \nabla_o(\mathbf{u}_o^h)^n\right), \nabla_o(u_i^h)^n\right\rangle_{\Omega_I} + \left(r\nabla_o \cdot \left(v_i^h(\mathbf{u}_o^h)^{n+1/2}\right), \left(u_i^h \nabla_o \cdot \mathbf{u}_o^h\right)^n\right)_{\Omega_I} + \left(rv_i^h, (\mathbf{u}_o^h)^{n+1/2} \cdot (\nabla_o(f_i^h + g_i))^n\right)_{\Omega_I} + \left(r\nabla_o \cdot v^h(\mathbf{u}_o^h)^{n+1/2}, (\nabla_o p^h)_i^n\right)_{\Omega_I}\right\} , \quad \text{(F.6)}$$

  where $\mathbf{f}=\frac{\mu}{\rho}\left(\left(\nabla_o^2 u_r - \frac{u_r}{r^2}\right)\mathbf{r} + \left(\nabla_o^2 u_z\right)\mathbf{z}\right)+\mathbf{T}+\mathbf{Q}_o$. For nearly incompressible flows, viscous terms depending on velocity divergence are neglected.

Second order terms in last equations are constructed considering r as a constant value per element. The domain Ω is delimited by the axis of symmetry. Ω is subdivided by E elements Ω_j, $(j = 1, E)$ such that $\Omega = \bigcup \Omega_j$, while Ω_I is the domain without elements with sides belonging to the boundary.

References

[1] Baines, W.D. Air Cavities as Gravity Currents on Slope. *Journal of Hydraulic Engineering, ASCE*, 117:1600–1615, 1992.

[2] Barth, T.J. Aspects of unstructured grids and finite-volume solvers for the Euler and Navier-Stokes equations. *AGARD, Special Course on Unstructured Grid Methods for Advection Dominated Flows*, 1992.

[3] Bashiri-Atrabi, H. and Hosoda, T. The motion of entrapped air cavities in inclined ducts. *Journal of Hydraulic Research*, 1686:1–6, 2015.

[4] Bashiri-Atrabi, H., Hosoda, T., and Tada, A. Simulation of Air Cavity Advancing into a Straight Duct. *ASCE Journal of Hydraulic Engineering*, pages 1–9, 2015.

[5] Batchelor, G. *An Introduction to Fluid Dynamics (Cambridge Mathematical Library)*. Cambridge University Press, 2000.

[6] Baumbach, V., Hopfinger, E., and Cartellier, A. The transient behaviour of a large bubble in a vertical tube. *Journal of Fluid Mechanics*, 524:131–142, 2005.

[7] Bendiksen, K.H. On the motion of long bubbles in vertical tubes. *International Journal of Multiphase Flow*, 11:797–812, 1985.

[8] Benjamin, T.B. Gravity currents and related phenomena. *Journal of Fluid Mechanics*, 31:209–248, 1968.

[9] Bilger, C., Aboukhedr, M., Vogiatzaki, K., and Cant, R. Evaluation of two-phase flow solvers using level set and volume of fluid methods. *Journal of Computational Physics*, 345:665–686, 2017.

[10] Boris, J.P. and Book, D.L. Flux-corrected transport. I. SHASTA, a fluid transport algorithm that works. *Journal of Computational Physics*, 11:38–69, 1973.

[11] Brackbill, J.U., Kothe, D.B., and Zemach, C. A continuum method for modeling surface tension. *Journal of Computational Physics*, 100:335–354, 1992.

[12] Brezzi, F. and Fortin, M. *Mixed and hybrid finite element methods*, volume 15. Springer Science & Business Media, 2012.

[13] Brooks, A.N. and Hughes, T.J.R. Streamline upwind/Petrov-Galerkin formulations for convection dominated flows with particular emphasis on the incompressible Navier-Stokes equations. *Computer Methods in Applied Mechanics and Engineering*, 32(1-3):199–259, 1982.

[14] Cebral, J.R. and Löhner, R. Conservative load projection and tracking for fluid-structure problems. *AIAA journal*, 35:687–692, 1997.

[15] Chandrasekhar, S. *Hydrodynamic and hydromagnetic stability*. Courier Corporation, 2013.

[16] Chiodi, R. and Desjardins, O. A reformulation of the conservative level set reinitialization equation for accurate and robust simulation of complex multiphase flows. *Journal of Computational Physics*, 343:186–200, 2017.

[17] Cruchaga, M., Battaglia, L., Storti, M., and D'Elía, J. Numerical modeling and experimental validation of free surface flow problems. *Archives of Computational Methods in Engineering*, 23:139–169, 2016.

[18] Cruchaga, M., Celentano, D., and Tezduyar, T. A moving lagrangian interface technique for flow computations over fixed meshes. *Computer Methods in Applied Mechanics and Engineering*, 191:525–543, 2001.

[19] Cruchaga, M., Celentano, D., and Tezduyar, T. Moving-interface computations with the edge-tracked interface locator technique (etilt). *International Journal for Numerical Methods in Fluids*, 47:451–469, 2005.

[20] Cruchaga, M., Celentano, D., and Tezduyar, T. Collapse of a liquid column: numerical simulation and experimental validation. *Computational Mechanics*, 39:453–476, 2007.

[21] Davies, R.M. and Taylor, G.I. The mechanics of large bubbles rising through extended liquids and through liquids in tubes. *Proceedings of the Royal Society A*, 200:375–390, 1950.

[22] Desjardins, O., Moureau, V., and Pitsch, H. An accurate conservative level set/ghost fluid method for simulating turbulent atomization. *Journal of Computational Physics*, 227(18):8395–8416, 2008.

[23] Donea, J. A Taylor–Galerkin method for convective transport problems. *International Journal for Numerical Methods in Engineering*, 20:101–119, 1984.

[24] Dumitrescu, D.T. Strömung an einer luftblase im senkrechten rohr. *Zeitschrift fur Angewandte Mathematik und Mechanik*, 24:139–149, 1943.

[25] Garabedian, P.R. On steady-state bubbles generated by Taylor instability. *Proceedings of the Royal Society A*, 241:423–431, 1957.

[26] Gough, H., Gaitonde, A.L., and Jones, D. A dual-time central difference finite volume scheme for interface capturing on unstructured meshes. *International Journal for Numerical Methods in Fluids*, 60:149–175, 2009.

[27] Gross, S. and Reusken, A. *Numerical methods for two-phase incompressible flows*. Springer Science & Business Media, 2011.

[28] Guermond, J.L., Pasquetti, R., and Popov, B. Entropy viscosity method for nonlinear conservation laws. *Journal of Computational Physics*, 230:4248–4267, 2011.

[29] Guermond, J.L., Quezada de Luna, M., and Thompson, T. An conservative anti-diffusion technique for the level set method. *Journal of Computational and Applied Mathematics*, 321:448–468, 2017.

[30] Guo, Q. and Song, C.C.S. Dropshaft Hydrodynamics under Transient Conditions. *Journal of Hydraulic Engineering*, 117:1042–1055, 1991.

[31] Harten, A. The artificial compression method for computation of shocks and contact discontinuities. I. Single conservation laws. *Communications on Pure and Applied Mathematics*, 30:611–638, 1977.

[32] Harten, A., Engquist, B., Osher, S., and Chakravarthy, S.R. Uniformly High Order Accurate Essentially Non-oscillatory Schemes, III. *Journal of Computational Physics*, 131:3–47, 1997.

[33] Harten, A., Hyman, J. M., Lax, P. D., and Keyfitz, B. On finite-difference approximations and entropy conditions for shocks. *Communications on Pure and Applied Mathematics*, 29:297–322, 1976.

[34] Hirt, C. and Nichols, B. Volume of Fluid (VOF) method for the dynamics of free boundaries. *Journal of Computational Physics*, 39:201–225, 1981.

[35] Kees, C., Akkerman, I., Farthing, M., and Bazilevs, Y. A conservative level set method suitable for variable-order approximations and unstructured meshes. *Journal of Computational Physics*, 230:4536–4558, 2011.

[36] Kelecy, F. and Pletcher, R. The development of a free surface capturing approach for multidimensional free surface flows in closed containers. *Journal of Computational Physics*, 138:939–980, 1997.

[37] Kendoush, A.A. The Virtual Mass Theory of a Taylor Bubble Rising in Vertical Pipes. *Journal of Fluids Engineering*, 140(5):051202, 2018.

[38] Kim, H. and Liou, M.-S. Accurate adaptive level set method and sharpening technique for three dimensional deforming interfaces. *Computers & Fluids*, 44:111–129, 2011.

[39] Kleefsman, K.M.T., Fekken, G., Veldman, A.E.P., Iwanowski, B., and Buchner, B. A volume-of-fluid based simulation method for wave impact problems. *Journal of Computational Physics*, 206:363–393, 2005.

[40] Kundu, P.K., Cohen, I.M., and Dowling, D.R. *Fluid Mechanics*. 2012.

[41] Kuzmin, D. and Möller, M. *Algebraic flux correction I: Scalar Conservation Laws*, pages 155–206. Springer, 2005.

[42] Kuzmin, D. and Möller, M. *Algebraic flux correction II: Compressible Euler equations*, pages 207–250. Springer, 2005.

[43] Lauchlan, C., Escarameia, M., May, R., Burrows, R., and Gahan, C. Air in pipelines-A literature review. 2005.

[44] Leon, A.S., Elayeb, I.S., and Tang, Y. An experimental study on violent geysers in vertical pipes. *Journal of Hydraulic Research*, 57:283–294, 2019.

[45] LeVeque, R.J. High-resolution conservative algorithms for advection in incompressible flow. *SIAM Journal on Numerical Analysis*, 33:627–665, 1996.

[46] Liu, X.D., Osher, S., and Chan, T. Weighted Essentially Non-oscillatory Schemes. *Journal of Computational Physics*, 115:200–212, 1994.

[47] Löhner, R. *Applied computational fluid dynamics techniques: an introduction based on finite element methods*. John Wiley & Sons, 2008.

[48] Löhner, R., Morgan, K., Peraire, J., and Vahdati, M. Finite element flux-corrected transport (FEM–FCT) for the Euler and Navier–Stokes equations. *International Journal for Numerical Methods in Fluids*, 7(10):1093–1109, 1987.

[49] Löhner, R., Yang, C., and Oñate, E. On the simulation of flows with violent free surface motion. *Computer Methods in Applied Mechanics and Engineering*, 195:5597–5620, 2006.

[50] Martin, J., Moyce, W., Price, A., and Thornhill, C. Part IV. An experimental study of the collapse of liquid columns on a rigid horizontal plane. *Phil. Trans. R. Soc. Lond. A*, 244:312–324, 1952.

[51] Mikaelian, K.O. Approximate treatment of density gradients in Rayleigh-Taylor instabilities. *Physical Review A*, 33:1216—1222, 1986.

[52] Molina, J. and Ortiz, P. A conservative flux–corrected continuous FEM for fluid interface dynamics. *International Journal for Numerical Methods in Fluids*, 91:287–310, 2019.

[53] Molina, J. and Ortiz, P. A continuous finite element solution of fluid interface propagation for emergence of cavities and geysering. *Computer Methods in Applied Mechanics and Engineering*, 359:112746, 2020.

[54] Molina, J. and Ortiz, P. Propagation of large air pockets in ducts. Analytical and numerical approaches (Under Review). *?*, ?:?, 2021.

[55] Muller, K.Z., Wang, J., and Vasconcelos, J.G. Water displacement in shafts and geysering created by uncontrolled air pocket releases. *Journal of Hydraulic Engineering*, 143:04017043, 2017.

[56] Nguyen, H., Cheng, J.C., Berger, C.R., and Savant, G. A mass conservation algorithm for adaptive unrefinement meshes used by finite element methods. *Procedia Computer Science*, 9:727–736, 2012.

[57] Nicklin, D.J. Two-phase flow in vertical tubes. *Trans. Inst. Chem. Engr.*, 40:61–68, 1962.

[58] Nigmatulin, T.R. and Bonetto, F.J. Shape of Taylor Bubbles in Vertical Tubes. *Int. Comm. Heat Mass Transfer.*, 24:1177–1185, 1997.

[59] Olsson, E. and Kreiss, G. A conservative level set method for two phase flow. *Journal of computational physics*, 210:225–246, 2005.

[60] Olsson, E., Kreiss, G., and Zahedi, S. A conservative level set method for two phase flow II. *Journal of Computational Physics*, 225:785–807, 2007.

[61] Ortiz, P. A positive definite continuous FEM model for advection. *Advances in Water Resources*, 32:1359–1371, 2009.

[62] Ortiz, P. Non-oscillatory continuous FEM for transport and shallow water flows. *Computer Methods in Applied Mechanics and Engineering*, 223-224:55 – 69, 2012.

[63] Ortiz, P. Shallow water flows over flooding areas by a flux–corrected finite element method. *Journal of Hydraulic Research*, 52:241–252, 2014.

[64] Ortiz, P., Zienkiewicz, O., and Szmelter, J. Hydrodynamics and transport in estuaries and rivers by the CBS finite element method. *International Journal for Numerical Methods in Engineering*, 66:1569–1586, 2006.

[65] Osher, S. and Sethian, J.A. Fronts propagating with curvature-dependent speed: Algorithms based on Hamilton-Jacobi formulations. *Journal of Computational Physics*, 79:12–49, 1988.

[66] Pozos, O., Gonzalez, C.A., Giesecke, J., Marx, W., and Rodal, E.A. Air entrapped in gravity pipeline systems. *Journal of Hydraulic Research*, 48:338–347, 2010.

[67] Puckett, E.G., Almgren, A.S., Bell, J.B., Marcus, D.L., and Rider, W.J. A high-order projection method for tracking fluid interfaces in variable density incompressible flows. *Journal of Computational Physics*, 130:269–282, 1997.

[68] Quan, S. and Schmidt, D.P. A moving mesh interface tracking method for 3D incompressible two-phase flows. *Journal of Computational Physics*, 221:761–780, 2007.

[69] Quezada, M., Kuzmin, D., and Kees, C.E. A monolithic conservative level set method with built–in redistancing. *Journal of Computational Physics*, 379:262–278, 2019.

[70] Rajaratnam, N. Hydraulic jumps. volume 4 of *Advances in Hydroscience*, pages 197–280. Elsevier, 1967.

[71] Rusche, H. *Computational fluid dynamics of dispersed two-phase flows at high phase fractions*. PhD thesis, Imperial College London (University of London), 2003.

[72] Sousa, R.G., Pinto, A.M.F.R., and Campos, J.B.L.M. Effect of gas expansion on the velocity of a Taylor bubble: PIV measurements. *International Journal of Multiphase Flow*, 32:1182–1190, 2006.

[73] Sussman, M. A second order coupled level set and volume-of-fluid method for computing growth and collapse of vapor bubbles. *Journal of Computational Physics*, 187:110–136, 2003.

[74] Sussman, M. and Fatemi, E. An efficient, interface-preserving level set redistancing algorithm and its application to interfacial incompressible fluid flow. *SIAM Journal on scientific computing*, 20:1165–1191, 1999.

[75] Sussman, M., Smereka, P., and Osher, S. A Level Set Approach for Computing Solutions to Incompressible Two-Phase Flow. *Journal of Computational Physics*, 114:146–159, 1994.

[76] Talvy, C.A., Shemer, L., and Barnea, D. On the interaction between two consecutive elongated bubbles in a vertical pipe. *International Journal of Multiphase Flow*, 26:1905–1923, 2000.

[77] Ubbink, O. and Issa, R.I. A Method for Capturing Sharp Fluid Interfaces on Arbitrary Meshes. *Journal of Computational Physics*, 153:26–50, 1999.

[78] van der Pijl, S.P., Segal, A., Vuik, C., and Wesseling, P. A mass-conserving level-set method for modelling of multi-phase flows. *International Journal for Numerical Methods in Fluids*, 47:339–361, 2005.

[79] Vasconcelos, J.G. and Wright, S.J. Geysering generated by large air pockets released through water-filled ventilation shafts. *Journal of Hydraulic Engineering*, 137:543–555, 2011.

[80] Wang, L.F., Xue, C., Ye, W.H., and Li, Y.J. Destabilizing effect of density gradient on the Kelvin–Helmholtz instability. *Physics of Plasmas*, 16:112104, 2009.

[81] Wilkinson, D.L. Motion of air cavities in long horizontal ducts. *Journal of Fluid Mechanics*, 118:109, 1982.

[82] Wright, S.J., Lewis, J.W., and Vasconcelos, J.G. Geysering in rapidly filling storm-water tunnels. *Journal of Hydraulic Engineering*, 137:112–115, 2011.

[83] Wylie, E.B., Suo, L., and Streeter, L. *Fluid transients in systems*. Prentice Hall Englewood Cliffs, NJ, 1993.

[84] Zalesak, S.T. Fully multidimensional flux-corrected transport algorithms for fluids. *Journal of Computational Physics*, 31:335–362, 1979.

[85] Zalesak, S.T. *The design of flux–corrected transport (FCT) algorithms on structured grids*. PhD thesis, George Mason University (USA), 2005.

[86] Zhao, L., Mao, J., Bai, X., Liu, X., Li, T., and Williams, J. Finite element implementation of an improved conservative level set method for two-phase flow. *Computers & Fluids*, 100:138–154, 2014.

[87] Zienkiewicz, O.C., Nithiarasu, P., Codina, R., Vázquez, M., and Ortiz, P. The characteristic-based-split procedure: An efficient and accurate algorithm for fluid problems. *International Journal for Numerical Methods in Fluids*, 31:359–392, 1999.

[88] Zienkiewicz, O.C., Taylor, R.L., and Nithiarasu, P. *The Finite Element Method for Fluid Dynamics*. Butterworth-Heinemann, Oxford, 7 edition, 2014.

[89] Zukoski, E.E. Influence of viscosity, surface tension, and inclination angle on motion of long bubbles in closed tubes. *Journal of Fluid Mechanics*, 25:821–837, 1966.